

# Three dimensional graphene composites for energy storage applications

by

**Bello Abdulhakeem**



A thesis submitted in partial fulfilment of the requirements for the degree of

**DOCTOR OF PHILOSOPHY (PHD) IN PHYSICS**

Faculty of Natural and Agricultural Sciences

University of Pretoria

Hatfield Pretoria

March 2014

Supervisor/promoter: **Prof. N. I. Manyala**

## **Three dimensional graphene composites for energy storage applications**

by

**Bello Abdulhakeem**

Submitted in partial fulfilment of the requirements for the degree PhD in Physics in the faculty of Natural and Agricultural Science, University of Pretoria.

Promoter: Prof. N. I. Manyala

### **Abstract**

The aim and objectives of this work is the development of a three dimensional graphene foam (GF) electrode for energy storage applications and study the electrochemical properties of the electrodes modified with different metal/metal oxides nanostructures. The GF was synthesised by chemical vapor deposition (CVD) and various metal/metal oxides were grafted on the surface of the GF by various method such as microwave irradiation (MW), aqueous chemical growth (ACG), successive ionic layer adsorption and reaction (SILAR) and reflux method. The interaction and formation mechanism between the GF and the metal/metal oxides nanostructures were all discussed. The obtained composite materials were characterized by Raman spectroscopy, X-ray diffraction (XRD), scanning and transmission electron microscopy (SEM and TEM). The composite materials synthesised revealed different morphologies as seen by the different characterization techniques. The major interest in the GF for electrochemical capacitors is due to its unique structure, good conductivity and large surface area which offer the possibility for deposition/adsorption of metal/metal oxides for practical applications. The composite synthesised were all investigated as electrode for electrochemical capacitors in different electrolytes and tested with different operating voltages vs silver/silver chloride (Ag/AgCl). The electron kinetics of the composite materials was studied and all show excellent electrochemical performance. All the results have clearly shown and demonstrated the great potential of three dimensional composite based novel electrode materials for energy storage applications.

## Declaration

I hereby declare that the matter embodied in this thesis entitled “*Three dimensional graphene composites for energy storage applications*” is the result of investigations carried out by me under the supervision of Prof. N. Manyala, in the Physics department at the University of Pretoria South Africa and that it has not been submitted elsewhere for the award of any degree or diploma. In keeping with the general practice in reporting scientific observations, due acknowledgement has been made whenever the work described is based on the findings of other investigators.

Signature \_\_\_\_\_

Date \_\_\_\_\_

## Acknowledgements

I would like to take this opportunity to express my sincere appreciation to those who have helped me throughout my study. First, I would like to express my sincere gratitude to my academic adviser Prof. N. Manyala for his support, encouragement, advice, guidance, constructive criticism, valuable suggestion and discussions.

I would like to acknowledge Prof. K. I. Ozoemena for some of the ideas and discussions we had. I am also grateful to the microscopy and microanalysis unit of the University of Pretoria, Mr Andre Botha for SEM analysis, Mr Chris van der Merwe for TEM analysis and Antoinette for her help in SEM work and training.

I would also like to appreciate head of the department Prof. C. Theron for some part-time work in the department to enable me supplement my finances and both the University of Pretoria and the South African national research foundation (NRF) financial support.

I am also thankful to Dr Linda Prinsloo, Dr Wilbert Mtangi, Mr P.J. Janse van Resenburg for all the assistance with measuring equipment and discussion in the laboratory.

I also want to express my appreciation to all carbon technology research group members such as Dr. J. K. Dangbegnon, Dr S. Khamlich, Dr D. Dodoo-Ahrin, Mr M. Fabiane, Mr D. Y. Momodu, Mr Isaac, Mr F. Barzega and S. Seymore for their encouragement, help, support, sharing of knowledge and useful discussion throughout my study. I am grateful to my colleagues in chemistry, K. Makgopa, J. N. Ikitima and O. O. Fashedemi not only for their collaboration but also rescuing me whenever I needed help.

My appreciation also goes to my senior colleagues in the department and friends at the University of Pretoria that have made my stay worthwhile, Mr K. O. Obodo, Mr C. N. M Ouma, Dr T. T. Hlastshwayo, Ms Opeyemi, Ms Thabsile, Dr A. A. Yusuf, Mr Shittu, Mr

Salisu, Mr M. Mbehou, Mr M.A.Y. Mogtaba, Mr A. Habibu and Mr U. Danbaba just to mention a few.

Last but not least, this research would not have been possible without the prayers, support and encouragement from my parents and family. I whole heartedly express my gratitude and really appreciate you all. Finally special thanks to my love for her patience, unconditional love and understanding during my study. Once again i say a big thanks to all the people who have helped me directly or indirectly.

## Table of Contents

Chapter 1.....	1
Introduction.....	1
1.1 General motivation.....	2
1.2 Aims and objectives.....	3
References.....	5
Chapter 2.....	7
Literature Review.....	7
2.1 The basic principle of electrochemical capacitors.....	7
2.2 Principle of energy storage.....	8
2.2.1 Energy storage mechanism of electrical double-layer capacitors (EDLCs).....	8
2.2.2 The energy storage mechanism of pseudo-capacitance.....	16
2.3 Testing an electrochemical cell.....	18
2.4 Fabrication of cell for a two electrode configuration.....	19
2.5 Evaluation of electrode material for electrochemical capacitors.....	20
2.5.1 Cyclic voltammetry and galvanostatic chronopotentiometry (GCP).....	20
2.5.2 Galvanostatic charge/discharge (GCD).....	22
2.5.3 Electrochemical impedance spectroscopy (EIS).....	24
2.6 Advantages and applications of ECs.....	26
2.7 Application of Electrochemical capacitors.....	27
2.8 Electrode materials.....	28
2.8.1 Carbon materials:.....	30
2.8.2 Conducting polymers (CPs).....	33
2.8.3 Transition metal oxides (TMO).....	34
2.8.4 Composite materials.....	38
2.9 Electrolytes.....	39
2.10 Graphene based materials for electrochemical capacitors.....	40
2.11 Properties of graphene.....	41
References.....	44
Chapter 3.....	53
Characterization and growth techniques.....	53
Introduction.....	53
3.1 Chemical vapor deposition (CVD).....	53
3.1.1 Aqueous chemical growth technique (ACG).....	56

3.1.2	The microwave (MW) technology .....	57
3.1.3	Successive Ionic Layer Adsorption and Reaction (SILAR).....	58
3.2	Materials Characterization .....	60
3.2.1	Raman Analysis .....	60
3.2.2	Morphological Analysis.....	64
3.2.3	Crystallinity and Qualitative Phase Analysis.....	66
3.2.4	Gas Adsorption Analysis .....	67
3.2.5	Electrochemical Analysis.....	68
	Reference .....	70
	Chapter 4.....	73
	Result and discussions .....	73
4.1	Interaction between graphene foam and silver metal particles .....	73
	Introduction.....	73
	Result and discussions .....	74
	Summary .....	85
	References.....	86
4.2	Adsorption between Nickel foam graphene (NF-G) and Nickel oxide (NiO).....	87
	Introduction.....	87
	Results and discussions.....	88
	Summary .....	97
	References.....	98
4.3	Aqueous chemical growth technique (ACG) of simonkolleite microplatelets on nickel foam-graphene.....	100
	Introduction.....	100
	Results and discussions.....	102
	Summary .....	110
	References.....	111
4.4	Microwave synthesis of manganese oxide (MnO <sub>2</sub> ) nanostructure on nickel foam-graphene as electrode for electrochemical capacitors.....	112
	Introduction.....	112
	Results and discussions.....	114
	Summary .....	120
	References.....	121
4.5	Symmetric electrochemical capacitor based on graphene foam (GF) and manganese oxide (MnO <sub>2</sub> ) .....	122

Introduction.....	122
Results and discussions.....	123
Summary .....	132
References.....	133
4.6 Non-covalent functionalization of graphene foam with pyrene carboxylic acid (PCA) as electrode for electrochemical storage .....	134
Results and discussions.....	135
Introduction.....	135
Summary .....	147
References.....	149
Chapter 5.....	152
General Conclusions .....	152
Chapter 6.....	155
Future work.....	155

# Chapter 1

## Introduction

Due to rapid depletion and high, consumption of fossil fuels and other natural resources there has been increased development and investigation of renewable and clean energy conversion/storage technology that can meet present energy and power consumption demands. Meanwhile, conventional energy storage devices like batteries which have high energy density with relatively low power output and conventional capacitors with low energy output and high power densities are not capable of meeting the increase in energy demand of future systems. In order to make effective use of renewable energy technology, it is important to develop high-performance, low-cost and environmental-friendly energy conversion and storage technology. Fuel cells and electrochemical capacitors are promising systems for future electrochemical energy conversion and storage [1–3]. However, the performance of these systems is related to the material properties. Therefore improving and optimizing the properties of these materials for energy storage technologies has become essential recently in scientific communities.

Electrochemical capacitors (ECs) also known as supercapacitors or ultracapacitors are promising alternative energy storage systems due to their relatively fast rate of energy storage and delivery, high power density and long cycle stability compared to batteries. Thus ECs have already been regarded as the suitable solution for energy storage applications [3–10]. Furthermore, significant progress has been made in developing alternative technologies to harvest and use clean and sustainable energy including solar energy, wind power, biofuels, and hydrogen in concomitance with clean energy technologies, such as fuel cells and lithium-ion batteries. Although these types of energy sources have played a major role in the past,

new technology is progressing to make alternative energy more practical and cost effective. Carbon based materials have been playing a significant role in the development of alternative clean and sustainable energy technology (batteries, supercapacitors, and fuel cells) due to their unique properties which includes high surface area, electrical conductivity, chemical stability and low cost [11–17].

Recently, looking back on the “gold digging days” of graphene [18] research with many low-scientific outputs we will be able to make a strong assessment (compared to “fullerene-rush” or “nanotube excitement” days that today’s research have led to some important outcomes, but are not considered fruitful. Graphene has been touted as an ideal carbon electrode material for supercapacitor due to its large theoretical specific surface area (SSA), high electrical conductivity, good mechanical properties and chemical stability [7,18–20]. An electrode material’s storage capacity is based on its interfacial double-layer capacitance ( $\mu\text{F}/\text{cm}^2$ ) and its surface area ( $\text{m}^2/\text{g}$ ). For high surface area materials such as graphene, it is critical to understand the components that affect interfacial capacitance resulting in charges that can be stored. It has been reported that interfacial capacitance for high surface area carbons has a space charge component [21]. Was also shown by the same authors that the development of higher surface area graphene materials alone will not be sufficient for the further increases in performance; hence modification of the properties will also be required [21]. Therefore it will be interesting to develop composite materials of graphene with high surface area as electrode materials.

## 1.1 General motivation

As mentioned earlier, graphene a two dimensional allotrope of carbon discovered in 2004 by A. K. Geim and K. S. Novoselov won the noble price in physics 2010 has emerged and possesses a wealth of new physics and many fascinating properties such as high electrical

conductivity and theoretical high surface area ( $2630 \text{ m}^2 \text{ g}^{-1}$ ) which makes it an excellent material for ECs applications [7]. Composite materials of graphene have also revealed numerous possibilities for ECs [22]. Depending on the method of production, the final properties of the produced graphene is usually affected [23]. To date, chemical modifications by Hummers method has been widely studied for the production of graphene. This method involves oxidation of graphite to graphene oxide (GO) and then subsequently reducing it to graphene [24–26]. However, the final products are often defective leading to inferior electronic properties of the graphene obtained. Although the theoretical SSA of a single-layer graphene can reach  $2630 \text{ m}^2 \text{ g}^{-1}$ , one critical problem is the restacking of graphene sheets during electrode preparation leading to low electrochemical performance. This work is an attempt to develop high performance graphene based composite electrode materials that prevent restacking of the sheets; In particular we focus on chemical vapor deposition (CVD) as an alternative approach for production of three dimensional graphene (graphene foam) which exhibits improved electronic properties when compared to GO and pristine graphene samples. These 3D graphene has a unique structure, well developed surfaces which play significant role in the development of composite materials. The various techniques for preparation of composite electrodes modified with metal oxide nanostructure are created in attempt to improve electrochemical performance. We believe the CVD technique is a method that can easily be scaled up for production of graphene if fully optimized.

## 1.2 Aims and objectives

The objectives of this research work are as follows:

- Preparation of a 3D graphene foam samples using a CVD system.

- Development of 3D graphene/metal oxides composite using different techniques such as hydrothermal, microwave irradiation, aqueous chemical growth, refluxing and investigate the formation mechanism of the various composite materials.
- Investigation of the morphological and microstructure composite with techniques such as Raman spectroscopy, energy dispersive x-ray (EDX), field emission-electron microscopy (FESEM), transmission electron microscopy (TEM) and x-ray diffraction (XRD).
- Investigation of capacitance performance/behaviour of 3D graphene/metal oxides composite electrodes by understanding the principle of its charge storage mechanism and the bonding properties between the graphene and each of the metal oxide material.

This work is divided into six chapters: Chapter 1 and 2 present's an introduction and literature review on ECs. Chapter 3 presents the experimental techniques while chapter 4 will deal with results and discussion. A summary of conclusions from each experimental result will be presented in chapter 5, while chapter 6 contains details of future work to be performed on the 3D graphene foam. Most importantly, we have been able to show that the nickel foam could be an excellent material for ECs application. We have also demonstrated improved energy density with the introduction of various pseudocapacitive materials into the 3D network of the graphene which serves as an excellent platform for adhesion and integration of these materials.

## References

- [1] Y.-G. Guo, J.-S. Hu, L.-J. Wan, *Adv. Mater.* **20** (2008) 2878.
- [2] L. Carrette, K.A. Friedrich, U. Stimming, *ChemPhysChem* **1** (2000) 162.
- [3] B. Conway, *Electrochemical supercapacitors: scientific fundamentals and technological applications*, kluwer academic/plenum: new york, 1999.
- [4] P. Simon, Y. Gogotsi, *Nat. Mater.* **7** (2008) 845.
- [5] A. Burke, *J. Power Sources* **91** (2000) 37.
- [6] E. Frackowiak, *Phys. Chem. Chem. Phys.* **9** (2007) 1774.
- [7] M.D. Stoller, S. Park, Y. Zhu, J. An, R.S. Ruoff, *Nano Lett.* **8** (2008) 3498.
- [8] C. Portet, G. Yushin, Y. Gogotsi, *Carbon* **45** (2007) 2511.
- [9] X. Lang, A. Hirata, T. Fujita, M. Chen, *Nat. Nanotechnol.* **6** (2011) 232.
- [10] A.G. Pandolfo, A. F. Hollenkamp, *J. Power Sources* **157** (2006) 11.
- [11] E. Frackowiak, F. Beguin, F. Béguin, *Carbon* **39** (2001) 937.
- [12] E. Frackowiak, F. Beguin, *Carbon* **40** (2002) 1775.
- [13] Y.P. Wu, E. Rahm, R. Holze, *J. Power Sources* **114** (2003) 228.
- [14] B.J. Landi, M.J. Ganter, C.D. Cress, R.A. DiLeo, R.P. Raffaele, *Energy Environ. Sci.* **2** (2009) 638.
- [15] K.S. Subrahmanyam, S.R.C. Vivekchand, A. Govindaraj, C.N.R. Rao, *J. Mater. Chem.* **18** (2008) 1517.
- [16] L.L. Zhang, X.S. Zhao, *Chem. Soc. Rev.* **38** (2009) 2520.
- [17] Y. Sun, Q. Wu, G. Shi, *Energy Environ. Sci.* **4** (2011) 1113.
- [18] A.K.A. Geim, K.S.K. Novoselov, *Nat. Mater.* **6** (2007) 183.
- [19] Y. Zhu, S. Murali, W. Cai, X. Li, *Adv. Mater.* **22** (2010) 3906.
- [20] B. Luo, Y. Fang, B. Wang, J. Zhou, H. Song, L. Zhi, *Energy Environ. Sci.* **5** (2012) 5226.
- [21] M.D. Stoller, C.W. Magnuson, Y. Zhu, S. Murali, J.W. Suk, R. Piner, R.S. Ruoff, *Energy Environ. Sci.* **4** (2011) 4685.

- [22] H.-J. Choi, S.-M. Jung, J.-M. Seo, D.W. Chang, L. Dai, J.-B. Baek, *Nano Energy* **1** (2012) 534.
- [23] D. Dreyer, S. Park, C. W. Bielawski, R. S. Ruoff *Chem. Soc. Rev.* **39** (2010) , 228.
- [24] W.S. Hummers and R.E. Offeman, *J. Am. Chem. Soc.* **80** (1958) 1339.
- [25] D. Chen, H. Feng, J. Li, *Chem. Rev.* **112** (2012) 6027.
- [26] Y. Zhu, S. Murali, W. Cai, X. Li, J.W. Suk, J.R. Potts, R.S. Ruoff, *Adv. Mater.* **22** (2010) 3906.

# Chapter 2

## Literature Review

### 2.1 The basic principle of electrochemical capacitors

Electrochemical capacitors (ECs) are energy storage devices like batteries, but uses different storage mechanisms. Batteries store energy chemically (bulk phenomenon), while ECs store energy physically through dielectric polarization or electronic double layer of ions and electron (surface phenomenon) [1–4]. Using chemical storage allows batteries to store relatively large amounts of energy compared with ECs, but have relatively short cycle lifetime, slow power delivery or uptake and thermal management are issues related with batteries. ECs are power devices that can be fully charged or discharged in seconds; as a consequence, they have low energy density than batteries, but have a much higher power delivery or uptake that can be achieved in shorter times [1]. Figure 2.1 is the Ragone plot which shows the various comparisons within the energy systems. It shows that batteries usually exhibit higher energy densities compared to ECs but have low power densities.

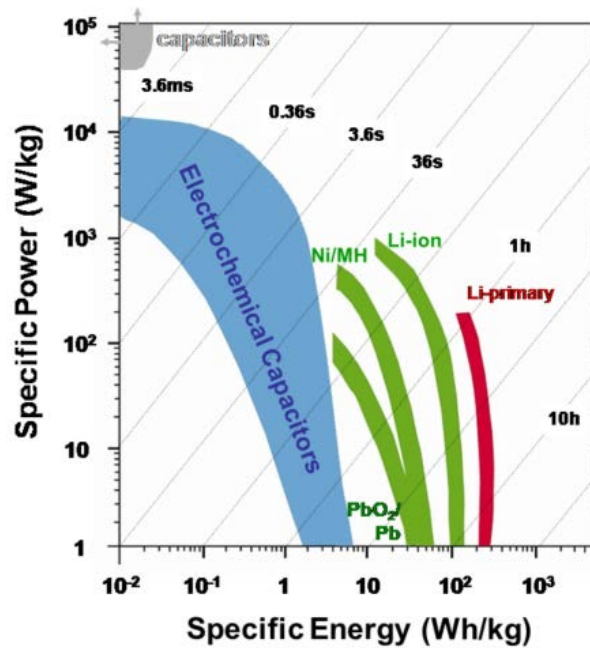


**Figure 2.1** shows the plot of power against energy density for different energy systems. Extracted from reference 18

## 2.2 Principle of energy storage

### 2.2.1 Energy storage mechanism of electrical double-layer capacitors (EDLCs).

Generally ECs can be classified into two types based on their energy storage mechanism: pseudocapacitor which is due fast and reversible redox processes and electric double-layer capacitor from pure electrostatic charge accumulation at the electrode interface as shown in figure 2.2. ECs can be viewed as two reactive porous parallel plates, or electrodes, immersed in an electrolyte, with a voltage potential applied across the two collectors. A porous dielectric separator between the two electrodes prevents the charge from moving between the two electrodes. A schematic diagram of porous electrodes and electrolytic solution is shown in figure 2.3.

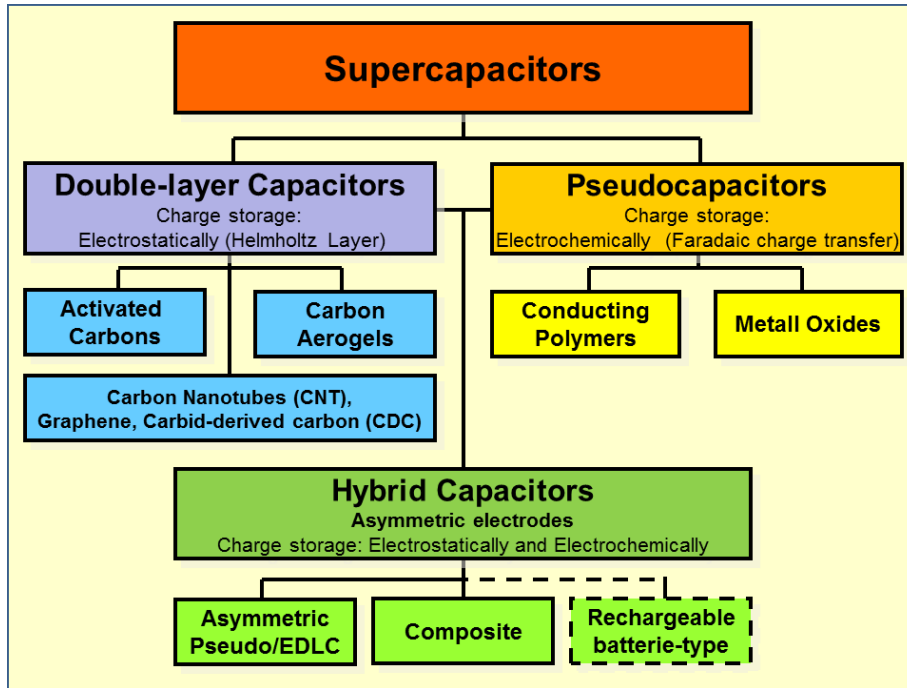


**Figure 2.2** Classification of electrochemical capacitors

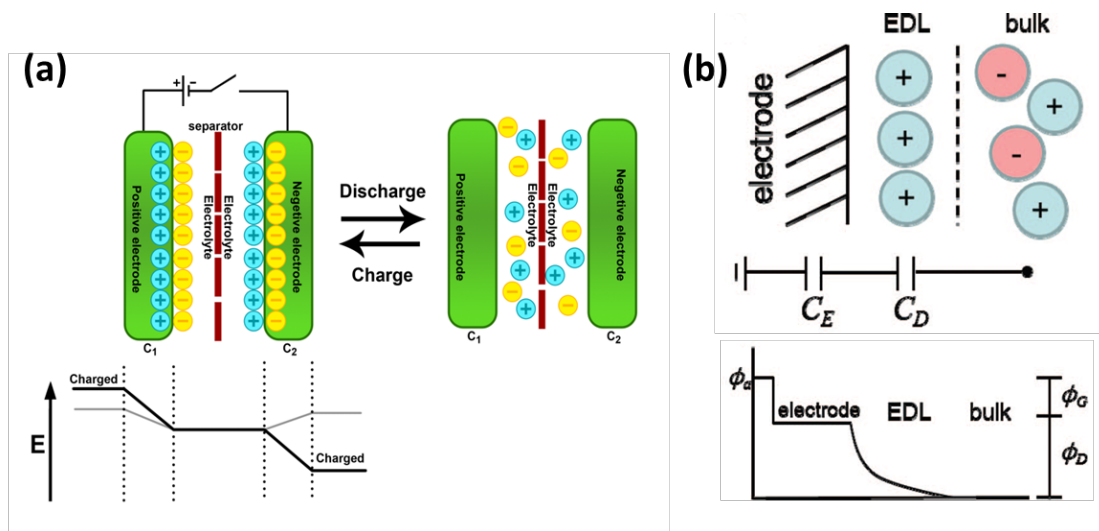
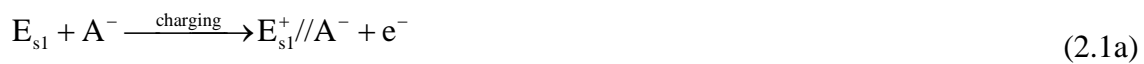


**Figure 2.3** Principle of an electrochemical capacitor (charged and discharge states of an electric double layer capacitor).

During the process of charging, the electrons are supplied by an external power source from the negative electrode to the positive electrode. Within the electrolyte, cations move towards the negative electrode while anions move towards the positive electrode. During the discharge the reverse process takes place i. e. electrons move from the negative electrode to

the positive electrode through the load, and ions are released from the electrode surface and moved back into the electrolyte. As observed from the overall reaction, the salt ( $C^+A^-$ ) in the electrolyte is consumed during charge, therefore the electrolyte can be considered as an active material [5]. However, in an ideal ECs system, there is no charge transfer across the electrode/electrolyte interface, and no net ion exchanges occur between the electrode and the electrolyte. This implies that the total/bulk electrolyte concentration remains unchanged during the charging and discharging processes [6]. Therefore at the interface the local concentration of ions may vary [7]. The electrochemical processes (charging and discharging) for a double-layer capacitor can thus be expressed as [5,6,8]:

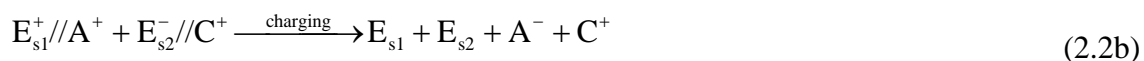
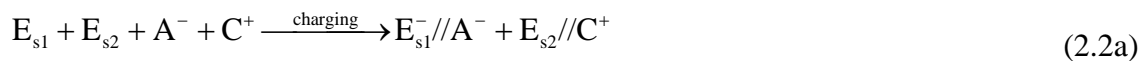
On positive electrode:



On negative electrode:



And the overall charging and discharging process can be expressed as equation (2.2a) and (2.2b):



Where  $E_{s1}$  and  $E_{s2}$  designates the surface of the carbon electrode, // designates the double-layer where charges accommodate, and  $C^+$  and  $A^-$  are known as the cations and anions of the electrolyte, respectively. Each electrode can be treated as a single capacitor of capacitance

( $C_1$ ) or ( $C_2$ ) which supposed to be a simple proportional increase to the surface area  $A$  of the electrode/electrolyte interface and to the electrolyte permittivity  $\epsilon$ . “However, several authors observed significant deviations from this simple law, which were interpreted either as an ion size effect or non-accessibility of small micropores from the electrolyte”. The capacitance limitation can be ascribed to a space constriction for charge accommodation inside the pore walls [9]. They store energy at the electrode-electrolyte interface through reversible ion adsorption onto the surface of electrode, thus charging the so-called ‘double-layer capacitance’.

This double-layer capacitance, was first coined and modelled by Helmholtz in the 19<sup>th</sup> century and later modified by Gouy & Chapman and Stern & Geary, [10–12] is schematically shown in figure 2.4. They have suggested that the presence of a diffuse layer in the electrolyte is due to the accumulation of ions close to the surface of electrode which is basically the difference with batteries, since no redox reaction is involved and the charge is stored only on the surface of the electrode material.

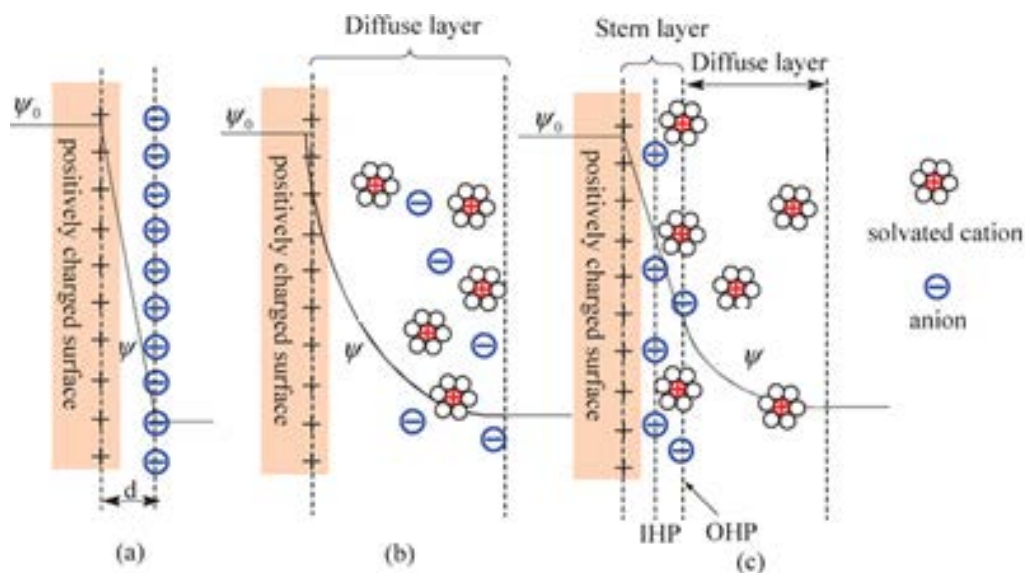


**Figure 2.4** Models of EDL at a positively charged surface: (a) the Helmholtz model, (b) the Gouy–Chapman model, and (c) the Stern model, (from ref 4).

The Helmholtz double layer model states that two layers of opposite charges form at the electrode/electrolyte interface and are separated by an atomic distance which is similar to that of a conventional two parallel capacitors [4]. Later on, this model was modified by Gouy and Chapman based on a continuous distribution of electrolyte ions in the electrolyte solution, governed by thermal motion [10,11], which was referred to as the diffuse layer figure 2.4b. However, this model leads to overestimation of the capacitance and was also modified by Stern [12] who proposed a model which combined the Helmholtz model and the Gouy-Chapman models. He explicitly identified two regions of ion distribution namely, the inner region called the compact layer and the diffuse layer (see figure 2.4c). The capacitance is defined according to conventional capacitance as

$$C = \frac{\epsilon\epsilon_0 A}{d} \quad (2.3)$$

where  $\epsilon$  is the dielectric constant or permittivity of electrolyte,  $\epsilon_0$  is the permittivity of free-space ( $8.854 \times 10^{-12} \text{ F m}^{-1}$ ),  $A$  is the surface area and  $d$  the distance between the centre of the ion and the porous electrode surface. The total EDL ( $C_T$ ) capacitance is controlled by a combination of capacitance from both regions at the electrode/electrolyte interface represented as a series of  $C_Q$  and  $C_D$ , according to the equation:

$$\frac{1}{C_T} = \frac{1}{C_Q} + \frac{1}{C_D} \quad (2.4)$$

where  $C_Q$  is the compact layer and  $C_D$  is the diffusion layer. With the  $C_Q$  and  $C_D$  values calculated above,  $C_T$  can be estimated as a function of applied potential  $\phi_a$  (with respect to the potential of the bulk electrolyte, i.e.,  $\phi_a = \phi_G + \phi_D$ ). The relationship between  $C_Q$  and  $C_D$  with  $\phi_a$  was obtained through  $\sigma$ ; using  $C_Q/C_D \propto \sigma \phi_G/\phi_d$ . The  $C_T$  curve is U-shaped, in direct contrast to the bell-shaped  $C_D$  curve as shown in figure 2.3 (b) this is apparently attributed to the dominance of  $C_Q$  when  $\phi_a$  is sufficiently small ( $|\phi_a| < 1.0 \text{ V}$ ). With increasing  $\phi_a$ , the

contribution of  $C_D$  becomes important. Quantum capacitance may also be a limiting factor to performance of the double layer. The quantum capacitance of graphene is defined as  $C_Q = d\sigma/d\phi_G$ , where  $d\sigma$  and  $d\phi_G$  refer to the variations of charge density and local potential in carbon materials for example graphene [13]. The factors that determine the performance and behavior of a double-layer across the surface of electrode are the type of electrode material, the type of electrolyte, the affinity between the ions and the electrode surface area.

To enhance the capacitance performance of a double layer capacitor, it is necessary to use electrically conducting electrodes with high specific surface area, which are electrochemically stable and highly conductive. Carbonaceous material such as activated carbon and carbide-derived carbons possess most of the requirements for this purpose [14]. Surface area is generally increased by the development of porosity in the bulk of carbon materials, leading to a porous network. However, the capacitance increase was limited for most porous carbonaceous materials. Nevertheless, from series of experiments performed for activated carbon materials with different pore sizes distribution, in various electrolytes, it was shown that there is no direct linear relationship between the specific surface area and the capacitance [9,15]. which could be due to charge screening, ion size effect or non-accessibility of small micropores from the electrolyte, electrochemical doping of density of states and quantum capacitance [9,15] .

A porous network in carbon material can be produced by processes known as activation and template carbonization to produce carbonaceous material with exceptionally large specific surface area and finely tuned porosity [16]. This porous network structure of carbon can be characterized by a broad distribution of pore size such as micropores (<2 nm in size), mesopores (2–50 nm) and macropores (>50 nm) which can be created in carbon grains. Longer activation time or higher temperature leads to larger mean pore size. For activated carbon (AC) specific capacitance values ranges from 100 to 200 F g<sup>-1</sup> in aqueous medium and

from 80 to 100 F g<sup>-1</sup> in organic medium [17]. A typical cyclic voltammogram of a two-electrode EDLC laboratory cell is presented in figure 2.5. Its rectangular shape is characteristic of a pure double layer capacitance storage mechanism [18]:

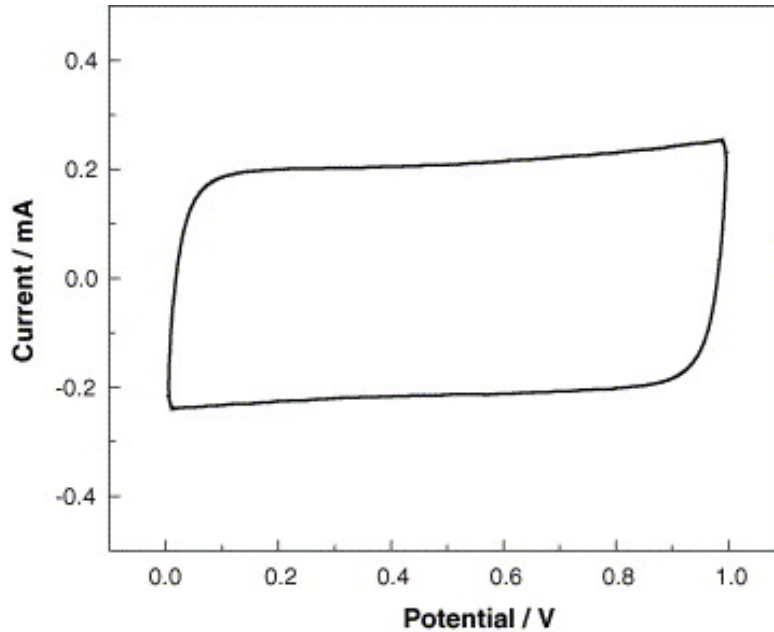


**Figure 2.5** Typical cyclic voltammetry diagram for an EDLCs carbon electrodes (Extracted from 57)

The capacitance of an EDLC can be obtained from the expression below:

$$I = C \times \frac{dV}{dt} \quad (2.5)$$

where I is the current, (dV/dt) is the potential scan rate and C is the double layer capacitance.

The energy density of the electrode material is determined from the specific capacitance of the electrode and the operating voltage according to equation 2.6 [19]. The specific capacitance describes the charge density per unit voltage and per unit weight or volume of the active material on single electrode.

$$E_e = \frac{1}{8} C_{sp} V^2 \quad (2.6)$$

While the maximum energy ( $\text{Wh kg}^{-1}$ ) and power ( $\text{W kg}^{-1}$ ) of the cell is related to the capacitance (C) and voltage (V) by Eqn. 2.7a and 2.7b below, respectively.

$$E_{\max} = \frac{1}{2 \times 3600} \frac{CV^2}{M} \quad (2.7a)$$

$$P_{\max} = \frac{V^2}{4 \times (\text{ESR}) \times M} \quad (2.7b)$$

where  $C_{\text{sp}}$  is the specific capacitance, C is the capacitance of the cell in farads, V is the voltage (volts) and M is the total active material weight on the two electrodes and ESR is the equivalent series resistance.

The energy and power values are usually normalized by the mass or volume of the device or the electrode (it is very important to distinguish between those) to obtain energy and power densities as shown in equation 2.7. The capacitance depends on the electrode material used and stability of the operating voltage in different electrolyte. The maximum operating voltage is mainly limited by the decomposition of the solvent or the salt in the electrolyte. As observed from equation 2.7 both the power and energy density are dependent on the voltage thus the use of high-capacitive materials with a very large potential window is a key factor for the improvement in the energy density.

The performance of supercapacitor is mainly evaluated based on their charge storage mechanism, power density, energy density, fast charge/discharge processes, excellent cyclability, safe operation and low cost. The fundamental aspects and features that differentiate supercapacitors from batteries are discussed below.

**Charge storage:** charges are stored at the surface of the carbon-active material for ECs, where as in batteries the charge is stored in the bulk of the material (in the chemical bonds) via electrochemical redox reactions. This surface storage phenomenon explains the low

energy density of the supercapacitors when compared with Li-ion batteries. Nevertheless, this storage mechanism also allows a very fast delivery of the stored charges. Thus, EC devices can deliver most of the stored energy in a short time; about 5 seconds the entire process is reversible and energy update can be achieved within the same period of time [14,20].

**Cycling stability:** Cycling performance of ECs is not limited or affected by the volume change of the active electrode material between the charged and the discharged states (no ageing effect) contrary to batteries. For an electrostatic and surface charge storage process, the faradic efficiency or Columbic efficiency (discharge time per charge time at the same current) of ECs is almost 100 per cent, which is higher compared to that of batteries [20].

**Low temperature operation:** Working temperature in ECs is different from that of batteries since there is no limitation in the choice of solvent, as no carbonate is needed [14,21]. The use of electrolyte such as acetonitrile (AN) guarantees an operation at temperatures down to -40 °C although with degrading performances. For ionic liquid electrolytes operating at maximum voltage of 3.5 V an unprecedented 130 °C (from -50 to 80 °C) temperature window can be attained [22]. Maximum temperature is in the same range as that of batteries, i.e. +70 °C. This limitation is a result of electrolyte decomposition onto the high-surface-area carbon electrodes as well as of carbon oxidation [20].

### **2.2.2 The energy storage mechanism of pseudo-capacitance.**

Double layer capacitors are complemented by capacitors based on pseudocapacitance, which arises in some electro-sorption processes and in redox reaction at electrode surfaces. In contrast with double layer capacitance which arises from potential-dependence of surface density and stores charges electrostatically (non-Faradaic); pseudocapacitance arises from thermodynamic conditions and is due to charge acceptance ( $\Delta q$ ) and a change in voltage ( $\Delta V$ ) [1]. It is Faradaic in origin, involving the passage of charges across the double layer so that a derivative  $C = d(\Delta q)/(d\Delta V)$  is equivalent to the measured capacitance and referred to

as pseudocapacitance. Three types of Faradaic processes occur for pseudocapacitors namely: reversible adsorption, redox reactions of transition metal oxides, and reversible electrochemical doping and undoping in polymer based electrodes [1]. The most commonly studied materials for the pseudocapacitor electrodes are transition metal oxides [4,6,23,24], conducting polymers [25–28], transition metal nitrides [29,30] and carbon materials enriched with oxygen/nitrogen containing functional groups [31–33]. In contrast to the mechanism of an EDLC, Faradaic charge transfer takes place in the pseudocapacitor electrode. However, pseudo-capacitance has demonstrated extended working voltage and can provide higher capacitance than EDLCs. The major disadvantage of the pseudocapacitive system is their surface which are higher affine to degradation and redox-dependent solid state kinetics, leading to low power performance due to poor electrical conductivity and lack of stability during cycling, compared to pure EDLCs systems [4].

The most representative electrode materials for pseudocapacitance are transition metal oxides.  $\text{RuO}_2$  and  $\text{RuO}_2 \cdot x\text{H}_2\text{O}$  have been studied extensively and shown to exhibit a much higher specific capacitance ( $720 \text{ F g}^{-1}$ ). This has been attributed to the mixed proton-electron conductivity within  $\text{RuO}_2 \cdot x\text{H}_2\text{O}$  [34]. The electrochemical reaction mechanism for  $\text{RuO}_2$  electrodes can be expressed as [1,5]:

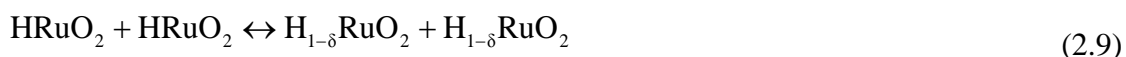
Positive electrode



Negative electrode



Overall reaction



where  $0 < \delta < 1$ ,  $\text{RuO}_2$  and  $\text{HRuO}_2$  are representative of both the positive and the negative electrodes at fully charged states, respectively.  $\text{HRuO}_2$  represents electrodes which are at the

fully discharged state. As observed, electrons travel through the external power source while protons migrate from one electrode to another during the charge and the discharge process. Nevertheless, there is no net ion exchange between the electrode and the electrolyte. The concentration of the electrolyte may vary due to some polarization, some formation of EDL and presence of redox reactions during the entire charge and discharge process which is the reverse phenomenon in double-layer capacitor.

The excellent and superior electrochemical performance of  $\text{RuO}_2 \cdot x\text{H}_2\text{O}$  materials is related to its porous architecture, its high metallic conductivity as well as hydrous nature. As seen from the overall reaction, the reversible redox transitions depends on both proton exchange and electron-hopping processes [6]. The hydrous nature of  $\text{RuO}_2 \cdot x\text{H}_2\text{O}$  ensures a high rate of proton exchange. Because of their porous architecture and design, they have been demonstrated as promising electrode materials for energy storage. However, due to the high cost of  $\text{RuO}_2$  it has been limited for actual practical applications. As an alternative, significant effort have been put into developing cheaper and environmentally friendly materials that exhibit similar excellent properties to that of  $\text{RuO}_2$ . Alternative materials such as  $\text{NiO}$ ,  $\text{MnO}_2$ ,  $\text{Fe}_2\text{O}_3$ ,  $\text{Fe}_3\text{O}_4$ ,  $\text{SnO}_2$ , and  $\text{Co}_3\text{O}_4$  have all been explored and will be explained in section 2.8.3.

### **2.3 Testing an electrochemical cell**

For fundamental studies and research purposes, the performance of single electrode, can be investigated using the conventional three-electrode cell configuration which is suitable and comprises of working, counter and reference electrodes. Depending on the electrolyte being used, various counter and reference electrodes can be used. For example in acidic electrolyte, the counter electrode material can be a platinum or glassy carbon, and the reference electrode is a saturated calomel electrode (SCE) or a silver/silver chloride electrode ( $\text{Ag}/\text{AgCl}$ ). In neutral electrolyte solutions, basically the same configuration is used but nickel can be used

for a collector and the counter electrode. In alkaline aqueous solutions, a mercury/mercury oxide electrode (Hg/HgO) is used as the reference electrode. For non-aqueous electrolyte solutions the choice of reference electrode depends on the electrolyte to be investigated [35,36].

## 2.4 Fabrication of cell for a two electrode configuration

The preparation of cell device requires the active working electrode material such as, activated carbons (ACs), CNTs and graphene, which are usually mixed with a conductive agent, e.g., acetylene black and carbon black, and a binder, e.g., poly(tetrafluoroethylene) (PTFE) or poly(vinylidene fluoride) (PVDF), followed by rolling to film or forming a tablet using a compression moulding press, and then by pressing onto a collector mesh or foil. The electrode thickness is a few tens micrometres to sub-millimetres depending on the active materials used taking into account of the actual application. The mass of active materials in the electrode must be known and preferably the electrode volume should be measured.

In a two-electrode cell configuration the energy density, the power density and the cycle life of the cell are evaluated to determine the performance cell. Normally two same working electrodes are set across a separator, and the potential difference between the two is monitored and controlled. In a two-electrode configuration the cell capacitance measured in  $F\ g^{-1}$  is theoretically 1/4 of the single electrode capacitance measured in a three-electrode cell [37]. This capacitance value is based on the sum of active materials in both electrodes. The factor of 1/4 adjusts the capacitance of the cell and the combined mass of two electrodes to the capacitance and mass of a single electrode. If volume is more important for the targeted application, the electrode material's volume may be substituted for mass [37].

It is worth stating that the capacitance of single electrode measured in a two-electrode cell does not coincide with that in a three-electrode cell because of various factors, such as the difference in sizes between the solvated cation and anion, the different potential changes of positive and negative electrodes during charge/discharge measurements.

## 2.5 Evaluation of electrode material for electrochemical capacitors

The performance of the electrode is evaluated by cyclic voltammetry (CV), galvanostatic chronopotentiometry (GCP) and electrochemical impedance spectroscopy (EIS)

### 2.5.1 Cyclic voltammetry and galvanostatic chronopotentiometry (GCP)

Material capacitance measurements can be done by making a slurry and coating it on a current collector, then measure this electrode in a chosen electrolyte using electrochemical cyclic voltammetry (CV) to record cyclic voltammograms of the material, from which the capacitance can be calculated (see figure 2.6). This can be measured either in the two or three electrode configuration.

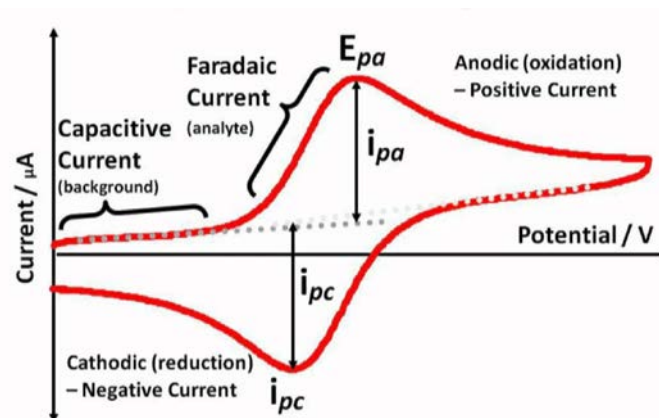


**Figure 2.6** Cyclic voltammetry of a typical pseudocapacitor. (Extracted from ref.2)

In this case a voltage is swept between two values at a fixed rate, when the voltage reaches  $V_2$  the scan is reversed and the voltage is swept back to  $V_1$ . The entire process has a mole fraction expressed as  $x = QM/mF$ . Here  $Q$  is the stored charge,  $M$  is the molecular weight,  $m$

is the mass, and  $F$  is the Faraday constant. The area under the CV curves represents the total amount of stored charge which arises from both faradaic and nonfaradaic processes. During faster sweep rates, only the highest intensity part of the storage transient is collected and so larger peaks are observed. With decreasing sweep rate, the total amount of stored charge increases which indicates that full storage has not been achieved due to kinetic limitations associated with the diffusion of material being investigated. The mole fraction of inserted material typically reaches a value of close to 0.5 when the lattice of the positive ion is fully lithiated which corresponds to a specific charge capacity. The total stored charge can be separated into three components: the faradaic contribution from the positive ion insertion process, the faradaic contribution from the charge transfer process with surface atom (referred to as pseudocapacitance) [38] and the nonfaradaic contribution from the double-layer effect. The latter two capacitive components cannot be separated and were characterized by analyzing the CV data at various sweep rates according to  $i = av^b$  where the measured current  $i$  obeys a power law relationship with the sweep rate  $v$ . Both  $a$  and  $b$  are adjustable parameters, with  $b$ -values determined from the slope of the plot of  $\log i$  vs  $\log v$  [38]. For a reversible electrochemical reaction the CV recorded has certain well defined characteristics.

1. The voltage separation between the anodic and cathodic current peaks should be close
2. The positions of peak voltage do not alter as a function of voltage scan rate
3. The ratio of the peak currents is equal to one
4. The peak currents are proportional to the square root of the scan rate

When the capacitance is simply originated from EDL, CV curves is rectangular and the capacity is estimated from the current density at the middle point of the potential range measured,  $I$ , and the potential scan rate,  $v$ , that is,  $C = I/v$ . The potential range,  $V$ , is dependent on the electrolyte solution. When a pseudocapacitive material is used instead, the

potential for capacitance calculation should be chosen carefully because the CV curve is not always rectangular, it shows the oxidation and reduction peaks of the material being investigated as shown in the figure above. As the scan rate ( $v$ ) increases the CV curve becomes distorted. However, the total capacitance can be calculated by integrating the CV curve. Generally, the capacitance decreases with increasing  $v$ , so that the value of  $v$  should be sufficiently low to enhance high capacitive performance. When the capacitance of material investigated shows EDL behaviour, the potential of chronopotentiogram  $V$ , changes linearly with time  $t$ , at constant current density  $I$ . Then the capacitance is given by the slope of linear relationship  $dV/dt$ , that is,  $C = I/(dV/dt)$ . Similar to CV, when there is a pseudo-capacitance contribution to the total capacitance, the chronopotentiogram deviates from the linear relationship. It leads to a non-linear behaviour, so that the capacitance is usually given by  $C=I \times \Delta T/\Delta V$ , where  $\Delta T$  is the total time for either positive or negative process and  $\Delta V$  is a potential difference after correcting an IR drop (voltage drop) which is estimated from the initial potential jump of chronopotentiogram. High potential may be a possible source of degradation during CV analysis.

### **2.5.2 Galvanostatic charge/discharge (GCD)**

In this, a current pulse is applied to the working electrode and its resulting potential is measured against a reference electrode as a function of time [39]. At the moment when the current is first applied, the measured potential is abruptly changed due to the  $iR$  loss, and because concentration overpotential is developed as the concentration of the reactant is exhausted at the electrode surface. If the current is larger than the limiting current, the required flux for the current cannot be provided by the diffusion process and, therefore, the electrode potential rapidly rises until it reaches the electrode potential of the next available reaction, and so on. The different types of chronopotentiometric techniques are depicted in figure. 2.7. In constant current chronopotentiometry, the constant anodic/cathodic current

applied to the electrode causes the electroactive species to be oxidized/reduced at a constant rate. The electrode potential accordingly varies with time as the concentration ratio of reactant to product changes at the electrode surface. The applied current can be varied with time, rather than being kept constant. For example, the current can be linearly increased or decreased (chronopotentiometry with linear rising current in the figure) and can be reversed after some time (current reversal chronopotentiometry in the figure) and can be reversed suddenly changed from an anodic to cathodic one, the product formed by the anodic reaction (i.e., anodic product) starts to be reduced. Then, the potential moves in the cathodic direction as the concentration of the cathodic product increases. On the other hand, the current is repeatedly reversed in cyclic chronopotentiometry. The typical chronopotentiometric techniques can be readily extended to characterize the electrochemical properties of insertion materials. In particular, current reversal and cyclic chronopotentiometries are frequently used to estimate the specific capacity and to evaluate the cycling stability of the battery and electrochemical capacitors, respectively.

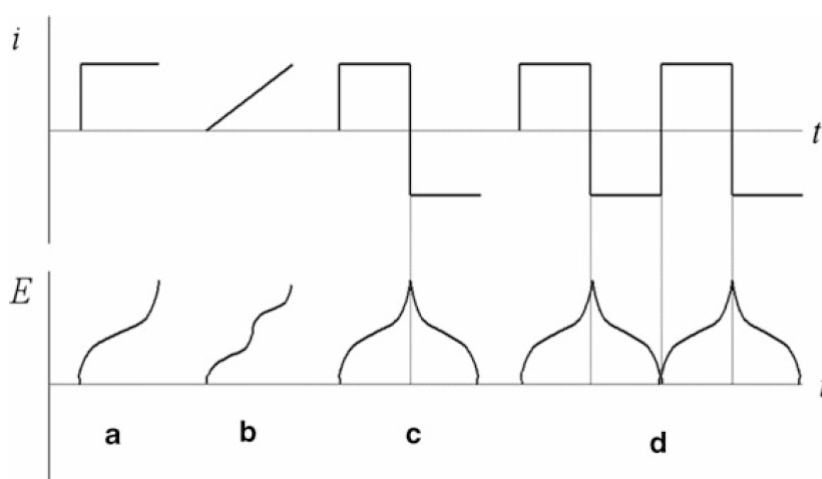


**Figure 2.7** Different types of chronopotentiometric experiments. (a) Constant current chronopotentiometry, (b) Chronopotentiometry with linearly rising current, (c) Current reversal chronopotentiometry, (d) Cyclic chronopotentiometry.

The capacitance value of  $C$  is measured the same way above, but it is for the full cell. In this case, attention has to be paid to the collector, electrolytes and solvents, since sometimes the electrode materials are damaged by high potentials. It is recommended to carry out both three-electrode cell and two-electrode cell measurements on the same electrode material. For practical purposes and application it is important to calculate the capacitance per volume ( $C_v$ , e.g.,  $F\ m^{-3}$ ) of the active material, however it is not easy to estimate accurately the volume in the laboratory scale. Alternatively the capacitance per mass ( $C_m$ , e.g.,  $F\ g^{-1}$ ) is used to estimate the performance of the active material.

### 2.5.3 Electrochemical impedance spectroscopy (EIS)

Electrochemical impedance spectroscopy (EIS) is a useful and prime tool used in for analysis of single parameters and evaluation of mechanism of electrode materials. EIS can be carried out at different voltages; thus probing the response of the material at different stages in the pure double layer range or in the redox regime. The impedance of an electrochemical system is usually carried out in an open-circuit potential measured by applying a low-amplitude alternative voltage  $\Delta V(\omega)$  to a steady-state potential  $V$  over a wide range of frequency ( $f$ ) e.g., 100 kHz -10 mHz, where  $\Delta V(\omega) = \Delta V_{\max} e^{j\omega t}$ , where  $\omega$  is the pulsation and  $\Delta V_{\max}$  the signal amplitude. This input signal gives rise to a sinusoidal output current  $\Delta I$ , with  $\Delta I(\omega) = \Delta I_{\max} e^{j(\omega t + \phi)}$ , where  $\phi$  is the phase angle of the current against the voltage and  $\Delta I_{\max}$  is the signal amplitude. The electrochemical impedance  $Z(\omega)$  is defined as:

$$Z(\omega) = \Delta V / \Delta I = |Z(\omega)| e^{-j\phi} = Z' + jZ'' \quad (2.11)$$

$$Z'^2 + Z''^2 = |Z(\omega)|^2 \quad (2.12)$$

Where  $Z'$  and  $Z''$  are the real part and the imaginary part of the impedance, respectively. The Nyquist plot is a representation of EIS shown in figure 2.8, where the real part of impedance  $Z(f)'$ , is plotted against the imaginary part of impedance  $Z(f)''$  [19,35]. Alternatively, a charge transfer resistance is given from the diameter of a semicircle of this plot. At high frequency, the impedance shows the conductivity of electrode materials and electrolyte, while at the medium frequency region (10 to 1 Hz) it shows a pseudo charge transfer resistance, which is attributed to the porous electrode materials used. At the low frequency region ( $< 1$  Hz), the impedance plot is the characteristic feature of pure capacitive behavior. Ideally, a pure capacitor should show a parallel line to the imaginary axis of the Nyquist plot (electron-transfer diffusion process). However, in all cases there is a deviation from this ideal behaviour, the plot showing lines which are inclined at angles between 45 and 90 to the real axis. This corresponds to the ion diffusion mechanism between Warburg diffusion and ideal capacitive ion diffusion (pseudo capacitance) [2,40].

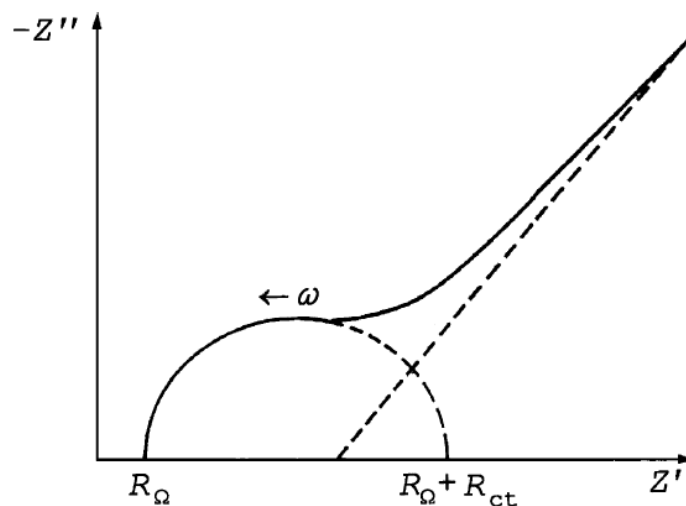


**Figure 2.8** Scheme of the impedance plane (Nyquist plot)

The Bode plot is another representation of the EIS; which is a relationship between the imaginary part of impedance  $Z''$  and frequency  $f$ . It provides information about the

capacitance of materials. The capacitance can be calculated from the Bode plot using the following expression  $C = 1/2\pi fZ''$  from the linear portion of a  $\log Z''$  vs.  $\log f$ .

## 2.6 Advantages and applications of ECs

Supercapacitors are particularly attractive due to the following advantages over batteries and conventional capacitors

(1) **High power density:** From the Ragone plot above (see figure. 2.1), It is clear that ECs display a much higher power delivery ( $1-10 \text{ kW kg}^{-1}$ ) when compared to lithium ion batteries ( $150 \text{ W kg}^{-1}$ ) [14]. Since ECs stores electrical charges both at the electrode surface and in the bulk near the surface of the solid electrode, rather than within the entire electrode, the charge-discharge reaction will not necessarily be limited by ionic conduction into the electrode bulk, so the charging and discharging rates are much faster than the electrochemical redox reactions inside batteries. These rapid rates lead to high power density in ECs. For example, an ECs can be fully charged or discharged in seconds ( $\sim 30 \text{ s}$ ), and the energy can be taken from it rapidly, within  $0.1 \text{ s}$  [41,42]. For batteries, the charging time is normally on the scale of hours.

(2) **Long life expectancy:** The storage of electrochemical energy in batteries is realized through faradaic reactions, which often involve irreversible interconversion of the chemical electrode reagents and irreversible phase changes. In contrast, when energy is stored in an ECs, no or negligibly small chemical charge transfer reactions and phase changes are involved in charging and discharging, so an ECs can have almost unlimited cyclability. ECs do not need any maintenance during their lifetimes and can withstand a huge number of charge-discharge cycles, up to  $1\ 000\ 000$ . Although fast redox reactions are involved during charging and recharging, their life expectancy is also much longer than that of batteries. The

life expectancy for ECs is estimated to be up to 30 years, which is much longer than for lithium ion batteries (1000-10000 cycles and a life expectancy of only 5-10 years).[1,42–44].

(3) **High efficiency:** ECs are reversible with respect to charging and discharging throughout their complete operating range of voltage, and the energy loss to heat during each cycle is relatively small and readily removed (i.e., heat management is easy). This means that the cycle efficiency of ECs is high (around 95 %) even when operating at rates above  $1 \text{ kW kg}^{-1}$  [21].

(4) **Wide range of operating temperatures:** ECs can function effectively at extremely high and low temperatures. The typical operating temperature for ECs ranges from  $-40$  to  $70 \text{ }^{\circ}\text{C}$ . This is advantageous for military applications, where reliable energy storage is required to run proprietary electronic devices under all temperature conditions during war.

(5) **Safe and environmentally friendly:** ECs can work effectively at extremely high and low temperatures and are environmentally friendly. The typical operating temperature for ECs ranges from  $-40$  to  $70 \text{ }^{\circ}\text{C}$  [1]. In general, they do not contain hazardous or toxic materials, and their waste materials are easily handled and disposed compared to most batteries e.g. lithium-ion batteries.

## 2.7 Application of Electrochemical capacitors

Because of their many advantages over batteries, ECs have become very attractive candidate for applications in hybrid electric vehicles, digital communication devices, digital cameras, mobile phones, electrical tools, pulse laser techniques, uninterruptible power supplies and memory back-up system [21,45,46]. Report by Miller *et al* [21] has presented a summary which clearly distinguishes the opportunities for electrochemical supercapacitors into three main categories namely energy management applications, power tools applications and day-

night storage applications. For example, in memory back-up, batteries poorer cycle life makes their frequent replacement expensive (adding 20 % onto the price of battery operated appliances). In addition, in battery powered electric vehicles, batteries with lower power density cannot meet peak load requirements, originating from accelerating or climbing. With advantages such as long life-time and high power density, ECs can solve these problems. Combining ECs with batteries can yield improved performance in hybrid electric vehicles, including powerful acceleration, braking energy recovery, excellent cold weather starting, and increased battery life. Thus, ECs has the potential to play an important role in complementing or replacing batteries in the energy conversion and storage fields [47]. Due to their relatively low energy density and high cost, the market development of ECs is still in the early commercialization stage. Analyst persists in its forecast of 30 % compound growth of this market over the coming decade. The total global market for supercapacitors was worth \$470 million in 2010, according to “Supercapacitors: Technology Developments and Global Markets”. That value is projected to grow to \$1.2 billion in 2015, after increasing at a five-year compound annual growth rate (CAGR) of 20.6 % [48].

## **2.8 Electrode materials**

Materials play a very important role in generation and storage of energy in ECs, hence development of electro active materials that can meet the required energy demand is of utmost importance [49]. The capacitance of ECs depends on the specific surface area of the electrode materials, however, it has been shown that there is no a linear relationship between the area and the measured capacitance [9]. This is because the entire surface area is not fully accessible to the electrolyte electrochemically, also, charge screening, ion size effect or non-accessibility of small micropores from the electrolyte, electrochemical doping of density of states and quantum capacitance all have effect on the capacitance of the material. Thus, for

those electrochemically accessible surface area or useful surface area, a definition called the “electrochemical active surface area” may be more accurate in describing the electrode capacitance behavior. The pore size as well as the pore size distribution (PSD) of the electrode material also play an important role and thus have a great impact on the capacitance [14]. According to Largeot *et al.* [47], the pore size of electrode materials that yielded maximum double-layer capacitance was very close to the ion size of the electrolyte (with respect to an ionic liquid electrolyte), and both larger and smaller pores led to a significant drop in capacitance. However, increasing the pore size can also increase the average distance  $d$  between the pore walls and the center of an ion, making the capacitance of materials with larger pores decreased according to the following equation  $C = A\epsilon/4\pi d$  [47]. This phenomenon is also explained by Mathew *et al.* [50], and referred to as “interfacial confinement effects” their simulation results provide an atomic scale depiction of ion transport dynamics in aqueous electrolyte which allow for the examination of size trends within specific geometries as well as trends in concentration. The electrode pores are modelled as planar graphite sheet which facilitates focused ion motion under slightly confining conditions. As a result, the ion’s diffusivities are enhanced in the direction of the slit or pore. Further confining the system leads to decreased ion diffusivities. The ions are fully hydrated in all but the smallest slits and pores with those sizes showing increased ion pairing. These provide strong evidence of charge separation perpendicular to the surface at all size scales, concentrations, and ion types, providing a useful baseline for examining differential capacitance behavior and energy storage [50]. Pore size distribution in the range of 2-5 nm, which is larger than the size of two solvated ions, has been identified as a way to improve the energy and power performance of electrochemical capacitors. The porosity relevant to the development of high capacitance is itself not a simple parameter, involving both pore sizes and pore-size distribution for a given overall specific area ( $\text{m}^2 \text{g}^{-1}$ ) of the

material. Therefore, ECs capacitance strongly depends on the surface area of the electrode accessible to the electrolyte. Generally, electrode materials for ECs can be classified into three categories namely: carbon materials, conducting polymers, metal transition oxides and their composites [1,51].

### **2.8.1 Carbon materials:**

Carbon materials are the only materials used as electrode for industrial applications. They have excellent properties including good electrical conductivity and high specific surface area; they are abundant, cheap, highly chemical inert and have wide operating temperature range [2,17,52,53]. Carbon materials can be grouped into different structures namely, onion-like carbon (OLC), carbon nanotubes (CNTs), graphene, activated carbons (ACs), and carbide-derived carbons (CDC). OLCs are zero-dimensional (“quasi 0D”) quasi-spherical nanoparticles consisting of concentric graphitic shells materials prepared by annealing nanodiamond powders in vacuum or argon or detonation nanodiamond, giving rise to bulk nanoparticles of few nanometres. They offer specific surface area (SSA) between 500-600 m<sup>2</sup> g<sup>-1</sup> compared to activated carbon (AC) which is mostly accessible to ion adsorption because there is no porous network inside the particles. OLC have demonstrated modest gravimetric capacitance in previous studies, at about one-third that of activated carbon [53–55].

Carbon nanotubes (CNTs) which are one-dimensional (“quasi 1D”), have been extensively studied for electrochemical capacitors in the past few years due to their unique pore structure, superior electrical properties, good mechanical and thermal stability. CNTs can be categorized as single-walled carbon nanotubes (SWNTs), double-walled carbon nanotubes (DWCNTs) and multi-walled carbon nanotubes (MWNTs), all of which have been widely explored as energy storage electrode materials. CNTs are usually regarded as the choice of a high-power electrode material because of their good electrical conductivity and readily

accessible surface area. Moreover, their high mechanical resilience and open tubular network make them a good support for active materials. The energy density is, however, a concern due to their relatively small specific surface area ( $<500 \text{ m}^2 \text{ g}^{-1}$ ) as compared to ACs. Single wall carbon nanotubes (SWCNTs) with high surface area has been demonstrated to have an energy density of about  $35 \text{ Wh kg}^{-1}$  in organic electrolytes [56]. Capacitive properties of double-walled carbon nanotubes (DWCNTs) have not been so frequently reported, because of difficulty in synthesising pure DWCNTs. Generally, DWCNT and multi-walled carbon nanotubes (MWCNTs) have less SSA than SWCNT. Nevertheless, there have been lots of reports on capacitive properties of MWCNTs because they are relatively easy to prepare. The preparation techniques determine the morphology and surface areas obtained which ultimately determine the performance in various electrolytes. Values between  $10\text{-}200 \text{ F g}^{-1}$  have been reported [57–59].

Activated carbon (AC) have been tested as the electrode material for ECs because of its high surface area. It is generally prepared through an activation process (oxidation of bulk carbon in water vapor, KOH, or  $\text{CO}_2$ ) this process creates a three-dimensional porous network of in the carbon materials with micropores (pore size  $<2 \text{ nm}$ ) and mesopores ( $2\text{-}50 \text{ nm}$ ) which are responsible for the high SSA ( $2000 \text{ m}^2 \text{ g}^{-1}$ ). Low-cost activated carbons can be produced from carbonization and activation of natural carbon precursors such as wood, coconut shells, palm kernel shell, or anthracite. They are all amorphous and their network structure consists of mainly  $\text{sp}^2$  and some  $\text{sp}^3$  bonded atoms. This network structure contains chemical moieties such as oxygen, nitrogen, and other atoms with oxygen-containing functional groups which lead to a decrease in conductivity and hence require addition of acetylene black or carbon black to AC electrodes [60]. Capacitive performance of AC electrodes have gradually increased from  $120 \text{ F g}^{-1}$  to about  $200 \text{ F g}^{-1}$  in organic electrolytes during the past years [61]. With a density higher than that of CNTs and graphene, about  $0.5 \text{ g cm}^{-3}$ , activated carbon

volumetric capacitance reaches 50-80 F cm<sup>-3</sup>. Due to the scalable manufacturing, reasonable cost, and high capacitance, activated carbons are widely used in commercial devices.

Carbide-Derived Carbon (CDC) are a large family of carbon materials derived from carbide precursors that are transformed into pure carbon via physical (e.g., high-temperature treatment or thermal decomposition) or chemical (e.g., chlorination or halogenation) processes [62,63] by a reaction like



For many binary carbides (e.g., M=Si, Ti, Zr), the above yields both gaseous MCl<sub>4</sub> and solid carbon in the temperature range of interest [64]. The unique properties of porous CDC obtained by halogenation, such as a high specific surface area and tunable pore size with a narrow size distribution, makes it an ideal absorbent or supercapacitor electrode. CDCs have been derived from many precursors (SiC, TiC, Mo<sub>2</sub>C, VC, etc.) using a variety of treatment conditions that lead to a broad range of useful properties. Depending on the synthesis method used, a high bulk porosity (>50 vol. %) with a high specific surface area (SSA more than 2000 m<sup>2</sup> g<sup>-1</sup>) can be obtained [65]. The bulk porosity of CDC is largely determined by the carbide structure. When metal atoms are extracted from the carbide lattice, the remaining carbon forms microporous CDC structures. CDC with controllable nanostructure and pore characteristic obtained from different techniques and precursors have been studied as electrode for ECs. Differences in total pore volume, pore size distribution and carbon structure of CDC prepared from the different carbides are reflected in the capacitance. Gravimetric capacitance of 190 and 150 F g<sup>-1</sup> was found for ZrC-CDC and TiC-CDC, respectively, in H<sub>2</sub>SO<sub>4</sub>. While the carbide precursor, particle size and other parameters affect CDC capacitance, the synthesis temperature has the most significant impact on the capacitance of CDC, because it affects the pore size. Tunability of pore size in CDC

facilitated a major breakthrough in understanding capacitive charge storage in porous carbon. Chmiola *et al.* reported an increase in the gravimetric and volumetric capacitance at lower chlorination temperatures, although the specific surface area and pore size of CDC decreased [66]. Traditionally, a decrease in capacitance was expected for submicrometer pores that are inaccessible to the electrolyte. Studies performed on CDC with 0.7 to 1.1 nm pores [66] have shown that for small pores, the solvation shell of the electrolyte ions is completely or partially removed leading to an increase in the capacitance. A later study on the correlation between pore size and capacitance corroborated an increase in capacitance when the pore size approaches that of the desolvated ion and a decrease once the pore size is smaller than the ion size [67]. Nano-fibrous felts (nano-felts) of carbide-derived carbon developed from electrospun titanium carbide (TiC) nanofelts were reported by Presser *et al.* [68]. The developed TiC-CDC nano-felts were mechanically flexible and can be used as electrode material for supercapacitor applications without the addition of binder. The TiC-CDC nanofelts show an average pore size of ~1 nm and a high specific surface area of 1390 m<sup>2</sup> g<sup>-1</sup>. TiC-CDC with a narrow pore size distribution having a mean value between 0.6 and 1.1 nm was also prepared by changing the synthesis temperature [63].

### **2.8.2 Conducting polymers (CPs)**

CPs possess excellent properties [69,70] such as high conductivity, high potential window, good storage capacity/reversibility, adjustable redox activity through chemical modification and low cost, making them suitable materials for ECs applications [25,71,72]. CPs makes use of redox processes. When oxidation occurs, ions are transferred to the polymer backbone, and when reduction takes place, the ions are released from this backbone into the electrolyte. The most commonly studied CPs in supercapacitor applications are polyaniline (PANI) [25], polypyrrole (PPy) [26], polythiophene (PTh) [71], poly(3,4-ethylene-dioxythiophene) (PEDOT) [28,73]. A high specific capacitance of 608 F g<sup>-1</sup> was reported for an electrode

modified with pure PANI [74]. However, the swelling and shrinking of CPs during the intercalating/deintercalating process leads to mechanical degradation of the electrode and low electrochemical performance during cycling, and thus hindering the commercialization of CPs electrode materials.

### 2.8.3 Transition metal oxides (TMO)

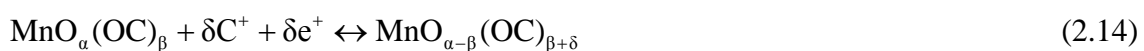
Transition metal oxides exhibit electrochemical faradaic reactions between electrode materials and ions within appropriate potential windows [75] TMO such as  $\text{RuO}_2$ , [76–78]  $\text{MnO}_2$  [79,80],  $\text{NiO}$  [81–83],  $\text{Co}_3\text{O}_4$  [84–86],  $\text{SnO}_2$  [87], and  $\text{V}_2\text{O}_5$  [88–90] have all been studied. They can provide higher energy density for ECs than carbon materials and better electrochemical stability than conducting polymer materials. The general requirements for metal oxides in ECs applications are as follows [1]:

- (1) The oxide should be electronically conductive,
- (2) The metal can exist in two or more oxidation states that coexist over a continuous range with no phase changes involving irreversible modifications of a 3-dimensional structure.
- (3) The protons can freely intercalate into the oxide lattice on reduction and out of the lattice on oxidation, allowing facile inter-conversion of  $\text{O}^{2-} \leftrightarrow \text{OH}^-$ .

**Hydrous  $\text{RuO}_2$ :** As mention earlier,  $\text{RuO}_2$  has been extensively studied as a material for ECs application. For example, amorphous  $\text{RuO}_2$  materials in the  $\text{H}_2\text{SO}_4$  electrolyte exhibited a specific capacitance of  $720 \text{ F g}^{-1}$  upon calcination at  $150 \text{ }^\circ\text{C}$  and a capacitance of  $710 \text{ F g}^{-1}$  was obtained in a  $\text{KOH}$  electrolyte for the crystalline state after calcination at  $200 \text{ }^\circ\text{C}$  [34]. In acidic electrolyte solution, the reaction mechanism is as follows  $\text{RuO}_2 + x\text{H}^+ + x\text{e}^- \leftrightarrow \text{RuO}_{2-x}(\text{OH})_x$ . Rapid reversible electron transfer is accompanied by

electro-adsorption of protons on the surface of RuO<sub>2</sub> particles, where Ru oxidation states can change from Ru (II) to Ru (IV) [1,34,91]. In an alkaline medium, it was suggested that the RuO<sub>2</sub> in the electrode will be oxidized to RuO<sub>4</sub><sup>2-</sup>, RuO<sub>4</sub><sup>-</sup>, RuO<sub>4</sub>, and when it is discharged these high valence states will be reduced to RuO<sub>2</sub> [92,93]. Nevertheless, the relatively high cost of this noble metal is a major drawback of RuO<sub>2</sub> based electrodes and this has limited it from being commercialized [94]. Hence, much effort has been aimed to searching for alternative inexpensive electrode materials with good capacitive characteristics, such as manganese oxide, cobalt oxide, nickel oxide, and vanadium oxide

**MnO<sub>2</sub>**: manganese oxides (MnO<sub>x</sub>) were earlier reported in 1999 [95] and have been extensively studied as electrode material for ECs application due to relatively low cost, low toxicity, environmental safety, and theoretical high capacities ranging from 1100 to 1300 F g<sup>-1</sup> [80,96–98]. Manganese oxides mainly exhibit pseudocapacitance, which is attributed to reversible redox reaction involving the exchange of protons and/or cations with the electrolyte, as well as the transitions between Mn (III)/Mn (II), Mn (IV)/Mn (III), and Mn (VI)/Mn (IV) within the electrode potential window of the electrolyte. The proposed mechanism is expressed in equation 2.14 [99–101]:



where C<sup>+</sup> denotes the protons and alkali metal cations (Li<sup>+</sup>, Na<sup>+</sup>, K<sup>+</sup>) in the electrolyte, and MnO<sub>α</sub>(OC)<sub>β</sub> and MnO<sub>α-β</sub>(OC)<sub>β+δ</sub> indicate MnO<sub>2n</sub>H<sub>2</sub>O in high and low oxidation states, respectively. The above equation suggests that both protons and alkali cations are involved in the redox process, and that the MnO<sub>x</sub> material must have high ionic and electronic conductivity [80]. It has also been shown that MnO<sub>x</sub>-based electrodes exhibit rectangular-shaped cyclic voltammetry curves contrary to non-faradaic energy storage mechanisms [102].

As reported, both the physical properties (e.g. microstructure and surface morphology) and chemical factors (valence and the hydrous state of the oxide) properties affect the pseudocapacitive performance of Mn oxides. It was found that the cycle stability of Mn oxides is mainly controlled by their microstructure, while their specific capacitance is governed primarily by their chemically hydrous state [103].

*Co<sub>3</sub>O<sub>4</sub>/Co(OH)<sub>2</sub>*: has been considered as alternative electrode material for ECs. The pseudocapacitance of Co<sub>3</sub>O<sub>4</sub> originates from the following redox reaction:[104]



Research activities have focused on Co<sub>3</sub>O<sub>4</sub> with various morphology for example, microspheres, nano-sheets, nanowires, nanorods, nanotubes as well as thin films have all been reported [84,86,105]. Mesoporous microspheres of Co<sub>3</sub>O<sub>4</sub> have been tested and found to exhibit a specific capacitance of 102 F g<sup>-1</sup> with a smaller inner resistance of about 0.4 Ohm [106]. A specific capacitance of 118 F g<sup>-1</sup> and 165 F g<sup>-1</sup> have also been reported for a cobalt oxide electrode using cobalt chloride precursor and chemical modified cobalt oxide copper substrates [107,108]. Self-supported hollow Co<sub>3</sub>O<sub>4</sub> nanowire arrays exhibit superior supercapacitor performances with high specific capacitances of 599 F g<sup>-1</sup> at 2 A g<sup>-1</sup> and 439 F g<sup>-1</sup> at 40 A g<sup>-1</sup> as well as excellent cycle life, making them suitable for high-rate supercapacitor application [86]. Co(OH)<sub>2</sub>-based electrode materials are also interesting due to their layered structure and huge interlayer spacing, which provides high surface area and a fast ion reaction rate [109–111]. The possible reaction mechanism is as follows [75,112]:



They have also been shown to give much higher specific capacitances than  $\text{Co}_3\text{O}_4$ . However, such high specific capacitance is only located in low potential ranges, which limits the materials' practical application in ECs.

**NiO/Ni(OH)<sub>2</sub>:** Nickel oxide are also promising electrode material for EC due to its easy synthesis, theoretical high specific capacitance of  $3750 \text{ F g}^{-1}$ , low cost and environment friendliness [113,114]. The redox reaction of nickel oxide in a KOH medium can be expressed as [82,115]:



It has been established that the structure and morphology of NiO nanostructure influence the electrochemical behavior. Mesoporous nickel oxide nano-architecture, synthesized via electrodeposition, demonstrated a specific capacitance of  $167 \text{ F g}^{-1}$  at a current density of  $1 \text{ A g}^{-1}$  and  $156 \text{ F g}^{-1}$  at  $16.5 \text{ A g}^{-1}$  [116], Nano-sized NiO/Ni composite films obtained by a chemical method have been found to exhibit specific capacitance between  $50\text{-}64 \text{ F g}^{-1}$  [81] while microwave-mediated synthesis shows hierarchical porous ball-like morphology with uniform ripple shaped pore and exhibited a specific capacitance of  $370 \text{ F g}^{-1}$  at a current density of  $2 \text{ A g}^{-1}$  [117]. ECs based on  $\text{Ni(OH)}_2$  have also been shown to yield higher specific capacitance than NiO [118], hexagonal nanoporous nickel hydroxide film with a maximum specific capacitance of  $578 \text{ F g}^{-1}$  was reported [75] and Hu *et al.* reported that an electrodeposited nickel hydrous oxide film could exhibit a specific capacitance as high as  $1000 \text{ F g}^{-1}$  [118]. NiO/Ni(OH)<sub>2</sub> based electrodes have been shown to exhibit good electrochemical performance. However, the challenges in using NiO-based electrode materials for EC involve: poor cycle performance and high internal resistance.

**Other oxides:** several other oxide materials, such as  $V_2O_5$  [119–121],  $Fe_2O_3$  [122],  $Fe_3O_4$  [123,124],  $SnO_2$  [125],  $IrO_2$  [126],  $MoO_2$  [127] and transition metal nitride [128], have all been explored and investigated as electrode materials for EC applications.  $V_2O_5$  were studied due to their variable oxidation states, which can yield both surface and bulk redox reactions. Porous vanadium oxide ( $V_2O_5$ ) sample prepared by a sol–gel technique was found to exhibit a maximum specific capacitance of  $214\text{ F g}^{-1}$  at a scan rate of  $5\text{ mV s}^{-1}$  in a  $2\text{ M KCl}$  solution [129]. While  $Fe_2O_3$  electrode synthesized using chemical method exhibited a specific capacitance of  $178\text{ F g}^{-1}$  at scan rate  $5\text{ mV s}^{-1}$  in a  $1\text{ M NaOH}$  electrolyte [122] and hydrous  $IrO_2$  exhibited a specific capacitance of  $550\text{ F g}^{-1}$  [126]. Most of these oxides materials exhibit excellent electrochemical performance. However the major disadvantages which have led to their unrealistic application include their small potential, poor electron and ion exchange and low conductivity.

#### **2.8.4 Composite materials**

Composite materials offer an attractive alternative approach for combining materials with different properties. For example, combining the pseudo-capacitive metal oxides or conducting polymers with a capacitive carbon material to take advantages of properties offered by the individual material can lead to increase in electrochemical performance of ECs. This is due to the fact that the individual materials in the composites can have a synergistic effect through minimizing particle size, enhancing specific surface area, inducing porosity, preventing agglomerating of particles, facilitating electron and proton conduction, expanding active sites, extending the potential window, protecting active materials from mechanical degradation, improving cycling stability, and providing extra pseudocapacitance [6]. As a result, the obtained composites can overcome some of the major drawbacks of the individual material and hence achieve high electrochemical performance. However, it is worth stating that a reverse effect might occur and therefore there should be a compromise in

the individual substance composition and an optimized molar ratio of the individual constituent is deemed necessary for composite material.

## 2.9 Electrolytes

The choice of electrolyte system for ECs includes wide voltage window, high electrochemical stability, high concentration of charge carriers (cations and anions), low resistivity, low viscosity, low volatility, low toxicity and low cost. The favoured electrolyte systems for ECs can be classified into three types: (1) aqueous media, (2) organic media, and (3) ionic liquids (ILs). ECs voltage in aqueous electrolytes is limited by the electrolyte decomposition at high potentials. They have high conductivity due to their proton hopping transport mechanism but have a theoretical limit of about 1.23 V. Nevertheless, migrating from aqueous to organic electrolytes increases the operating voltage to about 3.5 V. Thus, non-aqueous electrolytes are mainly used in majority of the commercialized supercapacitors today because they can achieve a higher potential window than aqueous electrolytes like KOH or H<sub>2</sub>SO<sub>4</sub>, which are limited to about 1.23 V [17]. Conventional electrolytes containing a mixture of a solvent and a salt, like tetraethylammonium tetrafluoroborate ((C<sub>2</sub>H<sub>5</sub>)<sub>4</sub>BF<sub>4</sub>), tetraethylphosphonium tetrafluoroborate, and triethylmethylammonium tetrafluoroborate (TEMABF<sub>4</sub>) have all been used. Acetonitrile can dissolve large amounts of salts and hence leads to highly conducting electrolytes but suffers from environmental and toxicity problems. Propylene carbonate (PC)-based electrolytes are friendlier to the environment and provides a wide range of potential window. They can be used as replacement for acetonitrile (AN) with compromise to the power density since the electrolyte conductivity drops by a factor of ~4 [60].

Ionic liquids (ILs), are solvent-free electrolytes which are liquid at room temperature (organic salts). Their properties such as stability in a large potential window, low vapor pressure, high

thermal and chemical stability make them promising for application as electrolyte for ECs, but their low conductivity at and below room temperature has limited their practical use at high temperatures [130–132]. They are mainly made up of cations and anions thus their voltage window stability is determined by the electrochemical stability of ions. A careful and proper choice of both ions allows the design of high-voltage ECs [133]. The most studied ILs are imidazolium, pyrrolidinium, aliphatic ammonium salts such as tetrafluoroborate, trifluoromethanesulfonate, bis(trifluoromethanesulfonyl)imide, bis(fluorosulfonyl)imide or hexafluorophosphate, quaternary ammonium salts such as tetralkylammonium  $[R_4N]^+$ , and cyclic amines such as aromatic pyridinium, imidazolium and saturated piperidinium, pyrrolidinium [134–137]. ECs devices based on ILs have been reported relating the relationship between the pore size of carbon electrodes, ion size of the electrolyte, and the capacitance using ethyl-methyl-imidazolium-bis(trifluoromethane-sulfonyl)imide [47]. Hybrid activated carbon/conducting polymer devices also show an improved performance with cell voltages higher than 3 V [138]. However, the ionic conductivity of these liquids is low at room temperature, and can be improved by selecting appropriate eutectic IL mixture-carbon combinations [139].

## 2.10 Graphene based materials for electrochemical capacitors

Graphene, a two dimensional allotrope of carbon (Figure 2.9), has emerged as one of the most exciting material for research in the last few years [140–142] This two-dimensional (2D) material constitutes a one-atom-thick sheet of  $sp^2$ -bonded carbon atoms in a honeycomb crystal lattice with atoms arranged in hexagonal pattern. It is the thinnest material known in the world and is regarded as the basic building block for all other carbon materials. It can be rolled into one-dimensional (1D) carbon nanotubes (CNTs), and stacked into three-

dimensional (3D) graphite. With the addition of pentagons it can also be wrapped into a fullerene (0D) [140].

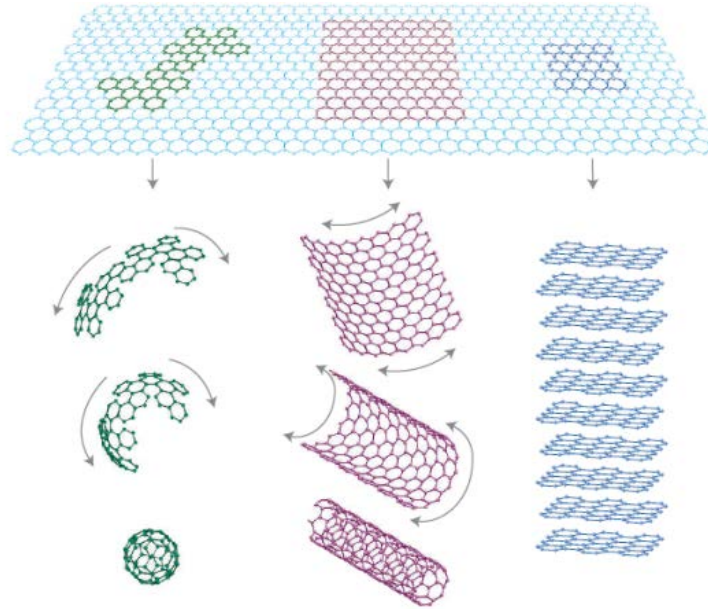


**Figure 2.9** Graphene: the mother of all graphitic forms. (Extracted from Ref. 127)

## 2.11 Properties of graphene

Graphene has unique electronic properties: it is a zero-gap semiconductor that exhibits linear dispersion at a high symmetry point in the reciprocal space, resulting in effective dynamics of electrons similar to that of massless relativistic Dirac Fermions [141]. Moreover, graphene possesses not only unique electronic properties, it also has excellent optical, thermal, mechanical and electrochemical properties that are superior to other allotropes of carbon such as graphite, CNTs and fullerene as shown in Table 1 below [141,143–147].

Allotropes of Carbon	Graphite	Diamond	Fullerene	Carbon nanotubes	Graphene
Dimensionality	Three	Three	Zero	One	Two
Hybridization	Sp <sup>2</sup>	Sp <sup>3</sup>	Mainly sp <sup>2</sup>	Mainly sp <sup>2</sup>	Sp <sup>2</sup>
Crystal system	Hexagonal	Octahedral	Tetragonal	Icosahedral	Hexagonal
Experimental specific surface area (m <sup>2</sup> g <sup>-1</sup> )	~10-20	~20-160	~80-90	~1300	~2675
Density (gcm <sup>-3</sup> )	2.09-2.23	3.5-3.53	1.72	>1	>1
Electrical conductivity (Scm <sup>-1</sup> )	Anisotropic 2,3X10 <sup>4</sup> <sup>a</sup> , 6 <sup>b</sup>		10 <sup>-10</sup>	Depends on the particular structure	2000
Electronic properties	Conductor	Insulator, semiconductor	Insulator	Depends on structure. Can be metallic or semiconducting	Semimetal, zero gap semiconductor
Thermal conductivity (Wm <sup>-1</sup> K <sup>-1</sup> )	1500-2000 <sup>a</sup> 5-10 <sup>c</sup>	900-2320	0.4	3500	4848-5300
Hardness tenacity	High	Ultrahigh	Highly elastic	High flexible elastic	Highest flexible elastic (single layer)
Optical properties	Uniaxial	Isotropic	Non-linear optical response	Structural dependent	97.7% optical transmittance
<sup>a</sup> a-direction <sup>b</sup> c-direction					

**Table 1** The properties of graphene and other carbon allotropes.

Because of its theoretical specific surface area of 2675 m<sup>2</sup> g<sup>-1</sup>, graphene has attracted attention as a potential electrode material for ECs. However, specific capacitance value of about 262 F g<sup>-1</sup> have only been achieved in aqueous electrolyte for pure graphene based supercapacitor [148–150]. This is due to the fact graphene sheet has a high tendency to restack during formation of electrode owing to the strong  $\pi$ – $\pi$  interactions between neighbouring sheets leading to significant decrease in the available surface area and consequently resulting in a lower specific capacitance values reported so far. To prevent the restacking problem and enhance the electrochemical performance of graphene based electrode it is necessary to functionalize graphene with chemical moieties such as carbonyl and hydroxyl groups [2] or graft the graphene sheets with pseudocapacitive materials which ultimately prevents the restacking of graphene, but also contributes to the total EDL capacitance of the electrode [151–158]. In regards to the latter, several hybrid composites of

graphene (or graphene oxide) have been reported. Composite such as graphene-metal oxide or metal hydroxide [147,154,159–167] and polymer [151,152] have all been investigated. In general, these studies have shown that the performance of ECs depends on the structure and porosity of the electrode. Recently, 3D graphene foam [168] has also attracted interest due to the unique porous structure offered which is essential for movement of ions in the electrolyte towards the surface of the electrode material. Significant efforts have also been made in the fabrication of composite materials based on the 3D form of graphene. In this thesis our aims are to synthesise composite materials based on this 3D graphene and develop electrodes for electrochemical capacitors

## References

- [1] B. Conway, *Electrochemical supercapacitors: scientific fundamentals and technological applications*, kluwer academic/plenum: New York, 1999.
- [2] E. Frackowiak, F. Beguin, F. Béguin, *Carbon* **39** (2001) 937.
- [3] R. Kötz, M. Carlen, *Electrochim. Acta* **45** (2000) 2483.
- [4] L.L. Zhang, X.S. Zhao, *Chem. Soc. Rev.* **38** (2009) 2520.
- [5] J.P. Zheng, J. Huang, T.R. Jow, *J. Electrochem. Soc.* **144** (1997) 2026.
- [6] G. Wang, L. Zhang, J. Zhang, *Chem. Soc. Rev.* **41** (2012) 797.
- [7] M. Deschamps, E. Gilbert, P. Azais, E. Raymundo-Piñero, M.R. Ammar, P. Simon, D. Massiot, F. Béguin, *Nat. Mater.* **12** (2013) 351.
- [8] Y.M. Vol'fkovich, T.M. Serdyuk, *Russ. J. Electrochem.* **38** (2002) 935.
- [9] O. Barbieri, M. Hahn, A. Herzog, R. Kötz, *Carbon* **43** (2005) 1303.
- [10] G. Gouy, *J. Phys* **9** (1910) 457.
- [11] D.L. Chapman, London, Edinburgh, Dublin *Philos. Mag. J. Sci.* **25** (1913) 475.
- [12] H. Stern-Hamburg, *S. F. Electrochem.* (1924) 508.
- [13] E. Paek, A.J. Pak, G.S. Hwang, *J. Electrochem. Soc.* **160** (2012) A1.
- [14] P. Simon, Y. Gogotsi, *Nat. Mater.* **7** (2008) 845.
- [15] J. Gamby, P.L. Taberna, P. Simon, J.F. Fauvarque, M. Chesneau, *J. Power Sources* **101** (2001) 109.
- [16] H. Nishihara, T. Kyotani, *Adv. Mater.* **24** (2012) 4473.
- [17] A.G. Pandolfo, A F. Hollenkamp, *J. Power Sources* **157** (2006) 11.
- [18] B. Xu, F. Wu, R. Chen, G. Cao, S. Chen, G. Wang, Y. Yang, *J. Power Sources* **158** (2006) 773.
- [19] P.L. Taberna, P. Simon, J.-F. Fauvarque, *J. Electrochem. Soc.* **150** (2003) A292.
- [20] P. Simon, Y. Gogotsi, *Philos. Trans. R. Soc. A Math. Phys. Eng. Sci.* **368** (2010) 3457.
- [21] J.R. Miller, A.F. Burke, *Electrochem. Soc. Interface* **17** (2008) 53.

- [22] W.-Y. Tsai, R. Lin, S. Murali, L. Li Zhang, J.K. McDonough, R.S. Ruoff, P.-L. Taberna, Y. Gogotsi, P. Simon, *Nano Energy* **2** (2013) 403.
- [23] C.-C. Hu, K.-H. Chang, M.-C. Lin, Y.-T. Wu, *Nano Lett.* **6** (2006) 2690.
- [24] H. Zhang, G. Cao, Z. Wang, Y. Yang, Z. Shi, Z. Gu, *Nano Lett.* **8** (2008) 2664.
- [25] K.S. Ryu, K.M. Kim, N.-G. Park, Y.J. Park, S.H. Chang, *J. Power Sources* **103** (2002) 305.
- [26] A. Clemente, S. Panero, E. Spila, B. Scrosati, *Solid State Ionics* **85** (1996) 273.
- [27] E. Frackowiak, V. Khomenko, K. Jurewicz, K. Lota, F. Beguin, *J. Power Sources* **153** (2006) 413.
- [28] K. Lota, V. Khomenko, E. Frackowiak, *J. Phys. Chem. Solids* **65** (2004) 295.
- [29] D. Choi, G.E. Blomgren, P.N. Kumta, *Adv. Mater.* **18** (2006) 1178.
- [30] T.-C. Liu, W.G. Pell, B.E. Conway, S.L. Roberson, *J. Electrochem. Soc.* **145** (1998) 1882.
- [31] T.A. Centeno, F. Stoeckli, *Electrochim. Acta* **52** (2006) 560.
- [32] W. Li, D. Chen, Z. Li, Y. Shi, Y. Wan, G. Wang, Z. Jiang, D. Zhao, *Carbon* **45** (2007) 1757.
- [33] E. Frackowiak, G. Lota, J. Machnikowski, C. Vix-Guterl, F. Béguin, *Electrochim. Acta* **51** (2006) 2209.
- [34] J.P. Zheng, P.J. Cygan, T.R. Jow, *J. Electrochem. Soc.* **142** (1995) 2699.
- [35] M. Inagaki, H. Konno, O. Tanaike, *J. Power Sources* **195** (2010) 7880.
- [36] D. Weingarh, A. Foelske-Schmitz, A. Wokaun, R. Kötz, *Electrochem. Commun.* **18** (2012) 116.
- [37] M.D. Stoller, R.S. Ruoff, *Energy Environ. Sci.* **3** (2010) 1294.
- [38] T. Brezesinski, J. Wang, J. Polleux, B. Dunn, S.H. Tolbert, *J. Am. Chem. Soc.* **131** (2009) 1802.
- [39] A.J. Bard, L.R. Faulkner, *Electrochemical methods: fundamentals and applications*, Wiley New York, 1980.
- [40] W. Sun, R. Zheng, X. Chen, *J. Power Sources* **195** (2010) 7120.
- [41] P. Thounthong, S. Raël, B. Davat, *J. Power Sources* **193** (2009) 376.
- [42] A. Kusko, J. DeDad, *Ind. Appl. Mag. IEEE* **13** (2007) 66.

- [43] A. Burke, *J. Power Sources* **91** (2000) 37.
- [44] Y. Zhang, H. Feng, X. Wu, L. Wang, A. Zhang, T. Xia, H. Dong, X. Li, L. Zhang, *Int. J. Hydrogen Energy* **34** (2009) 4889.
- [45] J.R. Miller, *Electrochim. Acta* **52** (2006) 1703.
- [46] R.N. Reddy, R.G. Reddy, *J. Power Sources* **124** (2003) 330.
- [47] C. Largeot, C. Portet, J. Chmiola, P.-L. Taberna, Y. Gogotsi, P. Simon, *J. Am. Chem. Soc.* **130** (2008) 2730.
- [48] P. Harrop and V. Zhitomirsky, *Electrochemical Double Layer Capacitors: Supercapacitors 2013-2023* (2014).
- [49] A.S. Aricò, P. Bruce, B. Scrosati, J.-M. Tarascon, W. Van Schalkwijk, *Nat. Mater.* **4** (2005) 366.
- [50] M.C.F. Wander, K.L. Shuford, *J. Phys. Chem. C* **114** (2010) 20539.
- [51] H. Lee, M.S. Cho, I.H. Kim, J. Do Nam, Y. Lee, *Synth. Met.* **160** (2010) 1055.
- [52] E. Frackowiak, *Phys. Chem. Chem. Phys.* **9** (2007) 1774.
- [53] C. Portet, G. Yushin, Y. Gogotsi, *Carbon* **45** (2007) 2511.
- [54] D. Pech, M. Brunet, H. Durou, P. Huang, V. Mochalin, Y. Gogotsi, P.-L. Taberna, P. Simon, *Nat. Nanotechnol.* **5** (2010) 651.
- [55] I. Kovalenko, D.G. Bucknall, G. Yushin, *Adv. Funct. Mater.* **20** (2010) 3979.
- [56] D.N. Futaba, K. Hata, T. Yamada, T. Hiraoka, Y. Hayamizu, Y. Kakudate, O. Tanaike, H. Hatori, M. Yumura, S. Iijima, *Nat. Mater.* **5** (2006) 987.
- [57] H. Pan, J. Li, Y. Feng, *Nanoscale Res. Lett.* **5** (2010) 654.
- [58] H. Zhang, G. Cao, Y. Yang, *Energy Environ. Sci.* **2** (2009) 932.
- [59] E. Frackowiak, K. Jurewicz, S. Delpeux, F. Béguin, *J. Power Sources* **822** (2001) 97.
- [60] P. Simon, Y. Gogotsi, *Acc. Chem. Res.* **46** (2012) 1094.
- [61] L. Wei, M. Sevilla, A.B. Fuertes, R. Mokaya, G. Yushin, *Adv. Energy Mater.* **1** (2011) 356.
- [62] Y. Gogotsi, A. Nikitin, H. Ye, W. Zhou, J.E. Fischer, B. Yi, H.C. Foley, M.W. Barsoum, *Nat. Mater.* **2** (2003) 591.
- [63] V. Presser, M. Heon, Y. Gogotsi, *Adv. Funct. Mater.* **21** (2011) 810.

- [64] G.N. Yushin, E.N. Hoffman, A. Nikitin, H. Ye, M.W. Barsoum, Y. Gogotsi, *Carbon* **43** (2005) 2075.
- [65] S.-H. Yeon, P. Reddington, Y. Gogotsi, J.E. Fischer, C. Vakifahmetoglu, P. Colombo, *Carbon* **48** (2010) 201.
- [66] J. Chmiola, G. Yushin, Y. Gogotsi, C. Portet, P. Simon, P.L. Taberna, *Science* **313** (2006) 1760.
- [67] J. Chmiola, C. Largeot, P.-L. Taberna, P. Simon, Y. Gogotsi, *Angew. Chem.* **47** (2008) 3392.
- [68] V. Presser, L. Zhang, J.J. Niu, J. McDonough, C. Perez, H. Fong, Y. Gogotsi, *Adv. Energy Mater.* **1** (2011) 423.
- [69] A. Malinauskas, J. Malinauskiene, A. Ramanavičius, *Nanotechnology* **16** (2005) R51.
- [70] C. Peng, J. Jin, G.Z. Chen, *Electrochim. Acta* **53** (2007) 525.
- [71] C. Arbizzani, M. Mastragostino, L. Meneghello, *Electrochim. Acta* **41** (1996) 21.
- [72] M. Kalaji, P.J. Murphy, G.O. Williams, *Synth. Met.* **102** (1999) 1360.
- [73] W. Li, J. Chen, J. Zhao, J. Zhang, J. Zhu, *Mater. Lett.* **59** (2005) 800.
- [74] H. Li, J. Wang, Q. Chu, Z. Wang, F. Zhang, S. Wang, *J. Power Sources* **190** (2009) 578.
- [75] D.-D. Zhao, S.-J. Bao, W.-J. Zhou, H.-L. Li, *Electrochem. Commun.* **9** (2007) 869.
- [76] T. Liu, W.G. Pell, B.E. Conway, *Electrochim. Acta* **42** (1997) 3541.
- [77] Y.R. Ahn, M.Y. Song, S.M. Jo, C.R. Park, D.Y. Kim, *Nanotechnology* **17** (2006) 2865.
- [78] T.-S. Hyun, J.-E. Kang, H.-G. Kim, J.-M. Hong, I.-D. Kim, *Electrochem. Solid-State Lett.* **12** (2009) A225.
- [79] N. Nagarajan, H. Humadi, I. Zhitomirsky, *Electrochim. Acta* **51** (2006) 3039.
- [80] M. Toupin, T. Brousse, D. Belanger, *Chem. Mater.* **16** (2004) 3184.
- [81] K.-C. Liu, M.A. Anderson, *J. Electrochem. Soc.* **143** (1996) 124.
- [82] V. Srinivasan, J.W. Weidner, *J. Electrochem. Soc.* **144** (1997) L210.
- [83] M.-S. Wu, H.-H. Hsieh, *Electrochim. Acta* **53** (2008) 3427.
- [84] Y. Gao, S. Chen, D. Cao, G. Wang, J. Yin, *J. Power Sources* **195** (2010) 1757.

- [85] S.K. Meher, G.R. Rao, *J. Phys. Chem. C* **115** (2011) 15646.
- [86] X. Xia, J. Tu, Y. Mai, X. Wang, C. Gu, X. Zhao, *J. Mater. Chem.* **21** (2011) 9319.
- [87] N. Miura, S. Oonishi, K.R. Prasad, *Electrochem. Solid-State Lett.* **7** (2004) A247.
- [88] X. Zhou, H. Chen, D. Shu, C. He, J. Nan, *J. Phys. Chem. Solids* **70** (2009) 495.
- [89] X. Zhou, C. Shang, L. Gu, S. Dong, X. Chen, P. Han, L. Li, J. Yao, Z. Liu, H. Xu, others, *ACS Appl. Mater. Interfaces* **3** (2011) 3058.
- [90] A.M. Glushenkov, D. Hulicova-Jurcakova, D. Llewellyn, G.Q. Lu, Y. Chen, *Chem. Mater.* **22** (2009) 914.
- [91] S. Trasatti, *Electrochim. Acta* **36** (1991) 225.
- [92] J.H. Jang, S. Han, T. Hyeon, S.M. Oh, *J. Power Sources* **123** (2003) 79.
- [93] J.P. Zheng, *Electrochem. Solid-State Lett.* **2** (1999) 359.
- [94] L.-Z. Fan, Y.-S. Hu, J. Maier, P. Adelhelm, B. Smarsly, M. Antonietti, *Adv. Funct. Mater.* **17** (2007) 3083.
- [95] H.Y. Lee, J.B. Goodenough, *J. Solid State Chem.* **144** (1999) 220.
- [96] J. Wei, N. Nagarajan, I. Zhitomirsky, *J. Mater. Process. Technol.* **186** (2007) 356.
- [97] J.-K. Chang, Y.-L. Chen, W.-T. Tsai, *J. Power Sources* **135** (2004) 344.
- [98] V. Subramanian, H. Zhu, B. Wei, *Chem. Phys. Lett.* **453** (2008) 242.
- [99] W. Wei, X. Cui, W. Chen, D.G. Ivey, *Chem. Soc. Rev.* **40** (2011) 1697.
- [100] C. Ye, Z.M. Lin, S.Z. Hui, *J. Electrochem. Soc.* **152** (2005) A1272.
- [101] S.-C. Pang, M. A. Anderson, T.W. Chapman, *J. Electrochem. Soc.* **147** (2000) 444.
- [102] E. Macheaux, T. Brousse, D. Bélanger, D. Guyomard, *J. Power Sources* **165** (2007) 651.
- [103] J.-K. Chang, C.-H. Huang, M.-T. Lee, W.-T. Tsai, M.-J. Deng, I.-W. Sun, *Electrochim. Acta* **54** (2009) 3278.
- [104] T.-C. Liu, W.G. Pell, B.E. Conway, *Electrochim. Acta* **44** (1999) 2829.
- [105] V.R. Shinde, S.B. Mahadik, T.P. Gujar, C.D. Lokhande, *Appl. Surf. Sci.* **252** (2006) 7487.
- [106] L. Wang, X. Liu, X. Wang, X. Yang, L. Lu, *Curr. Appl. Phys.* **10** (2010) 1422.

- [107] S.G. Kandalkar, D.S. Dhawale, C.-K. Kim, C.D. Lokhande, *Synth. Met.* **160** (2010) 1299.
- [108] S.G. Kandalkar, J.L. Gunjekar, C.D. Lokhande, *Appl. Surf. Sci.* **254** (2008) 5540.
- [109] L. Xie, K. Li, G. Sun, Z. Hu, C. Lv, J. Wang, C. Zhang, *J. Solid State Electrochem.* **17** (2013) 55.
- [110] V. Gupta, T. Kusahara, H. Toyama, S. Gupta, N. Miura, *Electrochem. Commun.* **9** (2007) 2315.
- [111] V. Gupta, S. Gupta, N. Miura, *J. Power Sources* **177** (2008) 685.
- [112] L. Cao, F. Xu, Y.-Y. Liang, H.-L. Li, *Adv. Mater.* **16** (2004) 1853.
- [113] K.-W. Nam, K.-H. Kim, E.-S. Lee, W.-S. Yoon, X.-Q. Yang, K.-B. Kim, *J. Power Sources* **182** (2008) 642.
- [114] M. Wu, Y. Huang, J. Jow, W. Yang, C. Hsieh, H. Tsai, *Int. J. Hydrogen Energy* **33** (2008) 2921.
- [115] P.A. Nelson, J.M. Elliott, G.S. Attard, J.R. Owen, *Chemistry of materials* **14** (2002) 524.
- [116] M.-S. Wu, Y.-A. Huang, C.-H. Yang, J.-J. Jow, *Int. J. Hydrogen Energy* **32** (2007) 4153.
- [117] S.K. Meher, P. Justin, G.R. Rao, *ACS Appl. Mater. Interfaces* **3** (2011) 2063.
- [118] Y. Hu, Y. V Tolmachev, D.A. Scherson, *J. Electroanal. Chem.* **468** (1999) 64.
- [119] W. Dong, D.R. Rolison, B. Dunn, *Electrochem. Solid-State Lett.* **3** (2000) 457.
- [120] W. Dong, J. Sakamoto, B. Dunn, *J. Sol-Gel Sci. Technol.* **26** (2003) 641.
- [121] K. Takahashi, S.J. Limmer, Y. Wang, G. Cao, *J. Phys. Chem. B* **108** (2004) 9795.
- [122] P.M. Kulal, D.P. Dubal, C.D. Lokhande, V.J. Fulari, *J. Alloys Compd.* **509** (2011) 2567.
- [123] S. Mitra, P. Poizot, A. Finke, J.-M. Tarascon, *Adv. Funct. Mater.* **16** (2006) 2281.
- [124] H. Zhu, D. Yang, L. Zhu, *Surf. Coatings Technol.* **201** (2007) 5870.
- [125] S.-W. Hwang, S.-H. Hyun, *J. Power Sources* **172** (2007) 451.
- [126] A.A.F. Grupioni, E. Arashiro, T.A.F. Lassali, *Electrochim. Acta* **48** (2002) 407.
- [127] J. Rajeswari, P.S. Kishore, B. Viswanathan, T.K. Varadarajan, *Electrochem. Commun.* **11** (2009) 572.

- [128] D. Choi, P.N. Kumta, *Electrochem. Solid-State Lett.* **8** (2005) A418.
- [129] R.N. Reddy, R.G. Reddy, *J. Power Sources* **156** (2006) 700.
- [130] M. Armand, F. Endres, D.R. MacFarlane, H. Ohno, B. Scrosati, *Nat. Mater.* **8** (2009) 621.
- [131] S. Pandey, *Anal. Chim. Acta* **556** (2006) 38.
- [132] A. Balducci, W.A. Henderson, M. Mastragostino, S. Passerini, P. Simon, F. Soavi, *Electrochim. Acta* **50** (2005) 2233.
- [133] T. Tsuda, C.L. Hussey, *Interface-Electrochemical Soc.* **16** (2007) 42.
- [134] M. Galiński, A. Lewandowski, I. Stępnia, *Electrochim. Acta* **51** (2006) 5567.
- [135] J.F. Wishart, *Energy Environ. Sci.* **2** (2009) 956.
- [136] G. Lakshminarayana, M. Nogami, *Electrochim. Acta* **55** (2010) 1160.
- [137] A. Lewandowski, A. Olejniczak, M. Galinski, I. Stepniak, *J. Power Sources* **195** (2010) 5814.
- [138] A. Balducci, R. Dugas, P.-L. Taberna, P. Simon, D. Plee, M. Mastragostino, S. Passerini, *J. Power Sources* **165** (2007) 922.
- [139] R. Lin, P. Taberna, V. Presser, R.P. Carlos, N.L. Rupesinghe, K.B.K. Teo, Y. Gogotsi, P. Simon, *J. Phys. Chem. Lett.* **2** (2011) 2396.
- [140] A.K. Geim, K.S. Novoselov, *Nat. Mater.* **6** (2007) 183.
- [141] K.S. Novoselov, A.K. Geim, S.V. Morozov, D. Jiang, I.V. Grigorieva, S.V. Dubonos, A.A. Firsov, M.I. Katsnelson, *Nature* **438** (2005) 197.
- [142] K.S. Novoselov, A.K. Geim, S. V Morozov, D. Jiang, Y. Zhang, S. V Dubonos, I. V Grigorieva, A.A. Firsov, *Science* **306** (2004) 666.
- [143] C.N.R. Rao, A.K. Sood, K.S. Subrahmanyam, A. Govindaraj, *Angew. Chemie* **48** (2009) 7752.
- [144] F. Schedin, A.K. Geim, S. V Morozov, E.W. Hill, P. Blake, M.I. Katsnelson, K.S. Novoselov, *Nat. Mater.* **6** (2007) 652.
- [145] S. Pisana, M. Lazzeri, C. Casiraghi, K.S. Novoselov, A.K. Geim, A.C. Ferrari, F. Mauri, *Nat. Mater.* **6** (2007) 198.
- [146] R.R. Nair, P. Blake, A.N. Grigorenko, K.S. Novoselov, T.J. Booth, T. Stauber, N.M.R. Peres, A.K. Geim, *Science.* **320** (2008) 1308.

- [147] Z.-S. Wu, G. Zhou, L.-C. Yin, W. Ren, F. Li, H.-M. Cheng, *Nano Energy* **1** (2012) 107.
- [148] Y. Wang, Z. Shi, Y. Huang, Y. Ma, C. Wang, M. Chen, Y. Chen, *J. Phys. Chem. C* **113** (2009) 13103.
- [149] S.R.C. Vivekchand, C.S. Rout, K.S. Subrahmanyam, A. Govindaraj, C.N.R. Rao, *J. Chem. Sci.* **120** (2008) 9.
- [150] Y. Zhu, S. Murali, W. Cai, X. Li, *Adv. Mater.* **22** (2010) 3906.
- [151] K. Zhang, L.L. Zhang, X.S. Zhao, J. Wu, *Chem. Mater.* **22** (2010) 1392.
- [152] L.L. Zhang, S. Zhao, X.N. Tian, X.S. Zhao, *Langmuir* **26** (2010) 17624.
- [153] Y. Chen, X. Zhang, D. Zhang, P. Yu, Y. Ma, *Carbon* **49** (2011) 573.
- [154] H. Wang, H.S. Casalongue, Y. Liang, H. Dai, *J. Am. Chem. Soc.* **132** (2010) 7472.
- [155] S. Wang, S.P. Jiang, X. Wang, *Electrochim. Acta* **56** (2011) 3338.
- [156] Z.-S. Wu, W. Ren, D. Wang, F. Li, B. Liu, H. Cheng, *ACS Nano* **4** (2010) 5835.
- [157] Z.-S. Wu, D.-W. Wang, W. Ren, J. Zhao, G. Zhou, F. Li, H.-M. Cheng, *Adv. Funct. Mater.* **20** (2010) 3595.
- [158] L.L. Zhang, T. Wei, W. Wang, X.S. Zhao, *Microporous Mesoporous Mater.* **123** (2009) 260.
- [159] X. Dong, L. Wang, D. Wang, C. Li, J. Jin, *Langmuir* **28** (2011) 293.
- [160] Y. Qian, S. Lu, F. Gao, *J. Mater. Sci.* **46** (2011) 3517.
- [161] B. Wang, J. Park, C. Wang, H. Ahn, G. Wang, *Electrochim. Acta* **55** (2010) 6812.
- [162] X.H. Xia, J.P. Tu, Y.Q. Zhang, Y.J. Mai, X.L. Wang, C.D. Gu, X.B. Zhao, *J. Phys. Chem. C* **115** (2011) 22662.
- [163] J. Yan, T. Wei, W. Qiao, B. Shao, Q. Zhao, L. Zhang, Z. Fan, *Electrochim. Acta* **55** (2010) 6973.
- [164] J. Yao, X. Shen, B. Wang, H. Liu, G. Wang, *Electrochem. Commun.* **11** (2009) 1849.
- [165] G. Yu, L. Hu, M. Vosgueritchian, H. Wang, X. Xie, J.R. McDonough, X. Cui, Y. Cui, Z. Bao, *Nano Lett.* **11** (2011) 2905.
- [166] J. Zhang, J. Jiang, X.S. Zhao, *J. Phys. Chem. C* **115** (2011) 6448.
- [167] Y. Zhang, H. Li, L. Pan, T. Lu, Z. Sun, *J. Electroanal. Chem.* **634** (2009) 68.

[168] Z. Chen, W. Ren, L. Gao, B. Liu, S. Pei, H. Cheng, *Nat. Mater.* **10** (2011) 424.

# Chapter 3

## Characterization and growth techniques

### Introduction

In this chapter all the experimental procedure used in this work will be discussed starting with the CVD technique for the production of graphene samples and characterization. In addition some important methods for the preparation of composite such as the hydrothermal growth technique will also be discussed.

### 3.1 Chemical vapor deposition (CVD)

Chemical vapor deposition (CVD) is an appealing growth technique for the preparation and production of graphene with excellent electronic properties which is very useful in a number of applications such as organic photovoltaic (OPV) devices, solar cells and supercapacitors [1,2]. This method is already well implemented in the semiconductor industry. For graphene production, this growth technique can be easily scaled up since it is a relatively inexpensive technique involving deposition on transition metal substrates which produces large-area graphene. During the CVD graphene growth process, gaseous precursors such ( $\text{Ar:H}_2\text{:CH}_4$ ) are fed into the reactor at atmosphere pressure and pass through a hot zone, where hydrocarbon precursor decomposes to carbon radicals at the metal substrate surface, forming single-layer, few and multi-layers graphene [3–5]. Ar is a carrier gas and role is to create an inert environment while  $\text{H}_2$  is to remove most of the impurities present in the material and also increase grain size of substrate (Ni or Cu) during the CVD growth. During the reaction, the metal substrate not only works as a catalyst to lower the energy barrier of the reaction, but also determines the graphene deposition mechanism [3]. Ni and Cu substrates are the most studied transition metal substrates for production of graphene [3,4]. In this chapter will focus

more on the Ni film which has a similar growth mechanism with Ni-foam used in this work. A schematic of the CVD system and the CVD system used in this work is shown below.

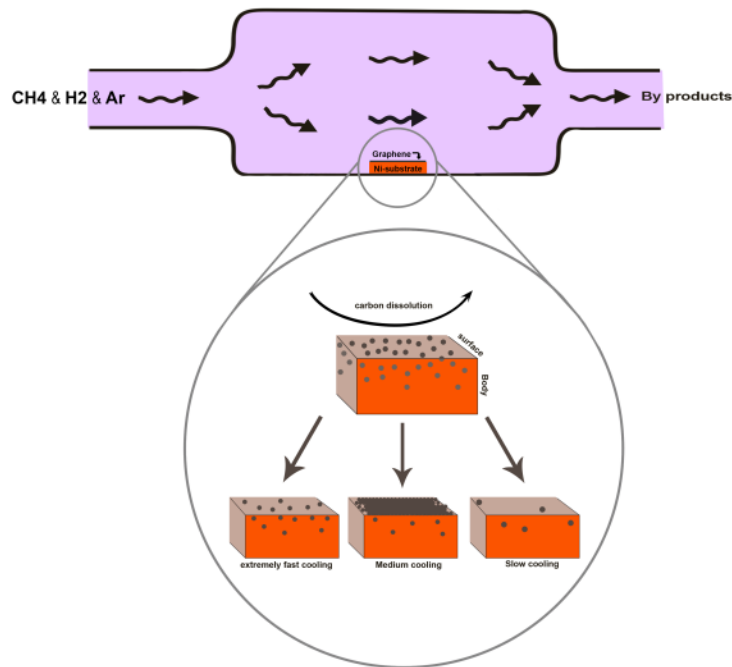


**Figure 3.1** Typical thermal chemical vapor deposition system showing different cooling rates of graphene on a nickel substrate.

Ni surface can serve as an excellent lattice-matched substrate for graphene growth. Basically, polycrystalline nickel foam (420-580 g m<sup>-2</sup> in areal density and 1.6-1.9 mm in thickness) are first annealed in Ar/H<sub>2</sub> atmosphere at 800-1000 °C to increase grain size and remove any

form of impurities as mentioned above before the introduction of hydrocarbon  $\text{CH}_4$  gas into the reaction chamber for a period of about 10 minutes to about an hour the Ar gas provides an inert environment while the  $\text{H}_2$  gas helps in the removal of impurities from the Ni foam. Firstly, hydrocarbon gas decomposes to carbon radicals and carbon atoms dissolve into the Ni to form a solid solution. Finally, samples are cooled down in argon gas which ultimately determines the thickness and uniformity of the deposition depending on the cooling rates. During the cooling process, carbon atoms diffuse out from the Ni-C solid solution and precipitate on the Ni surface to form graphene films [4]. The following cooling process can be achieved at fast, medium and slow rates as illustrated in figure 3.1 above. The graphene growth mechanism on Ni is based on carbon segregation and precipitation, the cooling behavior (cooling rates) strongly affects the thickness and quality of graphene films produced. Medium cooling rates are found to lead to optimal carbon segregation and produce few layer graphene while fast and slow cooling rates have been shown to give patches of graphene deposition on the Ni substrate [4]. The microstructure of Ni films also plays an important role in the formation of the graphene film morphology [6–8]. After the production of graphene, the nickel template has to be removed so that the film can be transferred to an arbitrary template for application purposes. This is usually done through a wet chemical etching. Briefly, the polymethyl methacrylate (PMMA) is dissolved in ethyl lactate and a thin layer of this PMMA solution is coated onto the graphene and then baked at  $180\text{ }^\circ\text{C}$  to evaporate the solvent and provide mechanical support for the graphene during etching. The PMMA coated graphene is then placed in a 3 M concentration of acid ( $\text{HCl}$  or  $\text{HNO}_3$ ) to remove the Ni template, leaving only the PMMA/graphene film. The film is washed with deionized (DI) water and then transferred onto a substrate such as glass or  $\text{Si/SiO}_2$ . Afterward, the PMMA can be removed by acetone or annealing in  $\text{Ar/H}_2$  atmosphere, leaving a graphene film on the targeted substrate. This process is also used to produce graphene foam to the

exception that no transfer to a substrate is necessary. In this work, we investigated both the etched and unetched three dimensional graphene foam samples for electrochemical applications. Composite materials of the graphene were made using hydrothermal methods such as the low temperature aqueous chemical growth (ACG) and the microwave irradiation technique.

### **3.1.1 Aqueous chemical growth technique (ACG)**

Aqueous chemical growth (ACG) technique is an inexpensive bottom-up approach that has been developed for the production of composite materials or thin films of various metal oxides at relatively low temperatures [9,10]. This technique allows the design and the production of nanostructured oxide materials with novel morphology and orientation which enable the probing and optimization of their physical properties [11]. The ACG technique involves the hydrolysis-condensation of hydrated metal ions onto the various substrates which allows for growth of different advanced nano, meso, micro and macro-particulate materials as well as different shapes and sizes of one, two and three-dimensional architecture [12,13]. The technique simply involves heating of an aqueous solution of metal precursors (salts or complexes) at a given pressure, concentration and pH, in the presence of substrates at low temperatures ( $< 100\text{ }^{\circ}\text{C}$ ) in a closed bottle as shown in the figure 3.2. Usually, during the ACG crystallites are nucleating and growing directly from the substrate at low temperatures, which result in a variety of substrates being, used e.g. amorphous, single crystalline, polycrystalline, transparent, conducting, flexible etc. Such diversity provides a higher degree of nanomaterials engineering and design. After the ACG reaction, the residual salts are easily washed out by water due to their high solubility [11]. In most cases, no additional heat or chemical treatments are necessary, which represents a significant improvement compared to other conventional techniques such as the sol-gel method. This

technique is generally safe, inexpensive, can easily be reproduced and is environmental-friendly.

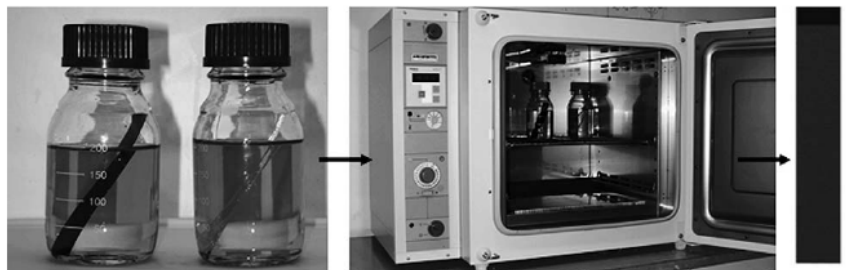


**Figure 3.2** The aqueous chemical growth (ACG) thin film processing technique: immersion of substrates in aqueous solutions of metal salt precursors (left), heat treatment in a conventional laboratory oven below 100 °C.(extracted from ref 11)

### 3.1.2 The microwave (MW) technology

The microwave technology is known to reduce reaction times and increase productivity yield of materials compared to other conventional reflux experiments. This technology makes use of two heating mechanisms namely dipolar polarization and ionic conduction. The dipoles in the reaction chamber are involved in the polarization effect, while the charged particles in a reaction chamber (usually ions) contribute to ionic conduction effects [14,15]. This technology ensures efficient internal volumetric heating which uniformly raise temperature throughout the whole liquid volume, by direct coupling of MW energy to the molecules that are present in the reaction mixture [16,17]. This phenomenon is usually dependent on the ability of a specific material (solvent or reagent) to absorb microwave energy and convert it into heat. This process of irradiation of materials at different frequencies results in the dipoles or ions aligning in the direction of applied electric field. However, as the applied field begins to oscillate, the dipole or ion field also attempts to realign itself with the alternating electric field which result to loss of energy in the form of heat through molecular friction and

dielectric loss [15]. The amount of heat generated by this process is directly related to the ability of the matrix to align itself with the frequency of the applied field [17–19].

Mechanistic studies and theoretical modelling have shown that the MW irradiation can give rise to different dimensionalities, size variation and shapes. Several circumstances can potentially interrupt isotropic growth evolution, leading to the formation of materials with anisotropic morphologies as diverse as nanorods, wires, bullets, platelets, ellipsoids, polypods and rings. Basically, suitable precursors bearing the atomic elements necessary to build up the particles are induced to react or decompose in a solution that contains specific functional species or additives under controlled atmosphere, selected temperature, power and pressure conditions for the reaction purposes. Once the synthesis is initiated, highly reactive intermediate species are generated, commonly referred to as the “monomers”, which induce the nucleation. Once the critical super-saturation threshold required to guarantee the thermodynamic stability of the particles is sustained, all particles will be allowed to evolve to progressively large dimensions. Finally, Ostwald ripening may occur depending on the reaction times, leading to dissolution of smaller particle size, consequently, providing extra monomers to sustain the growth of the larger like particles with a lamellar structure which tend to curl and assembly to form different hierarchical structure [17,20,21]. The ability to maintain a balance of nucleation and growth processes in liquid media is the basis of the formation of uniform nanostructure with predetermined structural, compositional and geometric features and precisely size-correlated properties.

### **3.1.3 Successive Ionic Layer Adsorption and Reaction (SILAR)**

The successive ionic layer adsorption and reaction (SILAR) method is advantageous due to layer-by-layer growth, which comprises excellent material utilization, good control over the deposition process and is specifically convenient for large area deposition [22,23]. This

method is an exothermic process mainly based on the adsorption and reaction of the ions from the solutions and rinsing between every immersion with deionized water to avoid homogeneous precipitation. The growth kinetics of a thin film deposition process is of two types: (i) ion-by-ion growth where the deposition process involves the ion-by-ion deposition at nucleation sites on the immersed surfaces and (ii) according to Lundin and Kitaev (1965) [24], nucleation takes place by adsorption of the particles due to attraction force between ions in the solution and surface of the substrate and growth takes place giving thin and adherent films [25]. A typical SILAR setup is shown in figure 3.3 below.

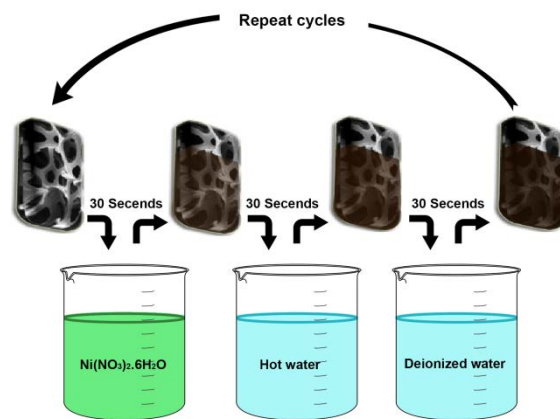


**Figure 3.3** Schematic SILAR set up used for the deposition of NiO on NF-G.

The growth mechanism involves the following steps: (i) specific adsorption of the most strongly adsorbed ions of the compound to be grown, by the substrate immersion in a solution of one of its cationic precursor, (ii) water rinsing of the excess solution still adhering to the substrate, and (iii) chemical reaction between the most strongly specific adsorbed cations and the less strongly adsorbed anions by the subsequent substrate immersion in the solution. In this first step, the cations present in the solvated cationic precursor solution are adsorbed on the surface of the substrate and form the Helmholtz electric double layer [23]. This layer is composed of two layers: the inner (positively charged) and outer (negatively charged) layers.

The positive layer consists of the cations and the negative forms the counter ions of the cations. In the second step, excess unabsorbed ions are rinsed away from the diffusion layer resulting in a saturated electrical double layer [26]. In the third step, the anions from anionic precursor solution are introduced to the system. Due to the low stability of the material, a solid substance is formed at the interface. The last step rinses the excess and unreacted species of both types of precursors and the reaction by-product from the diffusion layer are removed. By repeating these cycles, a thin layer of material can be grown. Following the above-mentioned steps, the maximum increase in film thickness per one reaction cycle is theoretically one monolayer. Dividing the measured overall film thickness by number of reaction cycles, growth rate can be determined [22,26].

## **3.2 Materials Characterization**

### **3.2.1 Raman Analysis**

Raman is a spectroscopic technique used to observe vibrational, rotational, and other low-frequency modes in a system [27]. Low frequency Raman modes (below  $400\text{ cm}^{-1}$ ) are generally associated with metal-ligand bonds. If one is interested in studying very low-frequency Raman modes which lie close to the laser line, it is important to choose a filter or filtering technique that provides a sharp transition between deep blocking of the Rayleigh scatter and transmission of the Raman signal. It relies on inelastic scattering or Raman scattering of monochromatic light, usually from a laser in the visible, near infrared or near ultraviolet range. The laser light interacts with molecular vibrations, phonons or other excitations in the system, resulting in the energy of the laser photons being shifted up or down. The shift in energy provides the chemical and structural information about the vibrational modes in the system.

Typically, in a Raman experiment the sample is irradiated with a monochromatic radiation (laser) depending on the sample type the laser light is scattered with a finite probability. If the sample is transparent most of the light is transmitted, a small fraction is elastically (Rayleigh) scattered and a very small fraction is inelastically (Raman) scattered. The inelastically scattered light is collected and dispersed and the results are presented as a Raman spectrum which plots the intensity of the inelastically scattered light as a function of energy or the shift in the wavenumber of the radiation [27,28].

For  $sp^2$  nanocarbons such as graphene and carbon nanotubes, Raman spectroscopy can give information about crystallite size, clustering of the  $sp^2$  phase, the presence of  $sp^2$ - $sp^3$  hybridization and the introduction of chemical impurities, the magnitude of the mass density, the optical energy gap, elastic constants, doping, defects and other crystal disorder, edge structure, strain, number of graphene layers, nanotube diameter, chirality, curvature, and finally the metallic vs semiconducting behavior and the science of excitons which make carbon nanotubes unique [29]. In this section various Raman features are discussed including the G-band at  $\sim 1582\text{ cm}^{-1}$ , which is common to all  $sp^2$  carbon forms, the radial breathing mode (RBM) that makes the diameter and optical transition energy analysis of nanotubes possible, and the D and G' bands that are significant in providing information about the electronic and geometrical structure through the double resonance process [29,30].

**The G-Band:** The stretching of the C-C bond in graphitic materials gives rise to the so-called G-band Raman feature which is common to all  $sp^2$  carbon systems (see figures 3.4). This spectral feature is similar for graphenes and nanotubes but yet has properties capable of distinguishing one carbon nanotstructure from another. When the bond lengths and angles of graphene are modified by strain, caused by the interaction with a substrate or with other graphene layers or due to external perturbations, the hexagonal symmetry of graphene is broken [31]. The G-band is, therefore, highly sensitive to strain effects in  $sp^2$  nanocarbons

and can be used to probe any modification to the flat geometric structure of graphene, such as the strain induced by external forces, by one graphene layer on another in few layer graphene or in multiwall nanotubes, or even by the curvature of the side wall when growing a SWNT [31].

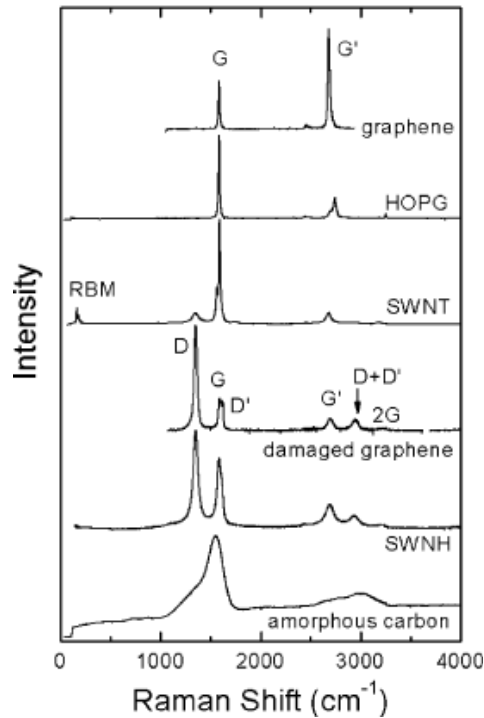


**Figure 3.4** Raman spectra from different types of  $sp^2$  nanocarbons. The graphene-related structures are labeled next to their respective spectra. The main features (RBM and disorder-induced D, D' and D+D' bands; first-order Raman-allowed G band; and second-order Raman overtones G' (2iTO) and 2G) are labeled in some spectra, but the assignment applies to all of them.

**The Radial Breathing Mode (RBM):** The radial breathing mode is especially important in two ways: (1) for the determination of the diameter of a nanotube through the dependence of  $\omega_{RBM}$  on  $d_t$ , and (2) for relating the  $\omega_{RBM}$  and the resonant optical transition energies  $E_{ii}$  for a given tube. Experimental data on the radial breathing mode frequency taken by many authors have been fit using the relation  $\omega_{RBM}=A/d_t+B$ . For water-assisted supergrowth samples,

values of  $A = (227.0 \pm 0.3) \text{ nm} \cdot \text{cm}^{-1}$  and  $B = (0.3 \pm 0.2) \text{ cm}^{-1}$  are obtained. However, all the other  $\omega_{\text{RBM}}$  results in the literature are upshifted from these values of A and B, due to the van der Waals interaction with the environment, and can be generally described by equation 1 where the parameter  $C_e$  in the equation describes environmental effects.

$$\omega_{\text{RBM}} = \frac{227}{d_t} \sqrt{1 + C_e d_t^2} \quad (1)$$

The  $C_e$  values fitting the RBM results for several samples in the literature range from 0.05 to 0.07 [30]. The RBM also has been important for understanding the effect of tube-tube interaction within multiwall carbon nanotubes, the prototype material for studying such interactions being double-wall carbon nanotubes (DWNTs).

***Dispersive G'-Band (2D) the Double Resonance Process:*** All kinds of  $\text{sp}^2$  carbon materials exhibit a strong Raman feature which appears in the range  $2500\text{-}2800 \text{ cm}^{-1}$ , as shown in figure 3.4. Together with the G band ( $1582 \text{ cm}^{-1}$ ), this spectrum is a Raman signature of graphitic  $\text{sp}^2$  materials and is called the G' band or 2D to emphasize that it is a Raman-allowed mode for  $\text{sp}^2$  carbons. Interestingly, the G' band is a second-order two-phonon process and intriguingly, it exhibits a strong frequency dependence on the excitation laser energy  $E_{\text{laser}}$ . This dispersive behavior ( $\omega_{\text{G}'i} = \omega_{\text{G}'i}(E_{\text{laser}})$ ) is unusual in Raman scattering, since Raman-active mode frequencies usually do not depend on  $E_{\text{laser}}$ . The G' band in particular is a second-order process related to a phonon near the K point in graphene, activated by double resonance (DR) processes [31] which are responsible for its dispersive nature and cause a strong dependence on any perturbation to the electronic and/or phonon structure of graphene. For this reason, the G' feature provides a very sensitive probe for characterizing specific  $\text{sp}^2$  nanocarbons. For example, the G' band can be used for

differentiating between single and double-layer graphene with AB interlayer stacking [31] and for probing aspects of the electronic structures of SWNTs.

***Disorder-Induced D Band:*** The presence of disorder in  $sp^2$ -hybridized carbon systems leads to rich and intriguing phenomena in their resonance Raman spectra, thus making Raman spectroscopy one of the most sensitive and informative techniques to characterize disorder in  $sp^2$  carbon materials. Raman spectroscopy has thus become a key tool and is widely used to identify disorder in the  $sp^2$  network of different carbon structures, such as diamond-like carbon, amorphous carbon, nanostructured carbon, as well as carbon nanofibers, nanotubes, and nanohorns [29].

In our experiment Raman spectroscopy data were collected using both the Jobin Yvon Horiba X 6400 micro-Raman spectrometer equipped with LabSpec (Ver. 5.78.24) analytical software with analysed with a 514 nm argon excitation laser (1.5 mW laser power on the sample to avoid thermal effects), a 50x objective with recording times ranging from 120 s and a resolution of  $2\text{ cm}^{-1}$ . A WiTec-alpha 300R+ confocal Raman spectrometer (WiTec GmbH) operating with excitation source of 532-nm laser (2.33 eV) through a numerical aperture of 0.9 and 100x magnification was also used. This analysis is ideal and was performed to know the amount of layers of graphene deposited and also to check the quality of the graphene samples produced (defect density).

### **3.2.2 Morphological Analysis**

#### **Scanning electron microscope (SEM)**

The scanning electron microscope (SEM) is a routinely instrument used to generate high-resolution images of shapes of objects and to show spatial variations in chemical compositions [32]: The SEM uses a focused beam of high-energy electrons to generate a variety of signals at the surface of solid specimens. The accelerated electrons in the SEM carry significant amounts of kinetic energy, and this energy is dissipated as a variety of

signals produced by electron-sample interactions when the incident electrons are decelerated in the solid sample [33]. The signals derived from electron-sample interactions reveal information about the sample including external morphology (texture), chemical composition, and crystalline structure and orientation of materials making up the sample. In most SEM applications, data are collected over a selected area of the surface of the sample, and a 2-dimensional image is generated that displays spatial variations in these properties [33]. The surface morphology and microstructure of all samples in our experiment were investigated using a Zeiss Ultra Plus 55 field emission scanning electron microscope (FE-SEM) operated at 2 kV in secondary electron detection mode. Samples were prepared by placing the powder on the carbon stickers attached to an aluminium holder.

Energy-dispersive (EDS) were performed on scanning electron microscope (SEM) (JEOL 5800LV) equipped with energy dispersive operated at 20kV. EDS systems are typically integrated into SEM instrument and include a sensitive x-ray detector, a liquid nitrogen dewar for cooling, and software to collect and analyze energy spectra. (EDS) detector is used to separate the characteristic x-rays of different elements into an energy spectrum and EDS software is used to analyze the energy spectrum in order to determine the specific elements present in the sample [34]. EDS can also be used to find the chemical composition of materials down to a spot size of a few microns, and to create element composition. These capabilities provide fundamental compositional information for a wide variety of materials. These analyses were performed in order to know the qualitative and quantitative elemental composition of the samples produced.

### **Transmission electron microscopy (TEM)**

TEM makes use of electron beam to illuminate specimen and thus creates an image [33]. In TEM, the source of illumination is a beam of electrons of very short wavelength (high energy), emitted from a tungsten filament at the top of a cylindrical column. The electrons

with high accelerating voltage pass through the sample and are scattered in different degree, losing or prevailing initial energy. The elastically scattered electrons form an imaging contrast. [35]. The spatial variation in this information (the "image") is then magnified by a series of magnetic lenses until it is recorded by hitting a fluorescent screen, photographic plate, or light sensitive sensor like CCD (charge-coupled device) camera. The image detected by the CCD may be displayed in real time on a monitor or computer [33,35]. A transmission electron microscopy (TEM) JEOL JEM-2100F microscope operated at 200 kV was used for our experimental work. During sample preparation, graphene/composite powders were prepared by dispersing them in ethanol using an ultrasonic bath. Several drops of the dispersion were then placed onto a copper grid coated with holey carbon film.

### **3.2.3 Crystallinity and Qualitative Phase Analysis**

X-ray powder diffraction (XRD) is a rapid analytical technique basically used for phase identification of crystalline materials [36]. It is based on constructive interference of monochromatic X-rays and a crystalline sample. XRD consist of three basic elements namely an X-ray tube, a sample holder, and an X-ray detector and they all lie on the circumference of the circle, which is known as the focusing circle. The angle between the plane of the specimen and the x-ray source is  $\theta$ , the Bragg angle. The angle between the projection of the x-ray source and the detector is  $2\theta$ . X-rays are generated in a cathode ray tube by heating a filament to produce electrons, accelerating the electrons toward a target by applying a voltage, and bombarding the target material with electrons [36,37]. As the sample and detector are rotated, the intensity of the reflected X-rays is recorded. When the geometry of the incident X-rays impinging the sample satisfies the Bragg equation ( $n\lambda=2d \sin \theta$ ) where  $n$  is an integer,  $\lambda$  is the wavelength of incident wave,  $d$  is the spacing between the planes in the atomic lattice, and  $\theta$  is the angle between the incident ray and the scattering planes, a constructive interference occurs. A detector records and processes this X-ray signal and

converts the signal to a count rate which is then output to a device such as a printer or computer monitor [38]. In this work XRD patterns of all samples were collected on an XPERT-PRO diffractometer (PANalytical BV, Netherlands) with theta/theta geometry, operating a cobalt tube at 35 kV and 50 mA.

### 3.2.4 Gas Adsorption Analysis

Adsorption is the phenomenon marked by an increase in density of a fluid near the surface, of a solid. Similar to surface tension, adsorption is a consequence of surface energy. Most atoms that make up a solid are bound on all sides by other atoms in the bulk of the solid. The atoms on the surface of the solid, however, are incompletely bound. Due to van der Waals forces of interaction, these surface atoms are more reactive and they attract gas, vapor, and liquids to satisfy the imbalance of atomic forces. Adsorption isotherms analysis provides information about specific surface area, porosity, pore sizes and pore distributions of materials. To determine the surface area, solid samples are pretreated by applying some combination of heat, vacuum, and /or flowing gas to remove adsorbed contaminants acquired (typically water and carbondioxide) from atmospheric exposure. The solid is then cooled, under vacuum, usually to cryogenic temperature (77 K-195 °C). An adsorptive (typically nitrogen) is dosed to the solid in controlled increments. After each dose of adsorptive, the pressure is allowed to equilibrate and the quantity adsorbed is calculated. The quantity adsorbed at each pressure (and temperature) defines an adsorption isotherm, from which the quantity of gas required to form a monolayer over the external surface of the solid is determined. With the area covered by each adsorbed gas molecule known, the surface area can be calculated [39,40]. The data collected is displayed in the form of a BET isotherm, which plots the amount of gas adsorbed as a function of the relative pressure. Surface area analysis was performed with liquid nitrogen gas sorption at 77 K on a Micromeritics ASAP 2020. This was performed to know the surface area of the CVD grown graphene and its composite materials.

### 3.2.5 Electrochemical Analysis

Capacitive behavior of all samples were investigated using cyclic voltammetry (CV) and galvanostatic charge discharge (CD) on an Autolab PGSTAT workstation 302 (ECONCHEMIE) driven by the general purpose electrochemical system (GPES) software in the voltage range of 0 to 1 V. Electrochemical Impedance spectroscopy (EIS) was on performed on the same workstation in the frequency range of 10 m Hz-100 kHz at different voltages. Some electrochemical characterization was also performed on the SP-300 biologic PGSTAT. The PGSTAT is an electronic instrument designed to control the potential difference applied to an electrochemical cell between the working electrode (WE) where there is a current flow and a reference electrode (RE) where there is no current. At a glance, a potentiostat measures the potential difference between the working and the reference electrode, applies the current through the counter electrode (CE) and measures the current as an  $iR$  voltage drop [41,42]. An electrochemical cell is used to generate voltage and current from chemical reactions or induce chemical reactions by the input of electrochemical signals. The most commonly used electrochemistry system is the three-electrode system consisted of WE, RE and CE. The working electrode makes contact with the analyte, its surface is then place where the reaction occurs. After the working electrode is applied with a certain potential, the transfer of electrons between electrode and analyte takes place. The current observed at the electrode will pass through the CE for balance [43]. The RE has a known reduction potential, while no current passes through it. It only acts as a reference when measuring the WE potential. The PGSTAT provide curves such as cyclic voltammetry (CV), galvanostatic charge discharge (CD) and electrochemical impedance spectroscopy (EIS). CV is basically referred to as techniques with the common characteristics that the potential of the working electrode is controlled and the resulting current flow is measured. One of the most general applications is “linear-sweep voltammetry (LSV or LV)” where the potential is linearly scanned over time in

either the negative or positive direction. “Cyclic voltammetry (CV)” is a set of LSV experiments in which anodic and cathodic scans are repeated alternately [41]. The CV gives us information on the possible thermodynamics of redox reactions of the system, including the Faradaic insertion and extraction reaction, adsorption processes and the kinetics of electron transfer reactions of the materials been investigated. In electrochemical impedance spectroscopy (EIS), the system under investigation (typically in the equilibrium state) is excited by a small amplitude ac sinusoidal signal of potential or current in a wide range of frequencies and the response of the current or voltage is measured. Since the amplitude of the excitation signal is small enough for the system to be in the quasi-equilibrium state, EIS measurements can be used to effectively evaluate the system properties without significantly disturbing them. Frequency sweeping in a wide range from high-to low-frequency enables the reaction steps with different rate constants, such as mass transport, charge transfer, and chemical reaction.

## Reference

- [1] L.G. De Arco, Y. Zhang, C.W. Schlenker, K. Ryu, M.E. Thompson, C. Zhou, **4** (2010) 2865.
- [2] J. Wu, H.A. Becerril, Z. Bao, Z. Liu, Y. Chen, P. Peumans, *Appl. Phys. Lett.* **92** (2008) 263302.
- [3] X. Li, W. Cai, J. An, S. Kim, J. Nah, D. Yang, R. Piner, A. Velamakanni, I. Jung, E. Tutuc, S.K. Banerjee, L. Colombo, R.S. Ruoff, *Science* **324** (2009) 1312.
- [4] Q. Yu, J. Lian, S. Siriponglert, H. Li, Y.P. Chen, S.-S. Pei, *Appl. Phys. Lett.* **93** (2008) 113103.
- [5] K.S. Kim, Y. Zhao, H. Jang, S.Y. Lee, J.M. Kim, K.S. Kim, J.-H. Ahn, P. Kim, J.-Y. Choi, B.H. Hong, *Nature* **457** (2009) 706.
- [6] A. Reina, S. Thiele, X. Jia, S. Bhaviripudi, M.S. Dresselhaus, J. A. Schaefer, J. Kong, *Nano Res.* **2** (2010) 509.
- [7] L.G. De Arco, Y. Zhang, A. Kumar, C. Zhou, *Nanotechnology*, *IEEE Trans.* **8** (2009) 135.
- [8] X. Li, C.W. Magnuson, A. Venugopal, J. An, J.W. Suk, B. Han, M. Borysiak, W. Cai, A. Velamakanni, Y. Zhu, L. Fu, E.M. Vogel, E. Voelkl, L. Colombo, R.S. Ruoff, *Nano Lett.* **10** (2010) 4328.
- [9] L. Vayssieres, *Int. J. Nanotechnol.* **1** (2004) 1.
- [10] L. Vayssieres, A. Hagfeldt, S.E. Lindquist, *Pure Appl. Chem.* **72** (2000) 47.
- [11] L. Vayssieres, C. Chanéac, E. Tronc, J.P. Jolivet, *J. Colloid Interface Sci.* **205** (1998) 205.
- [12] L. Vayssieres, *Comptes Rendus Chim.* **9** (2006) 691.
- [13] C.F. Baes, R.E. Mesmer, *The Hydrolysis of Cations*, Wiley 1976.
- [14] M. Baghbanzadeh, L. Carbone, P.D. Cozzoli, C.O. Kappe, *Angew. Chemie* **50** (2011) 11312.
- [15] C.O. Kappe, *Chem. Soc. Rev.* **37** (2008) 1127.
- [16] J.D. Moseley, C.O. Kappe, *Green Chem.* **13** (2011) 794.
- [17] C.O. Kappe, D. Dallinger, *Mol. Divers.* **13** (2009) 71.
- [18] C.O. Kappe, D. Dallinger, S. Murphree, *Practical microwave synthesis for organic chemists: strategies, instruments, and protocols* Wiley 2009.

- [19] C.O. Kappe, A. Stadler, D. Dallinger, *Microwaves in organic and medicinal chemistry*, John Wiley & Sons, 2012.
- [20] Y. Li, J. Wang, Y. Zhang, M.N. Banis, J. Liu, D. Geng, R. Li, X. Sun, *J. Colloid Interface Sci.* **369** (2012) 123.
- [21] C.O. Kappe, *Chem. Soc. Rev.* **42** (2013) 4977.
- [22] H.M. Pathan, C.D. Lokhande, **27** (2004) 85.
- [23] R.S. Mane, C.D. Lokhande, *Mater. Chem. Phys.* **65** (2000) 1.
- [24] D.P. Dubal, R. Holze, *New J. Chem.* **37** (2013) 403.
- [25] G. Hodes, *Chemical solution deposition of semiconductor films*, CRC press, 2002.
- [26] B.R. Sankapal, R.S. Mane, C.D. Lokhande, *Mater. Res. Bull.* **35** (2000) 177.
- [27] D.J. Gardiner, P.R. Graves, H.J. Bowley, *Practical Raman spectroscopy*, springer-verlag heidelberg, Germany, 1989.
- [28] Ken-ichi Sasaki, *NTT Tech. Rev.* (2013) **1**.
- [29] A.C. Ferrari, J. Robertson, *Philos. Trans. A. Math. Phys. Eng. Sci.* **362** (2004) 2477.
- [30] MS Dresselhaus, A Jorio, M Hofmann, G Dresselhaus, R Saito *Nano letters* **10** (2010) 751.
- [31] L.M. Malard, M.A. Pimenta, G. Dresselhaus, M.S. Dresselhaus, *Phys. Rep.* **473** (2009) 51.
- [32] A.R. Clarke, C.N. Eberhardt, *Microscopy techniques for materials science*, woodhead publishing, 2002.
- [33] R.F. Egerton, *Physical principles of electron microscopy: an introduction to TEM, SEM, and AEM*, springer, 2005.
- [34] J. Goldstein, D.E. Newbury, D.C. Joy, C.E. Lyman, P. Echlin, E. Lifshin, L. Sawyer, J.R. Michael, *Scanning electron microscopy and x-ray microanalysis*, springer, 2003.
- [35] D.B. Williams, C.B. Carter, *The transmission electron microscope*, springer, 1996.
- [36] B.D. Cullity, S.R. Stock, *Elements of x-ray diffraction*, prentice hall upper saddle river, NJ, 2001.
- [37] B.E. Warren, *X-ray diffraction*, Dover publications 1969.
- [38] D.M. Moore, R.C. Reynolds Jr, *X-ray diffraction and the identification and analysis of clay minerals*, Oxford University Press, 1989.

- [39] Y.-S. Bae, A.O. Yazayd, R.Q. Snurr, *Langmuir* **26** (2010) 5475.
- [40] S. Brunauer, L.S. Deming, W.E. Deming, E. Teller, *J. Am. Chem. Soc.* **62** (1940) 1723.
- [41] A.J. Bard, L.R. Faulkner, *Electrochemical methods: fundamentals and applications*, Wiley New York, 1980.
- [42] D. Dobos, *Electrochemical data: a handbook for electrochemists in industry and Universities*, Elsevier scientific publishing company Amsterdam, 1975.
- [43] C.G. Zoski, *Handbook of electrochemistry*, access online via Elsevier, 2007.

# Chapter 4

## Result and discussions

### 4.1 Interaction between graphene foam and silver metal particles

#### Introduction

Generally, metal nanostructures such as silver (Ag) have evolved as a different class of materials with great technological applications at the nanoscale: because of their very high surface to volume ratio which increases the surface energy compared to that of their bulk counterpart [1]. The high surface-to-volume ratio combined with size effects gives them unique chemical, electronic and optical properties. In many studies silver particles were deposited on graphene sheet to study the morphology and chemical reactivity of the composite. The investigation of the physicochemical properties of Ag particles grafted on graphene has been of paramount importance because it exhibits electrochemical properties suitable for sensing for example [2–4]. Depending on the synthesis method different shape of Ag particles can be synthesised.

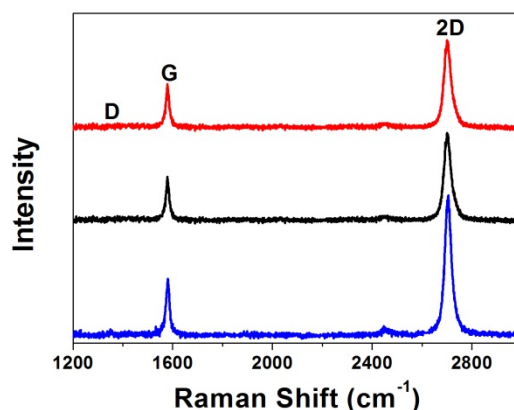
Herein, i report on the synergetic properties of the composite arising from the interaction between graphene foam and Ag particles for electrochemical application. The GF was synthesised using CVD while Ag particles were deposited using the physical electron beam (e-beam) and characterized using different techniques. This section outlines the results obtained.

## Result and discussions



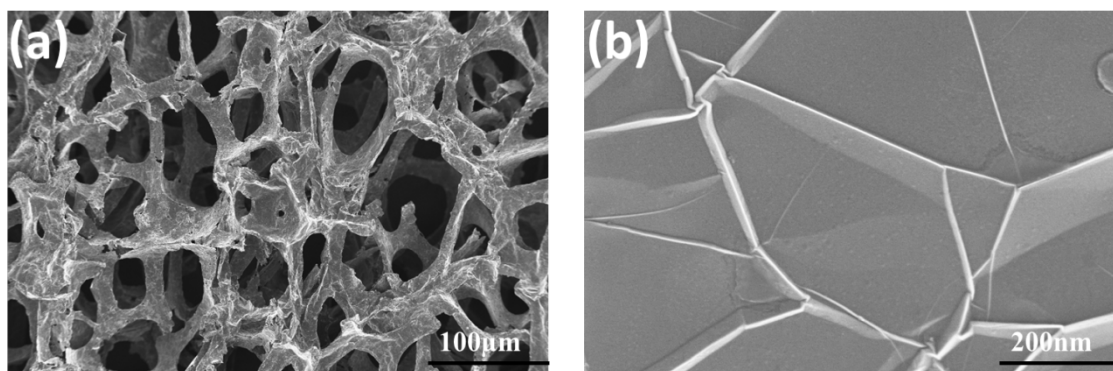
**Figure 4.1.1** Graphene foam (GF) sample on glass substrate

Figure 4.1.1 shows the GF after the nickel template was removed. The 3D GF network was mainly characterized by Raman spectroscopy to ascertain its quality and defect density. The Raman spectra of the sample obtained from different spots are shown in figure 4.1.2 below, revealing two prominent features known as the G and 2D peaks, the intensity ratios of both peaks suggested that the GF networks contain single, bilayer and few-layer. The so-called G band appearing at ( $1578\text{ cm}^{-1}$ ) is due to the bond stretching of all pairs of  $sp^2$  atoms in both rings and chains while the 2D peak is due to two phonons with opposite momentum in the highest optical branch near the K point of the Brillouin zone and the D peak is due to intervalley scattering process of in-plane optical phonon modes around K which is active by double resonance and is strongly dispersive with excitation energy [5–7]. The relative intensity 2D/G ratio of 1.0 and FWHM of  $38.8\text{ cm}^{-1}$  were attributed to few layer graphene. The absence of the D-peak (disorder) at  $1350\text{ cm}^{-1}$  showed that the graphene foam was of good quality, with a low defect density.



**Figure 4.1.2** Raman spectra of the 3D GF network taken at different spots.

A clear evolution of the porous and 3D structure of the sample after the Ni template was removed can be observed in the SEM shown in figure 4.1.3 (a).



**Figure 4.1.3** SEM of (a) the 3D GF sample after the Ni template was removed and (b) shows high magnification image of the GF revealing wrinkles and ripples.

The figure shows that the graphene mimics the shape of the template used for the CVD growth and high magnification image in 4.1.3 (b) reveals that the 3D network consist of ripples and wrinkles. This can provide support for metal particles and thus facilitate the use of e-beam technique for deposition of particles in order to form silver particles graphene foam (GF/Ag) composite for electrochemical application. We chose silver nanoparticles (as model electro-active nanoparticles) due to the fact that they possess a very high surface area to volume ratio, and have been shown to exhibit electrochemical properties that make them

suitable for potential application in electrochemical devices such as sensors. The e-beam deposition was performed at high vacuum ( $10^{-7}$  mbar) at a rate of  $0.5 \text{ \AA}/\text{min}$  using a standard electron beam evaporator with an e-Vap CVS-10 (MDC) power supply. The basic principle of operation of e-beam could be explained as follows using the figure 4.1.4 below.

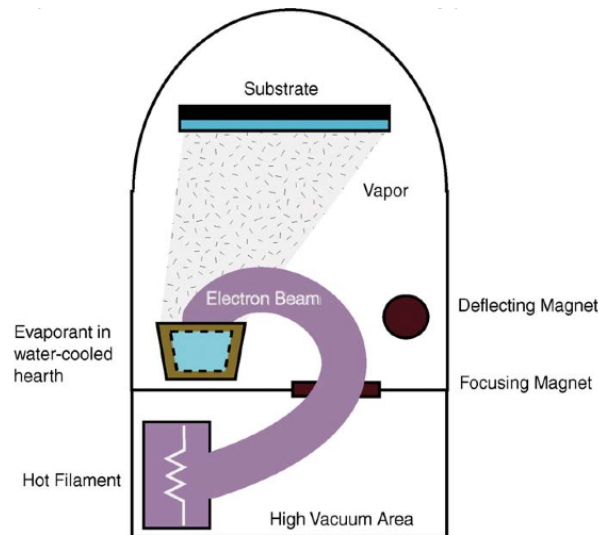


**Figure 4.1.4** The electron beam apparatus setup

The material that is to be deposited is the evaporation in water-cooled hearth meanwhile, the material that is to be coated is shown as the substrate. The electron beam is produced by a hot filament which is represented by the symbol of resistor. The process of the evaporation is taken place in a high vacuum area to allow molecules to move freely in the chamber and hence condense on all surfaces including the substrate. A detail description of the parameter used is presented in the attached publication. Figure 4.1.5 (a) show the SEM image of the 3D GF after deposition of Ag particles and 4.1.5 (b) reveals high magnification showing dense and uniform coating of the entire surface area of the 3D GF with Ag particles.

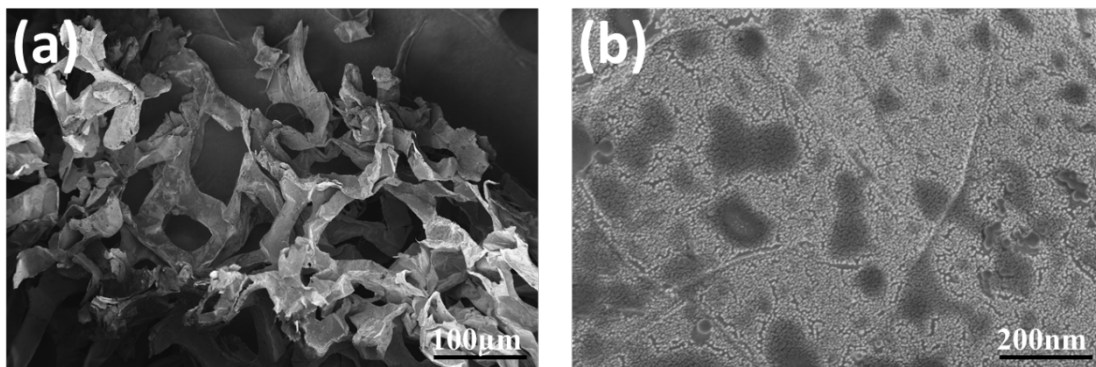


**Figure 4.1.5** SEM of (a) the 3D GF coated with Ag particles and (b) high magnification of Ag particles uniformly coated on the 3D GF revealing spherical agglomeration.

The electrical and electrochemical influence of the Ag particles grafted on the GF was investigated. The electrical conductance measurements at room temperature for both GF and GF/Ag were performed using a four-point probe equipped with a Keithley 2636B source meter. Figure 4.1.6 (a) and 4.1.6 (b) show the current and voltage curves for both GF and GF/Ag. Based on the slope of these curves, the conductance values were estimated to be  $\sim 7.6 \times 10^{-2} \text{ S/m}$  and  $\sim 15 \times 10^{-2} \text{ S/m}$  respectively. These values show that after the deposition of silver nanoparticles, the conductance of the GF/Ag is twice that of GF.

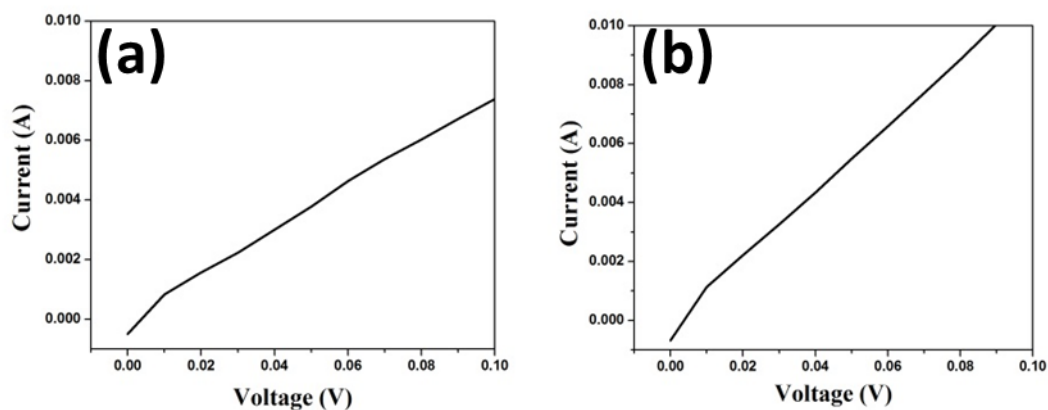


**Figure 4.1.6** Current-voltage curves for both (a) GF and (b) GF/Ag composite

The electrochemical performance of the GF and GF/Ag composite as electrode were analyzed using cyclic voltammetry (CV), galvanostatic charge–discharge (CD) and electrochemical impedance spectroscopy (EIS) measured in a 2 M KOH solution in the potential range from 0 to 0.5 V. The composite exhibits a slightly higher capacitance performance ( $110 \text{ F g}^{-1}$ ) when compared to the GF ( $\sim 17 \text{ F g}^{-1}$ ). This improved performance was attributed to the synergistic effect between the graphene and the silver nanoparticles, which is probably due to the enhanced electrical conductivity and the uniform loading of the silver nanoparticles onto the surface of the 3D GF. The CV shows reduction and oxidation peaks which were attributed to the one-electron process of the Ag composite, the anodic current at the peak potential of 0.4 V (oxidation of  $\text{Ag}^{2+}$  to  $\text{Ag}^{3+}$ ) and the cathodic current at the peak potential of 0.2 V (reduction of  $\text{Ag}^{3+}$  back to  $\text{Ag}^{2+}$ ) [8]. A detailed analysis of the characterization, electrochemical behaviour and comparison of both GF and GF/Ag composite is given in the attached publication.

# Publication 1: Silver nanoparticles decorated on a three-dimensional graphene scaffold for electrochemical applications

Journal of Physics and Chemistry of Solids ■ (■■■■) ■■■–■■■



Contents lists available at ScienceDirect

Journal of Physics and Chemistry of Solids

journal homepage: [www.elsevier.com/locate/jpcs](http://www.elsevier.com/locate/jpcs)



## Silver nanoparticles decorated on a three-dimensional graphene scaffold for electrochemical applications

A. Bello<sup>a</sup>, M. Fabiane<sup>a</sup>, D. Dodoo-Arhin<sup>a</sup>, K.I. Ozoemena<sup>b,c</sup>, N. Manyala<sup>a,\*</sup>

<sup>a</sup> Department of Physics, Institute of Applied Materials, SARChI Chair in Carbon Technology and Materials, University of Pretoria, Pretoria 0002, South Africa

<sup>b</sup> Council for Scientific and Industrial Research, Meiring Naude Road, Brummeria, PO Box 395, Pretoria 0001, South Africa

<sup>c</sup> Department of Chemistry, University of Pretoria, Pretoria 0002, South Africa

### ARTICLE INFO

Article history:  
Received 24 January 2013  
Received in revised form  
13 August 2013  
Accepted 5 September 2013

Keywords:  
Graphene foam  
CVD  
Electron beam evaporation  
Silver nanoparticles  
Electrochemical capacitor

### ABSTRACT

Silver metal nanoparticles were decorated by electron beam evaporation on graphene foam (GF) grown by chemical vapour deposition. X-ray diffraction, Raman spectroscopy, scanning and transmission electron microscopy, and atomic force microscopy were used to investigate the structure and morphology of the graphene foam/silver nanoparticles (GF/Ag). Both samples were tested as electrodes for supercapacitors. The GF/Ag exhibited a significantly higher capacitive performance, including a specific capacitance value of ( $\sim 110 \text{ Fg}^{-1}$ ) and excellent cyclability in a three-electrode electrochemical cell. These results demonstrate that graphene foam could be an excellent platform for metal particles for investigating improved electrochemical performance.

© 2013 Crown Copyright. Published by Elsevier Ltd. All rights reserved.

### 1. Introduction

The discovery of graphene has inspired much research activity to understand its unique physicochemical properties and possible applications. Graphene [1] is a single layer of graphite consisting of a two-dimensional honeycomb lattice of  $sp^2$ -bonded carbon atoms with a unique electronic structure that exhibits linear dispersion at a high symmetry point in the reciprocal space, resulting in effective dynamics of electrons [2]. It has been touted as an electrode material due to its theoretically high surface area ( $2630 \text{ m}^2 \text{ g}^{-1}$ ), high electrical conductivity, chemical stability and excellent mechanical properties [3–9]. Graphene is thus being considered as a building block for electrochemically active materials [10] and as a suitable platform for the loading of metal nanoparticles [11]. These subtle properties make graphene exceptional for both micro- and macroscopic applications.

Recently, graphene–metal composites have been considered as electrode materials for electrochemical applications [12]. Metal nanoparticles such as Ag, Pd, Pt and Au exhibit large surface area to volume ratios at the nanoscale and hence are excellent materials where large surface areas are required. A variety of successful approaches for preparing graphene–metal composites have been reported. For instance, electrodeposition [13,14], chemical reduction [15–18], epitaxial deposition [19] and chemical vapour deposition [20] have been used. However, it is usually

difficult to achieve uniform and homogeneous coating of the graphene surface through some of these deposition techniques [21].

Chen et al. [22] reported on three-dimensional (3D) flexible and conductive interconnected graphene networks grown by chemical vapour deposition (CVD) using a nickel foam template. Since then, the 3D form of graphene has attracted application in fuel cells [23], batteries [24] and electrochemical cells [25] due to its high porosity, high specific surface area and high electrical conductivity.

To the best of our knowledge, only a few pioneering studies on 3D graphene–metal composites have been done [23,25–28]. In this study, we report on the enhanced electrochemical performance of CVD-grown graphene foam (GF) decorated with silver nanoparticles using a physical technique (electron beam evaporation). The electrochemical effect of the Ag nanoparticles on the GF is discussed. We chose silver nanoparticles (as model electro-active nanoparticles) due to the fact that they possess a very high surface area to volume ratio, and have been shown to exhibit electrochemical properties that make them suitable for potential application in electrochemical devices such as sensors [29–31] and in fuel cells (i.e. hydrogen-evolution reaction [32] and oxygen-reduction reaction [33]).

### 2. Experimental

Graphene foam (GF) was synthesised by CVD onto a catalytic nickel foam (Alantum Innovation in alloy foam, Munich, Germany),

\* Corresponding author. Tel.: +27 12 420 3549; fax: +27 420 2516.

E-mail addresses: [ncholu.manyala@up.ac.za](mailto:ncholu.manyala@up.ac.za), [manyalancholu@gmail.com](mailto:manyalancholu@gmail.com) (N. Manyala).

420 g<sup>-2</sup> in areal density and 1.6 mm in thickness. The details of the synthesis procedure are given in our previous paper [34]. To provide mechanical support for the 3D structure of the GF during etching of the nickel, polymethylmethacrylate (PMMA) was drop-coated onto the sample and baked at 180 °C for 30 min. This solidifies the PMMA onto the nickel-graphene surface. The samples were placed in a 3 M HCl solution at 80 °C and left overnight to ensure that the nickel was completely etched away. The GF was then placed in acetone at 50 °C to remove the PMMA, after which the samples were rinsed in deionised water and then dried. Ag particles were deposited on the GF at a rate of 0.5 Å/min in a 10<sup>-7</sup> mbar vacuum using a standard electron beam evaporator with an e-Vap CVS-10 (MDC) power supply capable of accelerating electrons at 10 keV energy and equipped with a crystal monitor for film-thickness monitoring.

Raman spectroscopy data were collected on a Jobin Yvon Horiba TX 6400 micro-Raman spectrometer equipped with a triple monochromator system to eliminate contributions from Rayleigh lines and using LabSpec (Ver. 5.78.24) analytical software. All the samples were analysed with a 514 nm argon excitation laser (1.5 mW laser power on the sample to avoid thermal effects), a 50 × objective with recording times ranging from 120 s and a resolution of 2 cm<sup>-1</sup>. To confirm the presence of the Ag nanoparticles and the corresponding microstructure, X-ray powder diffraction (XRD) patterns of the GF samples were collected on an XPERT-PRO diffractometer (PANalytical BV, Netherlands) with theta/theta geometry, operating a cobalt tube at 35 kV and 50 mA. The goniometer is equipped with an automatic divergence slit and a PW3064 spinner stage. The instrumental resolution function was characterised with the NIST SRM 660a (LaB6) standard. The XRD patterns of all samples were recorded in the 40.0–80° 2θ range with a step size of 0.017° and a counting time of 15.240 s per step. Qualitative phase analysis of the samples was conducted using the X'pert Highscore search-match software.

Morphological characterisation of the samples was performed on an Agilent 5500 atomic force microscope in acoustic mode at a frequency of ~150 kHz. Images were obtained with a high-resolution Zeiss Ultra Plus 55 field emission scanning electron microscope (FE-SEM) operated at 2.0 kV, and with a JEOL JEM-2100F transmission electron microscope (TEM) operated at 200 kV.

Finally, electrochemical measurements such as cyclic voltammetry (CV) and galvanostatic charge-discharge were performed using an Autolab PGSTAT workstation 302 (ECO-CHEMIE) driven by GPES software in a three-electrode setup. The GF/Ag served as the working electrode, a glassy carbon plate as the counter electrode, Ag/AgCl (3 M KCl) as the reference electrode and 2 M KOH was used as the electrolyte. Electrochemical impedance

spectroscopy (EIS) was performed in the frequency range of 100 kHz to 10 mHz.

The electrical resistance of both samples was measured via the four-point method. The current and voltage were provided by a source-measure unit (Keithley 2636B). The values of applied current, *I*, and their corresponding voltages, *V*, were recorded and the resistance, *R*, was calculated from Ohm's law, i.e. from  $R=V/I$ . The cross-sectional area of the samples was calculated and the conductivity,  $\sigma$ , was then estimated according to  $\sigma=1/AR$ .

### 3. Results and discussion

Fig. 1(a) shows the Raman spectrum of the GF which consisted of two major peaks at (1578 cm<sup>-1</sup>) and (2703 cm<sup>-1</sup>), corresponding to the typical G- and 2D-bands of graphene [35]. The absence of the D-peak (disorder) around 1350 cm<sup>-1</sup> on the spectrum shows that the GF is of good quality [36]. Fig. 1(b) shows the Raman spectrum of the GF/Ag sample. The appearance of a D-peak at 1350 cm<sup>-1</sup> could be attributed to the strain effect on the atomic position of the carbon atoms caused by the Ag particles. Both Raman spectra show weak bands at G' (2450 cm<sup>-1</sup>) which originates from the double resonance process involving two iTO phonons around the K-point in the phonon dispersion of a two-dimensional graphite [37]. The 2D band also originate from the same double resonance phenomenon and correspond to a fully-dispersive  $q=2k$  while the 2450 cm<sup>-1</sup> band correspond to non-dispersive  $q=0, k$  for the electron and  $q$  for the phonon are measured from the K-point. From the corresponding phonon frequency and dispersion, the 2450 cm<sup>-1</sup> band has been modelled with an inter-valley process involving one iTO and one LA phonon and assigned as an overtone of LO phonon mode [38,39].

The relatively low intensity of the D-peak implies that the carbon atoms still maintain the honeycomb structure. The intensity of both the G- and 2D-peaks is greatly enhanced after the deposition of the Ag particles. The enhancement factors of the G- and 2D-bands of graphene after Ag deposition are ~4.5 and ~5.5 respectively. The low values could be attributed to the weak van der Waals interaction between Ag and graphene, which may change the structure of the graphene. The results here are similar to those obtained by Lee et al. [40] who proposed that the Raman signal in Ag-deposited graphene is due to the first-order process and therefore that the interaction between Ag nanoparticles and graphene could lead to a change in the electronic structure.

The phase analysis of the samples was obtained by XRD measurement. Fig. 2 shows the XRD patterns of the as-grown GF and GF/Ag samples. The peaks at 2θ values of 44.7° and 51.9° are assigned respectively to the (111) and (200) crystallographic

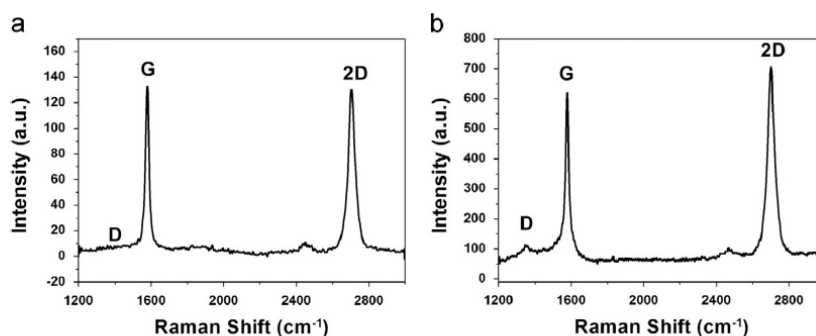


Fig. 1. Raman spectra of the samples: (a) graphene foam (GF); and (b) graphene foam with silver nanoparticles (GF/Ag).

planes of the fluid catalytic cracking (FCC) silver nanoparticles. Due to the small quantity and size broadening at higher angles of the silver nanoparticles, peaks such as the (200) and (220) at peak positions  $51.9^\circ$  and  $76.7^\circ$  are almost in the background.

The structure and morphologies of the graphene foam were also examined by FE-SEM and TEM. The scanning electron micrographs in Fig. 3(a) show that the GF takes the shape of the template and reveals a microporous nature. A high magnification of the GF is shown in Fig. 3(b) and reveals that the GF consists of wrinkles and ripples. The ripples are attributed to the different thermal expansion coefficients of nickel and graphene during the CVD synthesis, while the wrinkles can provide high surface area and good mechanical properties [25,41]. Fig. 3(c, d) shows SEM images of

the Ag nanoparticles decorated on the GF. Fig. 3(c) reveals uniform coverage of the GF by the Ag nanoparticles, while Fig. 3(d) shows that the silver nanoparticles are spherical and form agglomerates. TEM images of the GF and GF/Ag nanoparticles are shown in Fig. 3(e, f). Fig. 3(e) shows that the GF sheets overlap each other in the 3D network structure (the bright and dark regions respectively), while Fig. 3(f) shows that the GF is decorated by the Ag nanoparticles. The 3D and porous nature of the GF allowed the uniform distribution of the particles, as observed from both the SEM and TEM images.

The atomic force micrographs in Fig. 4(a) show that the GF is decorated with Ag nanoparticles that are spherical and agglomerate on the surface. The average particle size was estimated to be 106 nm. Fig. 4(b) shows the particle size distribution which reveals that more than 60% of the particles are within the range of 85–106 nm. The RMS surface roughness of the GF/Ag nanoparticles was 21.4 nm.

Electrochemical studies were performed to investigate the effect of the Ag nanoparticles on the GF. The cyclic voltammetry (CV) and galvanostatic charge–discharge were measured in a 2 M KOH solution in the potential range from 0 to 0.5 V, as shown in Fig. 5. Fig. 5(a) shows the CV evolutions of the GF and GF/Ag at  $25 \text{ mV s}^{-1}$ . It can be seen that the GF showed insignificant current response compared with the GF/Ag. The weak redox couple observed on the GF is presumably due to the  $\text{Ni}^{2+}/\text{Ni}^{3+}$  redox process arising from the nickel impurities during the etching process [42]. The well-defined redox process on the GF/Ag is related to the one-electron process of the Ag nanoparticles, the anodic current at the peak potential of 0.4 V (oxidation of  $\text{Ag}^{2+}$  to  $\text{Ag}^{3+}$ ) and the cathodic current at the peak potential of 0.2 V (reduction of  $\text{Ag}^{3+}$  back to  $\text{Ag}^{2+}$ ) [12]. The ratio of the anodic to cathodic peak current ( $I_{pa}/I_{pc}$ ) is approximately unity, clearly indicating that the redox reaction of silver nanoparticles on the GF is a reversible process.

Fig. 5(b) compares the galvanostatic charge–discharge curves of both the GF and GF/Ag nanoparticles at a constant current density of  $0.5 \text{ Ag}^{-1}$ . The non-linearity of the GF/Ag curves is due to the

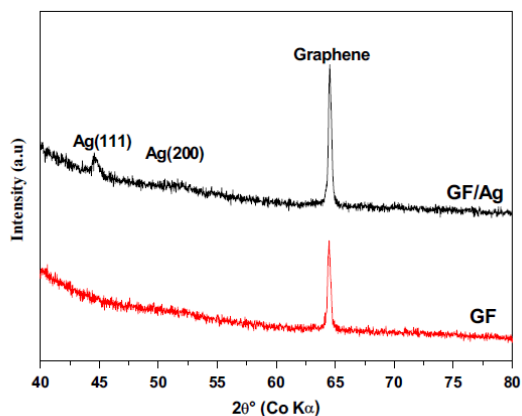


Fig. 2. XRD patterns of samples: graphene foam (GF), and graphene foam with the silver nanoparticles (GF/Ag).

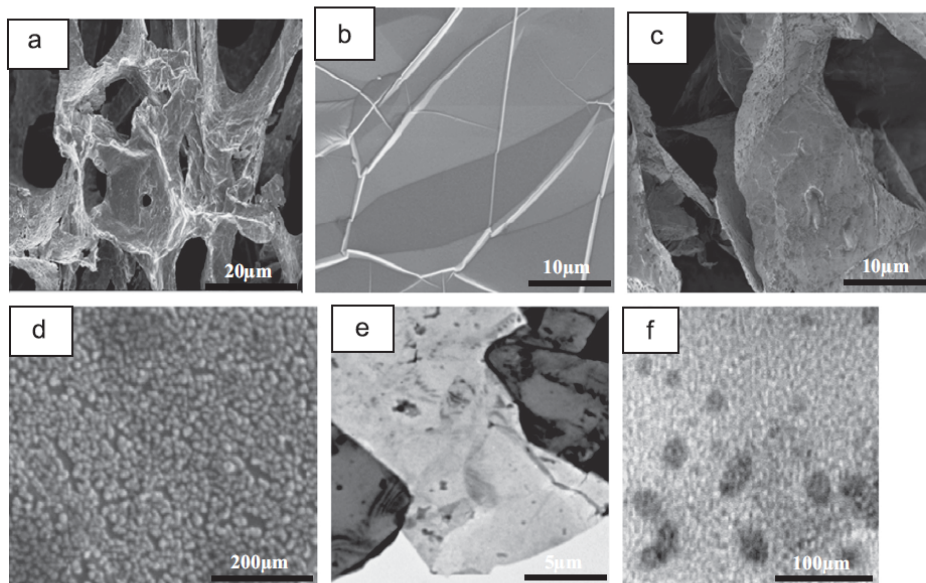


Fig. 3. Scanning electron micrographs: (a, b) graphene foam (GF); (c, d) graphene foam with the silver nanoparticles at different magnifications (GF/Ag); (e, f). Transmission electron micrographs: (GF) and (GF/Ag).

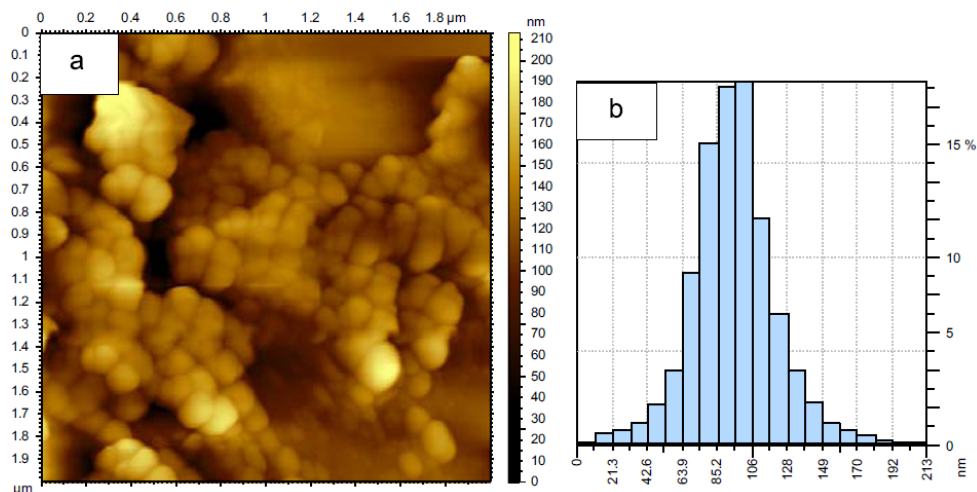


Fig. 4. Atomic force micrographs: (a) GF/Ag showing the spherical nature of the particles and also revealing agglomeration; and (b) particle size distribution of the particles.

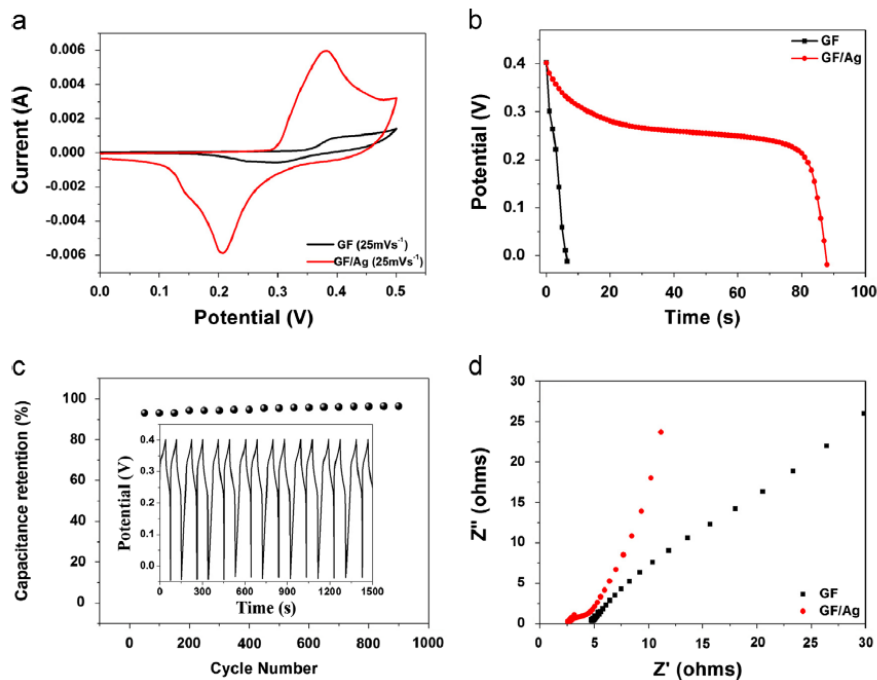


Fig. 5. Electrochemical measurements of graphene foam (GF) and GF/Ag composites: (a) cyclic voltammetry of both GF and GF/Ag at 25 mV s<sup>-1</sup>; (b) galvanostatic charge-discharge of both GF and GF/Ag measured at a current density of 0.5 Ag<sup>-1</sup>; (c) capacitance retention of GF/Ag; and (d) EIS plot of both GF and GF/Ag.

redox process of the silver nanoparticles on the GF (i.e. pseudocapacitance), corroborating the CV observed in Fig. 5(a).

The specific capacitance was calculated from the discharge curve using the following equation:

$$C_s = \frac{I \Delta t}{\Delta V m} \quad (1)$$

where  $C_s$  is the specific capacitance,  $m$  is the mass of working electrode,  $I$  is the current (A),  $\Delta V$  is the voltage applied and  $\Delta t$  is the discharge time. The specific capacitance of the GF was

estimated to be  $\sim 10 \text{ Fg}^{-1}$ , while that of the GF/Ag was about  $110 \text{ Fg}^{-1}$ . This increase in capacitance of the GF/Ag is due to the synergy arising from the high redox activity or Faradaic process (i.e. pseudocapacitance) of the silver nanoparticles, combined with the high conductivity and non-Faradaic process (i.e. electric double layer capacitance) of the GF. The 3D and porous nature of the GF also allows for a large and uniform deposition of the silver nanoparticles, thereby giving easy access to the electrolytes. Although the value of the specific capacitance is comparable with previous reported value [12], it is high compared to graphite and

carbon materials [45,46]. It demonstrates the feasibility of having a graphene sample with a low defect density as compared with reduced graphene oxide which is normally regarded as being functionalized by the reducing agents, and also demonstrates the ability of e-beam evaporation to load nanoparticles for improved electrochemical and catalytic applications. Fig. 5(c) shows the continuous charge–discharge curve of the GF/Ag sample and the capacitance retention at a current density of 0.5 A/g. The electrode material is electrochemically stable after 1000 cycles and retains 93% of its initial capacitance.

EIS is an excellent tool for investigating the electrochemical characteristics of an electrode/electrolyte interface using a Nyquist plot, which is a representation of the real and imaginary parts of the impedance in the samples. The Nyquist plot of the electrode is shown in Fig. 5(d). It is worth stating that for ideal supercapacitors, the EIS (Nyquist) plot should be a line perpendicular to the imaginary axis. From the Nyquist plot, the slope at low frequencies can also be used to evaluate the capacitive performance [43]. However, a comparison of both samples shows that the Nyquist plot of GF/Ag is much closer to the ideal behaviour, thus indicating a better capacitive behaviour. This could be attributed to the three-dimensionality of the graphene foam, which allows a uniform adsorption of silver nanoparticles, and to the high redox activity of the silver nanoparticles, coupled with the good conductivity of the GF.

The equivalent series resistance (ESR), including the resistance of aqueous electrolyte, the intrinsic resistance of the composite material and the contact resistance at the electrode interface, can be obtained from the X-intercept of the Nyquist plot [44]. As shown in Fig. 5(d), the ESR of the GF/Ag sample ( $2.6 \Omega$ ) is much lower than that of the GF sample ( $4.3 \Omega$ ). These results are supported by electrical conductance measurements at room temperature for both GF and GF/Ag, for which the values of  $\sim 7.6 \times 10^{-2} \text{ S/m}$  and  $\sim 15 \times 10^{-2} \text{ S/m}$  were obtained respectively. It is clear from both results that GF/Ag exhibits half the ESR value and twice the conductance value with respect to those of GF. These results suggest that 3D GF can serve as an efficient support for metal nanoparticles for potential electrochemical applications, such as in the construction of electrochemical capacitors, electrocatalytic devices and electrochemical sensors.

#### 4. Conclusions

In this work, GF was decorated with Ag nanoparticles using the electron beam evaporation technique and the effect of Ag on the electrochemical behaviour and specific capacitance of the GF/Ag composites was investigated. The interaction of the silver metal with the graphene foam was characterised using various microscopy and spectroscopy techniques. The morphologies reveal that the 3D structure of the GF provides support for adsorption and integration of the metal nanoparticles. Also, the enhanced electrochemical performance of the GF/Ag sample that was observed is due to the synergistic effect between the graphene and the silver nanoparticles, which could be attributed to the good electrical conductivity and uniform loading of the silver nanoparticles onto the surface of the GF. These results demonstrate that 3D GF could serve as an excellent platform for depositing metal nanoparticles for fundamental and applied electrochemical studies.

#### Acknowledgements

This work is based on research supported by the South African Research Chairs Initiative (SARCHI) of the Department of Science and Technology (DST) and the National Research Foundation

(NRF). Any opinion, findings and conclusions or recommendations expressed in this work are those of authors and therefore the NRF and DST do not accept any liability with regard thereto. A. Bello acknowledges the financial support from the University of Pretoria for his study. We thank Dr Patricia Forbes for supplying the nickel foams.

#### References

- [1] A. Geim, K. Novoselov, *Nature Materials* 6 (2007) 183–191.
- [2] K.S. Novoselov, A.K. Geim, S.V. Morozov, D. Jiang, M.I. Katsnelson, I.V. Grigorieva, S.V. Dubonos, A.A. Firsov, *Nature* 438 (2005) 197–200.
- [3] M.I. Katsnelson, *Materials Today* 10 (2007) 20–27.
- [4] K. Novoselov, A. Geim, S. Morozov, *Science* 306 (2004) 666–669.
- [5] M.D. Stoller, S. Park, Y. Zhu, J. An, R.S. Ruoff, *Nano Letters* 8 (2008) 3498–3502.
- [6] Y. Wang, Z. Shi, Y. Huang, Y. Ma, C. Wang, M. Chen, Y.S. Chen, *Journal of Physical Chemistry C* 113 (2009) 13103–13107.
- [7] Z.-S. Wu, W. Ren, D.-W. Wang, F. Li, B. Liu, H.-M. Cheng, *ACS Nano* 4 (2010) 5835–5842.
- [8] Y. Zhu, S. Murali, W. Cai, X. Li, *Advanced Materials* 22 (2010) 3906–3924.
- [9] Y. Sun, Q. Wu, G. Shi, *Energy and Environmental Science* 4 (2011) 1113–1132.
- [10] X. Huang, X. Qi, F. Boey, H. Zhang, *Chemical Society Reviews* 41 (2012) 666–686.
- [11] S. Park, R.S. Ruoff, *Nature Nanotechnology* 4 (2009) 217–224.
- [12] K.-S. Kim, I.-J. Kim, S.-J. Park, *Synthetic Metals* 160 (2010) 2355–2360.
- [13] X. Sun, M. Xie, G. Wang, H. Sun, A.S. Cavanagh, J.J. Travis, S.M. George, L. Jie, *Journal of the Electrochemical Society* 159 (2012) A364–A369.
- [14] X. Dong, Y. Cao, J. Wang, M.B. Chan-Park, L. Wang, W. Huang, W.H. Peng, *RSC Advances* 2 (2012) 4364–4369.
- [15] X. Li, B.K. Tay, J. Li, D. Tan, C.W. Tan, K. Liang, *Nanoscale Research Letters* 7 (2012) 205.
- [16] S. Liu, J. Tian, L. Wang, X. Sun, *Carbon* 49 (2011) 3158–3164.
- [17] Y.-K. Yang, C.-E. He, W.-J. He, L.-J. Yu, R.-G. Peng, X.-L. Xie, W. Xian-Bao, M. Yiu-Wing, *Journal of Nanoparticle Research* 13 (2011) 5571–5581.
- [18] J. Tian, S. Liu, Y. Zhang, H. Li, L. Wang, Y. Luo, A.M. Asiri, A.O. Al-Youbi, X. Sun, *Inorganic Chemistry* 51 (2012) 4742–4746.
- [19] G.F. Ndlovu, W.D. Roos, Z.M. Wang, J.K. Asante, M.G. Mashapa, C.J. Jafta, B.W. Mwakikunga, K.T. Hillie, *Nanoscale Research Letters* 7 (2012) 173.
- [20] Y.H. Kahng, S. Lee, W. Park, G. Jo, M. Choe, J.-H. Lee, Y. Hyunung, L. Takhee, L. Kwanghee, *Nanotechnology* 23 (2012) 075702.
- [21] H. Wang, H.S. Casalongue, Y. Liang, H. Dai, *Journal of the American Chemical Society* 132 (2010) 7472–7477.
- [22] Z. Chen, W. Ren, L. Gao, B. Liu, S. Pei, H. Cheng, *Nature Materials* 10 (2011) 424–428.
- [23] T. Maiyalagan, X. Dong, P. Chen, X. Wang, *Journal of Materials Chemistry* 22 (2012) 5286–5290.
- [24] H. Ji, L. Zhang, M. Pettes, H. Li, S. Chen, *Nano Letters* 12 (2012) 2446–2451.
- [25] X. Cao, Y. Shi, W. Shi, G. Lu, X. Huang, Q. Yan, Q. Zhang, H. Zhang, *Small* 7 (2011) 3163–3168.
- [26] J.-S. Lee, H.-J. Ahn, J.-C. Yoon, J.-H. Jang, *Physical Chemistry Chemical Physics* 13 (2011) 7943 (2011).
- [27] T. Lu, Y. Zhang, H. Li, L. Pan, Y. Li, Z. Sun, *Electrochimica Acta* 55 (2010) 4170–4173.
- [28] X.-C. Dong, H. Xu, X.-W. Wang, Y.-X. Huang, M.B. Chan-Park, H. Zhang, L.-H. Wang, W. Huang, P. Chen, *ACS Nano* 6 (2012) 3206–3213.
- [29] C.M. Welch, C.E. Banks, A.O. Simm, R.G. Compton, *Analytical and Bioanalytical Chemistry* 382 (2005) 12–21.
- [30] X. Dai, G.G. Wildgoose, R.G. Compton, *Analyst* 131 (2006) 1241–1247.
- [31] M. Tominaga, T. Shimazoe, M. Nagashima, H. Kusuda, A. Kubo, Y. Kuwahara, T. Isao, *Journal of Electroanalytical Chemistry* 590 (2006) 37–46.
- [32] F.W. Campbell, S.R. Belding, R. Baron, L. Xiao, R.G. Compton, *Journal of Physical Chemistry C* 113 (2009) 14852–14857.
- [33] M. Chatenet, M. Arousseau, R. Durand, F. Andolfatto, *Journal of Applied Electromagnetics* 263 (2002) 1131–1140.
- [34] A. Bello, K. Makgopa, M. Fabiane, D. Dodoo-Ahrin, K.I. Ozoemena, N. Manyala, *Journal of Materials Science* 48 (2013) 6707–6712.
- [35] A.C. Ferrari, J.C. Meyer, V. Scardaci, C. Casiraghi, M. Lazzeri, F. Mauri, S. Piscanec, D. Jiang, K.S. Novoselov, S. Roth, A.K. Geim, *Physical Review Letters* 97 (2006) 1–4.
- [36] M.S. Dresselhaus, A. Jorio, M. Hofmann, G. Dresselhaus, R. Saito, *Nano Letters* 10 (2010) 751–758.
- [37] T. Shimada, T. Sugai, C. Fantini, M. Souza, L.G. Cancado, A. Jorio, M.A. Pimenta, R. Saito, A. Grüneis, G. Dresselhaus, M.S. Dresselhaus, Y. Ohno, T. Mizutani, H. Shinohara, *Carbon* 43 (2005) 1049–1054.
- [38] D.L. Mafra, G. Samsonidze, L.M. Malard, D.C. Elias, J.C. Brant, F. Plentz, E.S. Alves, M.A. Pimenta, *Physical Review B* 76 (2007) 233407.
- [39] L.M. Malard, M.A. Pimenta, G. Dresselhaus, M.S. Dresselhaus, *Physics Reports* 473 (2009) 51–87.
- [40] J. Lee, K. Novoselov, H. Shin, *ACS Nano* 5 (2010) 608–612.
- [41] S.J. Chae, F. Güneş, K.K. Kim, E.S. Kim, G.H. Han, S.M. Kim, H.J. Shin, S. Yoon, J. Choi, M.H. Park, C.W. Yang, D. Pribat, Y.H. Lee, *Advanced Materials* 21 (2009) 2328–2333.

- [42] L.-R. Zhang, J. Zhao, M. Li, H.-T. Ni, J. Zhang, X.-M. Feng, Y.-W. Ma, Q.-L. Fan, X.-Z. Wang, Z. Hu, W. Huang, *New Journal of Chemistry* 36 (2012) 1108.
- [43] E. Frackowiak, F. Béguin, *Carbon* 39 (2001) 937–950.
- [44] J. Zhang, L.-B. Kong, J.-J. Cai, Y.-C. Luo, L. Kang, *Journal of Solid State Electrochemistry* 14 (2010) 2065–2075.
- [45] T. Cassagneau, J.H. Fendler, *Journal of Physical Chemistry B* (1999) 1789–1793.
- [46] L. Jiang, M. Vangari, T. Pryor, Z. Xiao, N.S. Korivi, *Microelectronic Engineering* (2013) 52–57.

Please cite this article as: A. Bello, et al., *J. Phys. Chem. Solids* (2013), <http://dx.doi.org/10.1016/j.jpcs.2013.09.006>

## Summary

In conclusion, we have successfully synthesised a composite of GF/Ag with the use of e-beam. The interaction between Ag metal and GF have been studied, the various analyses show that GF was effectively coated with Ag nanoparticles. As a consequence we explored the application of as-synthesised GF/Ag in ECs. It was found that the GF/Ag exhibited improved electrochemical performance when compared with the pristine GF which could be due to the improved electrical conductivity and synergistic effect provided by Ag nanoparticles to the 3D GF. We believe that these results could further expand the applications of e-beam for composite materials with improved properties.

## References

- [1] V.E.T. Heredia, Thesis titled Silver Nanostructures: Chemical Synthesis of colloids and composites nanoparticles, plasmon resonance properties and silver nanoparticles monolayer films prepared by spin-coating. November (2011)
- [2] C.M. Welch, C.E. Banks, A O. Simm, R.G. Compton, *Analytical and Bioanalytical Chemistry* **382** (2005) 12.
- [3] X. Dai, G.G. Wildgoose, R.G. Compton, *The Analyst* **131** (2006) 1241.
- [4] F.W. Campbell, S.R. Belding, R. Baron, L. Xiao, R.G. Compton, *J. Phys.Chem. C* **113** (2009) 14852.
- [5] M. Dresselhaus, A. Jorio, M. Hofmann, G. Dresselhaus, R Saito *Nano* **10** (2010) 751.
- [6] A.C. Ferrari, J. Meyer, V. Scardaci, C. Casiraghi, M. Lazzeri, F. Mauri, S. Piscanec, D. Jiang, K.S. Novoselov, S. Roth, A.K. Geim *Phys. Revi.* **97** (2006) 187401.
- [7] A.C. Ferrari, *Solid State Comm.* **143** (2007) 47.
- [8] K-S. Kim, I-J. Kim, S-J. Park, *Synthetic Met.* **160** (2010) 2355.

## 4.2 Adsorption between Nickel foam graphene (NF-G) and Nickel oxide (NiO)

### Introduction

NiO is among the transition metal oxides that has attracted application in electrochemical capacitors due to its theoretical high capacitance, low cost and availability [1–3]. NiO exhibits intrinsically both the Faradaic charge transfer reaction (battery like) and non-diffusional charge reaction mechanism (capacitor like) as well as high bulk electronic conductivity which is required and interesting for ECs application [4]. Previous reports have shown that the properties of NiO are significantly influenced by its morphology and structure [5]. Therefore, it becomes highly desirable to tune and control the geometry and morphology of the NiO particles without compromising accessibility of the surface area and porosity. Different techniques such as spray pyrolysis [6], microwave irradiation [7], pulsed laser ablation [8,9], electrophoretic deposition [10], electrodeposition [11,12], chemical vapour deposition [13], sol-gel technology [14] and chemical bath deposition (CBD) [15,16] have been used to produce nickel oxide with different shapes and morphology.

Recently, extensive research aimed at developing graphene-based composites for electrochemical applications, especially composites that consist of graphene and transition-metal oxides such as NiO, because they can combine the merits of both components and may offer excellent properties through the modification of each other [17]. Just to mention a few NiO-graphene composites that had been reported; Xia *et al.* investigated a graphene sheet/porous NiO hybrid film for supercapacitor applications which exhibits excellent pseudocapacitive behavior with pseudocapacitance values of 400 and 324 F g<sup>-1</sup> at 2 and 40 A g<sup>-1</sup>, respectively [18]. Three-dimensional flower-like NiO supported on graphene sheets as electrode material for supercapacitors was also reported by Ge *et al.* This composite was found to exhibit a relatively high specific capacitance of 346 F g<sup>-1</sup> at 1.5 A g<sup>-1</sup>, a good rate performance and cycle stability in 2 M KOH [19]. Cao *et al.* reported a 3D graphene

composite network with NiO which exhibited a high specific capacitance of  $816 \text{ F g}^{-1}$  at a scan rate of  $5 \text{ mV s}^{-1}$  [20]. The latter represent the bench mark of research on the 3D form of graphene because they serve as an excellent platform for integration of metal oxide such as NiO for electrode for electrochemical applications.

Herein, i have investigated 3D nickel foam graphene decorated with NiO nanostructure synthesised via successive ionic layer adsorption and reaction (SILAR) The electrochemical performance of the composite using a three-electrode configuration in 2 M KOH aqueous solution was investigated.

## **Results and discussions**

Figure 4.2.1 (a) shows typical SEM images of graphene grown on the nickel foam substrates (NF-G) showing a 3D porous structure. The SEM images at a high magnification shown in figure 4.2.1 (b) indicated that graphene surface contained wrinkles and ripples as discussed in the previous section. The use of NF as substrate and 3D porous microstructure for CVD growth offered the advantage of adsorption of NiO to the graphene surface. The deposition mechanism, kinetics of deposition, structure and composition of the NiO formed by SILAR has been well documented [22–24] and has also been explained in chapter 3.

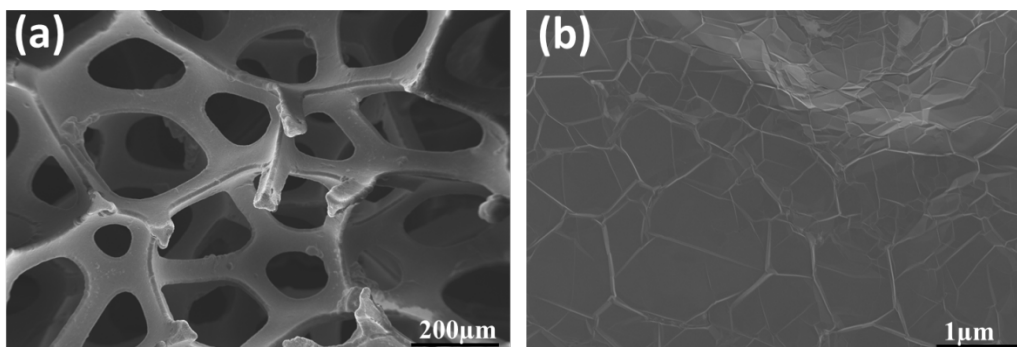


Figure 4.2.1 SEM of the graphene on nickel foam and (b) high magnification image of graphene showing wrinkles and ripples.

Figure 4.2.2 (a) shows the SEM image of the NF-G after deposition of NiO by the SILAR technique. The NiO particles totally cover the surface of the NF-G which indicates that NiO particles were adsorbed on the graphene surface. The high magnification SEM image shown in figure 4.2.2 (b) evidences that NiO particles were irregular in shape. The formation of NiO was also confirmed by XRD as will be shown shortly and is in a good agreement with results of previous reports [18,19].

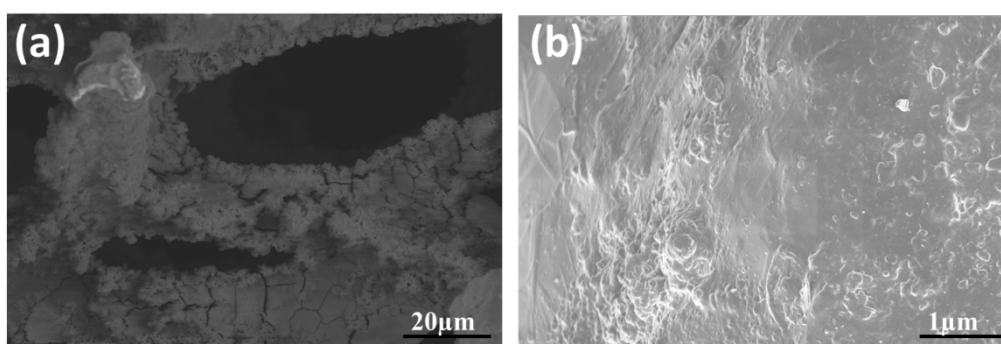


Figure 4.2.2 SEM of the (a) NF-G coated with NiO and (b) high magnification image of NiO showing irregular shaped nanostructure.

Electrochemical behaviour of the samples was investigated using CV, CD and EIS. Figure 4.2.3 shows CVs of NF-G/NiO composite synthesised with 30 and 60 SILAR cycles at different scan rates. No obvious change in electrochemical performance between the two CVs

was observed hence one decided to do most of the experiments with the 60 cycles to ensure proper coating of the graphene surface with NiO. The CVs curves exhibit a pair of redox peaks which are responsible for the pseudocapacitive behavior of the electrode materials. The 3D and porous structure of the composite electrodes was beneficial for easy access to electrolyte, hence resulting in improved electrochemical performance. The kinetics of the CVs show that the systems are diffusion controlled and hence a reversible process.

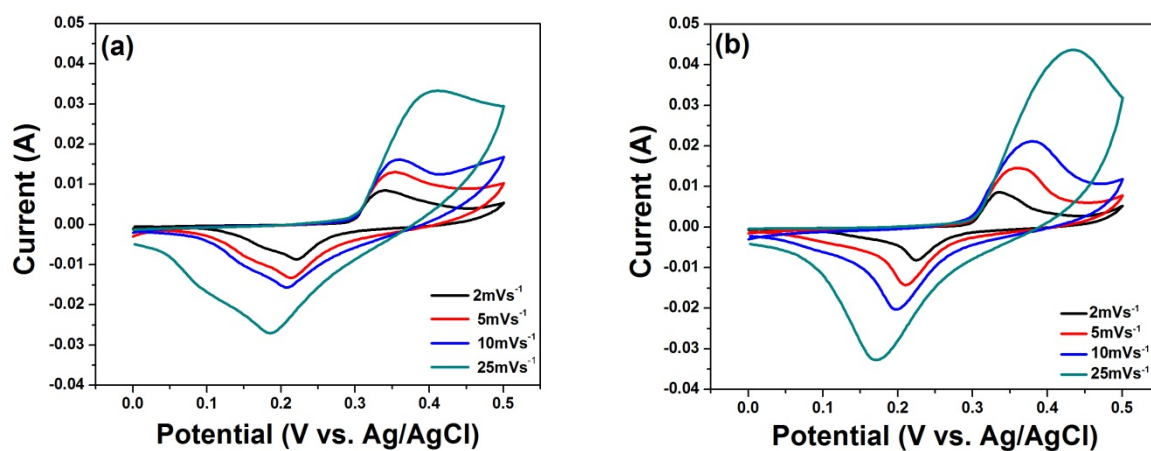


Figure 4.2.3 CV of (a) NF-G/NiO 30 SILAR cycles and (b) CV of NF-G/NiO 60 SILAR cycles

Detailed summary and electrochemical results obtained for the composite material of NF-G/NiO are given in the attached publication.

## Publication 2: Chemical adsorption of NiO nanostructures on nickel foam-graphene for supercapacitor applications

J Mater Sci (2013) 48:6707–6712  
 DOI 10.1007/s10853-013-7471-x

### Chemical adsorption of NiO nanostructures on nickel foam-graphene for supercapacitor applications

A. Bello · K. Makgopa · M. Fabiane ·  
 D. Dodoo-Ahrin · K. I. Ozoemena · N. Manyala

Received: 4 March 2013 / Accepted: 23 May 2013 / Published online: 4 June 2013  
 © Springer Science+Business Media New York 2013

**Abstract** Few-layer graphene was synthesized on a nickel foam template by chemical vapor deposition. The resulting three-dimensional (3D) graphene was loaded with nickel oxide nanostructures using the successive ionic layer adsorption and reaction technique. The composites were characterized and investigated as electrode material for supercapacitors. Raman spectroscopy measurements on the sample revealed that the 3D graphene consisted of mostly few layers, while X-ray diffractometry and scanning electron microscopy revealed the presence of nickel oxide. The electrochemical properties were investigated using cyclic voltammetry, electrochemical impedance spectroscopy, and potentiostatic charge–discharge in aqueous KOH electrolyte. The novelty of this study is the use of the 3D porous cell structure of the nickel foam which allows for the growth of highly conductive graphene and subsequently provides support for uniform adsorption of the NiO onto the graphene. The NF-G/NiO electrode material showed excellent properties as a pseudocapacitive device with a high-specific capacitance value of  $783 \text{ F g}^{-1}$  at a scan rate of  $2 \text{ mV s}^{-1}$ . The device also exhibited excellent cycle stability, with 84 % retention of the initial capacitance after 1000 cycles. The results demonstrate that composites made

using 3D graphene are versatile and show considerable promise as electrode materials for supercapacitor applications.

#### Introduction

Supercapacitors are electrochemical capacitors (ECs) that have received considerable attention because of their excellent properties which include high power density, long cycle life, low temperature sensitivity, low maintenance cost, and their environmentally friendly nature [1–3]. Depending on the charge storage mechanism of the material, supercapacitors are classified as either electrochemical double-layer capacitors (EDLCs) using ion adsorption, or pseudocapacitors using a fast and reversible Faradic reaction. They fill the gap between batteries (which have high energy density) and electrolytic capacitors (which have high power density) [4]. However, the energy stored in supercapacitor devices ( $<10 \text{ W h kg}^{-1}$ ) is low compared with that of batteries ( $>100 \text{ W h kg}^{-1}$ ). This has posed significant and difficult challenges in employing supercapacitors as primary power sources for battery replacement [5, 6]. It has also restricted the use of supercapacitors for possible applications such as in memory back-up equipment, hybrid vehicles, cordless electric tools, cellular phones, and entertainment instruments [7]. Carbon-based materials such as activated carbon have been used as electrode material for EDLCs because of their high surface area and conductivity, while conducting polymers or transition metal oxides, as active electrode materials, have been used as pseudocapacitors [8, 9].

Graphene, a two-dimensional honeycomb lattice of  $\text{sp}^2$ -bonded carbon atoms, has emerged as an exciting material with numerous applications and has thus attracted intense

A. Bello · M. Fabiane · D. Dodoo-Ahrin · N. Manyala (✉)  
 Department of Physics, Institute of Applied Materials, SARChI  
 Chair in Carbon Technology and Materials, University of  
 Pretoria, Pretoria 0028, South Africa  
 e-mail: ncholu.manyala@up.ac.za

K. Makgopa · K. I. Ozoemena  
 Department of Chemistry, University of Pretoria, Pretoria 0002,  
 South Africa

K. I. Ozoemena  
 Council for Scientific and Industrial Research, Meiring Naude  
 Road, Brummeria, 395, Pretoria 0001, South Africa

 Springer

research activity [10–12]. More recently, it has been explored for electrochemical storage applications due to its high surface area ( $2630 \text{ m}^2 \text{ g}^{-1}$ ), high electrical conductivity, chemical stability, and excellent mechanical properties [13–17]. However, graphene sheet has a tendency to restack due to the strong  $\pi$ - $\pi$  bonds between the layers forming the graphite during the preparation of electrodes, thereby leading to inferior electronic properties for graphene-based supercapacitors. This drastically affects the performance of the supercapacitors [15]. To overcome this problem, fillers or pseudocapacitive materials can be introduced into the graphene layers which ultimately prevent restacking of the graphene and ensure maximum utilization of the graphene surface area, as well as contributing to the total-specific capacitance of the system [18].

Nickel oxide (NiO) is one of the transition metal oxides that have attracted much attention as an electrode material for ECs because of its high theoretical capacitance (pseudocapacitance), multiple reversible electrochemical reactions, high surface-to-volume ratio, and because it is inexpensive and easy to synthesize [19–22]. Recently, several techniques for the preparation, characterization, and application of various shapes and dimensions of NiO nanostructure for electrochemical applications have been reported. Techniques such as self-assembly [19], electrochemical preparation [23], hydrothermal preparation [24, 25], chemical-bath deposition [26], and chemical solution processes [27, 28] have all been investigated.

Chen et al. [29] recently reported growing 3D flexible and conductive interconnected graphene networks by chemical vapor deposition (CVD) using a nickel foam template. Such a graphene provides a highly conductive network due to the high intrinsic conductivity of defect-free graphene. The porous nature of the 3D network makes it an excellent platform for the incorporation of various nanoparticles or fillers to occupy the pore spaces for composite applications. Hence, 3D graphene has been considered an important component of various composite materials, especially of graphene/metal oxide composites. Dong et al. [30] also reported the preparation of a novel 3D graphene network with NiO using the potentiostatic electrodeposition method. A specific capacitance of  $816 \text{ F g}^{-1}$  was recorded at a scan rate of  $5 \text{ mV s}^{-1}$  for the graphene/NiO composite. Since then, several composites of 3D graphene foam have been investigated. For example, hybrid structures of zinc oxide nanorods on 3D graphene foam for supercapacitors and electrochemical sensor applications have also been reported [31], as well as electrodeposition of platinum particles on 3D interconnected graphene for fuel cell applications [32], and 3D graphene cobalt oxide electrodes for high-performance supercapacitors and enzymeless glucose detection [33]. Preparation of a nickel foam-supported graphene sheet/

porous NiO hybrid film by the combination of electrophoretic deposition and chemical-bath deposition was also investigated [34], and 3D flower-like NiO on graphene sheets was evaluated using a facile hydrothermal process and thermal treatment approach [35]. In addition, composite electrodes for supercapacitors were fabricated by impregnation of slurries of manganese dioxide nanofibres and multiwalled carbon nanotubes into porous nickel foam current collectors [36].

In this article we have employed SILAR (successive ionic layer adsorption and reaction), a well-known, simple and reproducible chemical method, to synthesize novel nickel foam-graphene/nickel oxide (NF-G/NiO) in which the NiO nanostructures are anchored uniformly onto the surface of the graphene. The introduction of NiO into the graphene layers was expected to make maximum use of the surface area of the graphene and prevent agglomeration and restacking of the graphene sheet, thereby leading to improved conductivity of the composite and excellent electrochemical performance. The NF-G/NiO composite exhibited 3D porous interconnected network structure and was then tested as an electrode material for supercapacitors. The unique electrode structure not only enhanced easy access to ions from the electrolyte at the electrode/electrolyte interface but also served as a platform for the combination and integration of NiO with and into the NF-G.

## Experimental procedure

Graphene foam was synthesized by CVD onto a catalytic nickel foam (Alantum, Munich, Germany),  $420 \text{ g/m}^2$  in areal density and 1.6 mm in thickness. The nickel foam was annealed at  $800 \text{ }^\circ\text{C}$  in the presence of Ar and  $\text{H}_2$  for 20 min to remove impurities, before the introduction of the  $\text{CH}_4$  gas at  $1000 \text{ }^\circ\text{C}$ . The flow rates of the gases ( $\text{CH}_4$ : $\text{H}_2$ :Ar) were 10:200:300 sccm, respectively. After 5 min of deposition, the sample was rapidly cooled by pushing the quartz tube to a lower temperature region. The deposition of NiO onto the substrate (nickel foam-graphene) was done using the SILAR method. This is a stepwise chemical deposition technique based on immersion of the substrate into separately placed cationic and anionic precursors and rinsing after every immersion cycle with deionized water to avoid homogeneous precipitation [37–39]. The cationic precursor for this study was a mixture of  $0.01 \text{ M Ni}(\text{NO}_3)_2 \cdot 6\text{H}_2\text{O}$  and aqueous ammonia. Initially, precipitate of  $\text{Ni}(\text{OH})_2$  was formed from  $0.01 \text{ M Ni}(\text{NO}_3)_2 \cdot 6\text{H}_2\text{O}$ , which was dissolved upon addition of ammonia to adjust the pH to  $\sim 12$ , thereby forming hexaamminonickel (II) complex. The anionic precursor source was a hot water bath. When the substrate was immersed in the precursor solution ( $0.01 \text{ M Ni}(\text{NO}_3)_2 \cdot 6\text{H}_2\text{O}$ ) at room temperature for 30 s, nickel ions were

adsorbed onto the substrate surface. The substrate was then transferred to the hot water bath at a temperature of 90 °C for another 30 s to convert it into NiO, after which it was rinsed in distilled water for 30 s to remove the loosely bound or excess nickel hydroxyl ions. The SILAR steps were repeated for 60 cycles. After deposition, the samples were dried at 50 °C in an oven for about 1 h. Typically, the NF-G/NiO composite contained 26 wt% NF-G and 74 wt% NiO. The important parameters in the SILAR technique are the concentration and pH of the precursor solution, the temperature, and the time for adsorption and rinsing.

Raman spectroscopy data were collected using a Jobin-Yvon Horiba TX 6400 micro-Raman spectrometer equipped with a triple monochromator system to eliminate contributions from Rayleigh scattering. The samples were analyzed with a 514-nm argon excitation laser (1.5 mW laser power on the sample to avoid thermal effects), using a 50× objective with recording times ranging from 120 s. X-ray diffraction (XRD) patterns of the samples were collected using an XPERT-PRO diffractometer (PANalytical BV, Netherlands) with theta/theta geometry, operating a cobalt tube at 35 kV and 50 mA. The goniometer is equipped with an automatic divergence slit and a PW3064 spinner stage. The instrumental resolution function was characterized with the NIST SRM 660a (LaB6) standard. The XRD pattern of all the samples was recorded in the 20.0°–80° 2θ, range with a step size of 0.017° and a counting time of 15.240 s per step. Qualitative phase analysis of the samples was conducted using X'pert Highscore search-match software. Surface morphology characterization of the samples was obtained using a high-resolution Zeiss Ultra Plus 55 field emission scanning electron microscope (FE-SEM) operated at 2.0 kV. The capacitive properties were investigated by the cyclic voltammetry (CV) method using an Autolab PGSTAT Workstation 302 (ECO-CHEMIE, Metrohm Autolab BV) driven by the GPES software. The as-prepared NF-G/NiO served as the working electrode, glassy carbon plate as the counterelectrode, and Ag/AgCl (3 M KCl) as the reference electrode in 2 M KOH electrolyte. Electrochemical impedance spectroscopy (EIS) was performed in the frequency range of 100 kHz–1 MHz.

## Results and discussion

Figure 1 shows the Raman spectrum of the graphene on the nickel foam. The spectrum has two major peaks corresponding to the first-order bond stretching G band at ~1581 cm<sup>-1</sup> and two phonon 2D bands at ~2702 cm<sup>-1</sup>. The shape of the 2D bands, the  $I_{2D}/I_G$  ratio, and the FWHM indicate that the graphene consists of mostly few layers. The absence from the spectrum of the D-peak (disorder) at

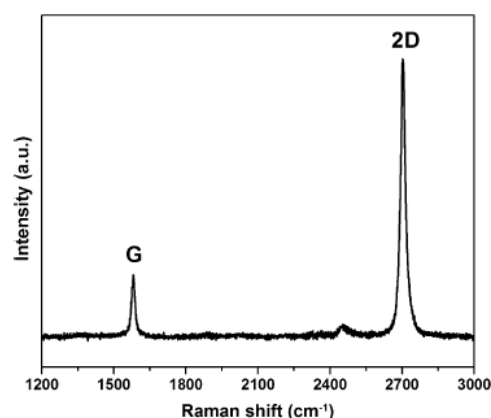


**Fig. 1** Raman spectrum of graphene on nickel foam showing the G and the 2D bands, with the absence of the D band at 1350 cm<sup>-1</sup>

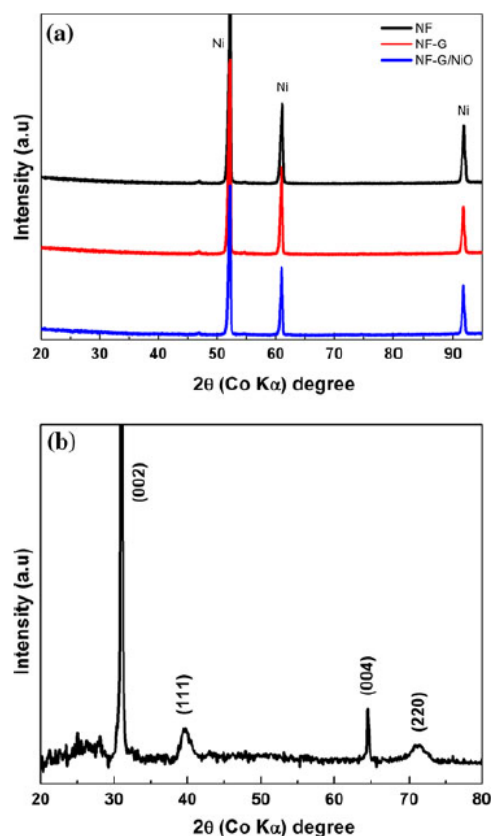


**Fig. 2** XRD patterns of a nickel foam (NF), nickel foam-graphene (NF-G), and nickel foam-graphene/NiO (NF-G/NiO) and b graphene foam/NiO (GF/NiO) showing the presence of NiO in the sample

1350 cm<sup>-1</sup> shows that the graphene is free from defects [40]. The XRD patterns of the nickel foam, nickel foam-graphene, and nickel foam-graphene coated with NiO are shown in

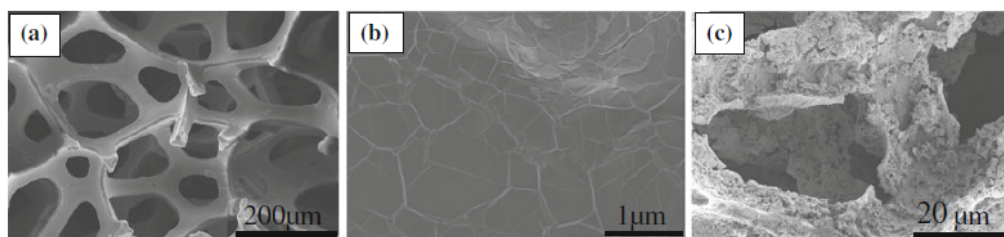
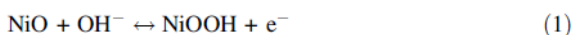


**Fig. 3** SEM images of a, b NF-G at different magnifications revealing the 3D network and wrinkled structure of the graphene and c NF-G coated with NiO showing the NiO nanostructure uniformly anchored onto the surface of the graphene

Fig. 2a. All three strong peaks originated from the Ni foam, with the peaks belonging to graphene and NiO being invisible because they overlap with the Ni foam peaks. To confirm the presence of graphene and NiO in the sample, the same experiment was repeated for an etched sample where the nickel was removed and the graphene foam was coated with NiO. The two diffraction peaks at  $2\theta = 31^\circ$  and  $65^\circ$  shown in Fig. 2b correspond respectively to the (002) and (004) reflections of hexagonal graphitic carbon, which is an indication of the presence of graphene, while the peaks labeled (111) and (220) in the same figure belong to NiO.

The SEM micrographs of the as-grown nickel foam-graphene are shown in Fig. 3a, b. Figure 3a shows the porous structure of the nickel foam, while the micrograph in Fig. 3b of the same sample at higher magnification shows graphene wrapped around the Ni foam and reveals that the graphene consists of wrinkles and ripples which could be attributed to the different thermal expansion coefficients of Ni and graphene during the CVD synthesis [41, 42]. Figure 3c shows a SEM image of the NF-G coated with NiO. It can be seen that the NiO nanostructures successfully coat the entire surface area of the NF-G, thus forming a porous and continuous electro-conductive network structure. This unique structure or morphology makes it useful in ECs, leading to pseudocapacitance when ions are adsorbed onto the surface of the samples and thereby improving capacitive behavior. It also provides an excellent electrode–electrolyte interface for the exchange of ions from the electrolyte.

CV studies were performed at various scan rates in a potential window of 0–0.5 V to evaluate the capacitive behavior of the electrode materials. Figure 4a compares the CV curves of samples at a scan rate of  $10 \text{ mV s}^{-1}$ . The shapes of the curves differed from those of ideal electrochemical double-layer capacitance, showing two redox peaks which are responsible for the pseudocapacitive behavior of the electrode materials. The oxidation peak observed at 0.419 V is due to the conversion of NiO to NiOOH, while the reduction peak at 0.192 V is due to the reverse reaction [39, 43] as represented by Eq. (1) below:



The low-intensity current peaks observed in the NF-G sample are also due to the redox reaction of the nickel foam in the electrolyte [34]. However, the current response of NF-G/NiO is much higher than those of NF-G and NF–NiO, which is an indication that the NF-G/NiO electrode has a better capacitive performance than NF-G alone. This can be attributed to the fully utilized surface area of the graphene which provided support for uniform coating and loading of NiO in the samples.

The cyclic voltammetric curves of the NF-G/NiO electrode at different scan rates are shown in Fig. 4b. It can be seen that the CV current response of the sample increases gradually with increasing scan rate; all CVs show a typical pseudocapacitive behavior. Figure 4c compares the first discharge curves of the NF-G and NF-G/NiO at a current of 3 mA. They also show nonlinear behavior, demonstrating the redox process of the NiO on the NF-G (i.e., pseudocapacitance). This is in agreement with the cyclic voltammogram in Fig. 4a.

Figure 4d shows a plot of the specific capacitance as a function of the scan rate, in which the specific capacitance decreases with increasing scan rate. This observation is an indication of a good current response of the NF-G/NiO and the pseudocapacitive nature of the electrode material, which is also consistent with the shapes of the CV curves. The specific capacitance ( $C_s$ ) value can be calculated from either the CV measurement or the charge–discharge using either Eq. (2) or (3) below.

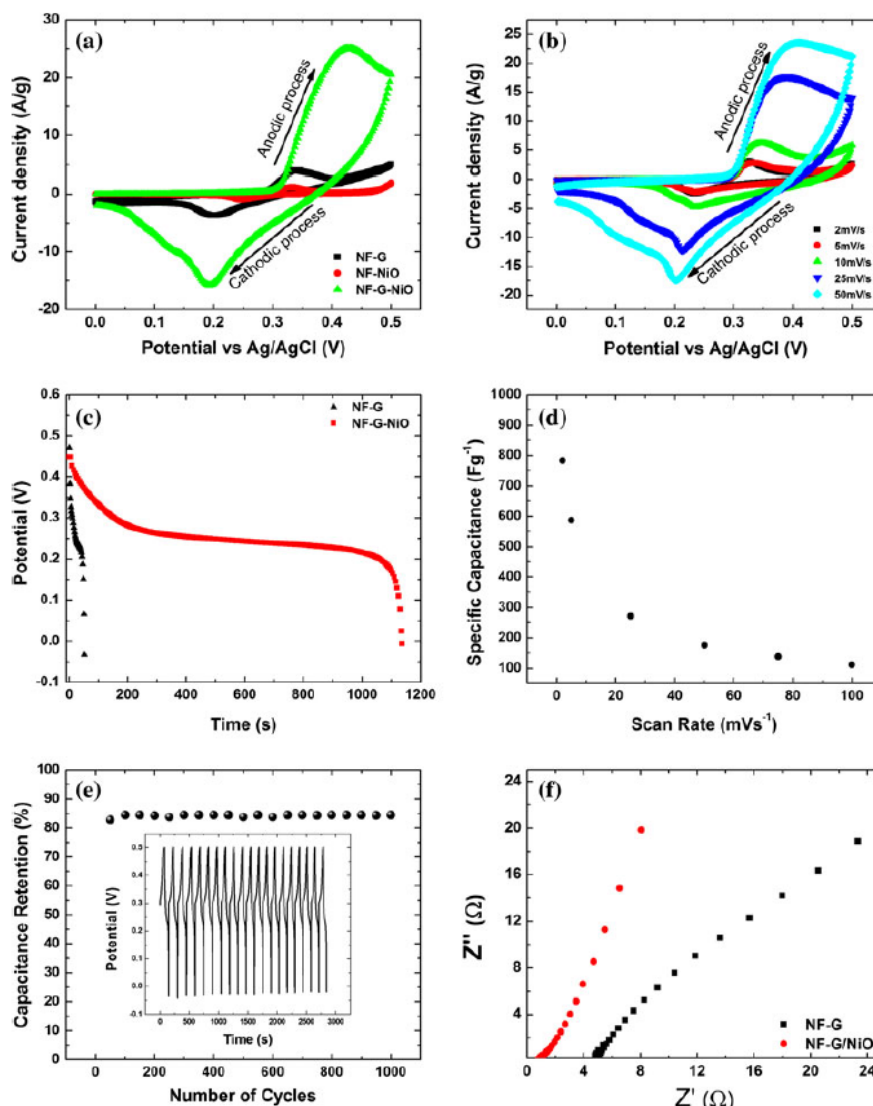
$$C_s = \frac{\bar{i}}{v \times m} \quad (2)$$

$$C_s = \frac{I \times \Delta T}{\Delta V} \quad (3)$$

where  $\bar{i}$  is the average current (A),  $v$  is the scan rate (mV/s),  $m$  is the mass of the electrode (g),  $I$  is the current,  $\Delta T$  is the discharge time, and  $\Delta V$  is the discharge voltage.

Using Eq. (2), a specific capacitance of  $261 \text{ F g}^{-1}$  at  $2 \text{ mV s}^{-1}$  was obtained for the NF-G, while specific capacitances of 783 and  $112 \text{ F g}^{-1}$  were obtained at 2 and

**Fig. 4** Electrochemical measurements of the NF-G/NiO composites: **a** comparison of the CV curves of NF, NF-G, and NF-G/NiO at a scan rate of  $10 \text{ mV s}^{-1}$ ; **b** cyclic voltammetry curves of NF-G coated with NiO at scan rates of 2, 5, 10, 25, and  $50 \text{ mV s}^{-1}$ ; **c** discharge curves for both samples at a current density of 3 mA; **d** specific capacitance as a function of scan rates for NF-G/NiO; **e** capacitance retention of the electrode material at a high current density of 10 mA; and **f** EIS (Nyquist) plots of both NF-G and NF-G/NiO



$100 \text{ mV s}^{-1}$ , respectively for NF-G/NiO. Using Eq. (3), a specific capacitance of  $813 \text{ Fg}^{-1}$  was obtained at a low current of 3 mA from the discharge curve for NF-G/NiO, which is closer to the specific capacitance that was obtained from the CV at a scan rate of  $2 \text{ mV s}^{-1}$ . These values are higher than those previously reported for G/NiO composites [34], but similar to those that Dong et al. [30] reported at a scan rate of  $5 \text{ mV s}^{-1}$  for graphene foam/NiO composite where the nickel template was etched away. This can be attributed to the high conductivity of 3D graphene sheets and the successful loading of NF-G/NiO by the SILAR method, resulting in improved electrochemical performance of the composite. Figure 4e shows the continuous charge–discharge curve of the NF-G/NiO

composite and the capacitance retention at a high current of 10 mA; the electrode is stable after 1000 cycles and retains 84 % of its initial capacitance.

EIS is a very powerful tool used to investigate the electrochemical characteristics of the electrode/electrolyte interface using a Nyquist plot, which is a representation of the real and imaginary parts of the impedance in a sample. The Nyquist plots of both NF-G and NF-G/NiO are shown in Fig. 4f. The intercept in the high frequency region on the  $x$ -axis corresponds to the resistance of the electrolyte solution ( $R_s$ ), and is also referred to as the equivalent series resistance (ESR), which consists of the resistance of the aqueous electrolyte, the intrinsic resistance of the composite material, and the contact resistance at the electrode

interface. The ESR values for the NF-G and NF-G/NiO electrodes were 4.8 and 0.9  $\Omega$ , respectively, as observed from Fig. 4f. It is worth stating that for ideal supercapacitors, the EIS (Nyquist) plot should be a line perpendicular to the real axis at low frequency. However, comparing both samples, the Nyquist plot of NF-G/NiO is much closer to the ideal behavior due to the low charge transfer of graphene and NiO, thus indicating a better capacitive behavior. This improved electrochemical performance is due to the synergistic effect between graphene and NiO, leading to improved conductivity of the composite and a decrease in the internal resistance of the electrode. The 3D porous network structure of the nickel foam also helps to provide easy access to ions from the electrolyte at the electrode/electrolyte interface.

## Conclusions

Graphene has been synthesized on nickel foam using CVD. The feasibility of using the SILAR to deposit nickel oxide onto the substrate (NF-G) has been tested. The results of the electrochemical experiments indicate that the as-grown NF-G when coated with NiO nanostructure exhibits good pseudocapacitive behavior. This is attributed mainly to the 3D nature of the NF which allows for 3D graphene growth, incorporation of NiO, and combination with the conductivity of the graphene, leading to improved capacitance. The results show that nickel foam can be used directly for the growth of graphene and for electrochemical applications, rather than removing the nickel template which often introduces impurities into the sample from the etching agent. Furthermore, the open network structure of the composite makes it easily accessible for electrolyte movement and ion exchange during electrochemistry. The results obtained demonstrate that the nickel foam-graphene composite could be a promising material for accommodating metal oxide materials for electrochemical applications.

**Acknowledgements** This study is based on research supported by the South African Research Chairs Initiative of the Department of Science and Technology (SARChI-DST) and the National Research Foundation (NRF). Any opinions, findings and conclusions, or recommendations expressed in this study are those of authors and therefore the NRF and DST do not accept any liability with regard thereto. AB thanks University of Pretoria and the NRF for financial support for his study, KM also thanks the NRF for a scarce-skills scholarship. We thank Dr. Patricia Forbes for supplying the nickel foams.

## References

- Conway BE (1999) *Electrochemical supercapacitors: scientific fundamentals and technological applications*. Kluwer Academic/Plenum, New York
- Kotz R, Carlen M (2000) *Electrochim Acta* 45:2483
- Zaho X, Sánchez BM, Dobson PJ, Grant PS (2011) *Nanoscale* 3:839
- Hall PJ, Mirzaei M, Fletcher SI, Sillars FB, Rennie AJR, Shitta-Bey GO, Wilson G, Cruden A, Carter R (2010) *Energy Environ Sci* 3:1238
- Frackowiak E (2007) *Phys Chem Chem Phys* 9:1774
- Burke A (2007) *Electrochim Acta* 53:1083
- Frackowiak E, Benguin F (2001) *Carbon* 39:937
- Simon P, Gogotsi Y (2008) *Nat Mater* 7:845
- Zhang LL, Zhao XS (2009) *Chem Soc Rev* 38:2520
- Geim AK, Novoselov KS (2007) *Nat Mater* 6:183
- Katsnelson MI (2007) *Mater Today* 10:20
- Novoselov KS, Geim AK, Morozov SV, Jiang D, Katsnelson MI, Grigorieva IV, Dubonos SV, Firsov AA (2004) *Science* 306:666
- Stoller MD, Park S, Zhu Y, An J, Ruoff RS (2008) *Nano Lett* 8:3498
- Wang Y, Shi Z, Huang Y, Ma Y, Wang C, Chen M, Chen YS (2009) *J Phys Chem C* 113:13103
- Liu C, Yu Z, Neff D, Zhamu A, Jang BZ (2010) *Nano Lett* 10:4863
- Zhu Y, Murali S, Cai W, Li X, Suk JW, Potts JR, Ruoff RS (2010) *Adv Mater* 22:3906
- Sun Y, Wu Q, Shi G (2011) *Energy Environ Sci* 4:1113
- Yu DS, Dai LM (2010) *J Phys Chem Lett* 1:467
- Yuan C, Zhang X, Su L, Gao B, Shen L (2009) *J Mater Chem* 19:5772
- Xi YY, Li D, Djuricic AB, Xie MH, Man KYK, Chan WK (2008) *Electrochim Solid State Lett* 11:D56
- Konstantinov K, Wang G, Lao ZJ, Liu HK, Devers T (2009) *J Nanosci Nanotech* 9:1263
- Bi RR, Wu XL, Cao FF, Jiang LY, Guo YG, Wan LJ (2010) *J Phys Chem C* 114:2448
- Liang K, Tang X, Hu W (2012) *J Mater Chem* 22:11062
- Li J, Zhao W, Huang F, Manivannan A, Wu N (2011) *Nanoscale* 3:5103
- Zhong W, Yun H, Xin-bo Z (2012) *J Electrochem* 18:151
- Xia XH, Tu JP, Wang XL, Gu CD, Zhao XB (2011) *J Mater Chem* 21:671
- Xia C, Yanjun X, Ning W (2011) *Sens Actuators B* 153:434
- Zhang X, Shi W, Zhu J, Zhao W, Ma J, Mhaisalkar S, Maria TL, Yang Y, Zhang H, Hang HH, Yan Q (2010) *Nano Res* 9:643
- Chen Z, Ren W, Gao L, Liu B, Pei S, Cheng H (2011) *Nat Mater* 10:424
- Dong X, Wang X, Wang L, Song H, Zhang H, Huang W, Chen (2012) *Appl Mater Interfaces* 4:3129
- Cao X, Shi Y, Shi W, Lu G, Huang X, Yan Q, Zhang Q, Zhang H (2011) *Small* 7:3163
- Xiaochen D, Yunfa C, Jing W, Mary BC, Lianhui W, Wei H, Chen P (2012) *RSC Adv* 2:4364
- Thandavarayan M, Xiaochen D, Peng C, Xin W (2012) *J Mater Chem* 22:5286
- Xia X, Tu J, Mai Y, Chen R, Wang X, Gu C, Zhao X (2011) *J Chem Eur* 17:10898
- Ge C, Hou Z, Zeng BH, Cao J, Liu Y, Kuan Y (2012) *J Sol Gel Sci Technol* 631:146
- Li J, Yang QM, Zhitomirsky I (2008) *J Power Sour* 185:1569
- Lokhande CD, Sankapala BR, Pathana HM, Muller M, Giersig M, Tributsch H (2001) *Appl Surf Sci* 181:277
- Chung J, Myoung J, Oh J, Lim SJ (2012) *Phys Chem Solids* 73:535
- Wu M, Wang M, Jow J (2010) *J Power Sour* 195:3950
- Ferrari AC (2007) *Solid State Commun* 143:47
- Wu M, Huang C, Lin K (2009) *J Power Sources* 186:557
- Chae SJ, Güneş F, Kim KK, Kim ES, Han GH, Kim SM, Shin H, Yoon S, Choi JY, Park MH, Yang CW, Pribat D, Lee YH (2009) *Adv Mater* 21:2328
- Xing W, Li F, Yan Z, Lu GQ (2004) *J Power Sour* 134:324

## **Summary**

SILAR method has been successfully used to synthesise NiO nanostructure on NF-G network. Composite was successfully characterized and was tested as electrode for electrochemical capacitor and was found to exhibit a high specific capacitance. The cause of the good electrochemical performance has been explained as due to the direct synthesis of graphene on the nickel foam via CVD which provide a 3D conducting network platform suitable for adsorption of NiO nanostructures.

## References

- [1] Y. Zheng, H. Ding, M. Zhang, *Mater. Res. Bull.* **44** (2009) 403.
- [2] Y-Z. Zheng, M-L. Zhang, *Mater. Lett.* **61** (2007) 3967.
- [3] G.H.A. Therese, P.V. Kamath, *Chem. Mater.* **12** (2000) 1195.
- [4] X. Xia, J. Tu, X. Wang, C. Gu, X. Zhao, *J. Mater. Chem.* **21** (2011) 671.
- [5] X. Zhang, W. Shi, J. Zhu, W. Zhao, J. Ma, S. Mhaisalkar, T.L. Maria, Y. Yang, H. Zhang, H.H. Hng, Q. Yan, *Nano Res.* **3** (2010) 643.
- [6] J.D. Desai, S.-K. Min, K-D. Jung, O-S. Joo, *Appl. Surf. Sci.* **253** (2006) 1781.
- [7] Y. Zhang, Y. Gui, X. Wu, H. Feng, A. Zhang, L. Wang, T. Xia, *Int. J. Hydrogen Energy* **34** (2009) 2467.
- [8] Y. Wang, Q-Z. Qin, *J. Electrochem. Soc.* **149** (2002) A873.
- [9] B. Sasi, K.G. Gopchandran, *Sol. Energy Mater. Sol. Cells* **91** (2007) 1505.
- [10] M-S. Wu, C-Y. Huang, K-H. Lin, *J. Power Sources* **186** (2009) 557.
- [11] M-S. Wu, Y-A. Huang, C-H. Yang, J-J. Jow, *Int. J. Hydrogen Energy* **32** (2007) 4153.
- [12] D-D. Zhao, M.W. Xu, W-J. Zhou, J. Zhang, H.L. Li, *Electrochim. Acta* **53** (2008) 2699.
- [13] K. Liu, M.A. Anderson, **143** (1996) 124.
- [14] A.A. Al-Ghamdi, W.E. Mahmoud, S.J. Yaghmour, F.M. Al-Marzouki, *J. Alloys Compd.* **486** (2009) 9.
- [15] C.D. Lokhande, D.P. Dubal, O-S. Joo, *Curr. Appl. Phys.* **11** (2011) 255.
- [16] U.M. Patil, R.R. Salunkhe, K.V. Gurav, C.D. Lokhande, *Appl. Surf. Sci.* **255** (2008) 2603.
- [17] G.M. Suppes, B.A. Deore, M.S. Freund, *Langmuir* **24** (2008) 1064.
- [18] X. Xia, J. Tu, Y. Mai, R. Chen, X. Wang, C. Gu, X. Zhao, *Chemistry* **17** (2011) 10898.
- [19] C. Ge, Z. Hou, B. He, F. Zeng, J. Cao, Y. Liu, Y. Kuang, *J. Sol-Gel Sci. Technol.* **63** (2012) 146.
- [20] X. Cao, Y. Shi, W. Shi, G. Lu, X. Huang, Q. Yan, Q. Zhang, H. Zhang, *Small* **7** (2011) 3163.

- [21] S.J. Chae, F. Güneş, K.K. Kim, E.S. Kim, G.H. Han, S.M. Kim, H-J. Shin, S-M. Yoon, J-Y. Choi, M.H. Park, C.W. Yang, D. Pribat, Y.H. Lee, G. Adv. Mater. **21** (2009) 2328.
- [22] H.M. Pathan, C.D. Lokhande, Bull. Mater. Sci. **27** (2004) 85.
- [23] R.S. Mane, C.D. Lokhande, Mater. Chem. Phys. **65** (2000) 1.
- [24] B.R. Sankapal, R.S. Mane, C.D. Lokhande, Mater. Res. Bull. **35** (2000) 177.

### 4.3 Aqueous chemical growth technique (ACG) of simonkolleite microplatelets on nickel foam-graphene

#### Introduction

The ACG technique was used to synthesise Simonkolleite ( $Zn_5(OH)_8Cl_2 \cdot H_2O$ ) on a nickel foam graphene (NF-G). This technique was employed because of its versatility for the design and the production of nanostructured oxide materials with novel morphology and orientation which have enhanced physiochemical properties [1,2]. Simonkolleite is a rhombohedral  $R\bar{3}m$  space group, containing two crystallographically distinct zinc sites, both of which are fully occupied by zinc. The Zn (1) site is coordinated by six hydroxyl (OH) groups in an octahedral geometry  $[Zn(OH)_6]$  while the Zn (2) site is coordinated by three OH groups, and one Chlorine (Cl) atom in a tetrahedral geometry  $[Zn(OH)_3Cl]$ . The  $[Zn(OH)_6]$  octahedra forms an edge-sharing dioctahedral sheet similar to that observed in dioctahedral micas [3]. On each site of the vacant octahedron, a  $[Zn(OH)_3Cl]$  tetrahedron is attached to three anions of the sheet and points away from the sheet. The sheets are held together by hydrogen bonding from OH groups of one sheet to Cl anions of adjacent sheets, and to interstitial  $H_2O$  groups [3–5]. The oxygen vacancies on the surface of simonkolleite are electrically and chemically active and thus may find application in electrochemical capacitors [6].

In this section, we will present an unprecedented Simonkolleite ( $Zn_5(OH)_8Cl_2 \cdot H_2O$ ) on a nickel foam graphene (NF-G), which possesses the advantages of uniform and homogenous hexagonal Simonkolleite distribution on NF-G. The NF-G possesses a large surface area which acts as nucleation site for growth of Simonkolleite leading to highly conductive free-standing NF-G/ Simonkolleite composite by the ACG method.

Electrochemical performance of the composite was found to be superior to that of the pristine NF-G samples. Detailed information regarding the study of this composite material of NF-G/Simonkolleite is given in the attached publication. This publication outlines the growth

procedure, structural and morphological characterization and the electrochemical results that were obtained and also includes conclusions drawn from this work.

# Results and discussions: Publication 3 Hydrothermal synthesis of simonkolleite microplatelets on nickel foam-graphene for electrochemical supercapacitors

J Solid State Electrochem  
 DOI 10.1007/s10008-013-2206-0

ORIGINAL PAPER

## Hydrothermal synthesis of simonkolleite microplatelets on nickel foam-graphene for electrochemical supercapacitors

S. Khamlich · A. Bello · M. Fabiane · B. D. Ngom · N. Manyala

Received: 20 June 2013 / Revised: 24 July 2013 / Accepted: 28 July 2013  
 © Springer-Verlag Berlin Heidelberg 2013

**Abstract** Nickel foam-graphene (NF-G) was synthesized by chemical vapour deposition followed by facial in situ aqueous chemical growth of simonkolleite ( $Zn_5(OH)_8Cl_2 \cdot H_2O$ ) under hydrothermal conditions to form NF-G/simonkolleite composite. X-ray diffraction and Raman spectroscopy show the presence of simonkolleite on the NF-G, while scanning and transmission electron microscopies show simonkolleite micro-plates like structure evenly distributed on the NF-G. Electrochemical measurements of the composite electrode give a specific capacitance of  $350 \text{ Fg}^{-1}$  at current density of  $0.7 \text{ Ag}^{-1}$  for our device measured in three-electrode configuration. The composite also shows a rate capability of  $\sim 87\%$  capacitance retention at a high current density of  $5 \text{ Ag}^{-1}$ , which makes it a promising candidate as an electrode material for supercapacitor applications.

**Keywords** Graphene · Composite structure · Simonkolleite · Supercapacitor

### Introduction

The energy and power densities of energy storage devices need to be improved significantly to meet the growing power supply demand of a variety of applications such as cordless electric tools, hybrid electric vehicles, day-night storage and industrial energy management [1]. In recent years, many researchers have focused on the development of electrode materials to increase

the energy density of electrochemical capacitors (also known as supercapacitors), while retaining their intrinsic high-power density. Furthermore, supercapacitors have generally used carbonaceous materials with a large surface area (e.g. carbon nanotubes [2], carbon [3] and graphene [4]) and transition metal oxides (e.g.  $\text{Co}_3\text{O}_4$  [5, 6], NiO [7],  $\text{RuO}_2$  [8],  $\text{SnO}_2$  [9],  $\text{MnO}_2$  [10],  $\text{V}_2\text{O}_5$  [11] and so forth). Recently, graphene has been shown to be an effective material for constructing supercapacitor electrodes due to its large surface area, high mechanical stability and electrical conductivity [12, 13]. Graphene electrode alone has been found to have specific capacitance of up to  $135 \text{ F/g}$  [13, 14]. On the other hand, nanocomposites consisting of graphene and transition metal oxides have attracted wide attention in the field of supercapacitors due to the synergistic effect arising from the combination of the redox reaction of the metal oxides with the high surface area/conductivity of graphene, which improves the electrochemical performance [15, 16]. This has been reported to be highly dependent on the quality and conductivity of the graphene [17].

Self-supporting graphene nanosheets (GNS), via chemical reduction of exfoliated graphite oxide, have shown great potential as flexible electrodes with excellent mechanical stiffness and strength [18–20]. However, in most cases, these GNS were assembled into macroscopic paper-like structures in a way that reduced the large accessible surface area of the two-dimensional (2D) GNS. This usually results from irreversible agglomeration and restacking of the individual GNS which hinders the potential applications of graphene materials in supercapacitor devices. The resulting GNS also exhibit inferior conductivity due to the abundant existence of defects and oxygen-containing chemical groups, and to numerous non-ideal contacts between the nanosheets. In addition, the strong  $\pi$ - $\pi$  interaction between GNS leads to severe aggregation and a considerable decrease in its specific surface area [21]. Both of these shortcomings seriously limit the performance of graphene-based supercapacitors, sensors and other devices.

S. Khamlich (✉) · A. Bello · M. Fabiane · N. Manyala (✉)  
 SARChI Chair in Carbon Technology and Materials, Institute of Applied Materials, Department of Physics, University of Pretoria, Private Bag X20, Hatfield 0028, South Africa  
 e-mail: skhamlich@gmail.com  
 e-mail: ncholu.manyala@up.ac.za

B. D. Ngom  
 NANOAFNET, MRD-iThemba LABS, National Research Foundation, 1 Old Faure road, Somerset West 7129, South Africa

Published online: 09 August 2013

 Springer

Chemical vapor deposition (CVD) is an alternative method for synthesizing a three-dimensional (3D) network of graphene on a nickel foam template [22] which exhibits high conductivity compared with that of GNS [23, 24]. This facilitates fast electron transport between the active materials and current collectors in supercapacitors [15, 17]. Furthermore, CVD-grown 3D graphene networks have high conductivity due to the high intrinsic conductivity of defect-free graphene and the absence of inter-sheet junction resistance in this seamlessly continuous network [21]. In addition, the porous nature of this new graphene material offers a large specific surface area (up to  $\sim 850 \text{ m}^2/\text{g}$ ) [22] and is suitable for the production of functional composites by filling the pores with metal oxide nanoparticles, polymers or other functional materials [25].

Similar to metal oxides,  $\text{Zn}_5(\text{OH})_8\text{Cl}_2 \cdot \text{H}_2\text{O}$  (simonkolleite) is also electrochemically active as an electrode material for supercapacitors [26]. Most reports on simonkolleite deal with its bulk properties, with a net focus on understanding the surface atmospheric corrosion products on Zn plates [26, 27]. Simonkolleite forms hexagonal microplatelet crystals with a perfect cleavage parallel to the (001) direction [28]. It is a soft compound with a Mohs hardness of  $\sim 1.5$  and a specific gravity of 3.2 [29]. The crystal structure of the synthesis analogue of simonkolleite was reported by Nowacki and Silverman [30] and Allmann [31]. Simonkolleite is electrically and chemically active due to the oxygen vacancies on its surface, as in the case of ZnO. These vacancies may then function as n-type donors and thus significantly increase the material's conductivity [29].

In this work, we present a novel two-step approach for growing a nickel foam-graphene/simonkolleite (NF-G/simonkolleite) 3D composite structure for electrochemical supercapacitors.

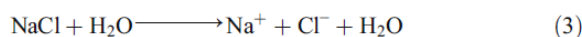
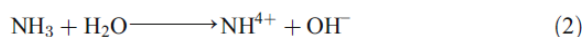
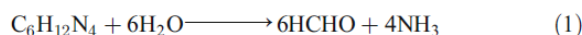
## Experiments and methods

### Growth of graphene on nickel foam

Nickel foams (Alantum, Munich, Germany),  $420 \text{ g}\cdot\text{m}^{-2}$  in a real density and 1.6 mm in thickness, was used as 3D scaffold templates for the CVD growth of graphene. It was cut into pieces of  $1 \times 2 \text{ cm}^2$  and placed in a quartz tube with an outer diameter of 5 cm and an inner diameter of 4.5 cm. The precursor gases were  $\text{CH}_4$ ,  $\text{H}_2$  and Ar. The nickel foam was annealed at  $800 \text{ }^\circ\text{C}$  in the presence of Ar and  $\text{H}_2$  for 20 min, before the introduction of the  $\text{CH}_4$  gas at  $1,000 \text{ }^\circ\text{C}$  (Fig. 1). The flow rates of the gases  $\text{CH}_4$ ,  $\text{H}_2$  and Ar were 10, 10 and 300 sccm, respectively. After 15 min of deposition, the sample was rapidly cooled by pushing the quartz tube to a lower temperature region.

### Growth of simonkolleite on graphene/nickel foam

Simonkolleite microplatelets ( $\text{Zn}_5(\text{OH})_8\text{Cl}_2 \cdot \text{H}_2\text{O}$ ) were deposited directly on the NF-G using the aqueous chemical growth technique (Fig. 1). A solution containing zinc nitrate hexahydrate ( $\text{Zn}(\text{NO}_3)_2 \cdot 6\text{H}_2\text{O}$ ), sodium chloride (NaCl) and hexamethylenetetramine (HMT,  $\text{C}_6\text{H}_{12}\text{N}_4$ ) was used for the deposition of simonkolleite plate-like structures. A 100 ml bottle with autoclavable screw cap was filled with an equimolar (0.1 M) aqueous solution of  $\text{Zn}(\text{NO}_3)_2 \cdot 6\text{H}_2\text{O}$ , HMT and NaCl. Subsequently, the NF-G samples fixed on glass slides were immersed in the solution and subjected to hydrothermal treatment at  $90 \text{ }^\circ\text{C}$  for 16 h. Thereafter, the autoclave was allowed to cool down to ambient temperature. The final NF-G/simonkolleite composite was obtained after washing and drying. The formation of  $\text{Zn}_5(\text{OH})_8\text{Cl}_2 \cdot \text{H}_2\text{O}$  is considered to proceed competitively in the solution following the successive chemical reaction:



First,  $\text{C}_6\text{H}_{12}\text{N}_4$  disintegrates into formaldehyde (HCHO) and ammonia ( $\text{NH}_3$ ) as shown in Eq. (1). Ammonia tends to disintegrate water to produce  $\text{OH}^-$  anions (Eq. 2). Secondly, sodium chloride disintegrates in water-forming sodium cations and chloride anions (Eq. 3). Furthermore,  $\text{Zn}(\text{NO}_3)_2 \cdot 6\text{H}_2\text{O}$  disintegrates into zincate ion  $\text{Zn}^{2+}$  and nitrate  $\text{NO}_3^-$  (Eq. 4). Finally,  $\text{OH}^-$  and  $\text{Cl}^-$  anions react with  $\text{Zn}^{2+}$  cations to synthesize simonkolleite nanoplatelets ( $\text{Zn}_5(\text{OH})_8\text{Cl}_2 \cdot \text{H}_2\text{O}$ ) (Eq. 5).

### Material characterization

The structural characterization of the NF-G/simonkolleite composite was investigated by X-ray diffraction (XRD) using a Bruker D8 Advance X-ray diffractometer equipped with  $\text{Cu K}\alpha$  radiation ( $\lambda = 1.5406 \text{ \AA}$ ), employing a scanning rate of  $0.2 \text{ }^\circ \text{ s}^{-1}$  and  $2\theta$  ranges from  $20$  to  $70 \text{ }^\circ$ . The Raman spectra were recorded using a WITEC-Alpha 300R Plus confocal Raman spectrometer (WITEC GmbH, Ulm, Germany). The excitation source was a 532-nm laser (2.33 eV, 1 mW power) through a numerical aperture of 0.9 and with  $\times 100$  magnification. Morphological characterization was performed on a high-resolution Zeiss Ultra Plus 55 field emission gun scanning electron microscope (FE-SEM) operated at 2.0 kV. Transmission electron microscopy (TEM) micro-images and selected area electron diffraction (SAED) observations were carried out with a JEOL

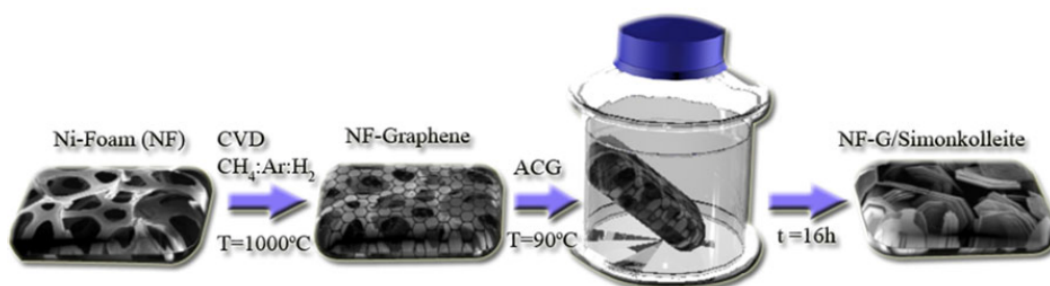


Fig. 1 Synthesis process scheme of the NF-G/simonkolleite composite

JEM-2100F microscope operated at 200 kV (Akishima-shi, Japan). The capacitive properties were investigated by the cyclic voltammetry (CV) method using an Autolab PGSTAT Workstation 302 (ECO-CHEMIE, Metrohm Autolab BV, Utrecht, the Netherlands) driven by the GPES software. The as-prepared NF-G/simonkolleite composite served as the working electrode, glassy carbon plate as the counter-electrode and Ag/AgCl (3 M KCl) as the reference electrode in 2.0 M KOH electrolyte. Electrochemical impedance spectroscopy (EIS) was performed in the frequency range of 100 kHz to 10 mHz.

## Results and discussions

Figure 2 shows the XRD pattern of the as-synthesized NF-G/simonkolleite composite. The diffraction peaks in the  $2\theta$  range  $20\text{--}70^\circ$  correspond to the characteristic reflections of simonkolleite material. The identification of all Bragg diffraction peaks confirms the crystallographic phase of the simonkolleite microplatelets and is ascribed to pure rhombohedral simonkolleite (JCPDS No. 07-0155) with lattice constants  $a$  and  $c$  of about  $\sim 6.337$  and  $\sim 23.643$  Å, respectively, and space group  $R3m$ . The relatively higher and sharper diffraction peaks observed are directly linked to the good crystallinity of the simonkolleite deposited on the NF-G. The strong diffraction peaks at the  $2\theta$  values  $44.38$  and  $51.71^\circ$  are associated with the Ni-foam and are indexed with an asterisk. In particular, the sharp peak at the  $2\theta$  value of  $26.43^\circ$  corresponds to graphene formation [32], which indicates a good crystalline structure with an interlayer spacing of  $0.339$  nm; this is consistent with the layer spacing of normal graphite.

Figure 3 shows the Raman spectra of the NF-G and the NF-G/simonkolleite composite. The Raman spectrum of NF-G shows two prominent peaks at  $\sim 1,591$  and  $2,726$   $\text{cm}^{-1}$ , corresponding to the characteristic G and 2D bands of graphene [33]. The D band (usually at  $\approx 1,350$   $\text{cm}^{-1}$ ), which is attributed to the disordered graphitic carbon and its intensity, provides information about the density of defects in the as-grown graphene. The fact that this band is not visible in the spectrum signifies that the sample is free of defects. The intensity ratio

$I_{2D}/I_G$  ( $\sim 0.71$ ) indicates that the as-grown graphene is mainly few-layered (i.e. it has fewer than five layers) [34]. This is clearly distinguishable from the 2D signal, as shown in the inset in Fig. 3 [35]. The Raman peaks at  $400$ ,  $488$  and  $732$   $\text{cm}^{-1}$  indexed by an asterisk, which agree very well with what are found in the literature ( $390$ ,  $482$  and  $730$   $\text{cm}^{-1}$ ) [36], were assigned to  $\text{Zn}_5(\text{OH})_8(\text{Cl})_2 \cdot \text{H}_2\text{O}$  (simonkolleite). A peak at  $293$   $\text{cm}^{-1}$  was attributed to the Zn–Cl bond and that at  $358$   $\text{cm}^{-1}$  to Zn–O which had a vibration characteristic of a simonkolleite structure. The O–H stretching bands are present at  $2,962$  and  $3,019$   $\text{cm}^{-1}$  [36]. Several smaller peaks at  $\sim 592$ ,  $\sim 926$ ,  $\sim 969$ ,  $\sim 1,077$ ,  $\sim 1,154$ ,  $\sim 1,466$  and  $\sim 1,778$   $\text{cm}^{-1}$ , also indexed by an asterisk, result from the multiple-phonon scattering process in the synthesized simonkolleite microplatelets.

The SEM micrographs in Fig. 4 clearly show the typical morphologies of the NF-G and the NF-G/simonkolleite composite. It can be seen from Fig. 4a that the 3D Ni-foam is a porous structure (pore size of  $\sim 0.15\text{--}2$  mm) with a smooth surface. Figure 4b displays a representative sample of the as-grown graphene on struts of Ni foam. After the CVD process, graphene layers with different wrinkles were coated on the surface of the Ni-foam (inset in Fig. 4 b). The 3D configuration of the Ni-foam was preserved in all cases due to the structural

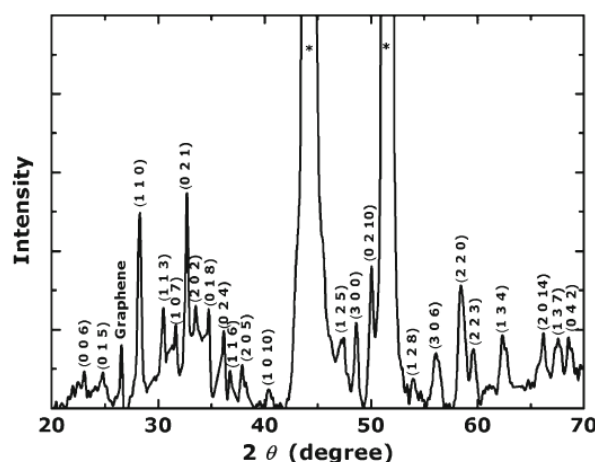


Fig. 2 X-ray diffraction pattern of the NF-G/simonkolleite composite

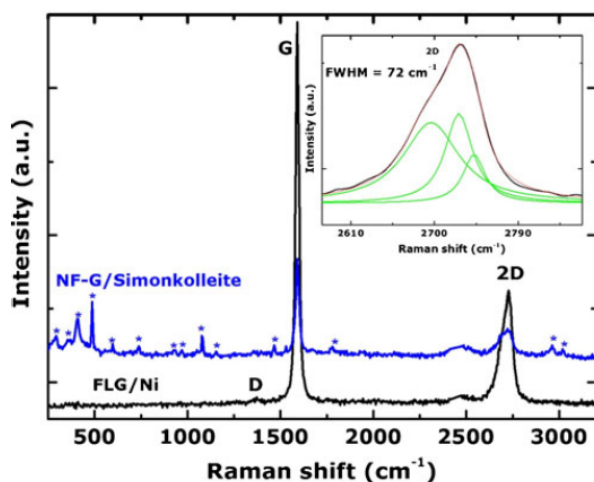


Fig. 3 Raman spectra of the NF-G and the NF-G/simonkolleite composite. The inset shows a fitted Lorentzian for 2D peak

template effect. In the NF-G/simonkolleite composite, microstructured simonkolleite is densely anchored onto both sides of the graphene surface (Fig. 4c). At higher magnification, it is observed that the simonkolleite microstructures are hexagonal and platelet-like (Fig. 4d). The diameter of the simonkolleite microplatelets is about 1.3–0.5  $\mu\text{m}$ , and the thickness is about 60 nm. In addition, there is no net spatial orientation either perpendicularly or parallel to the NF-G. The dense set of anisotropic microplatelets seems to grow faster along the basal plane and slower in the transversal direction, as shown in Fig. 4d. It seems from the SEM results that the growth is denser in the basal direction at the very early stages, when the particles

can be observed to be more flake-like. This could imply a growth mechanism similar to that of the ZnO nano/microscaled rods synthesized by a similar hydrothermal procedure [29]. If so, the growth mechanism should be a Frank-van der Merwe-driven process as well. Indeed, as supported by the high-resolution TEM image shown in Fig. 5a, one can distinguish flake-like structures with quasi-sharp edges on top of each other within the basal planes, as indicated by the arrows. Consequently, the growth mechanism is likely to be driven by a Frank-van der Merwe process. Figure 5b shows the SAED pattern of the simonkolleite microplatelets. It indicates the very high degree of crystallinity of the platelets with a net hexagonal symmetry and a possibly crystallographic preferential orientation. This crystallinity indicates that the plate-like  $\text{Zn}_5(\text{OH})_8\text{Cl}_2 \cdot \text{H}_2\text{O}$  possessed a smooth surface.

To determine the electrochemical properties of the NF-G/simonkolleite composite, we performed CV measurements using a three-electrode configuration. Figure 6a compares the CV curves of NF, NF-G, NF-simonkolleite and the NF-G/simonkolleite composite (with a mass ratio of graphene to simonkolleite, 34:66) measured in a potential window of 0–0.5 V at scan rate of  $25 \text{ mV} \cdot \text{s}^{-1}$  in 2.0 M KOH electrolyte. NF itself showed very poor CV measurements and the NF-G electrode measured under the same conditions exhibited low-intensity current peaks due to the redox reaction of the nickel foam in the electrolyte [37], and also to the quasi-super hydrophobicity which is attributed to poor surface wetting and thus the reduced accessibility and utilisation of the available surface area [38]. The CV curve of the NF-simonkolleite foam in Fig. 6a has an ill-defined shape. The reason for this could be twofold: (1) there may have been an increase in the particle

Fig. 4 SEM micrographs of a bare 3D Ni foam, b NF-G (inset shows a high-magnification view of the graphene deposited on the Ni foam), c NF-G/simonkolleite composite, d high-resolution image of the simonkolleite microplatelets

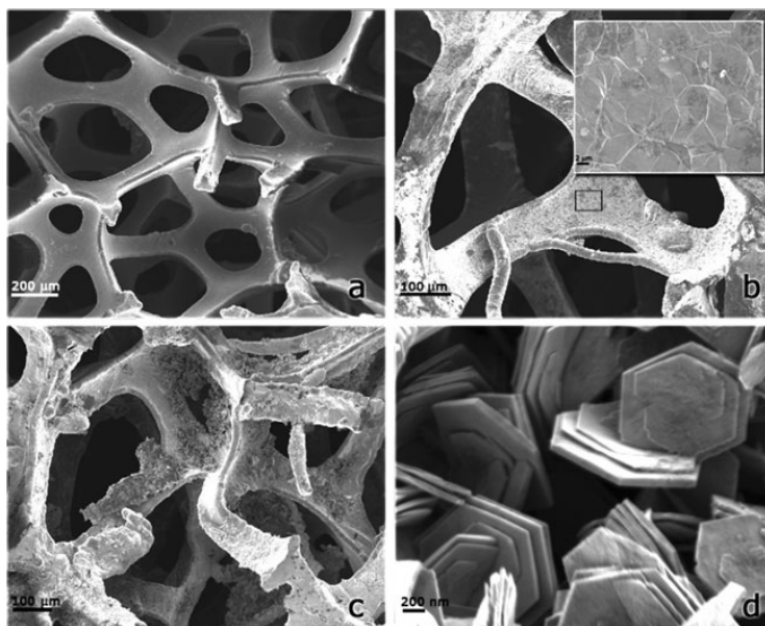
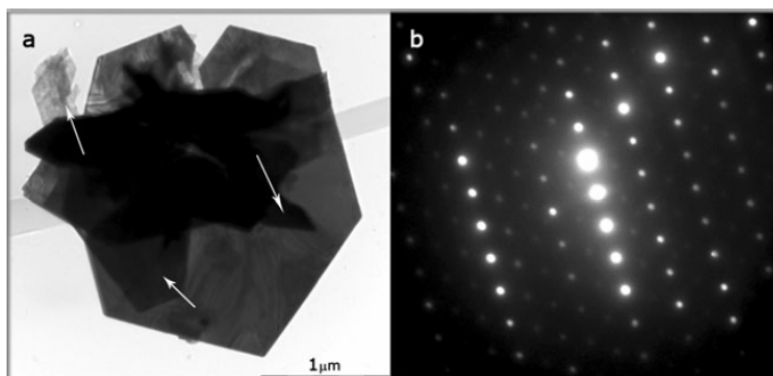


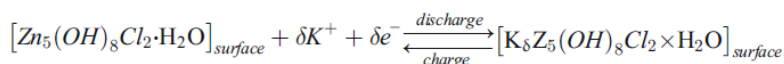
**Fig. 5** a TEM of a single simonkolleite microplatelet. The *arrows* show the flake-like simonkolleite; b corresponding SAED pattern of the simonkolleite microplatelets



size of the simonkolleite owing to aggregation, resulting in retarded transport of electrolyte ions, and (2) a fast scan rate may have induced a fast drop as a result of the high resistance of the simonkolleite microplatelets. Compared with the curve of the NF-simonkolleite, that of the NF-G/simonkolleite composite showed a much better mirror image with respect to the zero-current line and a more rapid current response on voltage reversal at each end potential. These results indicate the much higher electrochemical reversibility of the NF-G/simonkolleite composite between 0 and 0.5 V.

This is probably due to the fact that graphene becomes entangled with simonkolleite and provides unobstructed pathways for  $K^+$  transport during the rapid charge–discharge process. In addition, the high conductivity of the graphene facilitates the transport of electrolyte ions during a rapid charge–discharge process.

The CV of the NF-G/simonkolleite composite electrode (Fig. 6a) shows a pair of Faradaic redox peaks ( $\sim 0.23$  and  $0.39$  V). These peaks result from the intercalation and de-intercalation of  $K^+$  from the electrolyte into  $Zn_5(OH)_8Cl_2 \cdot H_2O$ :



From the CV curve of the NF-G/simonkolleite composite, one reversible electron-transfer process is observed. This is consistent with the reaction process mentioned above during the potential sweep of the simonkolleite ( $Zn_5(OH)_8Cl_2 \cdot H_2O$ ) electrode. It demonstrates that the capacitance of the NF-G/simonkolleite composite is based on the charge storage mechanism of ( $Zn_5(OH)_8Cl_2 \cdot H_2O$ )-based electrodes in mild electrolytes, which is ascribed to the rapid intercalation of alkali metal cations  $K^+$  in the electrode during reduction and oxidation processes [10]. Figure 6b shows the CV curves of the NF-G/simonkolleite composite electrode at different scan rates. The current response increased in accordance with increases in the scan rate, while no significant change in the shape of the CV curve was observed, indicating the good rate property of the NF-G/simonkolleite composite electrode.

To further evaluate the electrochemical capacitive performance of the NF-G/simonkolleite composite electrode, the galvanostatic charge–discharge curves were measured at different current densities within the potential range 0–0.5 V (Fig. 6c). The shape of the discharge curves does not show the characteristic of the pure double-layer capacitor but rather the pseudocapacitance; this is in agreement with the CV curves which show redox peaks. The curves display two

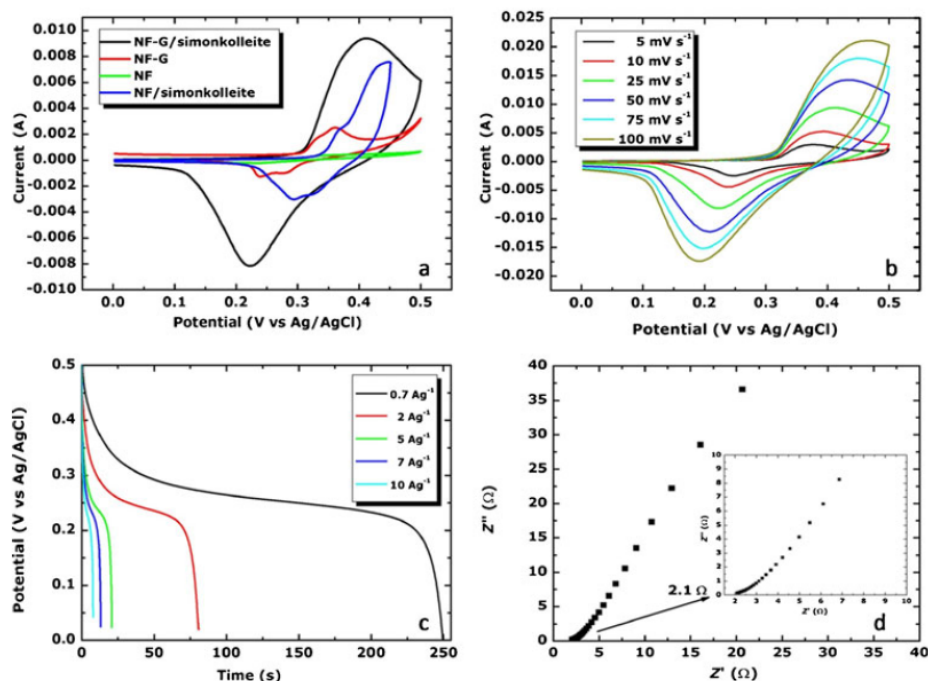
variations. First, there is a linear variation of the time dependence of the potential (below  $\sim 0.19$  V), indicating double-layer capacitance behaviour, which is caused by charge separation taking place between the electrode and the electrolyte. The other variation takes place in the potential range 0.5–0.19 V, indicating typical pseudocapacitance behaviour resulting from the electrochemical adsorption/desorption or redox reaction at the interface between the electrode and the electrolyte [39]. The specific capacitance value  $C_s$  can be evaluated as:

$$C_s = It / \Delta V m, \quad (6)$$

where  $I$  is the charge–discharge current (A),  $t$  is the discharge time (s),  $\Delta V$  is the potential window (V) and  $m$  is the mass (g) of the active NF-G/simonkolleite composite.

Based on Eq. (6), the values of the specific capacitance calculated from the discharge curves for the NF-G/simonkolleite composite are 350, 325.6, 212, 187 and 164  $Fg^{-1}$  at current densities of 0.7, 2, 5, 7 and 10  $Ag^{-1}$ , respectively. This demonstrates that the NF-G/simonkolleite electrode

**Fig. 6** **a** CV curves of bare Ni foam (NF), NF-G, NF-simonkolleite and NF-G/simonkolleite composites at a scan rate of  $25 \text{ mV}\cdot\text{s}^{-1}$  in  $2.0 \text{ M KOH}$  electrolyte; **b** CV curves of the NF-G/simonkolleite composite electrode at different scan rates; **c** galvanostatic charge–discharge curves of the NF-G/simonkolleite composite at different current densities; **d** Nyquist plot of the NF-G/simonkolleite composite. The inset in **d** shows the magnified plots in the high-frequency region



obtained possesses a high and stable specific capacitance at high charge–discharge rates. This feature is very important for electrode materials to provide a high power density.

EIS is a very powerful tool used to investigate the electrochemical characteristics of the electrode/electrolyte interface using a Nyquist plot, which is a representation of the real and imaginary parts of the impedance in a sample [40]. The Nyquist plot of the NF-G/simonkolleite composite is shown in Fig. 6d. The intercept on the X-axis in the high frequency region represents the intrinsic ohmic resistance of the internal resistance or equivalent series resistance (ESR) of the electrode material and the electrolyte [41]. The ESR value that was obtained from Fig. 6d for the NF-G/simonkolleite composite was  $2.1 \Omega$  in  $2 \text{ M KHO}$  aqueous electrolyte, which is less than that of the NF-G ( $4.8 \Omega$ ). In the Nyquist plot, the slope at low frequencies can be used to evaluate the capacitive behaviour of the electrode [42]. The nearly vertical slope of the NF-G/simonkolleite composite suggests that it has almost ideal capacitive behaviour.

For practical applications, the cycling/life stability of the NF-G/simonkolleite composite was studied. Figure 7 shows that  $\sim 87\%$  of the initial specific capacitance is preserved after 500 continuous charge–discharge cycles at the high current density of  $5 \text{ Ag}^{-1}$ . This is an indication that the prepared NF-G/simonkolleite composite electrode material has a long-term electrochemical stability and a high degree of charge–discharge reversibility. The excellent pseudocapacitive behaviour and high cycling stability can be attributed to the following: (1) graphene can provide a high electrical conductivity and a

high specific surface area, allowing rapid and effective ion charge transfer and electron transport; (2) simonkolleite ( $\text{Zn}_5(\text{OH})_8\text{Cl}_2\cdot\text{H}_2\text{O}$ ) microplatelets with excellent electrochemical activity and reversibility are grown directly on the graphene, and the chemical bonding that takes place between the simonkolleite microplatelets and the graphene favours electrochemical stability; (3) the graphene is deposited directly on the Ni-foam collector, which avoids increasing the contact resistance between the electrode and the collector.

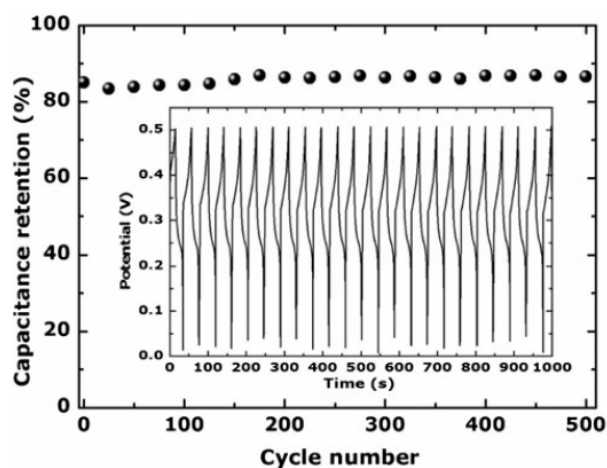


**Fig. 7** Cycle performance of the NF-G/simonkolleite composite at the current density of  $5 \text{ Ag}^{-1}$  in  $2.0 \text{ M KOH}$  solution. The inset shows the charge–discharge profile for the NF-G/simonkolleite composite

## Conclusion

Simonkolleite ( $Zn_5(OH)_8Cl_2 \cdot H_2O$ ) microplatelets were successfully deposited on Ni foam-graphene by the aqueous chemical growth method. The composite material exhibits excellent performance as an electrode for supercapacitors owing to its unique 3D architecture, the electrochemical properties of simonkolleite, the extraordinary electrical and mechanical properties of graphene and the synergistic integration of the two types of nanomaterial. The results discussed in this paper indicate that this nano-electrode possesses relatively high specific capacitance and long-term cycling stability, which offers great promise for applications in composite supercapacitors.

**Acknowledgments** This work was financially supported by the Vice-Chancellor of the University of Pretoria and the National Research Foundation (NRF) of South Africa.

## References

- Miller JR, Burke AF (2008) Electrochemical Capacitors: Challenges and Opportunities for Real-World Applications. *Electrochem. Soc Interf* 17:53–57
- Masarapu C, Zeng HF, Hung KH, Wei BQ (2009) Effect of temperature on the capacitance of carbon nanotube supercapacitors. *ACS Nano* 3:2199–2206
- Li GR, Feng ZP, Ou YN, Wu DC, Fu RW, Tong YX (2010) Mesoporous  $MnO_2$ /carbon aerogel composites as promising electrode materials for high-performance supercapacitors. *Langmuir* 26:2209–2213
- Du X, Guo P, Song HH, Chen XH (2010) Graphene nanosheets as electrode material for electric double-layer capacitors. *Electrochim Acta* 55:4812–4819
- Gao YY, Chen SL, Cao DX, Wang GL, Yin JL (2010) Electrochemical capacitance of  $Co_3O_4$  nanowire arrays supported on nickel foam. *J Power Sources* 195:1757–1760
- Yan J, Wei T, Qiao W, Shao B, Zhao Q, Zhang L, Fan Z (2010) Rapid microwave-assisted synthesis of graphene nanosheet/ $Co_3O_4$  composite for supercapacitors. *Electrochim Acta* 55:6973–6978
- Wang DC, Ni WB, Pang H, Lu QY, Huang ZJ, Zhao JW (2010) Preparation of mesoporous NiO with a bimodal pore size distribution and application in electrochemical capacitors. *Electrochim Acta* 55:6830–6835
- Pico F, Ibanez J, Rodenas L, Linares-Solano A, Rojas RM, Amarilla JM, Rojo JM (2008) Understanding  $RuO_2 \cdot xH_2O$ /carbon nanofibre composites as supercapacitor electrodes. *J. Power Sources* 176:417–425
- Li FH, Song JF, Yang HF, Gan SY, Zhang QX, Han DX, Ivaska A, Niu L (2009) One-step synthesis of graphene/ $SnO_2$  nanocomposites and its application in electrochemical supercapacitors. *Nanotechnology* 20:455602–455607
- Yan J, Fan ZJ, Wei T, Qian WZ, Zhang ML, Wei F (2010) Fast and reversible surface redox reaction of graphene- $MnO_2$  composites as supercapacitor electrodes. *Carbon* 48:3825–3833
- Qu QT, Shi Y, Li LL, Guo WL, Wua YP, Zhang HP, Guan SY, Holze R (2009)  $V_2O_5 \cdot 0.6H_2O$  nanoribbons as cathode material for asymmetric supercapacitor in  $K_2SO_4$  solution. *Electrochem Commun* 11:1325–1328
- Stoller MD, Park S, Zhu Y, An J, Ruoff RS (2008) Graphene-based ultracapacitors. *Nano Lett* 8:3498–3502
- Zhang LL, Zhou R, Zhao XS (2010) Graphene-based materials as supercapacitor electrodes. *J Mater Chem* 20:5983–5992
- Lake JR, Cheng A, Selverston S, Tanaka Z, Koehne J, Meyyappan M, Che B (2012) Graphene metal oxide composite supercapacitor electrodes. *J Vac Sci Technol B* 30:03D118
- Shi W, Zhu J, Sim DH, Tay YY, Lu Z, Zhang X, Sharma Y, Srinivasan M, Zhang H, Hng HH, Yan Q (2011) Achieving high specific charge capacitances in  $Fe_3O_4$ /reduced graphene oxide nanocomposites. *J Mater Chem* 21:3422–3427
- Zhu J, Zhu T, Zhou X, Zhang Y, Lou XW, Chen X, Zhang H, Hng HH, Yan Q (2011) Facile synthesis of metal oxide/reduced graphene oxide hybrids with high lithium storage capacity and stable cyclability. *Nano-scale* 3:1084–1089
- Wang H, Casalongue HS, Liang Y, Dai H (2010)  $Ni(OH)_2$  nanoplates grown on graphene as advanced electrochemical pseudocapacitor materials. *J Am Chem Soc* 132:7472–7477
- Li D, Muller MB, Gilje S, Kaner RB, Wallace GG (2008) Processable aqueous dispersions of graphene nanosheets. *Nat Nanotechnol* 3:101–105
- Dikin DA, Stankovich S, Zimney EJ, Piner RD, Dommett GH, Evmenenko G, Nguyen ST, Ruoff RS (2007) Preparation and characterization of graphene oxide paper. *Nature* 448:457–460
- Chen H, Müller MB, Gilmore KJ, Wallace GG, Li D (2008) Mechanically strong, electrically conductive, and biocompatible graphene paper. *Adv Mater* 20:3557–3561
- Dong X, Cao Y, Wang J, Chan-Park MB, Wang L, Huang W, Chen P (2012) Hybrid structure of zinc oxide nanorods and three dimensional graphene foam for supercapacitor and electrochemical sensor applications. *RSC Adv* 2:4364–4369
- Chen ZP, Ren WC, Gao LB, Liu BL, Pei SF, Cheng HM (2011) Three-dimensional flexible and conductive interconnected graphene networks grown by chemical vapour deposition. *Nat Mater* 10:424–428
- Li X, Cai W, An J, Kim S, Nah J, Yang D, Piner R, Velamakanni A, Jung I, Tutuc E, Banerjee SK, Colombo L, Ruoff RS (2009) Graphene films with large domain size by a two-step chemical vapor deposition process. *Science* 324:1312–1314
- Kim KS, Zhao Y, Jang H, Lee SY, Kim JM, Kim KS, Ahn JH, Kim P, Choi JY, Hong BH (2009) Large-scale pattern growth of graphene films for stretchable transparent electrodes. *Nature* 457:706–710
- Huang X, Qi XY, Boey F, Zhang H (2012) Graphene-based composites. *Chem Soc Rev* 41:666–686
- Pérez C, Collazo A, Izquierdo M, Merino P, Nóvoa XR (2000) Electrochemical impedance spectroscopy study of the corrosion process on coated galvanized steel in a salt spray fog chamber. *Corros* 56:1220–1232
- Zhu F, Persson D, Thierry D, Taxen C (2000) Formation of corrosion products on open and confined zinc surfaces exposed to periodic wet/dry conditions. *Corros* 56:1256–1265
- Hawthorne FC, Sokolova E (2002) Simonkolleite,  $Zn_5(OH)_8Cl_2 \cdot H_2O$ , a decorated interrupted-sheet structure of the form  $[M\varphi_2]_4$ . *Can Mineral* 40:939–946
- Sithole J, Ngom BD, Khamlich S, Manikanadan E, Manyala N, Saboungi ML, Knoessen D, Nemetudi R, Maaza M (2012) Simonkolleite nano-platelets: synthesis and temperature effect on hydrogen gas sensing properties. *App Surf Sci* 258:7839–7843
- Nowacki W, Silverman JN (1961) Die kristallstruktur von zinkhydroxychlorid II  $Zn_5(OH)_8Cl_2 \cdot 1H_2O$ . *Z Krist* 115:21–51
- Allmann R (1968) Verfeinerung der Struktur des Zinkhydroxychlorids II  $Zn_5(OH)_8Cl_2 \cdot 1H_2O$ . *Z Krist* 126:417–426
- Wu YP, Wang B, Ma YF, Huang Y, Li N, Zhang F, Chen YS (2010) Efficient and large-scale synthesis of few-layered graphene using an arc-discharge method and conductivity studies of the resulting films. *Nano Res* 3:661–669

33. Dong XC, Shi YM, Chen P, Ling QD, Huang W (2010) Aromatic molecules doping in single-layer graphene probed by Raman spectroscopy and electrostatic force microscopy. *J J Appl Phys* 49: 01AH04
34. Wei D, Mitchell JI, Tansarawiput C, Nam W, Qi M, Ye PD, Xu X (2013) Laser direct synthesis of graphene on quartz. *Carbon* 53:374–379
35. Reina A, Jia XT, Ho J, Nezich D, Son H, Bulovic V, Dresselhaus MS, Kong J (2009) Large area, few-layer graphene films on arbitrary substrates by chemical vapor deposition. *Nano Lett* 9:30–35
36. Bemard MC, Hugot-Le Goff A, Massinon D, Phillips N (1993) Underpaint corrosion of zinc-coated steel sheet studied by in situ Raman spectroscopy. *Corros Sci* 35:1339–1349
37. Xia X, Tu J, Mai Y, Chen R, Wang X, Gu C, Zhao X (2011) Graphene sheet/porous NiO hybrid film for supercapacitor applications. *J Chem Eur* 17:10898–905
38. Brownson Dale AC, Figueiredo-Filho Luiz CS, Ji X, Gómez-Mingot M, Iniesta J, Fatibello-Filho O, Kampouris DK, Banks CE (2013) Freestanding three-dimensional graphene foam gives rise to beneficial electrochemical signatures within non-aqueous media. *J Mater Chem A* 1:5962–5972
39. Lang JW, Kong LB, Wu WJ, Liu M, Luo YC, Kang L (2009) A facile approach to the preparation of loose-packed Ni(OH)<sub>2</sub> nanoflake materials for electrochemical capacitors. *J Solid State Electrochem* 13:333–340
40. Li X, Rong J, Wei B (2010) Electrochemical behavior of single-walled carbon nanotube supercapacitors under compressive stress. *ACS Nano* 4:6039–6049
41. Choi BG, Hong J, Hong WH, Hammond PT, Park H (2011) Facilitated ion transport in all-solid-state flexible supercapacitors. *ACS Nano* 5:7205–7213
42. Frackowiak E, Beguin F (2001) Carbon materials for the electrochemical storage of energy in capacitors. *Carbon* 39:937–950

## Summary

Very stable composite samples of NF-G and simonkolleite have been successfully synthesised using the aqueous chemical growth technique (ACG). This technique has the ability to produce different shapes of nanostructured materials depending on the concentration of the precursor materials used. We have demonstrated a novel 3D NF-G/simonkolleite composite which combines the properties offered by the graphene and simonkolleite and thus establish a synergistic effect for the composite material. Moreover, the electrochemical properties were higher than that of NF-G suggesting that such composite material could be promising electrode material in various electrochemical applications

## References

- [1] L. Vayssieres, C. Chanéac, E. Tronc, J.P. Jolivet, J. Colloid Interface Sci. 205 (1998) 205.
- [2] L. Vayssieres, Int. J. Nanotechnol. 1 (2004) 1.
- [3] F. C. Hawthorne and E. Sokolova, The Canadian Mineralogist 40 (2002) 939.
- [4] H. Tanaka, A. Fujioka, A. Futoyu, K. Kandori, T. Ishikawa, J. Solid State Chem. 180 (2007) 2061.
- [5] O.M. K. Schmetzer, G. Schnorrer-Kohler, Miner. Monatsh (1985) 145.
- [6] J. Sithole, B.D. Ngom, S. Khamlich, E. Manikanadan, N. Manyala, M.L. Saboungi, D. Knoessen, R. Nemutudi, and M. Maaza Appl. Surf. Sci. 258 (2012) 7839.

## 4.4 Microwave synthesis of manganese oxide (MnO<sub>2</sub>) nanostructure on nickel foam-graphene as electrode for electrochemical capacitors

### Introduction

As discussed earlier in chapter 2, the search for graphene composite material that are efficient, low-cost, and effectively stable for electrochemical application are of paramount importance. Transition metal oxides (TMO) are regarded as the next generation electrode materials and have been well investigated for such purposes [1,2]. In this section and the next, we focus on one of the TMO, manganese oxide (MnO<sub>2</sub>), a good candidate for incorporation into three dimensional graphene forming composite materials. As discussed earlier, MnO<sub>2</sub> mainly exhibits pseudocapacitance effect and has been extensively studied as an electrode material for electrochemical capacitors (ECs) application due to relatively low cost, low toxicity, environmental safety, and theoretical high capacitance [3–5]. The detailed mechanism of the proposed charging process has been explained in chapter 2. It has also been identified that the phase and crystallographic structure of MnO<sub>2</sub> strongly affects the electrochemical performance and depending on the growth technique or preparation method used, several phases such as  $\alpha$ -,  $\beta$ -,  $\epsilon$ -, and  $\delta$ -MnO<sub>2</sub> can be achieved [6–8]. MnO<sub>2</sub> can be added to conductive materials such as graphene or carbon nanotubes (CNTs) leading to production of porous conductive composite with improved electrochemical behaviour.

Several composites based on MnO<sub>2</sub> and graphene and its 3D counterpart have been reported as electrode for ECs application. For example, Cheng *et al.*, reported electrode based on graphene and nanostructured MnO<sub>2</sub> composite via electrodeposition and exhibited specific capacitance of 245 F g<sup>-1</sup> at a charging current of 1 mA and high-performance asymmetric supercapacitor based on graphene and MnO<sub>2</sub> nanostructured produced by electrodeposition was also investigated by Gao *et al.* [9,10]. Facile synthesis approach was also used to produce composite of graphene-MnO<sub>2</sub> nanospheres by Zhu *et al.* and He *et al.*, in which the composite

electrode material displayed an excellent capacitance of  $210 \text{ F g}^{-1}$  at a current density  $0.5 \text{ A g}^{-1}$  with 82.4 % retention of its initial capacitance over 1000 repeating cyclic voltammetry cycles [11]. Solution-processed method was also investigated by Yu *et al.* for a composite of graphene/ $\text{MnO}_2$  which exhibited a maximum power density of  $110 \text{ kW kg}^{-1}$ , an energy density of  $12.5 \text{ W h kg}^{-1}$  and excellent cycling performance of  $\sim 95 \%$  capacitance retention over 5000 cycles. Solution-processed technique has been shown to cost effective and offers great promise in large-scale energy storage device applications [12].

Recently, 3D counterparts composite were also investigated. 3D macroporous graphene frameworks with  $\text{MnO}_2$  as electrode for supercapacitors was reported and the device showed a high specific capacitance of  $389 \text{ F g}^{-1}$  at  $1 \text{ A g}^{-1}$  with 97.7 % capacitance retention at a high current density of  $35 \text{ A g}^{-1}$  [13]. Dong *et al.* synthesised a composite of  $\text{MnO}_2$ -graphene foam with controlled  $\text{MnO}_2$  particle shape and tested as electrode for supercapacitor which demonstrated an excellent electrochemical performance with a specific capacitance  $560 \text{ F g}^{-1}$  at the current density of  $0.2 \text{ A g}^{-1}$  [14]. Zhao *et al.* investigated composite based on  $\text{MnO}_2$ /graphene/nickel foam. The maximum specific capacitance of the electrode was  $476 \text{ F g}^{-1}$  at current density of  $1 \text{ A g}^{-1}$  in  $0.5 \text{ M Na}_2\text{SO}_4$  solution [15]. However, it's worth mentioning that most of these reports make use of electrodeposition  $\text{MnO}_2$ .

In this section, I focus on the deposition of  $\text{MnO}_2$  on nickel foam-graphene (NF-G) using the microwave (MW) irradiation technology. A detailed description of MW mechanism can be found in chapter 3. This technique was used because it has the ability to reduce reaction times and increase yield of materials compared to other conventional available techniques such as the electrodeposition [16,17]. A discussion of all the results obtained is given in the attached publication.

# Results and discussions: Publication 4 Microwave assisted synthesis of MnO<sub>2</sub> on nickel foam-graphene for electrochemical capacitor

Electrochimica Acta 114 (2013) 48–53



Contents lists available at ScienceDirect

Electrochimica Acta

journal homepage: [www.elsevier.com/locate/electacta](http://www.elsevier.com/locate/electacta)



## Microwave assisted synthesis of MnO<sub>2</sub> on nickel foam-graphene for electrochemical capacitor



A. Bello<sup>a</sup>, O.O. Fashedemi<sup>b</sup>, M. Fabiane<sup>a</sup>, J.N. Lekitima<sup>b</sup>, K.I. Ozoemena<sup>b,c</sup>, N. Manyala<sup>a,\*</sup>

<sup>a</sup> Department of Physics, Institute of Applied Materials, SARChI Chair in Carbon Technology and Materials, University of Pretoria, Pretoria 0028, South Africa

<sup>b</sup> Department of Chemistry, University of Pretoria, Pretoria 0002, South Africa

<sup>c</sup> Council for Scientific and Industrial Research, Pretoria South Africa, Meiring Naude Road, Brummeria, PO Box 395, Pretoria 0001, South Africa

### ARTICLE INFO

#### Article history:

Received 10 August 2013

Received in revised form

25 September 2013

Accepted 26 September 2013

Available online xxx

#### Keywords:

Nickel foam-graphene (NF-G)

CVD

Microwave irradiation

Nanostructure MnO<sub>2</sub>

Electrochemical capacitor

### ABSTRACT

A green chemistry approach (hydrothermal microwave irradiation) has been used to deposit manganese oxide on nickel foam-graphene. The 3D graphene was synthesized using nickel foam template by chemical vapor deposition (CVD) technique. Raman spectroscopy, X-ray diffraction (XRD), scanning electron and transmission electron microscopies (SEM and TEM) have been used to characterize structure and surface morphology of the composite, respectively. The Raman spectroscopy measurements on the samples reveal that 3D graphene consists of mostly few layers with low defect density. The composite was tested in a three electrode configuration for electrochemical capacitor, and exhibited a specific capacitance of 305 F g<sup>-1</sup> at a current density of 1 A g<sup>-1</sup> and showed excellent cycling stability. The obtained results demonstrate that microwave irradiation technique could be a promising approach to synthesis graphene based functional materials for electrochemical applications.

Crown Copyright © 2013 Published by Elsevier Ltd. All rights reserved.

### 1. Introduction

Supercapacitors are electrochemical double layer capacitors that have attracted much attention due to their high power density, long cycle life, low temperature sensitivity, low maintenance cost and environmentally friendly nature [1–3]. They fill the gap between batteries (high energy density) and electrolytic capacitors (high power density) [4]. However, the energy stored in supercapacitor devices (<10 Wh kg<sup>-1</sup>) is low compared to batteries (>100 Wh kg<sup>-1</sup>). This has imposed significant and difficult challenges in employing supercapacitors as primary power source for battery replacement [5,6]. It has also restricted the use of supercapacitors for possible applications such as memory back-up equipment, hybrid vehicles, cordless electric tools, cellular phones and entertainment instruments [7]. Carbon materials such as activated carbon have been used as electrode material for supercapacitors. However, their poor electrochemical performance has limited them for practical applications [8]. Conducting polymers, transition metal oxide and different composite materials are all being considered as alternatives to carbonaceous materials with limited performance [9–11].

Graphene, a two-dimensional honeycomb lattice of sp<sup>2</sup>-bonded carbon atoms, has emerged to be an exciting material with numerous potential applications. An exciting feature of graphene is its unique electronic structure that exhibits linear dispersion at a high symmetry point in the reciprocal space, resulting in effective dynamics of electrons thereby behaving like a Dirac solid [12,13]. More recently, the development of supercapacitors device has been concentrated on graphene due to its theoretical high surface area (2630 m<sup>2</sup> g<sup>-1</sup>), high electrical conductivity, chemical stability and excellent mechanical properties [14–19]. Graphene also offers a suitable platform for accommodating metal oxide materials or conducting polymers for energy storage applications [20,21]. This is usually attributed to the large surface area of graphene which allows for uniform loading and incorporation of these materials.

Recently, several groups have demonstrated the integration of manganese oxide (MnO<sub>2</sub>) on graphene as electrode for capacitive storage application. MnO<sub>2</sub> is a transition metal oxide that has attracted much attention as electrode due to its multiple reversible electrochemical reaction, natural abundance, low cost, and environmental compatibility [22–24]. For example, Zhao et al. recently reported a composite of MnO<sub>2</sub>/graphene/nickel foam using a facile electrochemical deposition strategy [25]. Several studies have attempted to synthesize various graphene/MnO<sub>2</sub> nanocomposite using techniques such as chemical [26,27], microwave irradiation [28], electrodeposition [29–31], redox deposition [32] and polymer-assisted chemical reduction [33]. However, most of the

\* Corresponding author. Tel.: +27 012 420 3549; fax: +27 012 420 2516.  
E-mail addresses: [ncholu.manyala@up.ac.za](mailto:ncholu.manyala@up.ac.za), [manyalancholu@gmail.com](mailto:manyalancholu@gmail.com) (N. Manyala).

synthesis routes make use of concentrated acid, strong reducing agents such as hydrazine (N<sub>2</sub>H<sub>4</sub>) and sodium borohydride (NaBH<sub>4</sub>) which distort the sp<sup>2</sup> honey comb lattice of the graphene leading to very high defective samples and inferior electronic properties. Synthesizing a three-dimensional defect free composite of graphene–MnO<sub>2</sub> with very good porosity and conductivity would be considered a step forward in the development of composite materials for electrochemical energy storage technology.

In this work, we present a simple green and very efficient approach to fabricate novel nickel foam-graphene/manganese oxide (NF-G/MnO<sub>2</sub>) composite. We also explore the potential of the NF-G/MnO<sub>2</sub> composite as an electrode for high performance supercapacitor applications. The NF-G/MnO<sub>2</sub> composite has a high electrochemical surface area and 3D porous interconnected network. The MnO<sub>2</sub> deposited by the microwave technique exhibited a flower-like structure uniformly anchored on 3D porous nickel foam-graphene. The unique electrode structure not only boosted ion and electron exchange in electrochemical processes but also serve as a 3D platform for combination and integration of MnO<sub>2</sub> on the NF-G. The composites (NF-G/MnO<sub>2</sub>) displayed good electrochemical behavior with good capacitance retention at high current density. Our results showed that NF-G provides a suitable platform for developing functional materials with enhanced electrochemical performance.

## 2. Experimental

Synthesis of graphene on nickel foam was done using chemical vapor deposition (CVD). The nickel foam serves as a template for the growth [34]. Nickel foams (Alantum innovation in alloy foam Munich Germany, 420 g m<sup>-2</sup> in area density and 1.6 mm in thickness) were used as the template. The nickel foam was annealed at 800 °C in the presence of Ar and H<sub>2</sub> for 20 min to remove any form of impurities present in the foam, before the introduction of the CH<sub>4</sub> gas at the temperature of 1000 °C. The flow rates of the gases CH<sub>4</sub>:H<sub>2</sub>:Ar were 10 sccm:200 sccm:300 sccm. After 10 min of deposition, the sample was rapidly cooled by pushing the quartz tube to a lower temperature region. NF-G/MnO<sub>2</sub> composite was synthesized by in situ hydrothermal reduction method using microwave irradiation. Originally, NF-G was immersed in 10 cm<sup>3</sup> of 0.02 M of KMnO<sub>4</sub> (Merck). The mixture was then transferred into a quartz vessel in a microwave reactor (Anton Paar Synthos 3000 multi-mode reactor, 1400 W magnetron power) equipped with a wireless pressure and temperature sensor. The reactor was operated in the pressure mode using a power of 400 W; the sample temperature was ramped at 10 °C/min to 110 °C and kept constant at this temperature for 2 h, ramp/hold time was 11/120 min while the pressure was maintained at 80 bars throughout the hold period. After cooling the reaction chamber to room temperature, the sample was repeatedly washed with deionized water to remove traces or excess of undeposited MnO<sub>2</sub>. Finally, samples were dried at 60 °C in an electric oven. After drying, the NF-G/MnO<sub>2</sub> composite was tested as electrode for electrochemical capacitor. To estimate the mass of graphene and MnO<sub>2</sub> in the composite, we take note of the mass of materials after each step of the experiment to obtain the NF-G/MnO<sub>2</sub>. Typical the NF-G/MnO<sub>2</sub> composite contains 72 wt.% MnO<sub>2</sub> and 28 wt.% graphene.

### 2.1. Characterization of the samples

The Raman spectra of NF-G and NF-G/MnO<sub>2</sub> composite were recorded using a WITTEC-alpha 300R+ confocal Raman spectrometer (WITTEC GmbH). The excitation source was the 532-nm laser (2.33 eV) through a numerical aperture of 0.9 and 100× magnification. Powder X-ray diffraction (XRD) was recorded using

an XPERT-PRO diffractometer (PANalytical BV, the Netherlands) with theta/theta geometry. Qualitative phase analysis of samples was conducted using the X'pert Highscore search match software. The surface morphology and microstructure of the composite was investigated using the high resolution Zeiss Ultra plus 55 Field emission scanning electron microscope (FE-SEM) operated at 2.0 kV. Transmission electron microscopy (TEM) images were obtained on a JEOL JEM-2100F microscope operated at 200 kV.

The electrochemical properties of the supercapacitor electrodes were studied in a three-electrode configuration system using an Autolab PGSTAT workstation 302 (ECO-CHEMIE) driven by the GPES software. The as-prepared NF-G/MnO<sub>2</sub> served as the working electrode, glassy carbon plate as the counter electrode and Ag/AgCl (3 M KCl) served as the reference electrode and 1 M Na<sub>2</sub>SO<sub>4</sub> was used as the electrolyte. Electrochemical impedance spectroscopy (EIS) was performed in the frequency range of 100 kHz to 10 mHz.

## 3. Results and discussion

The microwave technology has been known to reduce reaction times and increase productivity of materials compared to other conventional available techniques. This technology makes use of two heating mechanisms namely dipolar polarization and ionic conduction. The dipoles in the reaction chamber are involved in the polarization effect, while the charged particles in a reaction chamber (usually ions) contribute to ionic conduction effect [35]. When reaction chamber is irradiated, the dipoles or ions in the sample align themselves in the direction of applied electric field. When the applied field oscillates, the dipole or ion field realigns itself with the alternating electric field thereby losing energy in the form of heat through friction and dielectric loss [36]. The microwave irradiation induces a volumetric heating by direct coupling of microwave energy with the molecules that are present in the reaction chamber. This increases the temperature of the whole liquid volume in the chamber simultaneously, compared with conventionally heating system, where the reaction chamber in contact with the hot vessel walls is heated first [36,37]. Fig. 1 shows the schematic illustration for the fabrication process of NF-G/MnO<sub>2</sub>. The formation of the MnO<sub>2</sub> flower-like structure on NF-G forms as follows: Since microwave-enhanced irradiation is based on efficient interaction of molecules with the electromagnetic waves, the electromagnetic waves couple directly with the molecules of potassium permanganate (KMnO<sub>4</sub>) in the entire reaction vessel. This leads to a rapid rise in temperature and formation of large amount of nuclei in a short time converting aqueous permanganate (MnO<sub>4</sub><sup>-</sup>) to MnO<sub>2</sub>, which is followed by self-assembly of amorphous spheres. Since this process is not limited by the thermal conductivity, but Ostwald ripening process also occurs. In brief smaller particles dissociates while the bigger ones grow into sheet like particles with a lamellar structure, these sheet-like particles tend to curl and assemble forming the flower-like structure [38]. Under a neutral pH condition, the reaction between carbon (graphene) and KMnO<sub>4</sub> is also governed by the following equation [39]:

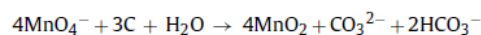


Fig. 2 shows the Raman spectrum of the graphene on the nickel foam which consists of two major peaks at 1580 cm<sup>-1</sup> and 2704 cm<sup>-1</sup>. These peaks correspond to the G and 2D modes of graphene. The intensity of the 2D, the I<sub>2D</sub>/I<sub>G</sub> ratio and the FWHM of 38.8 cm<sup>-1</sup> indicated that graphene consist of mostly few layers. The absence of the D-peak (disorder) at 1350 cm<sup>-1</sup> shows that our graphene is of good quality and low defect density [40]. The Raman spectrum of NF-G/MnO<sub>2</sub> composite showed an additional sharp peak at 649.9 cm<sup>-1</sup> which evidences the deposition of MnO<sub>2</sub> on the graphene foam. This peak and belongs to the A<sub>g</sub> mode arising from

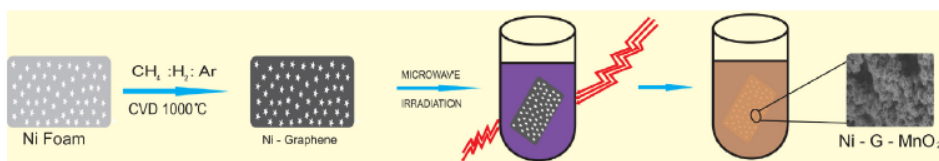


Fig. 1. Schematic illustration for the formation process of nickel foam-graphene/MnO<sub>2</sub> composite (NF-G/MnO<sub>2</sub>).

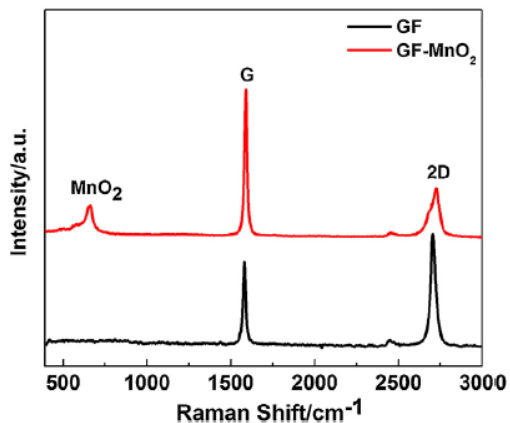


Fig. 2. Raman spectra of (a) nickel foam graphene (b) nickel foam-graphene/MnO<sub>2</sub> composite (NF-G/MnO<sub>2</sub>).

breathing vibrations of MnO<sub>6</sub> octahedral double chains. It also corresponds to the Mn–O stretching vibration mode in the basal plane of MnO<sub>6</sub> octahedral chains [41]. The well-defined Raman spectrum reflects the good crystallinity of the MnO<sub>2</sub> in the composite material. The observed reduction of the 2D peak intensity with respect to G peak is a clear indication of incorporation of MnO<sub>2</sub> as impurity to graphene foam which is due to the interaction of the graphene with MnO<sub>2</sub> [42].

The crystallographic structure of the composite was determined by XRD. Fig. 3 shows XRD patterns of NF-G and NF-G/MnO<sub>2</sub>. The two very strong XRD peaks recorded at 52.1° and 60.9° originate from Ni and could be assigned to the (1 1 1), (2 0 0) phase of nickel. The diffraction peak of the MnO<sub>2</sub> on NF-G is broad with very low intensity signal resulting from small average crystallite domain size of MnO<sub>2</sub>. The low intensity peaks is due to the fact that very strong signal intensities peaks originating from nickel foam overlaps and suppress that of graphene and MnO<sub>2</sub>. Fig. 3(b) is the EDX of the sample which shows the presence of manganese in the sample with little traces of potassium which likely comes from unreacted or residual KMnO<sub>4</sub> used as MnO<sub>2</sub> precursor.

Fig. 4(a) shows the FE-SEM micrograph of the nickel foam alone exhibiting three-dimensional porous network. Inset to the figure is the EDX spectra of the NF which shows elemental composition of the foam revealing the presence of nickel. Fig. 4(b) shows the image of graphene on the nickel foam. The graphene grows on the template material (NF) mimicking the three-dimensional porous network structure of the nickel-foam. Inset to this figure is the high magnification which shows the presence of graphene. It reveals that the graphene consists of wrinkles and ripples which is due to the different thermal expansion coefficients of Ni and graphene during the CVD synthesis [43]. This structure can be an excellent substrate for incorporation of oxide materials for electrochemical applications. Fig. 4(c)–(e) shows FE-SEM micrographs of NF-G/MnO<sub>2</sub> at different magnifications. It can be seen that the MnO<sub>2</sub> particles uniformly coat the whole surface of the NF-G thus exhibiting a porous

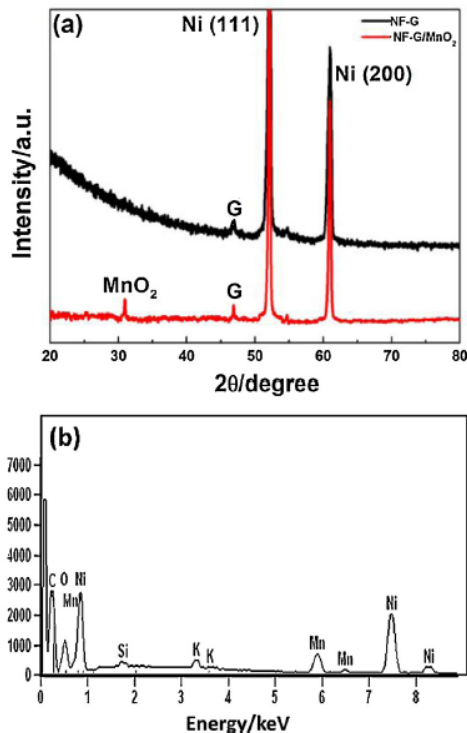


Fig. 3. (a) XRD patterns of nickel foam graphene and nickel foam-graphene/MnO<sub>2</sub> composite (b) EDX pattern of nickel foam-graphene/MnO<sub>2</sub>.

and continuous electroconducting network structure. This unique structure or morphology makes it useful in electrochemical capacitors when ions are adsorbed onto the surface of the samples thereby leading to improved capacitance behavior. It also provides a very good electrode–electrolyte interface for exchange of ions from the electrolyte. Fig. 4(d) reveals a high dense nanostructure of MnO<sub>2</sub> anchored onto the NF-G surface, while Fig. 4(e) shows that the nanostructured MnO<sub>2</sub> has a flower like structure that was formed by the self-assembly of nanosheets during the synthesis process [44]. Fig. 4(f) presents TEM images of NF-G/MnO<sub>2</sub> composite confirming the porous nature of the flower-like nanostructure shown in the SEM images.

Fig. 5(a) compares the CV of the NF and NF-G at a scan rate of 10 mV s<sup>-1</sup> and it can be clearly seen that the capacitance performance of the NF is negligible when compared with that of the NF-G. The CV of NF-G shows two redox peaks due to the Ni<sup>2+</sup>/Ni<sup>3+</sup> redox process arising from the nickel foam [45]. Fig. 5(b) shows the discharge curve of NF-G at a current density of 1 A g<sup>-1</sup> the curve displays a non-linear behavior indicating a pseudocapacitive effect. Fig. 6(a) shows the NF-G/MnO<sub>2</sub> CV curves at different scan rates, showing a relatively rectangular shape, which is a characteristic of an ideal capacitive behavior. The distortions from a perfect

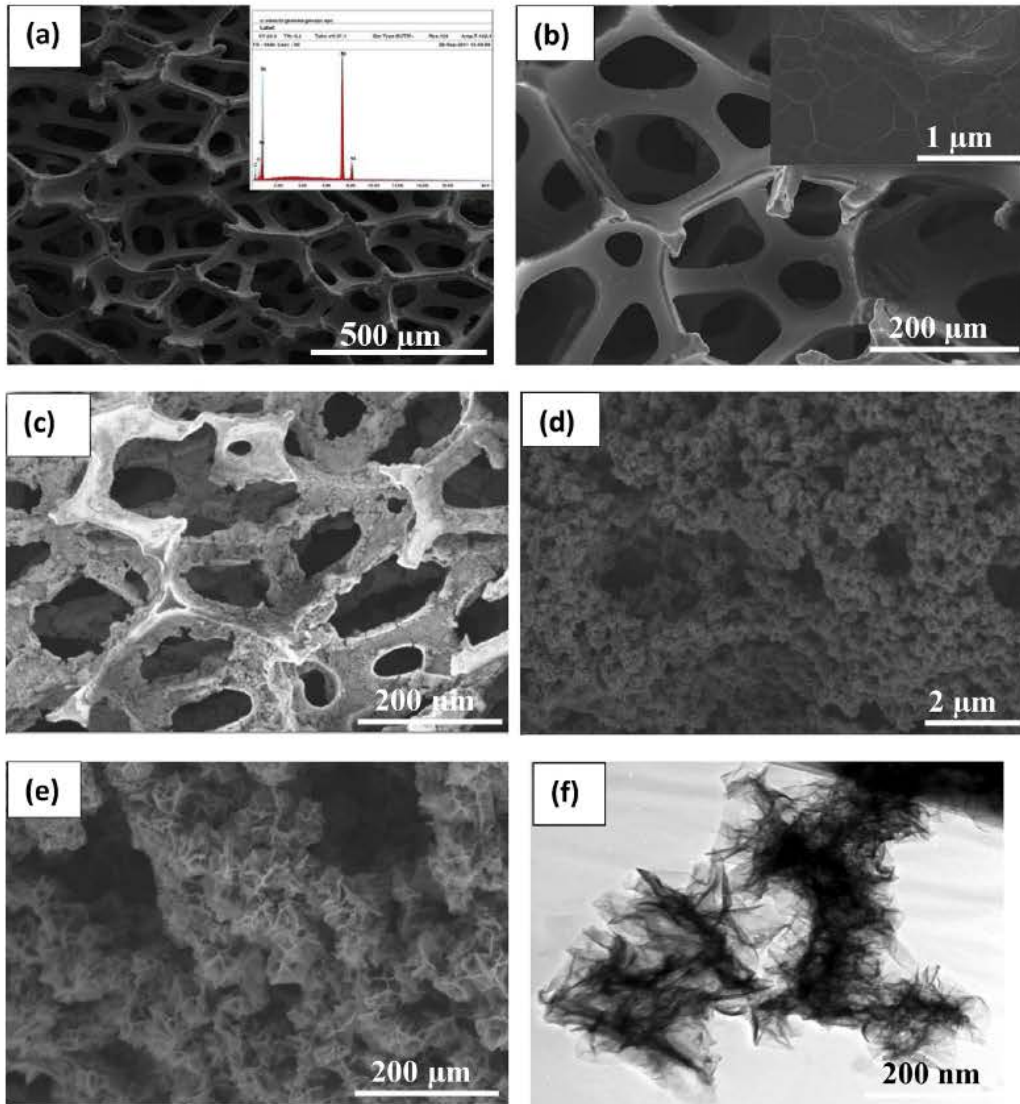


Fig. 4. SEM micrographs of (a and b) nickel foam-graphene (NF-G) at different magnifications, (c–e) nickel foam-graphene coated with MnO<sub>2</sub> (NF-G/MnO<sub>2</sub>) at different magnifications and 4 (f) TEM of the graphene foam/MnO<sub>2</sub> composite.

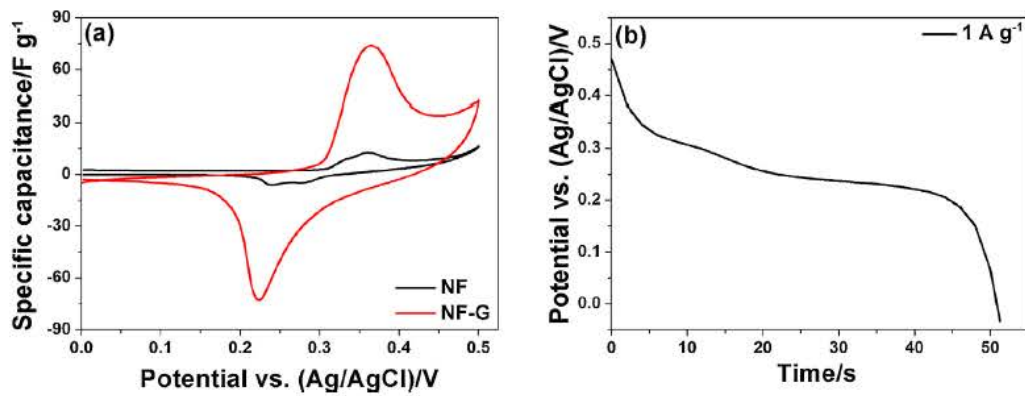


Fig. 5. (a) Cyclic voltammetry curves of NF and NF-G composite at scan rate of 10 mV s<sup>-1</sup>. (b) The discharge curve of NF-G at a current density of 1 A g<sup>-1</sup>.

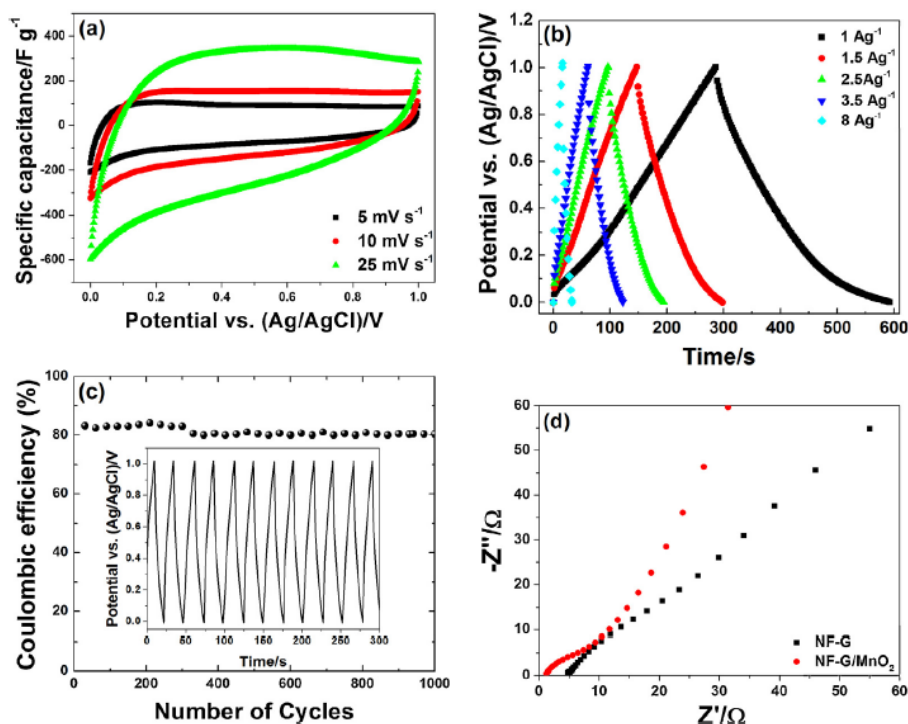


Fig. 6. Electrochemical results for NF-G/MnO<sub>2</sub> composite. (a) Cyclic voltammograms of NF-G/MnO<sub>2</sub> composite measured at different scan rates. (b) The galvanostatic charge-discharge curve at different current densities. (c) The Coulombic efficiency of the composite at a current density of 2.5 A g<sup>-1</sup> (the inset to the figure shows the continuous charge-discharge curve) and (d) EIS plot of both NF-G and NF-G/MnO<sub>2</sub>.

rectangular geometry demonstrate pseudocapacitive effects and contribution from MnO<sub>2</sub>. The figure also indicated that the composite electrodes exhibit good electrochemical reversibility between 0 and 1 V. Fig. 6(b) shows the galvanostatic charge-discharge curves of the NF-G/MnO<sub>2</sub> composite at different current densities. It can be observed that the NF-G/MnO<sub>2</sub> curves are almost linear and symmetrical, which is a typical characteristic of an ideal capacitor behavior. The specific capacitance ( $C_s$ ) and Coulombic efficiency ( $\epsilon$  also referred to as Faradaic or current efficiency) values were calculated from the charge-discharge curve using the following equations:

$$C_s = \frac{i \times \Delta T}{\Delta V \times m} \quad (2)$$

$$\epsilon = \frac{\Delta t_{\text{discharge}}}{\Delta t_{\text{charge}}} \times 100\% \quad (3)$$

where  $i$  is the current applied,  $\Delta T$  is the discharge time and  $\Delta V$  is voltage applied,  $m$  is the mass of active electrode material. Specific capacitances values of 305, 226, 222 and 211 F g<sup>-1</sup> were obtained at a current density of 1, 1.5, 2.5 and 3.5 A g<sup>-1</sup>. The specific capacitance value in this present work is low compared to the values reported by Zhao et al. [25], this may be due presence of potassium or other impurities in composite which may limit the redox efficiency. An optimum, impurity-free composite should give higher capacitance. However, here we have been able to demonstrate the feasibility of using nickel foam as a direct template for synthesis of 3D conducting porous graphene and subsequently loading it with crystalline MnO<sub>2</sub> rather than going through the process of chemical method for production of graphene oxide before finally reducing to the graphene which normally introduces defects in the samples and often leads to inferior electronic properties.

Fig. 6(c) shows that the galvanostatic cycling performance of the composite was found to be stable, with cycle efficiency (Coulombic efficiency) of about 80% for 1000 charge/discharge cycles which demonstrate the excellent stability and performance of the electrode. The improved electrochemical performance of NF-G/MnO<sub>2</sub> as compared to NF-G, is due to the synergistic effect between graphene and MnO<sub>2</sub> leading to improved conductivity of the composite. Also the 3D porous network structure of the nickel foam helps to provide easy access to ions from the electrolyte at the electrode/electrolyte interface.

The electrochemical impedance spectroscopy (Nyquist) plot of NF-G and NF-G/MnO<sub>2</sub> is shown in Fig. 6(d). It is a representation of the real and imaginary part of the impedance of the electrode material. It is worth stating that for ideal supercapacitors, the Nyquist plot should be a line perpendicular to the real axis at low frequency. From the Nyquist plot of NF-G/MnO<sub>2</sub>, we observe that it is much closer to the ideal behavior which might be attributed to the low charge transfer of graphene and MnO<sub>2</sub>; thus indicating a better capacitive behavior.

#### 4. Conclusions

This work has demonstrated the possibility of using hydrothermal microwave irradiation in synthesis of novel functional materials for high performance electrochemical applications. NF-G was synthesized using chemical vapor deposition (CVD). The 3D porous network structure of the NF-G allows for a uniform coating and efficient loading of MnO<sub>2</sub> through the hydrothermal microwave irradiation to form NF-G/MnO<sub>2</sub> composite. Raman spectroscopy, SEM and TEM reveal that high quality and defect free samples were synthesized by CVD system. Electrochemical investigation indicated that the NF-G/MnO<sub>2</sub> had a maximum capacitance

of  $305 \text{ F g}^{-1}$ . The uniform adsorption of  $\text{MnO}_2$  nanostructures onto the surface of NF-G provides a much larger surface area for reaction during electrochemical process, leading to the effective utilization of the electrode material. The electrode material also exhibits excellent performance and rate capability which is due to efficient charge transfer and ion diffusion in the porous network of the composite. The work shows that pseudocapacitance can be effectively loaded onto the surface of NF-G via microwave irradiation and has potential for high performance supercapacitor application.

### Acknowledgements

This work is based upon research supported by the South African Research Chairs Initiative of the Department of Science and Technology (SARCHI-DST) and the National Research Foundation (NRF). Any opinion, findings and conclusions or recommendations expressed in this work are those of authors and therefore the NRF and DST do not accept any liability with regard thereto. A. Bello, M. Fabiane, and O.O. Fashedemi acknowledge financial support from University of Pretoria and NRF for PhD bursaries.

### References

- [1] B.E. Conway, *Electrochemical Supercapacitors Scientific Fundamentals and Technological Applications*, Kluwer Academic/Plenum Publishers, 1999.
- [2] R. Kötz, Principles and applications of electrochemical capacitors, *Electrochim. Acta* 45 (2000) 2483–2498.
- [3] X. Zhao, B.M. Sánchez, P.J. Dobson, P.S. Grant, The role of nanomaterials in redox-based supercapacitors for next generation energy storage devices, *Nanoscale* 3 (2011) 839–855.
- [4] P.J. Hall, M. Mirzaei, S.I. Fletcher, F.B. Sillars, A.J.R. Rennie, G.O. Shitta-Bey, G. Wilson, A. Cruden, R. Carter, Energy storage in electrochemical capacitors: designing functional materials to improve performance, *Energy Environ. Sci.* 3 (2010) 1238–1251.
- [5] E. Frackowiak, Carbon materials for supercapacitor application, *Phys. Chem. Chem. Phys.* 9 (2007) 1774–1785.
- [6] A. Burke, R&D considerations for the performance and application of electrochemical capacitors, *Electrochim. Acta* 53 (2007) 1083–1091.
- [7] E. Frackowiak, F. Béguin, Carbon materials for the electrochemical storage of energy in capacitors, *Carbon* 39 (2001) 937–950.
- [8] D. Villers, D. Jobin, C. Soucy, D. Cossement, R. Chahine, L. Breaud, D. Be' langer, The influence of the range of electroactivity and capacitance of conducting polymers on the performance of carbon conducting polymer hybrid supercapacitor, *J. Electrochem. Soc.* 150 (2003) A747–A752.
- [9] F. Fusalba, H.A. Ho, L. Breaud, D. Be, Poly(cyano-substituted diheteroareneethylene) as active electrode material for electrochemical supercapacitors, *Chem. Mater.* 12 (2000) 2581–2589.
- [10] P. Simon, Y. Gogotsi, Materials for electrochemical capacitors, *Nat. Mater.* 7 (2008) 845–854.
- [11] L.L. Zhang, X.S. Zhao, Carbon-based materials as supercapacitor electrodes, *Chem. Soc. Rev.* 38 (2009) 2520–2531.
- [12] A.K. Geim, K.S. Novoselov, The rise of graphene, *Nat. Mater.* (2007) 183–191.
- [13] K.S. Novoselov, A.K. Geim, S.V. Morozov, D. Jiang, M.I. Katsnelson, I.V. Grigorieva, S.V. Dubonos, A.A. Firsov, Two-dimensional gas of massless Dirac fermions in graphene, *Nature* 438 (2005) 197–200.
- [14] K.S. Novoselov, A.K. Geim, S. Morozov, Electric field effect in atomically thin carbon films, *Science* 306 (2004) 666–669.
- [15] M.D. Stoller, S. Park, Y. Zhu, J. An, R.S. Ruoff, Graphene-based ultracapacitors, *Nano Lett.* 8 (2008) 3498–3502.
- [16] Y. Wang, Z. Shi, Y. Huang, Y. Ma, C. Wang, M. Chen, Y.S. Chen, Supercapacitor devices based on graphene materials, *J. Phys. Chem. C* 113 (2009) 13103–13107.
- [17] C. Liu, Z. Yu, D. Neff, A. Zhamu, B.Z. Jang, Graphene-based supercapacitor with an ultrahigh energy density, *Nano Lett.* 10 (2010) 4863–4868.
- [18] Y. Zhu, S. Murali, W. Cai, X. Li, Graphene and graphene oxide: synthesis, properties, and applications, *Adv. Mater.* 22 (2010) 3906–3924.
- [19] Y. Sun, Q. Wu, G. Shi, Graphene based new energy materials, *Energy Environ. Sci.* 4 (2011) 1113–1132.
- [20] S. Guo, S. Dong, Graphene nanosheet: synthesis, molecular engineering, thin film, hybrids, and energy and analytical applications, *Chem. Soc. Rev.* 40 (2011) 2644–2672.
- [21] T.Y. Kim, H.W. Lee, M.D. Stoller, D.R. Dreyer, C.W. Bielawski, R.S. Ruoff, K.S. Suh, High-performance supercapacitors based on poly(ionic liquid)-modified graphene electrodes, *ACS Nano* 5 (2011) 436–442.
- [22] X. Zhang, X. Sun, Y. Chen, D. Zhang, Y. Ma, One-step solvothermal synthesis of graphene/ $\text{Mn}_3\text{O}_4$  nanocomposites and their electrochemical properties for supercapacitors, *Mater. Lett.* 68 (2012) 336–339.
- [23] W. Wei, X. Cui, W. Chen, D.G. Ivey, Manganese oxide-based materials as electrochemical supercapacitor electrodes, *Chem. Soc. Rev.* 40 (2011) 1697–1721.
- [24] J. Liu, J. Essner, J. Li, Hybrid supercapacitor based on coaxially coated manganese oxide on vertically aligned carbon nanofiber arrays, *Chem. Mater.* 22 (2010) 5022–5030.
- [25] Y.-Q. Zhao, D.-D. Zhao, P.-Y. Tang, Y.-M. Wang, C.-L. Xu, H.-L. Li,  $\text{MnO}_2$ /graphene/nickel foam composite as high performance supercapacitor electrode via a facile electrochemical deposition strategy, *Mater. Lett.* 76 (2012) 127–130.
- [26] S. Chen, J. Zhu, X. Wu, Q. Han, X. Wang, Graphene oxide– $\text{MnO}_2$  nanocomposites for supercapacitors, *ACS Nano* 4 (2010) 2822–2830.
- [27] Y. Chen, Y. Zhang, D. Geng, R. Li, H. Hong, J. Chen, X. Sun, One-pot synthesis of  $\text{MnO}_2$ /graphene/carbon nanotube hybrid by chemical method, *Carbon* 49 (2011) 4434–4442.
- [28] J. Yan, Z. Fan, T. Wei, W. Qian, M. Zhang, F. Wei, Fast and reversible surface redox reaction of graphene– $\text{MnO}_2$  composites as supercapacitor electrodes, *Carbon* 48 (2010) 3825–3833.
- [29] H. Gao, F. Xiao, C.B. Ching, H. Duan, High-performance asymmetric supercapacitor based on graphene hydrogel and nanostructured  $\text{MnO}_2$ , *ACS Appl. Mater. Interfaces* 4 (2012) 2801–2810.
- [30] G. Yu, L. Hu, M. Vosgueritchian, H. Wang, X. Xie, J.R. McDonough, X. Cui, Y. Cui, Z. Bao, Solution-processed graphene/ $\text{MnO}_2$  nanostructured textiles for high-performance electrochemical capacitors, *Nano Lett.* 11 (2011) 2905–2911.
- [31] Q. Cheng, J. Tang, J. Ma, H. Zhang, N. Shinya, L.-C. Qin, Graphene and nanostructured  $\text{MnO}_2$  composite electrodes for supercapacitors, *Carbon* 49 (2011) 2917–2925.
- [32] Z. Li, J. Wang, S. Liu, X. Liu, S. Yang, Synthesis of hydrothermally reduced graphene/ $\text{MnO}_2$  composites and their electrochemical properties as supercapacitors, *J. Power Sources* 196 (2011) 8160–8165.
- [33] Y. Qian, S. Lu, F. Gao, Preparation of  $\text{MnO}_2$ /graphene composite as electrode material for supercapacitors, *J. Mater. Sci.* 46 (2011) 3517–3522.
- [34] A. Bello, K. Makgopa, M. Fabiane, D. Dodoo-Ahrin, K.I. Ozoemena, N. Manyala, Chemical adsorption of NiO nanostructures on nickel foam–graphene for supercapacitor applications, *J. Mater. Sci.* 48 (2013) 6707–6712.
- [35] M. Baghbanzadeh, L. Carbone, P.D. Cozzoli, C.O. Kappe, Microwave-assisted synthesis of colloidal inorganic nanocrystals, *Angew. Chem.* 50 (2011) 11312–11359.
- [36] C. Oliver Kappe, Microwave dielectric heating in synthetic organic chemistry, *Chem. Soc. Rev.* 37 (2008) 1127–1139.
- [37] C.O. Kappe, How to measure reaction temperature in microwave-heated transformations, *Chem. Soc. Rev.* 42 (2013) 4977–4990.
- [38] Y. Li, J. Wang, Y. Zhang, M.N. Banis, J. Liu, D. Geng, R. Li, X. Sun, Facile controlled synthesis and growth mechanisms of flower-like and tubular  $\text{MnO}_2$  nanostructures by microwave-assisted hydrothermal method, *J. Colloid Interface Sci.* 369 (2012) 123–128.
- [39] X. Jin, W. Zhou, S. Zhang, G.Z. Chen, Nanoscale microelectrochemical cells on carbon nanotubes, *Small* 3 (2007) 1513–1517.
- [40] A.C. Ferrari, Raman spectroscopy of graphene and graphite: disorder, electron–phonon coupling, doping and nonadiabatic effects, *Solid State Commun.* 143 (2007) 47–57.
- [41] T. Gao, H. Fjellvåg, P. Norby, A comparison study on Raman scattering properties of  $\alpha$ - and  $\beta$ - $\text{MnO}_2$ , *Anal. Chim. Acta* 648 (2009) 235–239.
- [42] Z. Ni, T. Yu, Z. Luo, Y. Wang, L. Liu, Probing charged impurities in suspended graphene using Raman spectroscopy, *ACS Nano* 3 (2009) 569–574.
- [43] S.J. Chae, F. Gunes, K.K. Kim, E.S. Kim, G.H. Han, S.M. Kim, H.-J. Shin, S.-M. Yoon, J.-Y. Choi, M.H. Park, C.W. Yang, D. Pribat, Y.H. Lee, Synthesis of large-area graphene layers on poly-nickel substrate by chemical vapor deposition: wrinkle formation, *Adv. Mater.* 21 (2009) 2328–2333.
- [44] H. Chen, J. He, C. Zhang, H. He, Self-assembly of novel mesoporous manganese oxide nanostructures and their application in oxidative decomposition of formaldehyde, *J. Phys. Chem. C* 111 (2007) 18033–18038.
- [45] L.-R. Zhang, J. Zhao, M. Li, H.-T. Ni, J.-L. Zhang, X.-M. Feng, Y.-W. Ma, Q.-L. Fan, X.-Z. Wang, Z. Hu, W. Huang, Preparation of graphene supported nickel nanoparticles and their application to methanol electrooxidation in alkaline medium, *New J. Chem.* 36 (2012) 1108–1113.

## Summary

Flower-like manganese oxide ( $\text{MnO}_2$ ) nanostructures have been grown directly on NF-G by hydrothermal microwave irradiation (MW). The decomposition of permanganate ( $\text{MnO}_4^-$ ) to form  $\text{MnO}_2$  and the formation mechanism of the flower-like structure have all been examined. This composite combines both the Faradaic (Graphene) and non-Faradaic (manganese oxide) properties offered by the individual materials and thus demonstrated a reasonable electrochemical performance with a specific capacitance of  $305 \text{ F g}^{-1}$  at a current density of  $1 \text{ A g}^{-1}$  and excellent stability with about 80 % Coulombic efficiency after 1000 charge/discharge cycles. These result shows that MW technology could be an efficient method for synthesis of composite material for improved electrochemical applications.

## References

- [1] B.E. Conway, *Electrochemical Supercapacitors Scientific Fundamentals and Technological Applications* 1999.
- [2] P. Simon, Y. Gogotsi, *Nat. Mater.* **7** (2008) 845.
- [3] J. Wei, N. Nagarajan, I. Zhitomirsky, *J. Mater. Pro. Techn.* **186** (2007) 356.
- [4] J-K. Chang, Y-L. Chen, W-T. Tsai, *J. Power Sources* **135** (2004) 344.
- [5] V. Subramanian, H. Zhu, B. Wei, *Chem. Phys. Lett.* **453** (2008) 242.
- [6] W. Wei, X. Cui, W. Chen, D.G. Ivey, *Chem. Soc. Rev.* **40** (2011) 1697.
- [7] S.W. Donne, A.F. Hollenkamp, B.C. Jones, *J. Power Sources* **195** (2010) 367.
- [8] C. Xu, F. Kang, B. Li, H. Du, *J. Mater. Res.* **25** (2010) 1421.
- [9] H. Gao, F. Xiao, C.B. Ching, H. Duan, *ACS Appl. Mater. & Inter.* **4** (2012) 2801.
- [10] Q. Cheng, J. Tang, J. Ma, H. Zhang, N. Shinya, L-C. Qin, *Carbon* **49** (2011) 2917.
- [11] J. Zhu, J. He, *ACS Appl. Mater. & Inter.* **4** (2012) 1770.
- [12] G. Yu, L. Hu, M. Vosgueritchian, H. Wang, X. Xie, J.R. McDonough, X. Cui, Y. Cui, Z. Bao, *Nano Letters* **11** (2011) 2905.
- [13] B.G. Choi, M. Yang, W.H. Hong, J.W. Choi, Y.S. Huh, *ACS Nano* **6** (2012) 4020.
- [14] X. Dong, X. Wang, J. Wang, H. Song, X. Li, L. Wang, M.B. Chan-Park, C.M. Li, P. Chen, *Carbon* **50** (2012) 4865.
- [15] Y-Q. Zhao, D-D. Zhao, P-Y. Tang, Y-M. Wang, C-L. Xu, H-L. Li, *Mater. Lett.* **76** (2012) 127.
- [16] C.O. Kappe, *Chem. Soc. Rev.* **42** (2013) 4977.
- [17] M. Baghbanzadeh, L. Carbone, P.D. Cozzoli, C.O. Kappe, *Ange. Chem.* **50** (2011) 11312.

## 4.5 Symmetric electrochemical capacitor based on graphene foam (GF) and manganese oxide (MnO<sub>2</sub>)

### Introduction

In this section I employed a chemical means (reflux technique) to produce a composite of GF/MnO<sub>2</sub>. This technique involves the condensation of vapor and the return of this condensate to the system from which it originated. This has aroused considerable interest for the production of nanostructured oxide materials for electrochemical and catalytic applications [1–4]. This method has the advantages of low-temperature processing and has similar growth mechanism as the microwave technology already discussed in section 4.4. In reflux method, the formation of MnO<sub>2</sub> films is the result of primary crystallization process [5]. Under conventional heating and stirring conditions, the particles undergo coalescence followed by Ostwald ripening to larger uniform crystals, which self-assemble randomly to transform into rod like structures [6–8].

The incorporation of MnO<sub>2</sub> into the three dimensional (3D) porous structure of GF is expected to prevent agglomeration of graphene sheets and also improve electrolyte-electrode accessibility. Symmetric supercapacitors were fabricated from the composite material and tested in a two-electrode configuration because it is a more realistic approach suitable for evaluating the performance of electrochemical test cells, as it imitates the physical properties such as internal voltages and charge transfer processes that occur in real life applications and thus provide the best indication of an electrode material's performance [9]. Detailed descriptions of the production of GF and formation mechanism of MnO<sub>2</sub> have been discussed in sections 4.1 and 4.4. A detailed publication discussing the results obtained is attached below.

## Results and discussions: Publication 5, High-performance symmetric electrochemical capacitor based on graphene foam and nanostructured manganese oxide

AIP ADVANCES 3, 082118 (2013)



### High-performance symmetric electrochemical capacitor based on graphene foam and nanostructured manganese oxide

Abdulahakeem Bello,<sup>1</sup> Omobosedo O. Fashedemi,<sup>2</sup> Joel N. Lekitima,<sup>2</sup> Mopeli Fabiane,<sup>1</sup> David Dodoo-Arhin,<sup>1</sup> Kenneth I. Ozoemena,<sup>2,3</sup> Yury Gogotsi,<sup>4</sup> Alan T. Charlie Johnson,<sup>5</sup> and Ncholu Manyala<sup>1,a</sup>

<sup>1</sup>Department of Physics, Institute of Applied Materials, SARChI Chair in Carbon Technology and Materials, University of Pretoria, Pretoria 0028, South Africa

<sup>2</sup>Department of Chemistry, University of Pretoria, Pretoria 0028, South Africa

<sup>3</sup>Energy Materials, Materials Science and Manufacturing, Council for Scientific and Industrial Research (CSIR), Pretoria 0001, South Africa

<sup>4</sup>Department of Materials and Engineering, and A.J Drexel Nanotechnology Institute Drexel University, 3114 Chestnut Street, PA 19104, USA

<sup>5</sup>Department of Physics and Astronomy, University of Pennsylvania, Philadelphia, Pennsylvania 19104, USA

(Received 2 July 2013; accepted 12 August 2013; published online 21 August 2013)

We have fabricated a symmetric electrochemical capacitor with high energy and power densities based on a composite of graphene foam (GF) with ~80 wt% of manganese oxide (MnO<sub>2</sub>) deposited by hydrothermal synthesis. Raman spectroscopy and X-ray diffraction measurements showed the presence of nanocrystalline MnO<sub>2</sub> on the GF, while scanning and transmission electron microscopies showed needle-like manganese oxide coated and anchored onto the surface of graphene. Electrochemical measurements of the composite electrode gave a specific capacitance of 240 Fg<sup>-1</sup> at a current density of 0.1 Ag<sup>-1</sup> for symmetric supercapacitors using a two-electrode configuration. A maximum energy density of 8.3 Whkg<sup>-1</sup> was obtained, with power density of 20 kWkg<sup>-1</sup> and no capacitance loss after 1000 cycles. GF is an excellent support for pseudo-capacitive oxide materials such as MnO<sub>2</sub>, and the composite electrode provided a high energy density due to a combination of double-layer and redox capacitance mechanisms. © 2013 Author(s). All article content, except where otherwise noted, is licensed under a Creative Commons Attribution 3.0 Unported License. [<http://dx.doi.org/10.1063/1.4819270>]

#### I. INTRODUCTION

Electric double-layer capacitors (EDLCs) are charge-storage devices with a high power density, long cyclic life and low maintenance cost.<sup>1-4</sup> They fill the gap between batteries (high energy density) and electrolytic capacitors (high power density).<sup>5,6</sup> Such properties make them potentially useful for a wide range of applications such as hybrid vehicles, cordless electric tools, memory back-up, cellular phones, medical devices, military and consumer electronics.<sup>7</sup>

Nevertheless, the energy stored in supercapacitors (<10 Whkg<sup>-1</sup>) is low compared to lithium ion batteries (>100 Whkg<sup>-1</sup>). This has imposed significant challenges in employing supercapacitors as primary power source for battery replacement.<sup>8,9</sup> However, the performance of these devices depends on the type, properties and morphologies of the materials being used. Therefore much attention has been given to developing novel nanostructured materials with high specific surface area (SSA), controlled pore size distribution, increased operating voltage and comprehensive understanding of electrode/electrolyte interfaces at the nanoscale.<sup>2,10-12</sup> This led to many research

<sup>a</sup>Author to whom correspondence should be addressed: Electronic mail: [ncholu.manyala@up.ac.za](mailto:ncholu.manyala@up.ac.za) (N. Manyala)

activities focused on developing electrode materials for supercapacitors that are capable of storing more energy without sacrificing cyclic life and power density. Pseudocapacitors are energy storage devices that undergo electron transfer reactions.<sup>13</sup> An example of such pseudocapacitive materials is manganese oxide (MnO<sub>2</sub>). MnO<sub>2</sub> has attracted much attention as an electrode material because of its multiple reversible electrochemical reactions, natural abundance, low cost, and environmental compatibility.<sup>14–16</sup> However, due to the low electrical conductivity of MnO<sub>2</sub>, the rate capability and performance of MnO<sub>2</sub> electrodes is limited, which has hindered its potential application. The redox activity, capacitive performance and utilization of MnO<sub>2</sub> can be increased by adding conductive materials, such as carbon nanotubes,<sup>17,18</sup> conducting polymers<sup>19,20</sup> or graphene.<sup>21,22</sup> Different morphologies and shapes of the MnO<sub>2</sub> particles have also been reported; for example, nano-whiskers have been shown to have excellent electrochemical properties because of their large surface area.<sup>23</sup>

Graphene has been explored for electrochemical storage applications due to its high specific surface area, high electrical conductivity, chemical stability and excellent mechanical properties.<sup>24,25</sup> Graphene also offers a suitable platform for accommodating metal oxides. This is attributed to its large surface area, which allows for uniform loading and binding sites for incorporation of the metal oxide materials such as MnO<sub>2</sub>. Also, the high conductivity of the graphene significantly improves the conductivity of the composite electrode.

Recently, Chen *et al.*<sup>26</sup> reported a three-dimensional (3D) flexible and conducting interconnected graphene network formed using chemical vapour deposition onto a catalytic nickel foam template. Graphene foam provides a desirable combination of a highly conductive network<sup>27,28</sup> and a high porosity support structure that is suitable for incorporation of nanoparticles or other fillers to occupy the pores for electrochemical applications.<sup>29,30</sup>

Several studies have reported on synthesis of various graphene foam/MnO<sub>2</sub> (GF/MnO<sub>2</sub>) nanocomposites using chemical synthesis,<sup>31</sup> microwave irradiation,<sup>32</sup> electrodeposition,<sup>33</sup> redox deposition<sup>34</sup> and polymer-assisted chemical reduction.<sup>35</sup> Recently, Dong *et al.*<sup>36</sup> reported a simple synthesis for 3D hybrid structures of MnO<sub>2</sub> on graphene foam in which the morphology of the MnO<sub>2</sub> nanostructures was controlled by the acidity of the solution. The large specific surface area of GF ensured a large loading capacity for MnO<sub>2</sub> nanostructures and a large active surface area for rapid charge transfer and a large double layer capacitance. They also showed that graphene-metal oxides composites offered good adhesion for the metal oxide particles, which prevented detachment and agglomeration, thereby leading to improved capacitance in the three electrode configuration.

In this study, we report on a symmetric electrochemical capacitor fabricated using GF/MnO<sub>2</sub> nanostructure composite electrodes based on a nickel foam current collector. Hydrothermal synthesis of MnO<sub>2</sub> on graphene was performed with the goal of combining double-layer and redox capacitance for achieving high energy and power densities in one device.

## II. EXPERIMENTAL SECTION

### A. Synthesis of graphene foam/MnO<sub>2</sub> composite

Graphene foam (GF) was synthesised by chemical vapour deposition (CVD) onto a catalytic nickel foam (Alantum Innovations in Alloy Foam Munich, Germany). The detailed procedure is described in our previous report.<sup>37</sup> To provide mechanical support for the GF during etching of nickel, polymethylmethacrylate (PMMA) was drop coated on the sample and baked at 180 °C for 30 minutes. The samples were then placed in 3 M HCl solution at 80 °C for 5 hours to ensure that nickel was completely etched away. The resulting GF sample was placed in acetone at 50 °C for 30 minutes to remove the PMMA. The samples were then rinsed in deionised water and dried.

GF/MnO<sub>2</sub> composites were prepared using a hydrothermal reduction technique. Typically, 15 mg of GF was dispersed in 50 mL of 0.02 M KMnO<sub>4</sub> (Merck), and the mixture was refluxed at 150 °C for 48 hours with continuous magnetic stirring. The resultant dispersion was then centrifuged and washed several times with deionized water, and finally dried at 60 °C in an oven. All chemicals used were of analytical grade and used as received. Deionized water was used throughout the synthesis process.

## B. Physical characterization of composite

Raman spectra of GF/MnO<sub>2</sub> composites were recorded using a WiTec-alpha 300R+ confocal Raman spectrometer (WiTec GmbH) with the laser power of 1.5 mW in order to minimize heating effects. The excitation source was a 532-nm laser through a numerical aperture of 0.9 and 100× magnification. The GF/MnO<sub>2</sub> composite crystal structure was characterized using powder X-ray diffraction (XRD). An XPERT-PRO diffractometer PANalytical BV, Netherlands with theta/theta geometry, operating a cobalt tube at 35 kV and 50 mA was used. The XRD patterns of all specimens were recorded in the 20.0°-80.0° 2θ range with a step size of 0.017° and a counting time of 15.240 seconds per step. Qualitative phase analysis of samples was conducted using the X'pert Highscore search match software. The surface morphology and microstructure of the composite were investigated using a Zeiss Ultra Plus 55 field emission scanning electron microscope (FE-SEM) operated at an accelerating voltage of 2.0 kV, nitrogen gas sorption analysis at 77 K (Micromeritics ASAP 2020) and transmission electron microscopy (TEM) JEOL JEM-2100F microscope operated at 200 kV. Typically, TEM samples were prepared by dispersing the samples in ethanol and dropped on lacey carbon grid for analysis.

## C. Electrochemical characterization

The working electrodes for electrochemical evaluation were prepared by mixing 80 wt.% of GF/MnO<sub>2</sub> with 10 wt. % carbon black and 10 wt. % polyvinylidene difluoride (PVdF) binder in an agate mortar. The mixture was then dissolved in 1-methyl-2-pyrrolidinone (NMP) to form a paste. The paste was coated on the Ni foam as a current collector with a diameter of 16 mm and dried at 60 °C in an oven for 8 hours to ensure complete evaporation of the NMP.

The electrochemical test of the GF/MnO<sub>2</sub> electrode was performed in a three electrode configuration using glassy carbon plate as counter electrode and Ag/AgCl (3 M KCl) as the reference electrode. The symmetric GF/MnO<sub>2</sub>/GF/MnO<sub>2</sub> system was investigated in a two-electrode configuration, with a glass microfiber filter paper as the separator and 1 M Na<sub>2</sub>SO<sub>4</sub> solution serving as the electrolyte in both configurations. The electrochemical properties of the supercapacitor were studied using cyclic voltammetry (CV), galvanostatic charge-discharge (GV) and electrochemical impedance spectroscopy (EIS) using an Autolab PGSTAT workstation 302 (ECO-CHEMIE) driven by the general purpose electrochemical system (GPES) software.

The CV tests were carried out in the potential range of 0 to 1 V at different scan rates ranging from 5 mV/s to 100 mV/s. The galvanostatic charge-discharge measurements were also carried out at different current densities from 0.1 Ag<sup>-1</sup> to 0.5 Ag<sup>-1</sup> and the EIS measurements were performed in the frequency range of 100 kHz-10 mHz. The EIS data were analyzed using Nyquist plots.<sup>1</sup>

The cell capacitance,  $C_{cell}$ , was then calculated from the slope of galvanostatic charge-discharge curves according to the following equation

$$C_{cell} = \frac{i \Delta t}{\Delta v} \quad (1)$$

where  $i$  is the constant current for charge-discharge,  $\Delta t$  is the discharge time and  $\Delta v$  is the discharge voltage. The specific capacitance (per unit mass) was then calculated according to the following equation<sup>38</sup>

$$C_{sp} = \frac{4C_{cell}}{m} \quad (2)$$

where  $m$  is the mass of a single electrodes in the cell.

## III. RESULTS AND DISCUSSIONS

Fig. 1(a) shows the Raman spectrum of the graphene foam, with prominent G and 2D peaks at 1582.2 cm<sup>-1</sup> and 2705.7 cm<sup>-1</sup>, respectively. The relative intensity 2D/G ratio of 1.2 and FWHM of 38.8 cm<sup>-1</sup> were attributed to few layer graphene. The absence of the D-peak (disorder) at 1350 cm<sup>-1</sup> showed that the graphene foam was of good quality, with a low defect density.<sup>40</sup> The Raman spectrum

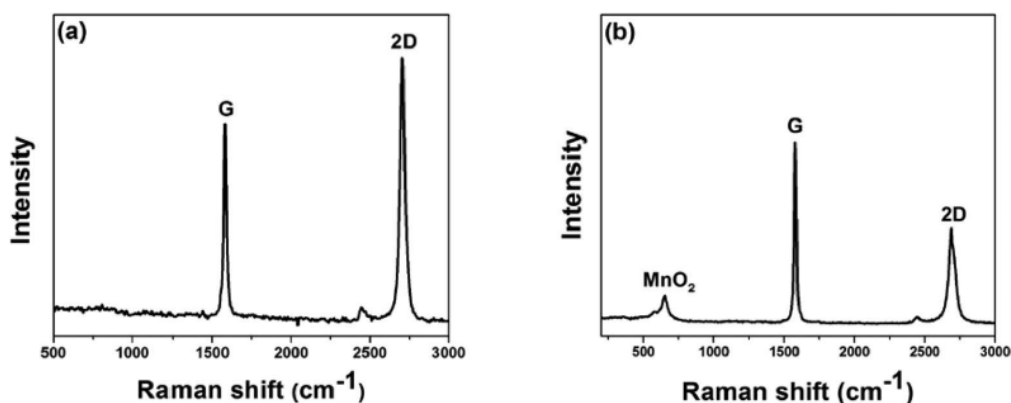


FIG. 1. Raman spectra of (a) graphene foam and (b) graphene foam/MnO<sub>2</sub> composite (GF/MnO<sub>2</sub>).

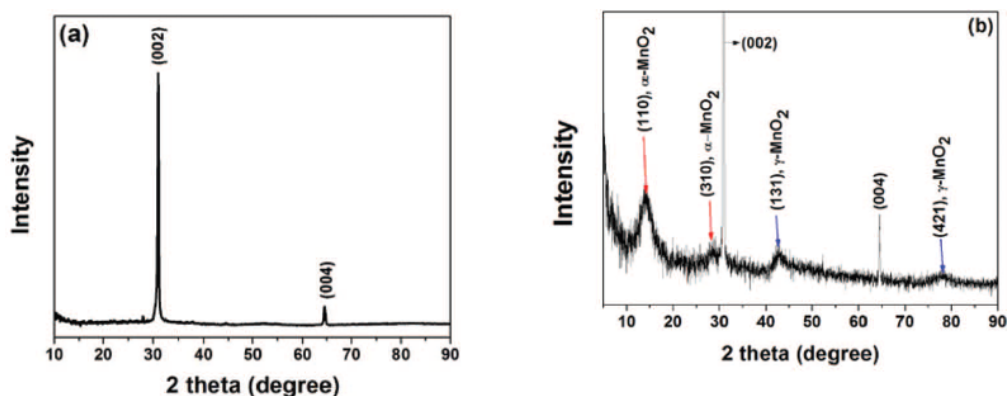


FIG. 2. XRD patterns of (a) graphene foam and (b) graphene foam/MnO<sub>2</sub> composite.

of the GF/MnO<sub>2</sub> composite (Fig. 1(b)) showed an additional sharp peak at 649.9 cm<sup>-1</sup>, which was ascribed to the A<sub>g</sub> mode arising from breathing vibrations of MnO<sub>6</sub> octahedral double chains. It also corresponds to the Mn-O stretching vibration mode in the basal plane of MnO<sub>6</sub> octahedral chains and symmetric stretching vibration Mn-O of MnO<sub>6</sub> groups.<sup>41</sup> The well-defined Raman spectrum reflects the good crystallinity of the MnO<sub>2</sub> in the composite. The observed reduction of the 2D/G intensity ratio after the formation MnO<sub>2</sub> may be due to the introduction of disorder during hydrothermal synthesis or electronic interactions between MnO<sub>2</sub> and GF.<sup>42</sup>

Both XRD patterns had narrow diffraction peaks at  $2\theta = 31^\circ$  and  $64.5^\circ$ , which correspond to the (002) and (004) reflections of hexagonal graphite, respectively. They show that the crystalline order of the CVD-grown multi-layer graphene foam was preserved after formation of the GF/MnO<sub>2</sub> composite. The data for the GF/MnO<sub>2</sub> composite (Fig. 2(b)) showed additional diffraction peaks at  $2\theta = 14.2^\circ$ ,  $28.8^\circ$ ,  $42.8^\circ$ , and  $77.7^\circ$ , which are representative of  $\alpha$  and  $\gamma$  phases of MnO<sub>2</sub>. The diffraction peaks at  $14.2^\circ$  and  $28.8^\circ$  were assigned to the (110) and (310) reflections of  $\alpha$ -MnO<sub>2</sub> phase in accordance with the ICDD PDF card No. 44-0141, while the peaks at  $42.8^\circ$  and  $77.7^\circ$  were assigned to (131) and (421) reflections of  $\gamma$ -MnO<sub>2</sub>,<sup>43</sup> in accordance with the ICDD PDF card No. 14-0644 respectively.

The surface area of both GF and GF/MnO<sub>2</sub> samples were measured using nitrogen gas sorption analysis at 77 K. Typically, the nitrogen adsorption and desorption show type II/IV isotherm as shown in Fig. 3 and the corresponding specific surface area values of 42 m<sup>2</sup>g<sup>-1</sup> and 98 m<sup>2</sup>g<sup>-1</sup> respectively.

SEM analysis showed that the nickel foam's three-dimensional (3D) porous network structure makes it an excellent template for CVD synthesis of a 3D graphene network. The SEM image of GF is shown in Fig. 4(a) after the nickel template was etched away. The GF retained the porous nature of the underlying Ni template, and therefore provided abundant surface binding sites for MnO<sub>2</sub>

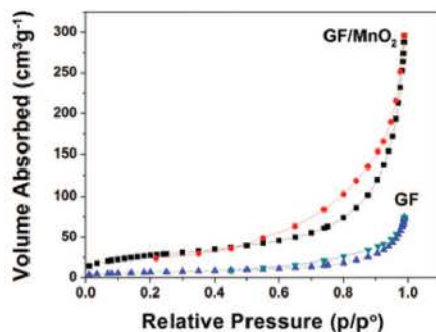


FIG. 3. Nitrogen adsorption and desorption isotherms for GF and GF/MnO<sub>2</sub> composite.

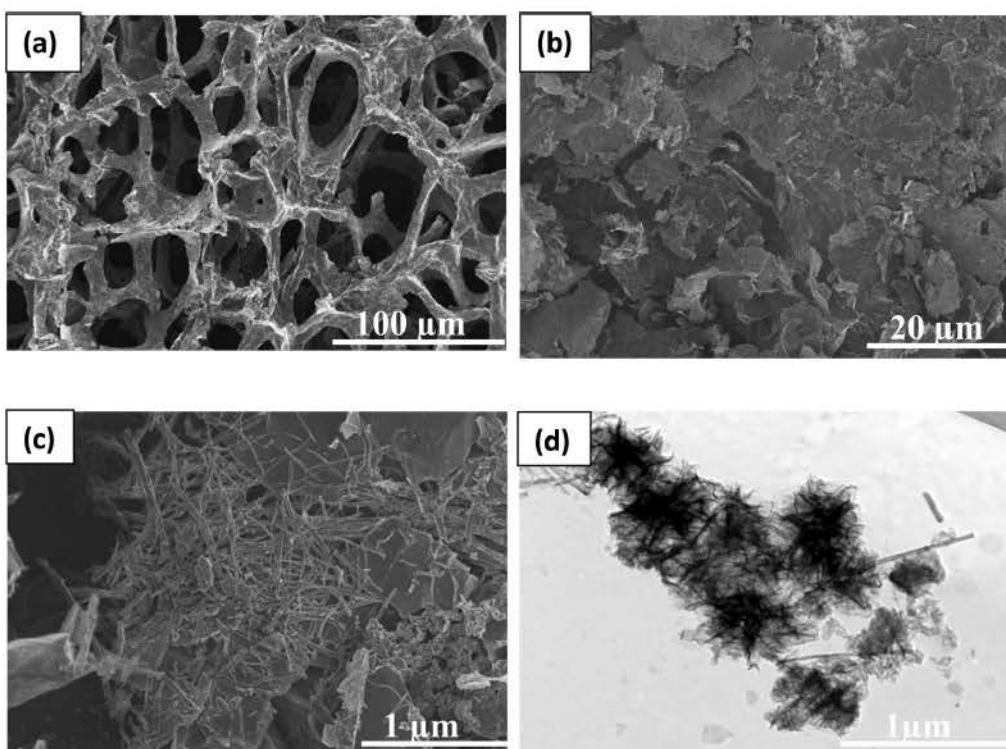


FIG. 4. SEM images of (a) graphene foam, (b, c) graphene foam/MnO<sub>2</sub> composite at different magnifications, and (d) TEM image of the graphene foam/MnO<sub>2</sub> composite.

deposition. Fig. 4(b)-4(c) are SEM images of the final GF/MnO<sub>2</sub> composite at different magnifications.

Fig. 4(c) reveals that most of the MnO<sub>2</sub> nanostructures took on a needle-like structure, which was further confirmed by transmission electron microscopy Fig. 4(d). TEM micrographs also revealed a porous, interconnected network of graphene flakes that was expected to improve the capacitive performance of the composite by enabling easy access of ions and high ionic mobility at the electrode/electrolyte interface.

Cyclic voltammetry (CV) of GF/MnO<sub>2</sub> electrode at different scan rates in a three electrode configuration is shown in Fig. 5(a), the CVs of the GF/MnO<sub>2</sub> exhibit square-like shape in a potential window of (0-1 V vs Ag/AgCl), indicating ideal capacitive performance. The galvanostatic charge-discharge curves measured at three different current densities are shown in Fig. 5(b). From these curves, the specific capacitance was calculated using equation (1). At current densities of 0.2 Ag<sup>-1</sup>, 0.5 Ag<sup>-1</sup> and 0.7 Ag<sup>-1</sup> the calculated specific capacitance values of GF/MnO<sub>2</sub> electrode are 478, 341, and 266 Fg<sup>-1</sup> respectively. The good capacitive performance can be attributed to

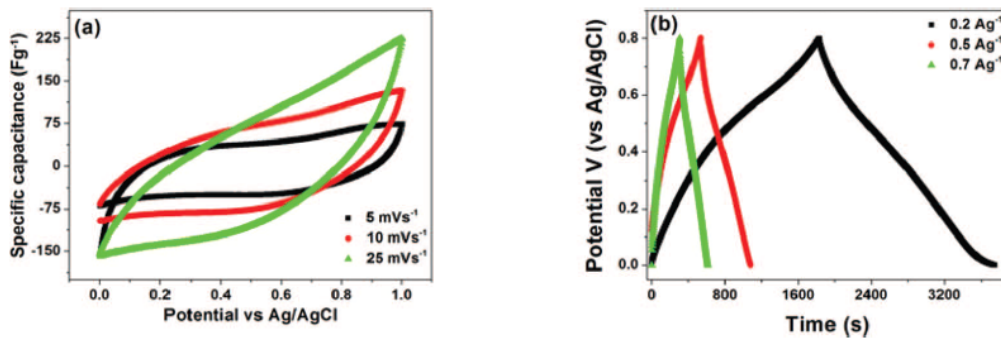


FIG. 5. (a) Cyclic voltammetry curves of GF/MnO<sub>2</sub> measured at 5, 10 and 25 mVs<sup>-1</sup>; (b) galvanostatic charge-discharge profiles of GF/MnO<sub>2</sub> electrode at three different current densities in a three electrode configuration.

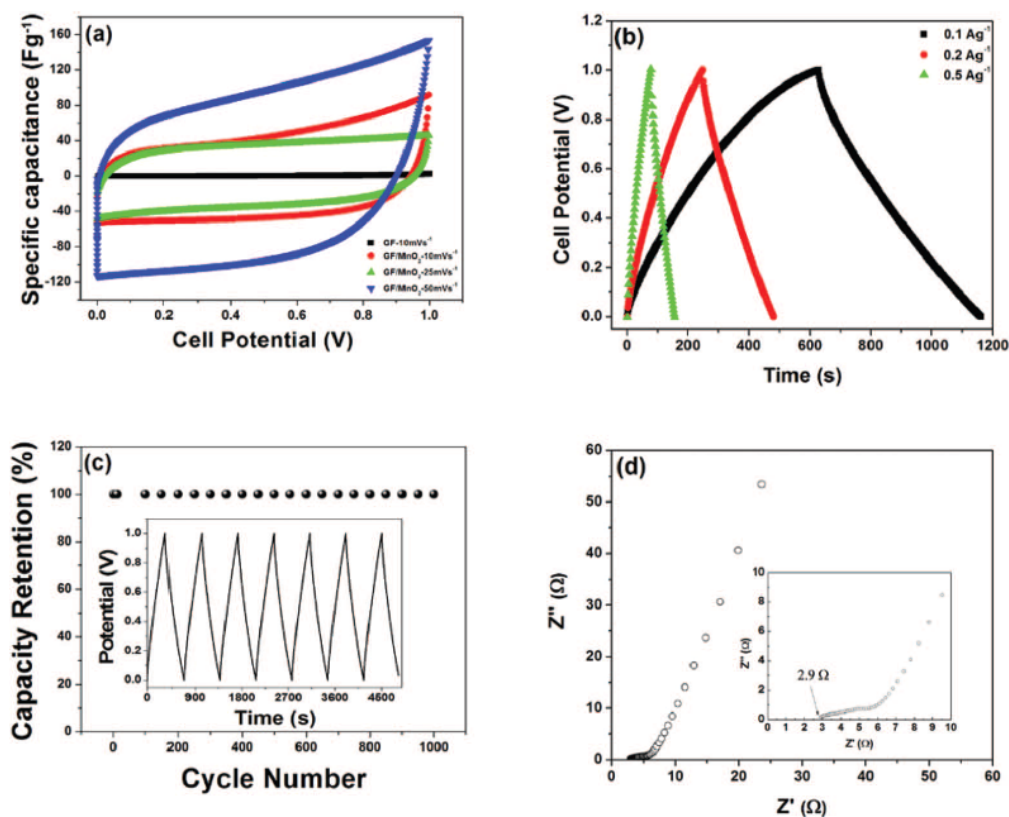


FIG. 6. Electrochemical characterizations of graphene foam/MnO<sub>2</sub> composites: (a) CVs of GF at scan rate of 10 mV/s and GF/MnO<sub>2</sub> composite at scan rates of 10, 25 and 50 mV/s; (b) the galvanostatic charge-discharge curves at three different current densities; (c) the capacity retention of the composite at a current density of 0.5 Ag<sup>-1</sup>, inset shows the continuous charge-discharge curve; and (d) Nyquist plot for the GF/MnO<sub>2</sub> composite.

the good contact made between the MnO<sub>2</sub> and GF, which enhances the low-conductivity of MnO<sub>2</sub> needle-like structure, thus enhancing the utilization of the composite in pseudocapacitive reaction leading to rapid charge transport mechanism which results in fast dynamics and easy access to ions in electrolyte thereby reducing the diffusion resistance.

Fig. 6(a) shows the Symmetric CV of the GF at a scan rate of 10 mV/s and of the GF/MnO<sub>2</sub> composite at scan rates of 10 mV/s, 25 mV/s and 50 mV/s. The CV data for the GF appears as a straight line in the plot, indicating that it had a very low capacitance compared to the GF/MnO<sub>2</sub> composite. In contrast, the CV loops for GF/MnO<sub>2</sub> composite supercapacitor are nearly rectangular in shape, which is an indication of good capacitive behaviour and low contact resistance.<sup>1</sup> The

enhanced capacitive result is attributed to the electrochemical capacitance from MnO<sub>2</sub> since it is obvious that the electric double-layer capacitance from GF is very small as seen from the CV. Thus, >90% of capacitance comes from MnO<sub>2</sub>, at least at low scan rates. CV loops expand with increasing scan rate and maintain the rectangular shape, which is a characteristic of increasing current response of the device, indicating a capacitive performance of the MnO<sub>2</sub> needle-like structure on GF up to 50 mV/s.

Cyclic performance of electrodes material is very important for practical applications. Galvanostatic charge-discharge measurements were performed on GF/MnO<sub>2</sub> composite at different current densities in the potential range from 0 to 1V and the data are presented in Fig. 6(b). It was observed that the GF/MnO<sub>2</sub> composite curves deviated from a linear shape, showing a contribution from redox processes. The capacitance of the cell was calculate using equation (1) while the maximum specific capacitance of the electrode material obtained using equations (2) was 240 Fg<sup>-1</sup> at a current density of 0.1 Ag<sup>-1</sup>, compared to 17 Fg<sup>-1</sup> for the GF at the same current density. The high specific capacitance was attributed to the presence of needle-like MnO<sub>2</sub>. The small voltage (IR) drop observed (from charge discharge curves) indicates a low internal resistance of the device, consistent with a good adhesion between the nanostructured oxide and GF surface that improved the conductivity of electrodes.

The capacitance retention as a function of cycle number is presented in Fig. 6(c). The figure shows that after 1000 cycles at a current density of 0.5 Ag<sup>-1</sup>, the GF/MnO<sub>2</sub> composite symmetric supercapacitor device retained its initial specific capacitance. The energy storage (*E*) per unit mass of the GF/MnO<sub>2</sub> electrode and the maximum energy density of the coin cell was calculated using the equation (3) for *C* corresponding to *C*<sub>sp</sub> and *C*<sub>cell</sub> respectively. The values were found to be 34 Whkg<sup>-1</sup> and 8.3 Whkg<sup>-1</sup>.

$$E = \frac{1}{2} \frac{C V^2}{M}, \quad (3)$$

where *V* is the potential window and *M* is the total mass of electrode material.

Fig. 6(d) shows the Nyquist plot of the GF/MnO<sub>2</sub> composite electrode. It is a representation of the real and imaginary parts of the impedance in the sample. The plot is divided into two regions; the high-frequency region, which is a characteristic of the charge transfer process taking place at the electrode\electrolyte interface and a straight line in the low-frequency region, which represents the electron-transfer diffusion process. The intercept at the high frequency region on the x-axis corresponds to the resistance of the electrolyte solution (*R*<sub>s</sub>), and is also referred to as the equivalent series resistance (ESR) which comprises of the resistance of aqueous electrolyte, the intrinsic resistance of the composite material and the contact resistance at the electrode interface. The inset to Fig. 6(d) shows that there is no loop at high frequency that might correspond to contact resistance and the ESR value for the GF/MnO<sub>2</sub> composite electrode is found to be 2.9 Ω. This is a good value for composite containing 80% of poorly conducting metal oxide. This can be attributed to the good conductivity of GF.

The maximum power density (*P*<sub>max</sub>) of the GF/MnO<sub>2</sub> electrodes was calculated using equation (4):

$$P_{\max} = \frac{V^2}{4MR_s} \quad (4)$$

where *V* is voltage applied (1 V), *R*<sub>s</sub> (2.9 Ω) is the ESR, and *M* (4.5 mg) is the total mass of active material in the two electrodes. The maximum power density obtained for the GF/MnO<sub>2</sub> composite is 20 kWkg<sup>-1</sup>.

Our symmetric (same anode and cathode) GF/MnO<sub>2</sub> composite supercapacitor exhibited a specific capacitance, energy density of electrode material and power density values of 240 Fg<sup>-1</sup>, 34 Whkg<sup>-1</sup> and 20 kWkg<sup>-1</sup> respectively, which are comparable to the values reported by Rakhi *et al.*<sup>39</sup> for symmetric supercapacitors with graphene nanoplatelets-(γ-MnO<sub>2</sub>/CNT)-nanocomposite electrodes in 1 M KOH. At the maximum voltage of 1 V they reported an electrode energy density of 43 Whkg<sup>-1</sup> and a power density of 26 kWkg<sup>-1</sup>. Higher energy and power density values were reported for asymmetric devices, the voltage window for which can be extended to 2 V. For example

Fan *et al.* have reported an energy density of  $51.1 \text{ Wh kg}^{-1}$  and power density of  $102.2 \text{ W kg}^{-1}$  for an asymmetric supercapacitor using a graphene/MnO<sub>2</sub> composite as a positive electrode and activated carbon nanofibers as a negative electrode in a neutral aqueous Na<sub>2</sub>SO<sub>4</sub> electrolyte,<sup>45</sup> while Choi *et al.* reported values of  $44 \text{ Wh kg}^{-1}$  and  $25 \text{ kW kg}^{-1}$  for energy and power densities of asymmetric supercapacitor device of chemically modified graphene e-CMG/e-CMG-MnO<sub>2</sub> composite.<sup>44</sup> Our results in the symmetric configuration with the maximum voltage window of 1 V give values that are comparable to those obtained in the asymmetric configuration. Therefore, GF with hydrothermally deposited MnO<sub>2</sub> needles-like structure is a promising candidate for capacitive energy storage.

#### IV. CONCLUSIONS

Graphene foam/MnO<sub>2</sub> composite electrodes have been fabricated by hydrothermal deposition of MnO<sub>2</sub> from KMnO<sub>4</sub>, and their electrochemical properties have been tested in a symmetric device with Na<sub>2</sub>SO<sub>4</sub> as the electrolyte. The 3D porous network structure of GF allows for a uniform coating and high loading of  $\alpha$ - and  $\gamma$ -MnO<sub>2</sub> needle-like structures. The composite exhibits a specific capacitance of  $240 \text{ F g}^{-1}$  at a current density of  $0.1 \text{ A g}^{-1}$  and no change in capacitance was observed after 1000 cycles at a current density of  $0.5 \text{ A g}^{-1}$ . The composite electrodes exhibited energy and power densities of  $34 \text{ Wh kg}^{-1}$  and  $20 \text{ kW kg}^{-1}$  respectively, which are among the highest values reported so far for symmetric two-electrode cells. The results obtained here indicate that graphene foam/MnO<sub>2</sub> composites are promising for electrochemical applications.

#### ACKNOWLEDGMENTS

This work is based upon research supported by the South African Research Chairs Initiative of the Department of Science and Technology (DST) and the National Research Foundation (NRF). Any opinion, findings and conclusions or recommendations expressed in this work are those of authors and therefore the NRF and DST do not accept any liability with regard thereto. A.T.C.J acknowledges support from the LRSM, through the U.S. National Science Foundation MRSEC, Grant No. DMR-1120901. Y.G. was supported by the US Department of Energy, Energy Storage Systems Research Program through Sandia National Laboratory. A. B. acknowledges the financial support from University of Pretoria for his study from both Energy Institutional research theme (IRT) and PhD bursary scheme.

- <sup>1</sup> B. E. Conway, *Electrochemical Supercapacitors Scientific Fundamentals and Technological Applications* 1999.
- <sup>2</sup> P. Simon and Y. Gogotsi, "Capacitive Energy Storage in Nanostructured Carbon-Electrolyte Systems," *Acc. Chem. Res.* **46**, 1094–1103 (2012).
- <sup>3</sup> J. Miller and A. Burke, "Electrochemical capacitors: challenges and opportunities for real-world applications," *Electrochem. Soc. Inter.* **17**, 53–57 (2008).
- <sup>4</sup> A. S. Aricò, P. Bruce, B. Scrosati, J.-M. Tarascon, and W. Van Schalkwijk, "Nanostructured materials for advanced energy conversion and storage devices," *Nat. Mater.* **4**, 366–77 (2005).
- <sup>5</sup> R. Kötz, "Principles and applications of electrochemical capacitors," *Electrochim. Acta* **45**, 2483–2498 (2000).
- <sup>6</sup> X. Zhao, B. M. Sánchez, P. J. Dobson, and P. S. Grant, "The role of nanomaterials in redox-based supercapacitors for next generation energy storage devices," *Nanoscale* **3**, 839–55 (2011).
- <sup>7</sup> P. J. Hall, M. Mirzaeian, S. I. Fletcher, F. B. Sillars, A. J. R. Rennie, G. O. Shitta-Bey, G. Wilson, A. Crude, and R. Carter, "Energy storage in electrochemical capacitors: Designing functional materials to improve performance," *Energy Environ. Sci.* **3**, 1238–1251 (2010).
- <sup>8</sup> A. Burke, "R&D considerations for the performance and application of electrochemical capacitors," *Electrochim. Acta* **53**, 1083–1091 (2007).
- <sup>9</sup> E. Frackowiak and F. Béguin, "Carbon materials for the electrochemical storage of energy in capacitors," *Carbon* **39**, 937–950 (2001).
- <sup>10</sup> S. W. Lee, B. M. Gallant, H. R. Byon, P. T. Hammond, and Y. Shao-Horn, "Nanostructured carbon-based electrodes: bridging the gap between thin-film lithium-ion batteries and electrochemical capacitors," *Energy Environ. Sci.* **4**, 1972–1985 (2011).
- <sup>11</sup> L. L. Zhang, R. Zhou, and X. S. Zhao, "Graphene-based materials as supercapacitor electrodes," *J. Mater. Chem.* **20**, 5983–5992 (2010).
- <sup>12</sup> F. Du, D. Yu, L. Dai, S. Ganguli, V. Varshney, and A. K. Roy, "Preparation of Tunable 3D Pillared Carbon Nanotube-Graphene Networks for High-Performance Capacitance," *Chem. Mater.* **23**, 4810–4816 (2011).
- <sup>13</sup> J. R. Miller and P. Simon, "Materials science. Electrochemical capacitors for energy management," *Science* **321**, 651–2 (2008).

- <sup>14</sup>W. Wei, X. Cui, W. Chen, and D. G. Ivey, "Manganese oxide-based materials as electrochemical supercapacitor electrodes," *Chem. Soc. rev.* **40**, 1697–721 (2011).
- <sup>15</sup>J. Liu, J. Essner, and J. Li, "Hybrid Supercapacitor Based on Coaxially Coated Manganese Oxide on Vertically Aligned Carbon Nanofiber Arrays," *Chem. Mater.* **22**, 5022–5030 (2010).
- <sup>16</sup>C.-Y. Chen, C.-Y. Fan, M.-T. Lee, and J.-K. Chang, "Tightly connected MnO<sub>2</sub>-graphene with tunable energy density and power density for supercapacitor applications," *J. Mater. Chem.* **22**, 7697–7700 (2012).
- <sup>17</sup>M. Sang-Bok, N. Kyung-Wan, Y. Won-Sub, Y. Xiao-Qing, A. Kyun-Young, O. Ki-Hwan, and K. Kwang-Bum, "Electrochemical properties of manganese oxide coated onto carbon nanotubes for energy-storage applications," *J. Power Sources* **178**, 483–489 (2008).
- <sup>18</sup>A. E. Fischer, K. A. Pettigrew, D. R. Rolison, R. M. Stroud, and J. W. Long, "Incorporation of homogeneous, nanoscale MnO<sub>2</sub> within ultraporos carbon structures via self-limiting electroless deposition: Implications for electrochemical capacitors," *Nano lett.* **7**, 281–286 (2007).
- <sup>19</sup>R. I. Jafri, A. K. Mishra, and S. Ramaprabhu, "Polyaniline–MnO<sub>2</sub> nanotube hybrid nanocomposite as supercapacitor electrode material in acidic electrolyte," *J. Mater. Chem.* **21**, 17601–17605 (2011).
- <sup>20</sup>J. Kim, K. H. Lee, L. J. Overzet, and G. S. Lee, "Synthesis and Electrochemical Properties of Spin-Capable Carbon Nanotube Sheet/MnO<sub>2</sub>," *Nano Lett.* **11**, 2611–2617 (2011).
- <sup>21</sup>H. Wang, C. Li-Feng, Y. Yang, H. S. Casalongue, J. T. Robinson, Y. Liang, Y. Cui, and H. Dai, "Mn<sub>3</sub>O<sub>4</sub>-Graphene Hybrid as a High Capacity Anode Material for Lithium Ion Batteries," *J. Am. Chem. Soc.* **132**, 13978–13980 (2010).
- <sup>22</sup>J. Zhu and J. He, "Facile synthesis of graphene-wrapped honeycomb MnO<sub>2</sub> nanospheres and their application in supercapacitors," *ACS appl. mater. interfaces* **4**, 1770–1776 (2012).
- <sup>23</sup>L. Li, Z.-Y. Qin, L.-F. Wang, H.-J. Liu, and M.-F. Zhu, "Anchoring alpha-manganese oxide nanocrystallites on multi-walled carbon nanotubes as electrode materials for supercapacitor," *J. Nanoparticle Res.* **12**, 2349–2353 (2010).
- <sup>24</sup>M. D. Stoller, S. Park, Y. Zhu, J. An, and R. S. Ruoff, "Graphene-based ultracapacitors," *Nano lett.* **8**, 3498–3502 (2008).
- <sup>25</sup>Y. Wang, Z. Q. Shi, Y. Huang, Y. Ma, C. Wang, M. Chen, and Y. Chen, "Supercapacitor Devices Based on Graphene Materials," *J. Phy. Chem. C* **113**, 13103–13107 (2009).
- <sup>26</sup>Z. Chen, W. Ren, L. Gao, B. Liu, S. Pei, and H-M Cheng, "Three-dimensional flexible and conductive interconnected graphene networks grown by chemical vapour deposition," *Nat. mater.* **10**, 424–428 (2011).
- <sup>27</sup>Y. Chen, X. Zhang, P. Yu, and Y. Ma, "Electrophoretic deposition of graphene nanosheets on nickel foams for electrochemical capacitors," *J. Power Sources* **195**, 3031–3035 (2010).
- <sup>28</sup>H. Ji, L. Zhang, M. Pettes, H. Li, and S. Chen, "Ultrathin graphite foam: A three-dimensional conductive network for battery electrodes," *Nano lett.* **12**, 2446–2451 (2012).
- <sup>29</sup>X. Huang, X. Qi, F. Boey, and H. Zhang, "Graphene-based composites," *Chem. Soc. rev.* **41**, 666–686 (2012).
- <sup>30</sup>Y. Xu, X. Huang, Z. Lin, X. Zhong, Y. Huang, and X. Duan, "One-step strategy to graphene/Ni(OH)<sub>2</sub> composite hydrogels as advanced three-dimensional supercapacitor electrode materials," *Nano Res.* **6**, 65–76 (2012).
- <sup>31</sup>S. Chen, J. Zhu, X. Wu, Q. Han, and X. Wang, "Graphene oxide–MnO<sub>2</sub> nanocomposites for supercapacitors," *Acs Nano* **4**, 2822–2830 (2010).
- <sup>32</sup>J. Yan, Z. Fan, T. Wei, W. Qian, M. Zhang, and F. Wei, "Fast and reversible surface redox reaction of graphene–MnO<sub>2</sub> composites as supercapacitor electrodes," *Carbon* **48**, 3825–3833 (2010).
- <sup>33</sup>Q. Cheng, J. Tang, J. Maa, H. Zhanga, N. Shinyaa, and L.-C. Qinc, "Graphene and nanostructured MnO<sub>2</sub> composite electrodes for supercapacitors," *Carbon* **49**, 2917–2925 (2011).
- <sup>34</sup>Z. Li, J. Wang, S. Liu, X. Liu, and S. Yang, "Synthesis of hydrothermally reduced graphene/MnO<sub>2</sub> composites and their electrochemical properties as supercapacitors," *J. Power Sources* **196**, 8160–8165 (2011).
- <sup>35</sup>Y. Qian, S. Lu, and F. Gao, "Preparation of MnO<sub>2</sub>/graphene composite as electrode material for supercapacitors," *J. Mater. Sci.* **46**, 3517–3522 (2011).
- <sup>36</sup>X. Dong, X. Wang, J. Wang, H. Song, X. Li, L. Wang, M. B. Chan-Park, C. M. Li, and P. Chen, "Synthesis of a MnO<sub>2</sub>-graphene foam hybrid with controlled MnO<sub>2</sub> particle shape and its use as a supercapacitor electrode," *Carbon* **50**, 4865–4870 (2012).
- <sup>37</sup>A. Bello, K. Makgopa, M. Fabiane, D. Dodoo-Ahrin, K. I. Ozoemena, and N. Manyala, "Chemical adsorption of NiO nanostructures on nickel foam-graphene for supercapacitor applications," *J. Mat. Sci.* (2013).
- <sup>38</sup>M. D. Stoller and Rodney S. Ruoff, "Best practice methods for determining an electrode material's performance for ultracapacitors," *Energy Environ. Sci.* **3**, 1294–1301 (2010).
- <sup>39</sup>R. B. Rakhi, W. Chen, D. Cha, and H. N. Alshareef, "Nanostructured Ternary Electrodes for Energy-Storage Applications," *Adv. Energy Mater.* **2**, 381–389 (2012).
- <sup>40</sup>A. C. Ferrari, "Raman spectroscopy of graphene and graphite: disorder, electron-phonon coupling, doping and nonadiabatic effects," *Solid State Comm.* **143**, 47–57 (2007).
- <sup>41</sup>T. Gao, H. Fjellvåg, and P. A. Norby, "comparison study on Raman scattering properties of  $\alpha$ - and  $\beta$ -MnO<sub>2</sub>," *Analytica Chim. Acta* **648**, 235–239 (2009).
- <sup>42</sup>Z. Ni, T. Yu, Z. Luo, Y. Wang, and L. Liu, "Probing charged impurities in suspended graphene using Raman spectroscopy," *ACS Nano* **3**, 569–574 (2009).
- <sup>43</sup>L. Chen, L.-J. Sun, F. Luan, Y. Liang, Y. Li, and X-X Liu, "Synthesis and pseudocapacitive studies of composite films of polyaniline and manganese oxide nanoparticles," *J. Power Sources* **195**, 3742–3747 (2010).
- <sup>44</sup>Z. Fan, J. Yan, T. Wei, L. Zhi, G. Q. Ning, T. Y. Li, and F. Wei, "Asymmetric Supercapacitors Based on Graphene/MnO<sub>2</sub> and Activated Carbon Nanofiber Electrodes with High Power and Energy Density," *Adv. Funct. Mater.* **21**, 2366–2375 (2011).
- <sup>45</sup>B. G. Choi, M. Yang, W. H. Hong, J. W. Choi, and Y. S. Huh, "3D macroporous graphene frameworks for supercapacitors with high energy and power densities," *ACS nano* **6**, 4020–8 (2012).

## Summary

A low-cost and scalable approach has been used for the production of uniformly distributed MnO<sub>2</sub> on GF to form a composite of GF/MnO<sub>2</sub> composite. Supercapacitor electrodes based on this composite material have been successfully fabricated and demonstrated excellent electrochemical performance in both two and three electrode configuration. At a current density of 0.2 A g<sup>-1</sup> the composite exhibited a specific capacitance of 478 F g<sup>-1</sup> in a three electrode configuration and a specific capacitance of 240 F g<sup>-1</sup>, power and energy density of 26 kW Kg<sup>-1</sup> and 34 W h Kg<sup>-1</sup> respectively in a two electrode cell configuration. These results contribute to an important advancement in the field of energy storage technology (supercapacitors) and demonstrate that electrodes based on the three dimensional form of graphene has a great potential for practical applications.

## References

- [1] H-J. Cui, J-W. Shi, F. Liu, M-L. Fu, *J. Mater. Chem.* **21** (2011) 18527.
- [2] D.Y. Li, H.D. Liu, Y.F. Chen, **32** (2011) 3657.
- [3] R.B. Rakhi, W. Chen, D. Cha, H.N. Alshareef, *Adv. Energy Mater.* **2** (2012) 381.
- [4] H. Yang, J. Jiang, W. Zhou, L. Lai, L. Xi, Y.M. Lam, Z. Shen, B. Khezri, T. Yu, *Nanoscale Res. Lett.* **6** (2011) 531.
- [5] S.K. Meher, P. Justin, G.R. Rao, *ACS Appl. Mater. Inter.* **3** (2011) 2063.
- [6] X. Wang, Y. Li, *J.Chem. Eur.* **9** (2003) 300.
- [7] H. Wang, Z. Lu, D. Qian, Y. Li, W. Zhang, *Nanotechnology* **18** (2007) 115616.
- [8] Z. Song, *J. Alloys Compd.* **560** (2013) 151.
- [9] M.D. Stoller, R.S. Ruoff, *Energy Environ. Sci.* **3** (2010) 1294.

## **4.6 Non-covalent functionalization of graphene foam with pyrene carboxylic acid (PCA) as electrode for electrochemical storage**

This section discusses the effect of functional groups on the graphene foam (GF) by a non-covalent approach. Functionalization of graphene with pseudocapacitive or chemical moieties have been described as a method to prevent the graphene from restacking or forming agglomeration during electrode preparation and hence improve its electrochemical performance [1,2]. Non-covalent functionalization is particularly attractive because of the possibility of adsorbing various functional groups onto the graphene surface through the weak van der Waals (vdW) interaction or the common non-destructive  $\pi$ - $\pi$  interaction mechanism thereby preserving superior physical and electronic properties of graphene [3]. The GF in this work was treated with pyrene carboxylic acid (PCA) which acts as a source of oxygen and/ or hydroxyl groups attached to the surface of the GF for improved electrochemical performance. A specific capacitance of  $133 \text{ F g}^{-1}$ , power density  $\sim 145 \text{ kW kg}^{-1}$ , and energy density  $\sim 4.7 \text{ W h kg}^{-1}$  was achieved based on the functionalized foam in 6 M KOH aqueous electrolyte. The results suggest that non-covalent functionalization might be an effective approach to overcome the restacking problem associated with graphene electrodes. Detailed procedure of the functionalization and fabrication of electrode will be discussed in the attached paper which was just accepted for publication in the journal of solid state electrochemistry.

## **Results and discussions: Publication6 Functionalized graphene foam as electrode for improved electrochemical storage**

### **Introduction**

Over the past few years, the interesting and fascinating properties of graphene has attracted a lot of research activities from various fields for both applied and fundamental studies [4]. This material is a two-dimensional (2D) allotrope of carbon comprises a monoatomic sheet of  $sp^2$  hybridized carbon atoms tightly bound in a honeycomb lattice that exhibits unique electronic structure, high specific surface area ( $2630 \text{ m}^2 \text{ g}^{-1}$ ), high electrical conductivity, chemical stability and structural flexibility [5–7]. These has led to explore of graphene and graphene based functional materials for a wide range of possible applications such as electronics, sensors, composite materials, photocatalysis, energy storage and conversion [8–13]. Supercapacitors are energy storage systems that have attracted interest because of its unique mechanism of storing energy [14]. They are power devices with versatile range of applications such as portable electronic devices, hybrid electric device and high-pulse power backup [15]. Due to the long cycle life and rapid charge-discharge supercapacitors could be used as hybrid systems in batteries and fuel cells [16]. However, such excellent devices require electrode materials with high specific surface area, excellent electrical conductivity and porosity. Carbonaceous material such as activated carbon [17,18], CNTs [19] and more recently graphene [20] are considered as energy storage material because of their conductivity and high surface to volume ratio. Therefore several research activities have been focused on modification of these materials for improved energy storage by increasing the contact area at the electrode-electrolyte interface.

Mechanical exfoliation of graphite is known to produce graphene flakes with exceptional electronic properties. However, this method of graphene production is suitable for

fundamental studies and is unsuitable for large scale production and practical applications [7]. To date, a great number of works have reported large scale production of graphene based on chemical modification of Hummer's method [21,22]. This technique involves the oxidation of graphite to graphene oxide using strong acids and oxidizing agent, and subsequently using strong reducing agent such as hydrazine ( $N_2H_4$ ) and sodium borohydride ( $NaBH_4$ ) for reduction of the graphene oxide to graphene. The graphene sheets obtained from this method are usually defective due to the oxidation or reduction steps, and hence restacking or irreversible aggregation of the sheets often lead to decrease in the electrical conductivity during the reduction process and hence exhibit low electrochemical performance [2,23]. The graphene sheets tend to aggregate forming graphite insolubility in most common solvent due to strong van der Waals interactions [24]. To overcome this problem, fillers, spacers or pseudocapacitive materials are considered which prevent restacking of the graphene sheet thereby improving the performance of the capacitors. Alternatively, functionalization of the graphene sheets with carbonyl or hydroxyl groups could also reduce the degree of aggregation of the sheets as well as creating pathways for ion transportation [1]. A variety of surface functionalization of graphene have been reported, some of which include; functionalization with aromatic molecules [25], amidation [26], polymers and esterification of carboxylic groups in poly(vinyl alcohol) PVA [27,28], salinization with hydroxyl groups [29] and composite reinforcement [30]. However, most of these functionalization techniques distort the  $sp^2$  structure of graphene and which tend to convert into  $sp^3$ , leading to decrease in charge mobility and inferior electronic properties [31]. To overcome this problem, non-covalent functionalization has been employed because of its ability to manipulate the electronic and chemical properties without disrupting the  $sp^2$  hybrid structure of graphene. Non-covalent functionalization is particularly attractive because of the possibility of adsorbing various functional groups onto the graphene surface through the

weak van der Waals (vdW) interaction or the common non-destructive  $\pi$ - $\pi$  interaction mechanism thereby preserving superior physical and electronic properties of graphene [3].

To date, a number of techniques for non-covalent functionalization of graphene for desirable applications have been investigated. For example, non-covalent molecular functionalization has been used to dope single layer graphene and to induce band-gap in bilayer graphene [32,33], for surface transfer doping of diamond (100) with tetrafluorotetracyanoquinodimethane [34], for reduction of sheet resistance in organic photovoltaic cells (OPVs) [35], to improve the selectivity and sensitivity of molecular biosensors [36,37] and for electrochemical storage applications [38,39]. Therefore, a step towards developing high performance electrode material for electrochemical capacitors based on functionalized graphene sheet is highly desirable. The high loading capacity of these functional groups onto the graphene sheet is essential for their application and development.

In this work we report on the growth of highly crystalline three dimensional graphene foam using nickel foam as a template via chemical vapour deposition (CVD) and modification of the sheets by employing non-covalent functionalization technique [40]. The successful functionalization has been achieved by a simple non-covalent functionalization with 1-pyrenecarboxylic acid (PCA) in N, N dimethylformamide (DMF). Due to the amphilic nature of PCA with high solubility in DMF, an effective complex is formed which leads to attachment of PCA molecules on the surface of the graphene. The as-functionalized material was used for fabrication of electrode for supercapacitor device. The device demonstrated good electrochemical performance including excellent cycle stability in a two electrode symmetric configuration.

## **Experimental**

### **Synthesis of graphene foam (GF).**

Graphene foam (GF) was synthesised by CVD onto a catalytic nickel foam (Munich Germany). The detailed procedure is described in our previous report [41]. To provide mechanical support for the GF during etching of the nickel, polymethylmethacrylate (PMMA) was drop coated on the sample and baked at 180 °C for 30 minutes. The samples were then placed in 3 M HCl solution at 80 °C, left overnight to ensure complete removal of the nickel. The resulting GF sample was placed in acetone at 50 °C for 30 minutes to remove the PMMA. The samples were then rinsed with deionised water and dried.

### **Thermal Treatment (Oxidation) of Graphene Foam in Air.**

The GF was transferred into a crucible boat and placed inside an open air furnace and heated at 550 °C for 1 h for oxidation of the sample.

### **Functionalization of graphene foam.**

The oxidised GF was functionalized via a non-covalent method using 1-pyrene carboxylic acid (PCA) and dimethylformamide (DMF). 0.5 g of PCA was dissolved in 50 ml of DMF solution. 20 mg of oxidised GF was then added to the mixture, ultrasonicated at 90 °C for 12 hours to obtain a homogeneous dispersed mixture. The functionalized graphene was separated by centrifugation at 5000 rpm and the supernatant solution was collected in a vial. The solid powder was washed with DMF several times and dried at 60 °C in an electric oven. Both, solution and solid powder will be analyzed in this work.

### **Characterization and measurements.**

X-ray diffraction (XRD) patterns of the samples were collected using an XPERT-PRO diffractometer (PANalytical BV, Netherlands) with theta/2θ geometry, operating with a cobalt tube at 35 kV and 50 mA. The concentration of the materials was determined by UV-vis spectra measurements using a Perkin Elmer Lambda 40 UV-Vis-NIR spectrophotometer.

All measurements were performed in air in the 250-500 nm range with a resolution of 1 nm. Raman spectra were recorded using a WiTec-alpha 300R+ confocal Raman spectrometer (WiTec GmbH). The excitation source was the 532-nm laser line focused through a numerical aperture of 0.9 and 100x magnification. The surface morphology of the sample was investigated using the high resolution Zeiss Ultra plus 55 field emission scanning electron microscope (FESEM) operated at 2.0 kV. Transmission electron microscopy (TEM) images were obtained with a JEOL JEM-2100F microscope operated at 200 kV. XPS measurements were obtained using a VersaProbe 5000 with an Al K $\alpha$  x-ray source.

The electrochemical measurements were carried out in a conventional two electrode configuration. The working electrodes were prepared by mixing 85 wt. % of GF with 10 wt. % carbon black and 5 wt. % polyvinylidene difluoride (PVdF) binder in an agate mortar. The mixture was then dissolved in 1-methyl-2-pyrrolidinone (NMP) to form a paste. The homogenous paste was coated onto a Ni foam current collector and dried at 60 °C in an oven for 8 hours to ensure complete evaporation of the NMP. The total mass of the active material in the working electrodes was ~ 4 mg, and the two electrodes with identical mass were selected for measurement. The coin cell was made by sandwiching both electrodes sandwiched between a Whatman filter paper separator. The cell was evaluated in a 6 M KOH aqueous electrolyte solution using cyclic voltammetry (CV), galvanostatic charge-discharge (GV) and electrochemical impedance spectroscopy (EIS) using a Bio-logic SP-300 PGSTAT. The EIS plot was evaluated in the frequency region of 100 kHz to 10 mHz.

## **Results and discussion**

XRD pattern and EDX of the GF is shown in figure 1: figure 1 (a) show diffraction peaks at  $2\theta=31^\circ$  and  $64.5^\circ$ , corresponds to the (002) and (004) reflections of hexagonal graphite, respectively. No diffraction peaks corresponding to nickel is evidenced revealing that nickel has been completely removed from the graphene foam during the etching process. EDX

elemental analysis was also used to confirm the removal of nickel as shown in figure 1 (b) evidencing only the presence of carbon in the sample.

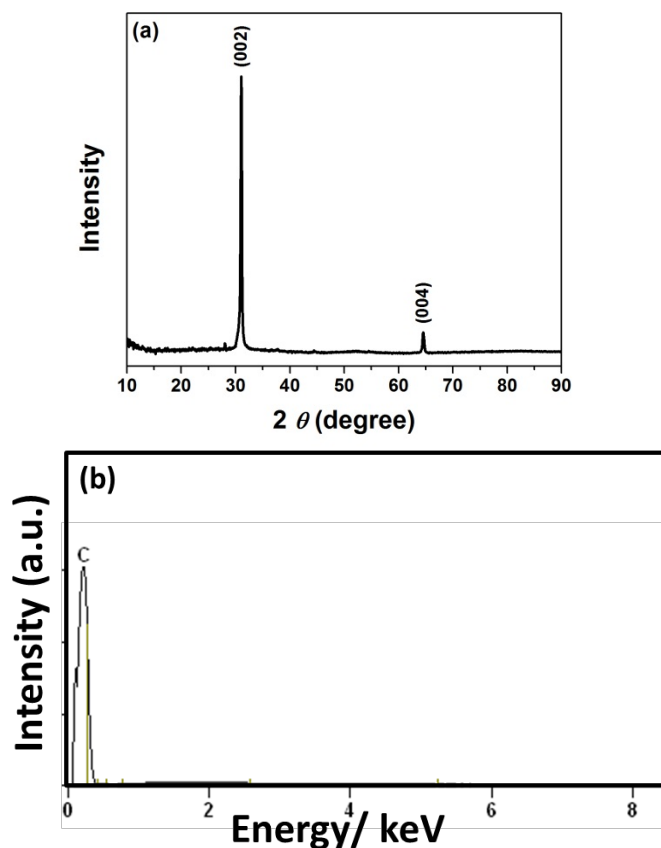


**Figure 1** XRD and EDX pattern of GF after etching process.

The formation of functionalized GF is confirmed by UV-vis absorption spectroscopy PCA is a polyaromatic hydrocarbon that contains a polar carboxylic acid group and a nonpolar pyrene group. The polar group makes it soluble in most common solvent such as DMF and methanol which also have polar groups attached to them. The pyrene group consists of a  $\pi$ -conjugated network structure surrounded by clouds of delocalized  $\pi$  electrons. The pyrene group has a mixed hexagonal and aromatic structure thereby forming a  $\pi$ - $\pi$  aromatic interaction. The resulting PCA-GF complex is soluble in DMF due to the presence of the polar group attached to the surface of the GF. Figure 2 shows the UV-vis absorption of the functionalized samples before and after washing them with DMF. The changing of color of

the solution color before and after reaction (shown in the inset to figure 2) also proves the addition of PCA molecules to the GF. The aqueous solution remains very stable with very little precipitates observed after one week of storage. Such excellent dispersibility of GF makes it very favourable for further applications. From this figure, very weak absorbance peaks are observed for unwashed functionalized GF. This weak absorbance is due to the presence of GF and excess unreacted PCA that renders the solution opaque [39]. This unreacted PCA was removed by washing and centrifuging the solution several times. After washing, absorption peaks for PCA became clearly distinguishable evidencing PCA molecules functionalized on the GF.

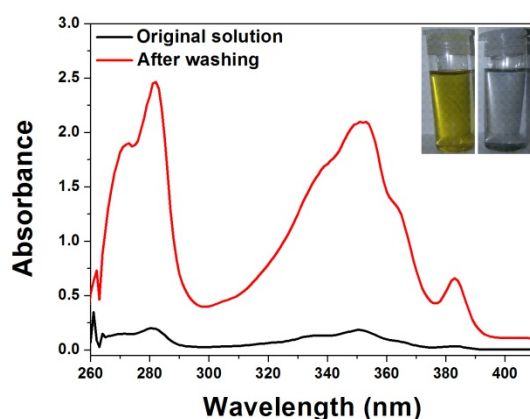


**Figure 2** UV-vis of functionalized GF before and after washing with DMF.

Figure 3 shows the Raman spectrum of few layer graphene flakes forming the GF. The spectrum consists of two major peaks at ( $1579.9\text{ cm}^{-1}$ ) and ( $2705.7\text{ cm}^{-1}$ ). These peaks correspond to the G and 2D modes of graphene. The G peak is due to the in-plane vibrations of the  $sp^2$  carbon atoms in the lattice while the 2D band originate from a second-order process, involving two in-plane transverse optical (iTO) phonons near the K point for the 2D band or one iTO phonon and one defect in the case of the D-band. The symmetric shape and higher intensity of the 2D peak compared to the G-peak indicates few layers graphene. The absence of the D-peak related to the presence of disorder at  $1350\text{ cm}^{-1}$ , shows that the GF is

of high crystallinity [42]. The absence of the disorder peak after functionalization also indicates that the sample preserved its  $sp^2$  hybridization. The inset to figure 3 evidences a red-shift of G-peak ( $1589.7\text{ cm}^{-1}$ ) after functionalization. The G band shift and reduction of the 2D are result of charge transfer between the graphene and PCA molecules [43,44], thus indicating surface functionalization of GF surface with PCA molecules via non-covalent method.

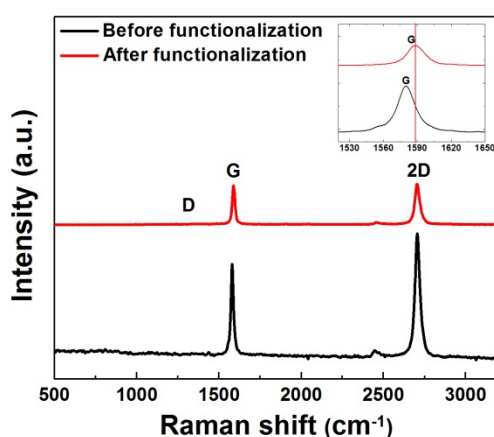


**Figure 3** Raman spectra of as grown GF and functionalized GF (f-GF).

To further confirm the modification of the GF by PCA X-ray photoelectron spectroscopy (XPS) was performed to know the content of oxygen and also to estimate the degree of functionalization. As shown in figure 4 the C1s spectrum of f-GF can be fitted into four peaks at 284.5, 285.1, 286.7, and 289.1 eV corresponding to carbon atoms in four functional groups: non-oxygenated carbon (C–C or C=C, 284.5 eV), carbon in C–O bonds (285.1 eV), carbonyl carbon (C=O, 286.7 eV) and carboxylate carbon (O–C=O, 289.1 eV) validating presence and significant amount of functional groups in the sample [45,46].

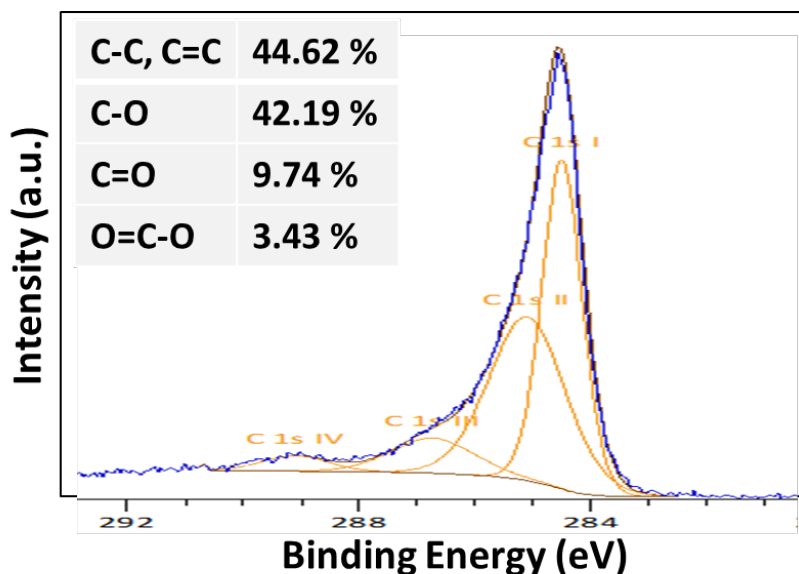


**Figure 4** C1s XPS profile of f-GF.

The structure of both GF and f-GF was characterized by scanning electron microscopy (SEM) and transmission electron microscopy (TEM). As shown in figure 5 (a), the graphene takes the Ni foam template which is three dimensional (3D) in shape. The 3D graphene structure provides abundant surface and binding sites for adsorption of hydroxyl groups. In other words this network structure of the GF provides an excellent platform for accommodating and integrating functional groups for applications due to the large inherent surface area of the GF. Inset to this figure shows high magnification image of the sheets which reveals high crystallinity. It also reveals the presence of wrinkles and ripples on the graphene sheets which is due to the different thermal expansion coefficients of Ni and graphene during the CVD synthesis [47]. Figure 5 (b) shows the image of the functionalized GF. It can be observed that the 3D structure was distorted during functionalization process (sonification) and the extremely small thickness of the resulting f-GF sheets lead to a wrinkling topology [30]. Inset also shows that the sheets still maintain their crystallinity after functionalization. A TEM image of f-GF is shown in figure 5 (c) which shows the presence of few layers as confirmed by Raman spectroscopy. The inset shows the selected area

electron diffraction (SAED) pattern that displays bright hexagonal rings corresponding to the (100) reflection from the graphene plane, suggesting the  $sp^2$  hybrid structure and electronic properties of the GF were preserved after functionalization. This is very important for preparation of electrode material based on the functionalized graphene foam.

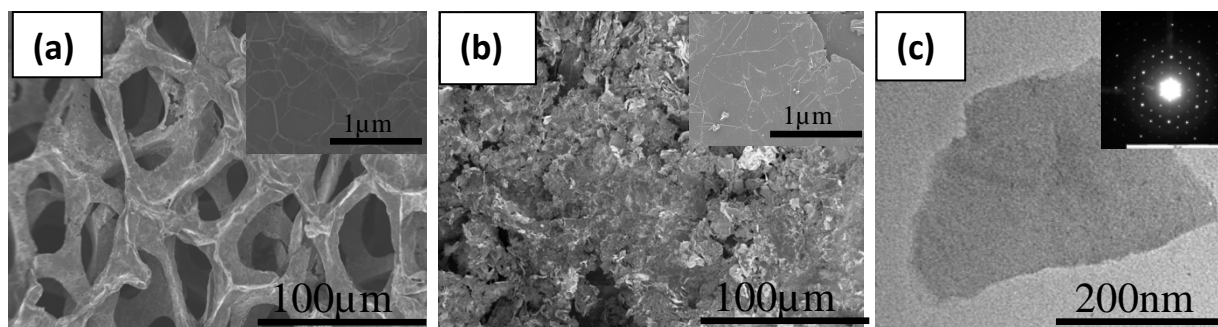


**Figure 5** SEM images of (a) GF, (b) f-GF (c) TEM image of f-GF.

The electrochemical behavior of GF and f-GF was characterized by cyclic voltammetry (CV), galvanostatic charge-discharge (CD) and electrochemical impedance spectroscopy (EIS). Figure 6 (a) compares CV curves for both GF and f-GF devices at a scan rate of  $100 \text{ mV s}^{-1}$ . Both CV curves exhibit rectangular shape which demonstrates pure Electrical double-layer capacitors (EDLC) behaviour. Inset show the CV of the GF however, the f-GF device exhibits a superior current response when compared to GF device. This could be attributed to the presence of oxygen containing functionalities contributing to the EDLC of the GF.

Cyclic performance and high life-cycle stability of an electrode material are very important parameters for evaluating a supercapacitor device for practical applications. Galvanostatic charge-discharge (CD) measurements were performed on the device at different current densities in the potential range of 0 and 1 V and are shown in figure 6 (b). It is observed that the CD curves were linear and symmetrical which are characteristic of ideal capacitor behaviour. The voltage (IR) drop observed (from charge discharge curve) was also very negligible, which indicates low internal resistance for the supercapacitor device. The cell

capacitance  $C$  in F was then calculated from the galvanostatic charge-discharge curves according to equation 1.

$$C_{cell} = \frac{i\Delta t}{\Delta v} \quad (1)$$

where  $i$  is the constant current for charge-discharge,  $\Delta t$  is the discharge time and  $\Delta v$  is the discharge voltage.

The specific capacitance ( $C_{sp}$  in F g<sup>-1</sup>) was then calculated according to the following equation 2.

$$C_{sp} = \frac{4C_{cell}}{m} \quad (2)$$

where  $m$  is the mass of active material in a single electrode in the cell.

The capacitance of the cell was calculated using equation (1) while the maximum specific capacitance of the electrode material obtained using equations (2) was 133 F g<sup>-1</sup> at a current density of 0.25 A g<sup>-1</sup>. In comparison with device made from the GF, the specific capacitance and energy density were higher compared to that shown in our previous work [48].

The energy storage ( $E$ ) per unit mass of the f-GF electrode and the maximum energy density of the coin cell was calculated using the equation (3) for  $C$  corresponding to  $C_{sp}$  and  $C_{cell}$  respectively. The values were found to be 18.5 W h kg<sup>-1</sup> and 4.7 W h kg<sup>-1</sup>, while the maximum power density ( $P_{max}$ ) for the f-GF device was calculated using equations (4) below and was found to be 145.3 kW kg<sup>-1</sup>.

$$E = \frac{1}{2} \frac{CV^2}{M}, \quad (3)$$

$$P_{\max} = \frac{V^2}{4MR_s} \quad (4)$$

Where  $V$  is voltage applied,  $R_s$  is the equivalent series resistance (ESR) obtained from the intercept of the real axis from the Nyquist and  $M$  is the total mass of active electrode material in the cell.

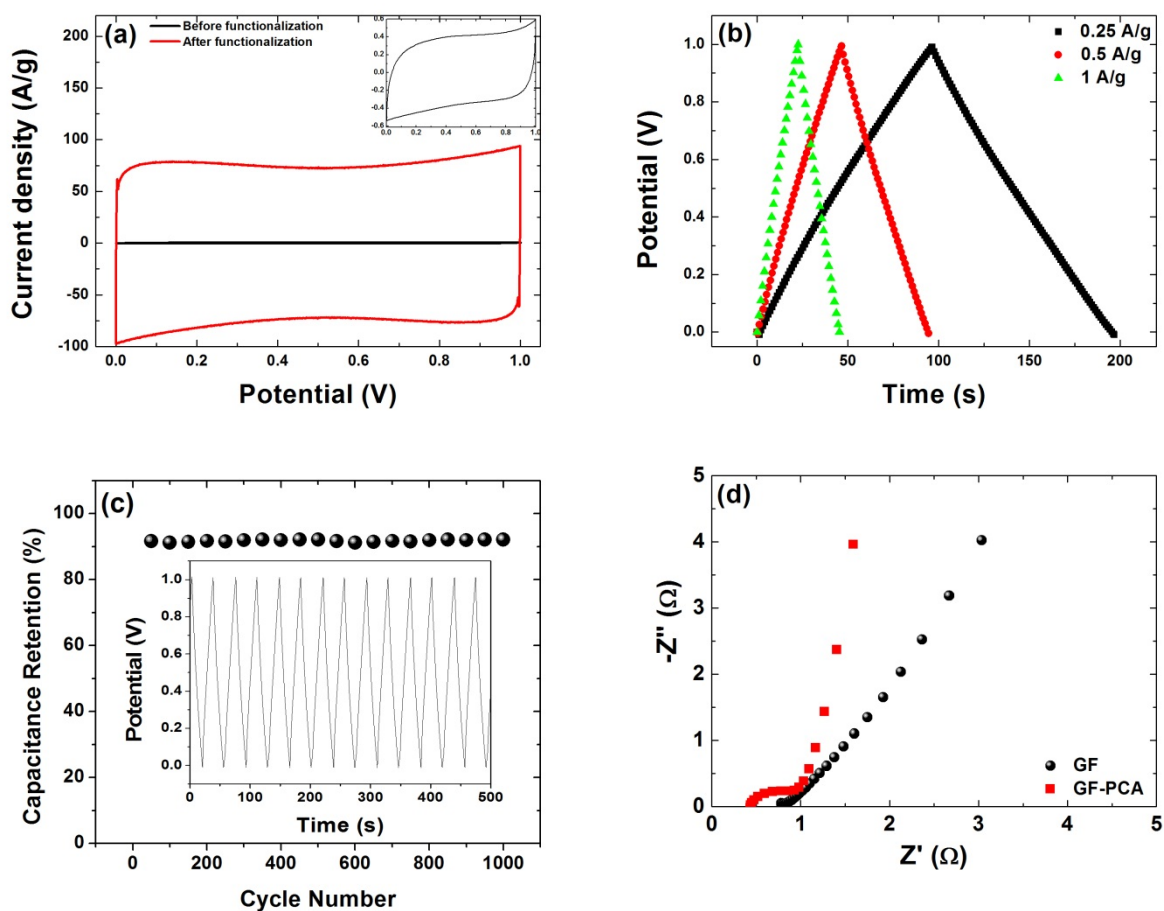


**Figure 6** (a) CVs of GF and f-GF at scan rate of  $100 \text{ mV s}^{-1}$  (b) galvanostatic charge-discharge curves at three different current densities of f-GF (c) the capacity retention of the composite at a current density of  $0.5 \text{ A g}^{-1}$ , inset shows the continuous charge-discharge curve. (d) Nyquist plot for the GF and f-GF.

The long-term cycling stability of supercapacitor is also a significant parameter for their practical application. Figure 6 (c) shows the variation of capacitance retention of f-GF with

cycle number for a potential between 0 and 1 V. It is obvious that f-GF based device displays excellent cycling stability over the entire cycle numbers and retains 91 % of the initial capacitance. This result indicates that f-GF based supercapacitor have good cycling stability and high reversibility in the repetitive charge-discharge process.

Electrochemical impedance spectroscopy (Nyquist plot) is a powerful tool for analysis of the electrochemical characteristics of electrode/electrolyte interfacial processes and evaluation of rate constants. Fig. 6 (d) shows of EIS GF and the f-GF electrode. It is a representation of the real and imaginary parts of the impedance of the device. The plot is divided into two regions; a partial semicircle in the high-frequency region, which is characteristic of the charge transfer process taking place at the electrode\electrolyte interface and a straight line in the low-frequency region, which represents the electron-transfer diffusion process [49]. The solution resistance refers to the resistance from the electrolyte, and the charge-transfer resistance corresponds to the total resistance at the electrode\electrolyte interface. The intercept at the high frequency region on the x-axis corresponds to the internal resistance of the electrolyte electrode and is also referred to as the equivalent series resistance (ESR) including the resistance of aqueous electrolyte, the intrinsic resistance of the f-GF material and the contact resistance at the electrode interface. From the figure, the ESR value for the electrodes of the f-GF was found to be 0.43  $\Omega$ . which is smaller than that of GF 0.9  $\Omega$ . This value demonstrates that there is efficient exchange of ions at the electrode/electrolyte interface.

## Summary

In summary, based on the results obtained it shows that PCA can be used successfully to functionalize GF without disrupting its  $sp^2$  hybrid structure via non covalent functionalization approach. This technique not only ensures efficient usage of the surface area offered by the foam but also reduces the agglomeration of the sheets due to the presence of oxygen

containing groups, and hydroxyls from the PCA molecules which lead to improve capacitance of the GF. The results clearly show that electrochemical performance of GF can be improved via functionalization with electro active materials.

## References

- [1] Y. Fang, B. Luo, Y. Jia, X. Li, B. Wang, Q. Song, F. Kang, L. Zhi, *Adv. Mater.* **24** (2012) 6348.
- [2] K. Loh, Q. Bao, P. Ang, J. Yang, *J. Mater. Chem.* **20** (2010) 2277.
- [3] Y. Xu, H. Bai, G. Lu, C. Li, G. Shi, *J. Am. Chem. Soc.* **130** (2008) 5856.
- [4] A. Geim, K. Novoselov, *Nat. Mater.* **6** (2007) 183.
- [5] A. Balandin, S. Ghosh, W. Bao, *Nano Lett.* **8** (2008) 907.
- [6] K. Novoselov, A. Geim, S. Morozov, *Science* **306** (2004) 666.
- [7] J.H. Changgu Lee, Xiaoding Wei, Jeffrey W. Kysar, *Science* **80** (2008) 321.
- [8] Y. Zhu, D. James, J. Tour, *Adv. Mater.* **24** (2012) 4924.
- [9] D. Chen, H. Feng, J. Li, *Chem. Rev.* **112** (2012) 6027.
- [10] Y. Zhu, S. Murali, W. Cai, X. Li, *Adv. Mater.* **22** (2010) 3906.
- [11] V. Dua, S.P. Surwade, S. Ammu, S.R. Agnihotra, S. Jain, K.E. Roberts, S. Park, R.S. Ruoff, S.K. Manohar, *Angew. Chem.* **49** (2010) 2154.
- [12] G. Eda, H. Unalan, *Appl. Phys. Lett.* **93** (2008) 233502.
- [13] G. Dimitrakakis, E. Tylianakis, G. Froudakis, *Nano Lett.* **8** (2008) 3166.
- [14] B.E. Conway, *Electrochemical Supercapacitors Scientific Fundamentals and Technological Applications* 1999.
- [15] P.J. Hall, M. Mirzaeian, S.I. Fletcher, F.B. Sillars, A.J.R. Rennie, G.O. Shitta-Bey, G. Wilson, A. Cruden, R. Carter, *Energy Environ. Sci.* **3** (2010) 1238.
- [16] Y. Wang, L. Cheng, Y. Xia, *J. Power Sources* **153** (2006) 191.
- [17] J. Yan, T. Wei, B. Shao, F. Ma, Z. Fan, *Carbon N. Y.* **48** (2010) 1731.
- [18] E. Frackowiak, F. Beguin, F. Béguin, *Carbon N. Y.* **39** (2001) 937.
- [19] C. Du, N. Pan, *Nanotechnology* **17** (2006) 5314.
- [20] C. Liu, Z. Yu, D. Neff, A. Zhamu, B.Z. Jang, *Nano Lett.* **10** (2010) 4863.
- [21] W.H. Jr, R. Offeman, *J. Am. Chem. Soc.* **80** (1958) 1339.

- [22] S. Stankovich, D. Dikin, R. Piner, Carbon N. Y. **45** (2007) 1558.
- [23] S. Park, J. An, I. Jung, R.D. Piner, S.J. An, X. Li, A. Velamakanni, R.S. Ruoff, Nano Lett. **9** (2009) 1593.
- [24] D. Dreyer, S. Park, Chem. Soc. Rev. **38** (2010) 228.
- [25] Q. Su, S Pang, V. Alijani, C. Li, X. Feng, Adv. Mater. **21** (2009) 3191.
- [26] S. Niyogi, E. Bekyarova, M. E. Itkis, J. L. McWilliams, M. A. Hamon, J. Am. Chem. Soc. **128** (2006) 7720.
- [27] S. Park, D. A. Dikin, S. T. Nguyen, J. Phys. Chem. C **113** (2009) 15801.
- [28] H. Salavagione, M. Gómez, G. Martínez, Macromolecules **42** (2009) 6331.
- [29] S. Hou, M. L. Kasner, S. Su, K. Patel, J. Phys. Chem. C **114** (2010) 14915.
- [30] H. Yang, F. Li, C. Shan, D. Han, Q. Zhang, L. Niu, A. Ivaska, J. Mater. Chem. **19** (2009) 4632.
- [31] H. Liu, Y. Liu, D. Zhu, J. Mater. Chem. **21** (2011) 3335.
- [32] X. Dong, D. Fu, W. Fang, Y. Shi, P. Chen, L. Li, Small **5** (2009) 1422.
- [33] X. Dong, Y. Shi, Y. Zhao, D. Chen, J. Ye, Y. Yao, Phys. Rev. Lett. **102** (2009) 135501.
- [34] P. Strobel, M. Riedel, J. Ristein, L. Ley, Nature **430** (2004) 8084.
- [35] C. Hsu, C. Lin, J. Huang, C. Chu, K. Wei, L. Li, ACS Nano **6** (2012) 5031.
- [36] H. Liu, J. Gao, M. Xue, N. Zhu, M. Zhang, T. Cao, Langmuir **25** (2009) 12006.
- [37] N.G. Shang, P. Papakonstantinou, M. McMullan, M. Chu, A. Stamboulis, A. Potenza, S.S. Dhesi, H. Marchetto, Adv. Funct. Mater. **18** (2008) 3506.
- [38] S. Ghosh, X. An, R. Shah, D. Rawat, B. Dave, S. Kar, S. Talapatra, J. Phys. Chem. C **116** (2012) 20688.
- [39] X. An, T. Simmons, R. Shah, C. Wolfe, K.M. Lewis, M. Washington, S.K. Nayak, S. Talapatra, S. Kar, Nano Lett. **10** (2010) 4295.
- [40] Z. Chen, W. Ren, L. Gao, B. Liu, S. Pei, H. Cheng, Nat. Mater. **10** (2011) 424.
- [41] A. Bello, K. Makgopa, M. Fabiane, D. Dodoo-Ahrin, K.I. Ozoemena, N. Manyala, J. Mater. Sci. **48** (2013) 6707.
- [42] A. Ferrari, Solid State Commun. **143** (2007) 47.

- [43] R. Kitaura, N. Imazu, K. Kobayashi, H. Shinohara, *Nano Lett.* **8** (2008) 693.
- [44] J. Zhou, H. Song, L. Ma, X. Chen, *RSC Adv.* **1** (2011) 782.
- [45] J. Hu, A. Ramadan, F. Luo, B. Qi, X. Deng, J. Chen, *J. Mater. Chem.* **21** (2011) 15009.
- [46] S. Park, J. An, R.D. Piner, I. Jung, D. Yang, A. Velamakanni, S.T. Nguyen, R.S. Ruoff, *Chem. Mater.* **20** (2008) 6592.
- [47] S. J. Chae, F. Gunes, K. K. Kim, E. S. Kim, Y.H.L.H. Han, S. M. Kim, H-J Shin, S-M Yoon, J-Y Choi, M. H. Park, C. W. Yang, D. Pribat, *Adv. Mater.* **21** (2009) 2328.
- [48] A. Bello, O.O. Fashedemi, J.N. Lekitima, M. Fabiane, D. Dodoo-Arhin, K.I. Ozoemena, Y. Gogotsi, A.T. Charlie Johnson, N. Manyala, *AIP Adv.* **3** (2013) 82118.
- [49] J. Gamby, P.. Taberna, P. Simon, J.. Fauvarque, M. Chesneau, *J. Power Sources* **101** (2001) 109.

# Chapter 5

## General Conclusions

Synthesis of various three dimensional (3D) composite of graphene with metal or metal oxide of high quality and purity has been successfully achieved using different techniques. Electrochemical characterizations were performed on these materials as possible electrodes for electrochemical capacitors and the electron kinetics have also being studies. Hybridization of this 3D graphene with different metal or metal oxide as well as non-covalent functionalization with PCA have all shown enhanced electrochemical properties of the final hybrid or functionalized electrode. These conclusions are given in the results and discussions where it has been demonstrated that the unique three dimensional structure of the graphene provides the surface area for the integration of various electro active species resulting in improved electrochemical performance of the composite materials.

In general, chemical vapor deposition (CVD) growth of graphene samples have revealed a unique and 3D network structure which has been explained as due to the inherent properties of the starting material (nickel foam). The morphology of the graphene foam reveals wrinkles and ripples which are possibly due to the difference in thermal coefficient expansion between the nickel foam and carbon during the CVD growth. The unique structure offers a suitable surface area for integration of electro active material as already explained.

In section 4.1 silver particles were deposited on the graphene foam by electron-beam which slightly introduces defect into the samples. The resulting composite showed increase in conductivity which enhances the entire performance of the composite as electrode material for electrochemical capacitor. The enhanced electrochemical performance could be due to the improved electrical conductivity and synergistic effect provided by Ag particles to the 3D

GF. The electron kinetics and diffusion properties shows that the composite electrodes exhibit a reversible process

Section 4.2 presents NiO deposited on the 3D graphene by successive ionic layer adsorption and reaction (SILAR). The composite also exhibited excellent electrochemical performance with a specific capacitance of  $783 \text{ F g}^{-1}$  at a scan rate of  $2 \text{ mV s}^{-1}$ . The enhanced electrochemical performance has been explained as due to the direct synthesis of graphene on the nickel foam by CVD which provide a 3D conducting network platform suitable for adsorption of NiO nanostructures.

Section 4.3 presents preparation of novel composite of simonkolleite and the 3D graphene using aqueous chemical growth (ACG). The composite also showed good electrochemical result and suggesting that simonkolleite might be excellent electrochemical active specie for improved electrochemical performance.

Sections 4.4 and 4.5 demonstrate the incorporation of  $\text{MnO}_2$  into the 3D structure of via reflux and microwave technique the resulting composite electrode presented enhanced performance. The microwaved samples exhibited a specific capacitance of  $305 \text{ F g}^{-1}$  at a current density of  $1 \text{ A g}^{-1}$  in a three electrode cell configuration while the composite from the reflux system exhibits a specific capacitance of  $240 \text{ F g}^{-1}$  at a current density of  $0.1 \text{ A g}^{-1}$  and exhibited energy and power densities of  $34 \text{ W h kg}^{-1}$  and  $20 \text{ kW kg}^{-1}$  with 100 % retention of its initial capacitance after 1000 cycles in a two electrode cell configuration and  $478 \text{ F g}^{-1}$  at a current density of  $0.2 \text{ A g}^{-1}$  in a three electrode configuration.

Section 4.6 presents the effect of surface functionalization on the 3D graphene using non-covalent functionalization approach. This technique not only ensures efficient usage of the surface area offered by the foam but also reduces the agglomeration of the sheets due to the presence of oxygen containing groups, and hydroxyls from the PCA molecules which lead to

improve capacitance of the GF. The results clearly show that electrochemical performance of GF can be improved via functionalization with electro active materials.

All these results have clearly demonstrated the great potential of 3D graphene based composite materials as novel electrode for energy storage application such as electrochemical capacitors.

## Chapter 6

### Future work

Material morphology is very important for improved electrochemical performance because it is related to the specific surface area (SSA) and the diffusion of ions in the electrode thus; three-dimensional network materials have been shown to be very promising for electrochemical capacitors as demonstrated by most of the results obtained due to its larger SSA. This unique structure of graphene allows for preparation several composites. Combining different materials to form composites is advantageous because the individual materials in the composites have a synergistic effect through particle size minimization, prevents agglomeration in the composite material and enhances specific surface area (SSA) for better electrochemical performance. Materials with large SSA such as layered double hydroxide and conducting polymers still need to be studied to get more information and insight on the effects of these materials on the 3D graphene foam. Also, one-step synthesis of these composite materials without the addition of conductive additives would be beneficial for electrode performance. Fully understand and optimize the growth parameters of the composite materials for optimum electrochemical performance. Study the nature of bonding and coupling effects between the 3D graphene foam and these materials and finally fabricate symmetric and asymmetric devices that can operate in the high voltage regions using different liquids such as organic or ionic liquid.